Université de Montréal

Study of Liquid Crystalline Light Responsive Dye-Polyelectrolyte Complexes

Par
Qian Zhang

Département de chimie
Faculté des arts et des sciences

Thèse présentée à la Faculté des études supérieures
en vue de l'obtention du grade de Philosophiae Doctor (Ph.D.) en chimie

Avril 2009

Université de Montréal
Faculté des études supérieures

Cette thèse intitulée

Study of Liquid Crystalline Light Responsive Dye-Polyelectrolyte Complexes

Présentée par :
Qian Zhang

A été évaluée par un jury composé des personnes suivantes :

Prof. J. X. Zhu, président-rapporteur
Prof. C. G. Bazuin, directrice de recherche
Prof. F. Winnik, membre du jury
Prof. P. Rochon, examinateur externe
Prof. J. X. Zhu, représentant du doyen de la FES

À ma famille et Prof. C. Géraldine Bazuin,

To my family and Prof. C. Geraldine Bazuin,

Résumé

Dans un premier temps, une série de complexes formés d'un polyélectrolyte avec différents colorants mésogènes, contenant de l'azobenzene et un espaceur conventionnel, ont été synthétisés et étudiés. Les effets de la polarité du mésogène, de la longueur de l'espaceur, et du solvant sur les propriétés thermiques et la structure ont été examinés. Une mésophase smectique A (SmA) a été observée pour les complexes contenant un espaceur alkyle long (10 CH_2), alors que les complexes contenant un espaceur plus court (6 CH_2) sont isotropes. Des différences systématiques dans la structure SmA en fonction de la polarité du mésogène ont été observées. Afin de tenir compte de cet effet, un nouveau modèle impliquant l'agencement des paires d'ions et des unités dipolaires a été proposé. L'ajout d'une petite quantité de solvant peut transformer les complexes amorphes en complexes cristal liquides. Pour cette série, la biréfringence photo-induite (PIB) présente, de manière générale, une relaxation significative, de par la présence de l'espaceur flexible, et est fortement influencée par l'humidité. L'utilisation d'une nouvelle technique de diffraction des rayons X *in situ*, couplée à un laser, a permis de mettre en évidence la photo-isotropisation d'une mésophase ordonnée.

Un complexe polyélectrolyte-colorant ne possédant pas d'espaceur a été obtenu à partir de la poly(4-vinyl pyridine) méthylée (PVP) et de l'orange de méthyle (MO) commercialement disponible. Ce complexe demeure rigide jusqu'à hautes températures et se dégrade avant sa température d'isotropization. De plus, ce complexe présente des valeurs élevées de PIB et une excellente stabilité thermique et temporelle, et peut être gravé par un réseau relief à la surface (en anglais: "surface relief gratings (SRG)). Par la suite, une série de complexes ne possédant pas d'espaceur a été étudiée en faisant varier la longueur et le type de la queue alkyle. Tous ces complexes présentent une phase liquide cristalline stable. Les valeurs de PIB et les amplitudes des SRG ont été reliées à la structure chimique, en particulier à la présence d'unités flexibles ou rigides.

Lors de la synthèse des colorants sans espaceur, un complexe colorant/surfactant a été obtenu via une synthèse en une seule étape. Une série de ces complexes avec des longueurs

de chaînes alkyle variables ont été préparés et étudiée. Une mésophase de type smectique T (SmT) a été identifiée pour les complexes contenant une longue chaîne alkyle (12 et 16 unités CH_2).

Finalement, le complexe MO/PVP a été utilisé pour modifier les SRG et pour l'obtention de fibres électrofilées. Nous avons montré que la qualité des SRG dépend des conditions d'humidité lors de la fabrication. Ce dernier paramètre influence aussi la relaxation lors d'une exposition subséquente à l'humidité. L'utilisation d'ombrage par de l'or suivie de l'exposition des SRG à l'humidité contrôlée s'avère utile pour obtenir des profils SRG inusités. Les fibres électrofilées obtenues à partir du mélange MO/PVP et du poly(méthacrylate de méthyle) (PMMA) présentent de l'orientation et de la biréfringence, même si le composé MO/PVP n'est pas orienté.

Mots clés: colorant, polyélectrolyte, azobenzène, cristaux liquides, propriétés optiques.

Abstract

A series of stoichiometric azobenzene-containing dye-polyelectrolyte complexes with a conventional n-alkyl spacer were synthesized and investigated. The effects of mesogen polarity, spacer length and solvent on the thermal properties and molecular packing structure of the complexes were examined. A smectic A (SmA) phase is found in most complexes with a long alkyl spacer (10 CH_2), while most shorter spacer complexes (6 CH_2) appear isotropic. Systematic differences in the SmA structure depend on the polarity of the mesogenic core. A novel model was proposed to account for this. Solvent molecules can switch amorphous complexes into liquid crystalline ones. Photoinduced birefringence (PIB) generally showed significant relaxation in this series due to the flexible spacer, and was strongly influenced by exposure to humidity. Photoisotropization of an ordered mesophase was demonstrated using a novel setup of *in situ* X-ray diffraction coupled with a laser.

A spacer-free liquid crystalline dye-polyelectrolyte complex was constructed from commercial "methyl orange" (MO) and methylated poly(4-vinyl pyridine) (PVP). The MO/PVP complex is rigid up to high temperature, and decomposes before isotropization. It shows high PIB values with excellent temporal and thermal stability, and can be inscribed with surface relief gratings (SRGs). Subsequently, a series of spacer-free complexes with varying types and lengths of tail were investigated. They all show a stable liquid crystalline phase. The PIB and SRG performances are related to the chemical structure, in particular, the presence of flexible versus rigidifying molecular moieties.

A novel one-pot synthesis of dye-surfactant complexes was discovered during synthesis of the spacer-free dyes. A series of these complexes with varying alkyl tail lengths were prepared and investigated. A SmT-like mesophase was identified in those with long alkyl tails (12 and 16 methylene units). This mesophase is subject to photoisotropization.

Finally, the MO/PVP complex was utilized to explore SRG manipulation and to make electrospun fibers. It was shown that SRG quality and its collapse during subsequent exposure to 100% RH are influenced by ambient humidity conditions during fabrication. A "bottom-up" approach for post-modification of SRGs using gold-shadowing was explored.

Electrospun fibers of blends of MO/PVP and poly(methyl methacrylate) (PMMA) showed good birefringence and orientation, although the MO/PVP component was not oriented.

Key words: Dye, Polyelectrolyte, Azobenzene, Liquid crystal, Optical properties.

Table of contents

List of figures

List of schemes

List of tables

List of abbreviations

AFM	Atomic Force Microscopy
ATRP	Atom Transfer Radical Polymerization
BOO	Bond Orientational Order
CD	Cyclodextrin
CHNS	Carbon Hydrogen Nitrogen and Sulphur (elemental analysis)
DMF	Dimethylformamide
DSC	Differential Scanning Calorimetry
EDS	Energy Dispersive Spectroscopy
IMDS	Inter-Material Dividing Surface
LC	Liquid Crystal
LCE	Liquid Crystal Elastomer
LCP	Liquid Crystal Polymer
MCLCP	Main Chain Liquid Crystal Polymer
MO	Methyl Orange
NLO	Nonlinear Optics
OO	Orientational Order
P4VP	Poly(4-vinyl pyridine)
P4VPMe, PVP	Methylated poly(4-vinyl pyridine)
PA	Polyacrylate
PBA	Poly(4-biphenyl acrylate)
PDM	Poly(dimethylaminoethyl methacrylate)
PEO	Poly(ethylene oxide)
PIB, LIB	Photoinduced Birefringence (Light-Induced Birefringence)
PLC	Polymer Liquid Crystal
PMA	Polymethacrylate
PO	Positional Order
POM	Polarized Optical Microscopy
PS	Polystyrene
PSS	Polystyrene Sulfonate

PVA	Poly(vinyl alcohol)
PVS	Poly(vinyl sulfonate)
RAFT	Reversible Addition-Fragmentation Chain Transfer
SANS	Small Angler Neutron Scattering
SCLCP	Side Chain Liquid Crystal Polymer
SEM	Scanning Electron Microscopy
SM	Surfactomesogen
SRG	Surface Relief Grating
T_c	Clearing Temperature = isotropization temperature
TEM	Transmission Electron Microscopy
T_g	Glass Transition Temperature
TGA	Thermogravimetric Analysis
T_m	Melting Temperature
XRD	X-ray Diffraction

Acknowledgments

I would like to thank my supervisor, Professor C. Geraldine Bazuin, for giving me the most precious opportunity to carry out this research towards my Ph.D. degree. Her super kindness, profound knowledge, penetrating mind, great patience, magnanimous personality, great care of students, invaluable experience, very professional style and critical advice will undoubtedly benefit me throughout my life.

This research wouldn't have been possible without the financial support from the Chemistry Department, Faculty of Arts and Science, University of Montreal; Natural Sciences and Engineering Research Council (NSERC); le Fonds québécois de la recherche sur la nature et les technologies (FQRNT); Center of Self-assembled Chemical Structures (CSACS).

I would like to thank, in particular, Professor Barrett at McGill University and his group members: Oleh Tanchak, Peter Xiaoyu Lu, Kevin Yager, Zahid S. Mahimwalla, and Annie Dorris, for the productive collaboration and selfless help and assistance.

I would like to thank all the professors in the Chemistry Department of the University of Montreal for their great teaching and very useful advice: Professor Robert E. Prud'homme, Julian X. X. Zhu, Françoise Winnik, Christian Pellerin, André L. Beauchamp, Suzanne Giasson, William Skene, Jean-François Masson, Michel Lafleur, Garry S. Hanan and all others contributing to the department.

I would like to thank all the talented students and postdoctoral fellows I have had the great honour to work with in the groups of Bazuin, Prud'homme, Zhu, Winnik, Skene, Pellerin, Wuest, S. Giasson, Hanan, Charette, R. Giasson, Hanessian, Lafleur, Masson, Carrington and Badia. They are Qing Lu, Ximin Chen, Xin Wang, Mohamed Benouazzane, Afizatou Fassassi, Amine Fourati, Xavier Sallenave, Pascal Vuillaume, Alexis Laforgue, Carmen Tibirna, Irène Perepichka and Maksym Kryuchkov (Bazuin group); Matthieu

Jalabert, Damien Maillard, Jian Chen, Carol Fraschini, Sébastien Roland, Frédéric Céré, Ziru He, Jie Dong, Belonda Kalala and David Gaspard (Prud'homme group); Junhua Zhang, Juntao Luo, Marc Gauthier, Huiyou Liu, Stephan Freiberg, Wilms E. Baille, Qiang Wu, Jie Zhang, Guillaume Giguere, Yujuan Wang, Heloïse Therien-Aubin, Kai Wu, Xin Jia, Yu Shao, Jiawei Zhang, Ning Zhao, Yilong Chen and Ya Cao (Zhu group); Stéphane Dufresne, Marie Bourgeaux, Michael Gaultois, Andréanne Bolduc, Alex Bourque and Sergio Perez (Skene group); Qinmin Pan (R. Giasson group); Josoph Jianhua Wang (Hanan group); Xiaogang Wang (Carrington group), Wei Lin (Charette group); Beatrice Lego (S. Giasson group); Zhihui Shao, Yihua Hou, and Xueling Mi (Hanessian group); Jacqueline Sanchez (Badia group); Damien Mauran (also thanked for help in preparing the French version of abstract of this thesis), Yongri Liang, Xiaoxiao Wang, Yang Liu and Dominic Valiquette (Pellerin group); Tao Tu, Chengsong Hu, Hui Zhou, Eric Gagnon (Wuest group); Xingping Qiu (Winnik group), Gaulthier Rydzek, Marc-André Gagnon (Lafleur group); Olivier Bolduc, Ludovic S. Live, Audrey Cunche (Masson group); and, specially, Dr. Yubao Zhang (Prud'homme group) from whom I benefitted with many discussions.

I would like to thank Bo Qi, Yi Zhao and Haiwen Gu (Prof. Yue Zhao's group in the University of Sherbrooke) and Jonathan Milette (Prof. Linda Reven's group at McGill University) for useful discussions.

I would like to thank all the support personnel in the Chemistry Department for their super kind personalities and professional help: Pierre Ménard-Tremblay, Sylvain Essiembre and Julie Boivin (GPC, XRD and thermal analysis); Dr. Minh Tan Phan Viet, Sylvie Bilodeau and Dr. Cédric Malveau (NMR); Patricia Moraille and Samir Elouatik (AFM); Dr. Alexandra Furtos and Karine Venne (LC-MS); Francine Bélanger-Gariépy, Huguette Dinel, Elena Nadezhina, Michel Simard and Thierry Maris in elemental analysis (EA) and crystallography; Stéphane Béranger, Sylvie Marceau, Hélène Laliberté (undergraduate lab); Martin Lambert, Jean-François Myre, Julien Deltesta (retired), Louis Beaumont and Yves Teasdale in mechanical and electronics workshops, glassblower Cédric Ginart; all the secretaries, Line Laurin, Line Massé, Karine Poirier, Kevin Filiatrault, etc.,

and the personnel in the chemistry library, Malivanh Sananikone, Ginette Lacoursière Gignac, Richard Labelle and Suzanne Pitre.

I would like to thank S. Kelly Sears and Jeannie Mui for the super nice assistance with the TEM facilities, Petr Fiurasek (CSACS) from McGill, and Monica Iliescu Nelea, Stéphane Méthot (EDS, ESEM), Jingkui Chen Wei Ouyang, Gaoping Chen, Anik Chevrier and Zhiyong Fan from École Polytechnique de Montréal for their help.

I would like to thank all the service people in Pavillon J.-Armand Bombardier (PJAB): Saverio Seminara, Claude Laprise, François Lavigne, Maude Le Grelle, Richard Pharand and Maurice Martin; and all very responsible security people: Christian Majeau, Martin Page, Paul Stevens Nord and Leila Anani.

I would like to thank my former M.Eng. supervisor, Professor Xiaodong Fan at Northwestern Polytechnical University in Xi'an, China for his precious initiating supervision in research. He was also a former Ph.D. student in the Bazuin group. I learned from him many invaluable treasures inherited from Professor Bazuin and her group.

I would like to thank Entraide Bénévole Métro (EBM), Mme Elizabeth K. Chewey, Letitia Wallis and all the other warm-hearted people there, for sharing their joy and love in serving seniors. Thanks to the family of Mr. Appulingham for support and sharing their happiness.

Finally I would like to thank all my family members' long-lasting support, especially Qing Lu and former teacher (Northwestern Polytechnical University) Qi Ge's great and endless support during my Ph.D. studies and in the dark period since some of my family members were sick.

And in memory of Xin Li, a good guy.

Chapter 1. Introduction and Literature Review

Matter and their interactions constitute the physical world, which is complex and vast, and also full of mysteries, making it the "playground" of science research.

Compared to the vastness of the physical world, this thesis deals with only a tiny area; namely, azobenzene-containing liquid crystals constructed using supramolecular chemistry. As shown in Figure 1.1, this subject is a cross-section of three separate areas; namely, azobenzenes, liquid crystals and supramolecular chemistry. The research focuses on structure-property relations in these materials.

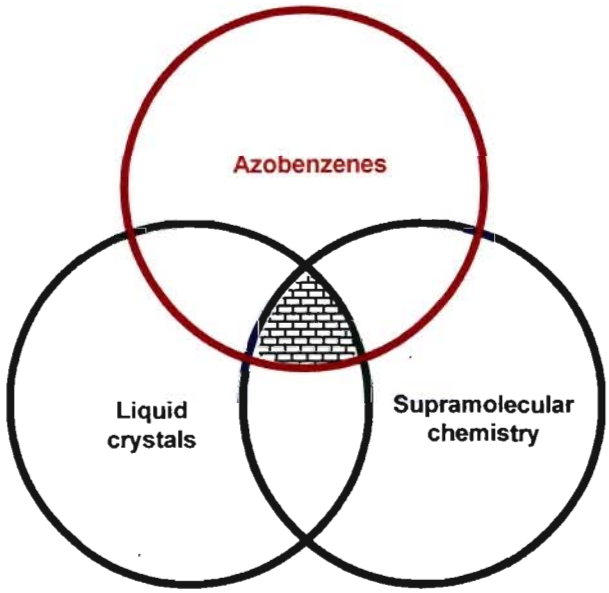

Figure 1.1 The cross section of the three areas represents the subject of this thesis.

This chapter will begin with an introduction to azobenzene (or azo for short), focusing mainly on its photoisomerization, photoinduced orientation and surface relief grating formation. Then, we will survey the science of liquid crystals and supramolecular chemistry, examining, in particular, the nature and photo-performance of azobenzene-containing liquid crystalline materials. This will be divided into two parts, conventional

covalent systems and supramolecular systems. Although it is impossible to cover everything, the intention of this introduction is that it reflects the great interest of azobenzene science, and the broadness and depth of research on azo-based materials.

1.1 Azo chromophores and colour chemistry

Ever since the discovery of diazo compounds in 1858 by Peter Griess,[1] thousands of azo compounds (based on -N=N-) have been prepared. This discovery was later stimulated by the demand for more efficient and vivid synthetic dyes which can be prepared on a much larger scale than natural ones.[2] Impressively, more than 60% of the manufactured dyes are azo dyes.[2] They have been widely applied for dying wool, silk, leather, and cellulosic and synthetic fibers.[2] They were also used as food colorants, although they are now strongly discouraged [for example, Sudan I and IV, both azo dyes, are not permitted as food colorants in Canada due to possible carcinogenicity (CBC News; Feb 24, 2005)].

The development of dyes and pigments is driven, in part, by the desire for colour, to satisfy visual aesthetics. In fact, our eyes can sense only a limited range of wavelengths, from 380 nm (violet) to 780 nm (red),[2] compared to a much wider range of useful wavelengths, from the picometer (10^{-12} m for gamma rays) to thousands of meters (10^{3} m for radio). The colour of dyes and pigments is determined by the light they absorb versus the nonabsorbed light. For example, a dye or pigment absorbing blue light (435-480 nm) in daylight is perceived as yellow.[2]

Most of the azo compounds studied in this thesis absorb light from 350 to 550 nm, and are usually coloured yellow, orange or dark red. The transition that causes absorption in this region is governed by the electronic energy levels between transitions.[3] Due to the highly conjugated property of azobenzene compounds (Figure 1.2), where the azo double bond is connected to phenyl groups, the main transition is the $\pi \rightarrow \pi^*$ transition.[3]

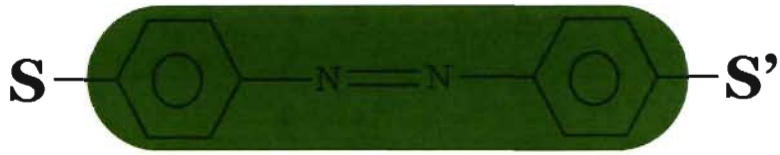

Figure 1.2 The azobenzene moiety (shaded in green). S and S' indicate substituents. Conjugation (p orbital overlap) takes place in the region indicated by the green shading.

1.2 Photoisomerization and classification of azobenzenes

Photoisomerization of azobenzene is considered as "one of the cleanest photoreactions known".[4] It involves the two azo isomers, "trans" and "cis". The trans form is generally more stable than the cis form (by about 50 kJ/mol in azobenzene[4,5]). Cis-trans interconversion can be triggered by light or heat. As indicated in Figure 1.3, thermal isomerization generally involves relaxation from cis to trans, while light-induced isomerization can be in either direction: light at 365 nm induces more cis than trans, however, 405 nm acts in reverse way.[6] A more detailed energy diagram can be found in reference 4.

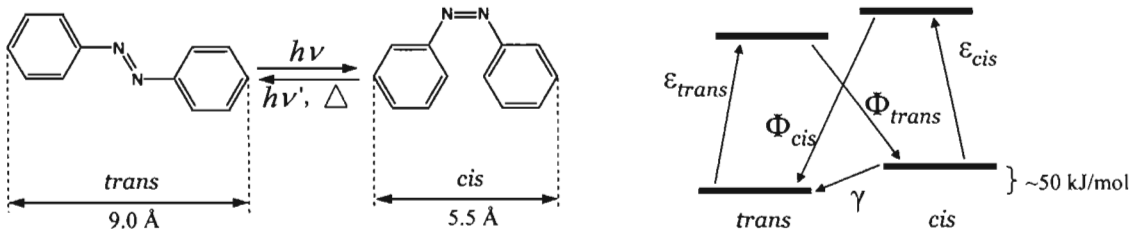

Figure 1.3 Photoisomerization of the azobenzene molecule (on the left),[4,7] and a simplified energy diagram taken from reference 8 (on the right), where ε denotes extinction coefficients, Φ quantum yields and γ the thermal relaxation rate constant.

Rau[4] has classified azobenzene-based molecules into three types; namely, azobenzene, aminoazobenzene and pseudostilbene, based on their spectroscopic characteristics, as shown in Figure 1.4. The UV-visible spectrum of azo molecules typically consists of a low-intensity n $\rightarrow$ π^* band (forbidden in the trans isomer) and a high-intensity $\pi \rightarrow \pi^*$

band.[4] For the azobenzene type, the n → π* band is located in the visible region and the π → π* band in the UV.[4] For the aminoazobenzene type, the two bands are close to each other and often the n → π* band overlaps the π → π* band; their positions are also sensitive to solvent polarity.[4] For the pseudostilbene type, the two bands are reversed on the energy scale, with the π → π* band at longer wavelengths.[4]

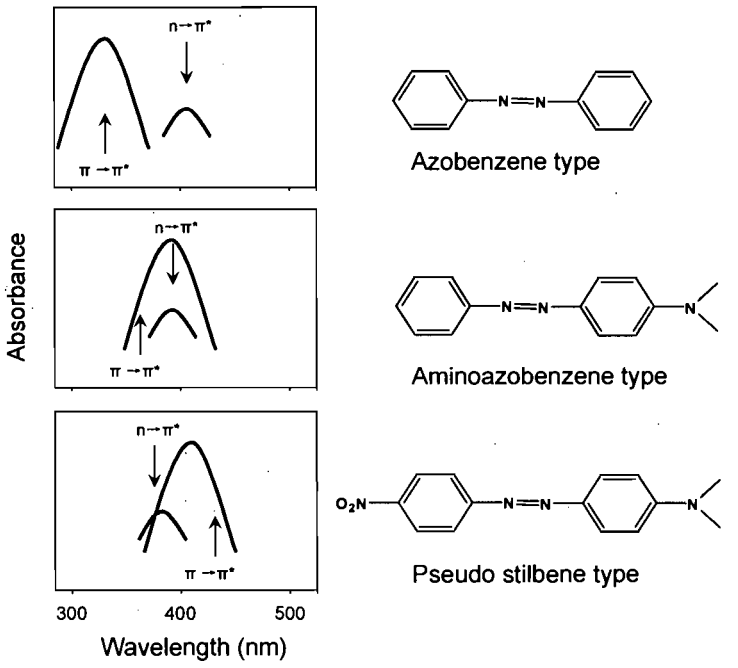

Figure 1.4 General classification of azobenzene molecules, according to Rau.[4]

The lifetime of the cis isomer depends on the azo type. Azobenzene types have a long lifetime, long enough that the cis form can even be isolated.[9] In contrast, the cis isomer lifetimes for the pseudstilbene type are generally very short, on the order of milliseconds.[4] In particular, electron-push and -pull substituents [for example, $N(CH_3)_2$ and NO_2] in para position relative to the azobenzene core lead to the pseudostilbene type[4] with rapid isomerization of the cis isomer at room temperature.[9] It must be added that cis-trans thermal relaxation also depends on the chromophore's environment, like steric or dipolar effects from neighbouring molecules.[10]

The mechanism of isomerization is not yet completely understood. In particular, there is controversy concerning the rotation versus inversion mechanism (shown in Figure 1.5).[4] In the rotation mode, one of the phenyl groups rotates around the azo bond to be out of the plane of the other phenyl group and continues the rotation to form the cis isomer. In the inversion mechanism, the lone electron pair in one of the nitrogens exchanges its position with the phenyl attached to the same nitrogen through an sp-hybridized nitrogen.[4] Rau reviewed[4] studies on the mechanism and concluded that rotation is the preferred mode, but inversion cannot be excluded. At different excited states, azobenzene can isomerize by different mechanisms with different yields.[11]

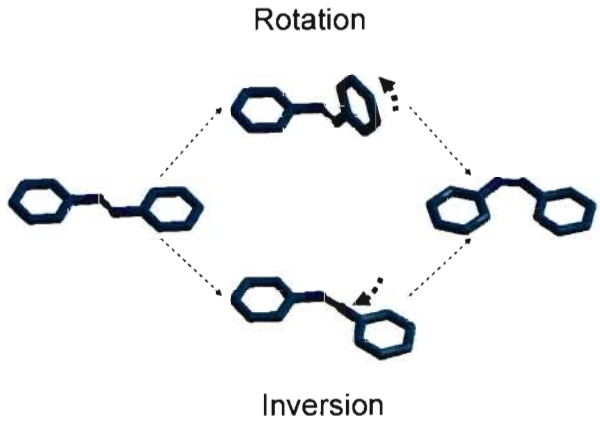

Figure 1. 5 The rotation and inversion mechanisms for azo isomerisation.[4]

1.3 Photoinduced orientation in azobenzene molecules

The studies of azobenzene and its isomerization up to the 1980's were reviewed by Kumar and Neckers.[7] In the early studies, azobenzene moieties were used as "probes" and "triggers" in polymeric materials.[7] They can be introduced at specific positions in the polymer chain, such as in side chains[12] or main chains,[13] to act as probes. By studying the photoisomerization, information on the molecular conformation can be obtained. For example, recently Spoerlein et al.[14] probed the conformational dynamics of a backbone-cyclized peptide with azobenzene derivatives using femtosecond time-resolved spectroscopy, as reviewed by Stolow and Jonas in *Science*.[15] Since the polarity and

symmetry change is quite large when isomerization occurs,[7] azobenzene can also work as a trigger, acting as the key light sensitive component. In this way, azo-containing polymers can show photoviscosity effects,[16,17] photomechanical effects,[18] photoresponsive solubility,[19] basicity,[20] conductivity changes.[19,21]

In the 1990's, interest in azobenzene shifted to well controlled photoinduced orientation investigations, reviewed in detail by Natansohn and Rochon.[22] The phenomenon can be summarized as follows (see Figure 1.6). The photoisomerization of azobenzene is activated only when the axis of the transition moment dipole (the long axis of the azobenzene molecules) of the chromophore has a component that is parallel to the linearly polarized light.[8,22,23] The molecules will not undergo isomerization when the long axis is perpendicular to the polarization direction. Consequently, the concentration of molecules oriented perpendicularly to the polarization direction increases with multiple cycles of trans-cis-trans under continuous illumination of polarized light until saturation. [This process is also called rotational diffusion.[24] A general name for this kind of photoanisotropy induced for organic dyes is the "Weigert effect".[22,25]] The outcome of the orientation of the azobenzene moieties is photoinduced birefringence (PIB), which is the difference of refractive index parallel and perpendicular to the uniaxial symmetry axis. It can be measured by the transmission of linearly polarized light through a known thickness placed between two crossed polarizers. It reflects the extent of optical anisotropy.

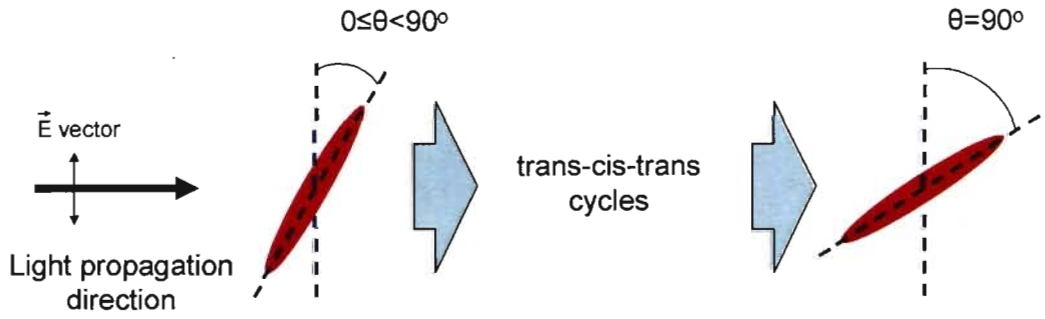

Figure 1. 6 Schematic demonstration of the photoinduced orientation process, adapted from reference 22.

The manipulation of orientational states is critical in data storage. Thus, high values, and thermal and temporal stability, of photoinduced birefringence are required in real applications. In amorphous polymers, higher stability can be achieved by increasing the rigidity of the material; for example, in materials with a high glass transition (T_g). Increased rigidity is believed to restrict the motion of the chromophore, thus avoiding unwanted orientation relaxation to develop. Polyimides were prepared for this reason, although they have poor processability.[26,27] High values of photoinduced birefringence can be obtained by increasing the anisotropy of polarizability on the molecular level in addition to orientational order. To this end, an azo-tolane liquid crystalline polymer was prepared in Ikeda's group.[28-30] It shows photoinduced birefringence of nearly 0.4, and the response can be faster with donor-acceptor substituents.[31]

Although the basic mechanism of photo-orientation is well-known,[8,22,32] it must be emphasized that the final result is that the azobenzene molecules lie in a plane that is perpendicular to the linear polarization direction of the incoming light beam. When circularly polarized light is applied, it randomizes the orientation of molecules that are in the film plane, but it may also align molecules parallel to the propagation direction of the light. This is illustrated in Figure 1.7. The demonstration assumes that light enters the film perpendicularly, and that the polarization does not change during the propagation of the light within the film. This idea was suggested[33-35] and used for 3D manipulation of the orientation of azo polymers.[36]

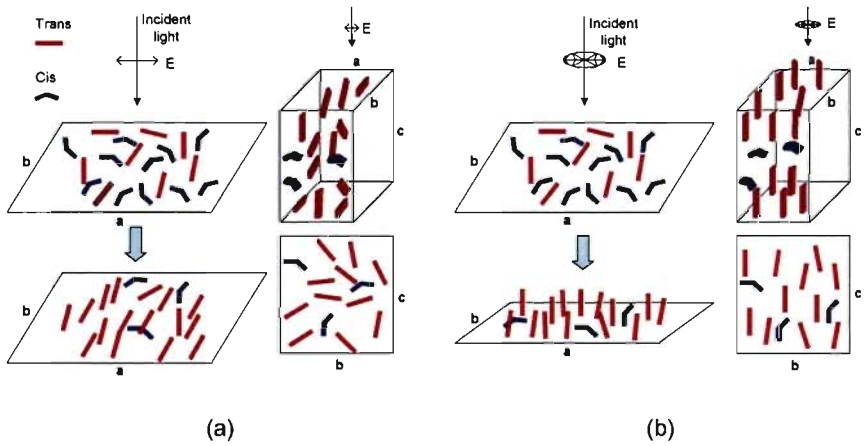

Figure 1.7 3D view of light induced orientation in azobenzene films using (a) linearly polarized light and (b) circularly polarized light. The 3D orientation is shown on the upper right side in each case. The film planes are defined by axes a-b and b-c.

Actually, the situation can be more complex than illustrated in Figure 1.7. This was recently shown in the study of photo-induced chirality in nonchiral azobenzene polymer films.[37] Photo-induced chirality was first discovered by Nikolova and coll.[38,39] They found a large circular anisotropy in liquid crystal azobenzene polymers illuminated by circularly polarized light.[39] It is believed that a chiral helix structure develops during exposure to circularly polarized light.[37,40-42] Practically, this phenomenon enables control over the switching of enantiomeric structures by circularly polarized light in devices.[40,42] Intrinsic order, such as exists in liquid crystals, seems to be important in this phenomenon.[39,40,42,43] For example, the arranged layered structure may assist in the twisting process when irradiated by circularly polarized light.[40] It was explained by interaction of the circularly polarized light with a sub-layer structure to induce elliptical polarization, which is transmitted through the film thickness to give the helix structure.[40] However, Kim et al. found that this phenomenon can also be observed in an amorphous system, which is possibly the result of a combination of linearly and circularly polarized light.[41]

Although the discovery of photoinduced orientation was made in the 1950's and 60's,[44,45] it only began to receive considerable attention in the 1980's after Todorov and coll. reported reversible photoinduced birefringence in a simple film of poly(vinyl alcohol) (PVA) and methyl orange,[46] and interest boomed in the 1990's. When reviewing this history, one might wonder why it took so long between the initial discovery and much later enthusiastic interest in this phenomenon. This can be understood by the absence of any real expectation of application for the phenomenon before the 1980's. Then, with the development of information technology, increasing access to computers and lasers, the appearance of laser printers, etc., the importance of making more efficient, fast, erasable and reliable information storage media was recognized. Todorov's discovery was recognized as having considerable potential for this application, leading to the publication of thousands of papers on this subject in the last 20 years.

1.4 Macroscopic motion of azobenzene and surface relief gratings (SRGs)

Natansohn and Rochon[22] pointed out that the photoinduced motion of azo-containing polymers can be divided into three types based on the length scale. Molecular motion, described in previous section, occurs at the smallest (sub-nano) scale. At the next level is "domain" motion. Because the azobenzene chromophore is bound to the polymer matrix, the photoisomerization that takes place at the molecular level has consequences at a higher length scale, notably near the nanometer level, especially when intrinsic order exists, as in liquid crystals and molecular monolayers. In this way, the local orientation of the chromophore is amplified by the intrinsic order of materials.

The third and highest level is "macroscopic" motion. When a film of an azo-containing polymer is exposed to a variation in the light intensity or polarization (discussed in later chapters) for some time, massive transport of material is observed. This phenomenon led to the discovery of surface relief gratings (SRGs), optically formed gratings with a periodic variation of the surface topography, in 1995.[47,48] Compared to photoinduced birefringence, SRGs have more practical applications in optics and thus raised enormous interest. In most cases, polymers were used for SRG inscription.[22] Very recently, organometallic compounds were also employed.[49]

Figure 1.8 shows an example of an SRG written in a liquid crystalline ionic complex,[50] along with typical setups for SRG fabrication based on the coherence of the laser and constructive interference on the material surface. In order to achieve a fast response of photoinduced birefringence or SRG inscription, pseudostilbene type of azobenzene is preferred because of the fast back-isomerization rate and consequently the faster trans-cis-trans cycles. This is critical for efficient photoinduced orientation[8,22] and is believed to be related to the mechanism of SRG formation.[8] The formation of SRGs is also influenced by the nature of the film surface. When a long perfluoro-octyl tail was used in a side chain liquid crystal homopolymer with a smectic A mesophase, SRG formation was completely prevented, according to a study from Ober's group recently.[51]

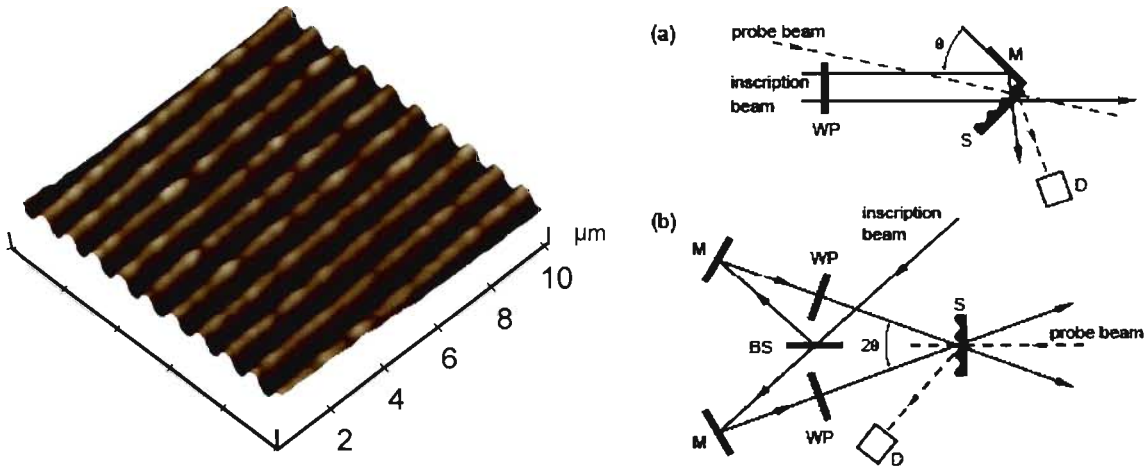

Figure 1.8 A surface relief grating (SRG, left) inscribed in an azo-containing material (see chapters 4 and 5), and two typical inscription setups (right), with (a) one beam and (b) two beams (taken from reference 8).

1.5 Science of liquid crystals

Liquid crystals are "nature's delicate phase of matter".[52] It consists of many different phases, which are distinguished by their intrinsic long-range order, specifically, orientational order (OO), positional order (PO) and bond orientational order (BOO),[53] as shown in Figure 1.9. OO refers to preferred directions in which anisotropic molecules are pointed (represented by the director, $\vec{n}$). PO refers to the position of molecules on a lattice. BOO refers to order along directional lines ("bonds") joining ordered objects, but where there is long-range progressive displacement of the objects relative to integer lattice positions, as illustrated in Figure 1.9.

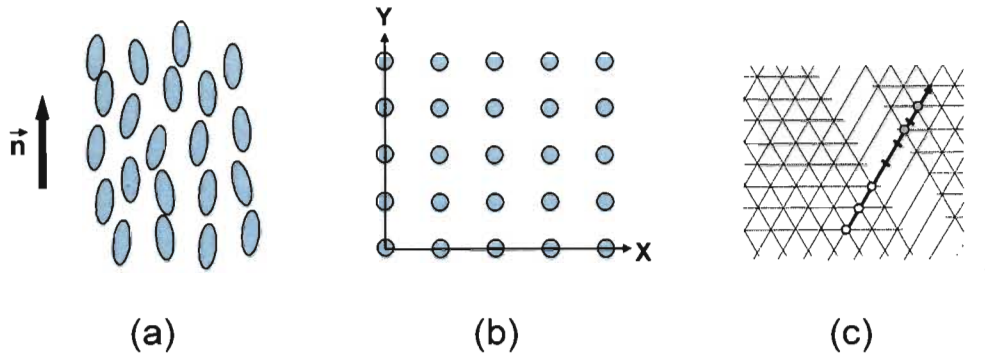

Figure 1.9 Schematic representation of the three basic types of order in liquid crystals: (a) orientational order (OO), (b) positional order (PO) and (c) bond orientational order (BOO), taken from ref. 53.

Isotropic liquids have no long-range order at all. Liquid crystals have long-range orientational order as well as partial positional order or complete positional disorder.[52,54] Bond orientational order is encountered in so-called hexatic phases.[53-55] Crystals have long-range 3D positional order. The intrinsic order in LCs gives rise to anisotropic properties, like optical anisotropy, mechanical anisotropy, etc, which are the basis for many applications.

To form LC phases, molecules must possess certain common characteristics, although this does not guarantee the appearance of LC phases. In particular, the molecules must possess pronounced anisotropy in molecular shape.[54] The common shapes are rod-like and disc-like, usually with a rigid core and flexible terminal groups.[55] Amphiphilic molecules like alkyl carboxylates can also be LC. The most common types of LC phases for rod-shaped molecules (the most studied shapes) are nematic and smectic, which are distinguished by whether or not a layered organization of molecules is present (Figure 1.10). Molecules with short alkyl terminal substituents favour nematic phases, whereas longer chains favour smectic phases. Attractive interactions lateral to the molecular long axis also favour the layer structure.[55,56] Figure 1.10 shows the structure of the nematic and smectic phases. The nematic phase has orientational order only, as indicated by the director $\vec{n}$. Smectic phases (smectic A and C) have one-dimensional positional order defined by the layers, but there is no positional order within the layers. In the smectic A phase, the orientational order (director $\vec{n}$) is perpendicular to the layers, whereas it is tilted in the

smectic C phase. Other layered LC phases have in-plane order of the BO type, notably smectic B, F and I (hexatic phases).[53,54] LC phases can also be chiral, where the director precesses in a periodic matter through space (chiral nematic phase) or through the layers (chiral smectic phases).[52]

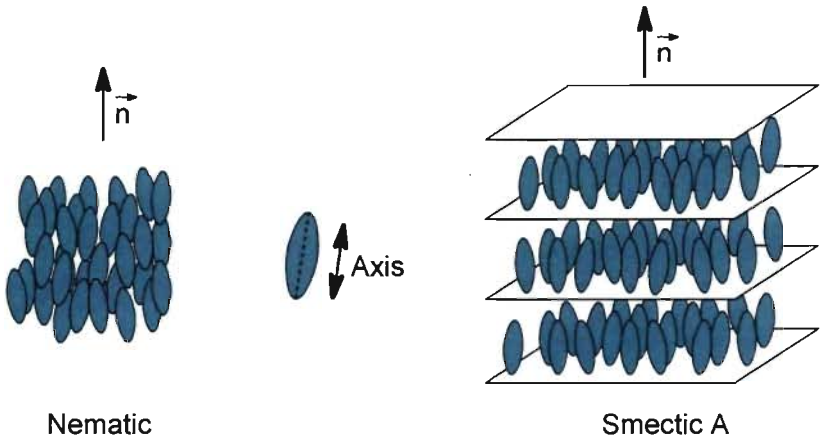

Figure 1.10 Common LC phases: nematic phase (left) and smectic A phase (right).

This thesis will mainly investigate LC polymers (LCPs). They combine the advantages of polymers, such as good mechanical properties, processibility and filmability with the advantages of LC order. The two major classes of LCPs are main-chain (MCLCP) and side-chain (SCLCP), based on whether the mesogenic group is incorporated into the polymer backbone or side chain, respectively (Figure 1.11).[56] More complex LCPs can be designed by combining MC and SC, or by using other types of polymer architechtures.[54] Usually, flexible spacers (most often, sequences of linear alkyl segments) link the mesogenic cores to one another (MCLCP) or to the polymer backbone (SCLCP).

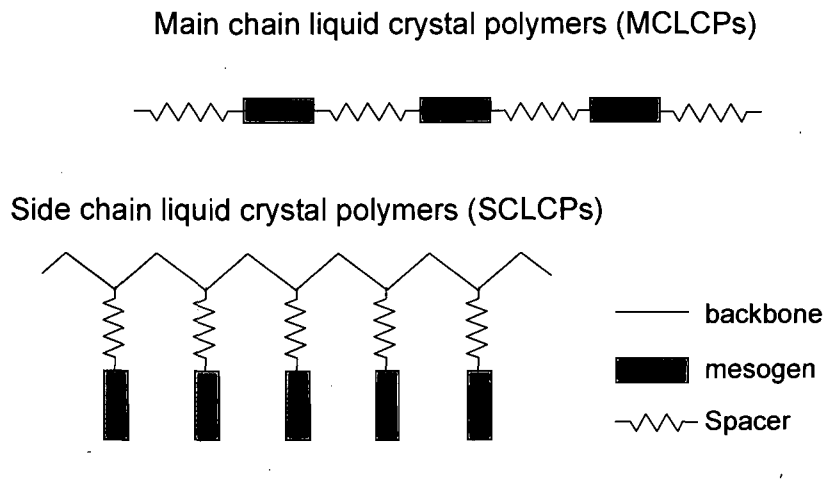

Figure 1.11 Two major classes of liquid crystal polymers (LCPs), MCLCP and SCLCP.

1.6 Supramolecular chemistry

Supramolecular chemistry[57] may be dated back to the Nobel Prize given in 1987 to Donald J. Cram, Jean-Marie Lehn and Charles J. Pedersen to recognize their achievements in the "development and use of molecules with structure-specific interactions of high selectivity". The essence of supramolecular chemistry can be expressed in different ways, such as "the branch of chemistry associated with the formation of complex multimolecular entities from relatively simple molecular components",[58] or "the study of systems involving aggregates of molecules or ions held together by non-covalent interactions, such as electrostatic interactions, hydrogen bonding, dispersion interactions and solvophobic effects".[59] Actually, supramolecular chemistry can be viewed as an old subject with a new name. Its strength lies in the new focus or viewing angle for constructing molecular entities. Through this, it has given rise to many new ideas like molecular cages and recognition elements.

In this thesis, we study LCPs based on supramolecular chemistry, where non-covalent bonds play an important role. The most widely used non-covalent bonds are the hydrogen bond and the ionic bond. Figure 1.12 shows representations of some supramolecular LCPs based on these bonds. For example, hydrogen bonds have been used by Griffin and coll. to

make MCLCPs from bifunctional small molecules with complementary functional groups.[60] It is even possible to fabricate LC fibers from the melt with these materials.[61,62] Kato and Fréchet first made supramolecular SCLCPs where an already existing LC phase in a SCLCP was stabilized through hydrogen bonding of acid-terminated side chains to a stilbazole derivative.[63] This was followed up by Kato and coll. with many other examples of supramolecular SCLCPs, generally with the hydrogen bond far from the polymer backbone.[64] The Bazuin and Imrie groups extended this work to commercially available polymers like poly(4-vinyl pyridine) (P4VP) and mesogenic molecules with a spacer group between the mesogenic core and the supramolecular functional group.[65-67] Other groups, notably Ruokolainen and coll., showed that simple alkyl phenol compounds H-bonded to P4VP also show LC character.[68,69] The first ionically bonded SCLCP was described by Ujiie and Iimura,[70] who complexed an ammonium-functionalized azo molecule to poly(vinyl sulfonate) (PVS), which forms a smectic A phase. The Bazuin group was subsequently the most active in investigating these kinds of ionic complexes between polyelectrolytes and functionalized mesogens (later termed "surfactomesogens"[71,72]). Many other groups, notably Antonietti and coll.,[73] investigated simple surfactant/polyelectrolyte complexes. A number of reviews have been written on these different supramolecular LCPs.[64,74-76]

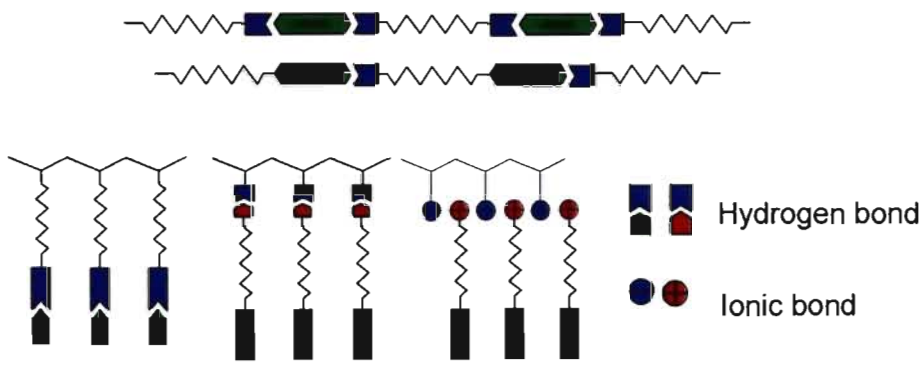

Figure 1.12 Representations of LCPs based on supramolecular interactions, specifically hydrogen and ionic bonds.

There are many advantages to designing LCPs with non-covalent bonds. Firstly, the synthesis is simplified, since supramolecular LCPs can be prepared by mixing simple components. Secondly, new properties can be introduced, such as those related to the temperature-dependent lability of the non-covalent bond. Thirdly, the properties can be easily tailored through the variety of simple components available (either from commercial sources or by relatively easy synthesis). The disadvantages may lie in where high bond stability or nonionic character is required.

1.7 Review of studies on azo-containing liquid crystal polymers (LCPs)

One of the most usual ways to obtain photosensitive LCs is by introducing azobenzene groups. This can be done either by simply mixing azo molecules with a host material (called "doping")[77-80] or by including azo moieties in the chemical structure through covalent, ionic or hydrogen bonds. Photoinduced birefringence (PIB) in LCPs can be quite different from that in amorphous polymers.[22] For the latter, stable PIB can be hard to achieve above the T_g, but for LCPs, a high isotropization temperature helps to stabilize the PIB above the T_g.[22] On the other hand, it is thought that a disadvantage of LCPs is the greater difficulty of PIB erasure.[22] Thus, optical properties in LCPs are more complex than that in amorphous polymers.

1.7.1 Photosensitive LCPs by doping

Doping LCPs[81] with small molecule azo dyes is attractive for its simplicity. High molecular weight azo polymers with different polymer architectures, such as dendrimer or comb-like polymers, have also been used as dopants.[80] The main drawbacks of doping are the low solubility of the dopant guest in the host material[82] (with resultant phase separation) and plasticization of the polymer by small molecules.[83] The former point is often resolved by covalent-bond attachment; i.e. in the form of all-covalent azo-containing LCPs both in main-chain and side-chain form, an area that has been investigated extensively.[56] An easier way to achieve high dopant content without phase separation[81] is by involving strong interactions between dopant and host, such as hydrogen bonding.[79]

1.7.2 All-covalent azo-containing LCPs

1.7.2.1 Azobenzene moiety in the main chain

The major interest in designing azo-containing MCLCPs is for applications in nonlinear optics (NLO).[83] MCLCPs can be designed to be molecular rigid, which leads to a high T_g[84] (lowered when flexible spacers exist) and a high isotropization temperature (T_c), and therefore high stability after poling (orientation in an electric field) and ease of quenching to lower temperatures. However, one of the challenges of rigid main-chain azo polymers is to overcome the insolubility in common solvents, which turns molecular rigidity into a disadvantage.[21,85]

The spacer length in MCLCPs strongly affects LC packing. Shorter spacers (typically, 0-6 CH_2 units) tend to lead to nematic phases, while longer ones (typically, 6-12 CH_2 units) tend to give mesophases with higher order.[56,86] Sometimes a longer spacer results in the amorphous phase, and copolymerization leads to a liquid crystalline phase.[87] X-ray investigations of oriented MCLCPs have shown that the smectic layers are predominantly parallel to the orientation direction, which suggests that main chain folding takes place in the spacer moieties.[88] An interesting series of LCPs with azobenzene groups in both the main chain and the side chain show mainly the nematic phase, the stability of which increases with greater electron-withdrawing ability of the substituents.[89] Some recent examples of MCLCPs containing the azobenzene moiety are shown in Figure 1.13.

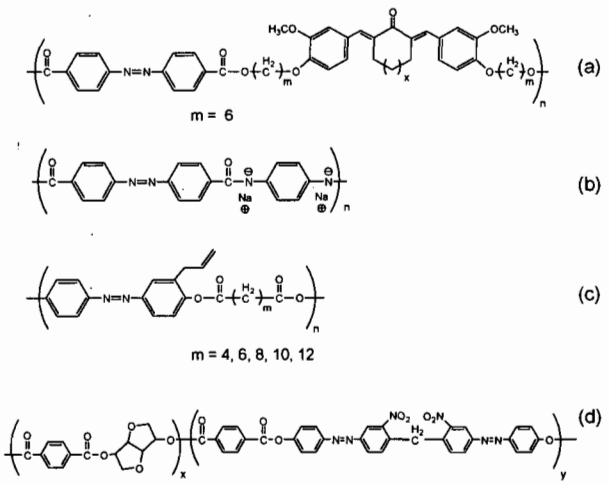

Figure 1.13 Examples of azo-containing MCLCPs, from refs. (a) 90, (b) 21, (c) 86 and (d) 84.

1.7.2.2 Azobenzene moiety in the side chain

The first thermotropic SCLCP was discovered by Magagnini et al. in 1971 in a no-spacer poly(4-biphenyl acrylate) (PBA) system.[91-93] Then, ever since the introduction of the spacer concept (see below) by Finkelmann and coll. [94,95] in 1978, the area of SCLCPs exploded. This may be due, in part, to the relative ease of functionality-oriented chemical structure design. Most of the MCLCPs were prepared by less conveniently controlled stepwise condensation polymerizations, which usually involve a reaction between carboxyl and hydroxyl groups, which limits the freedom of molecular design. For SCLCPs, as long as there exists an active double bond in the monomer, chain polymerization is possible. More polymerization strategies are also available, such as (normal or controlled) free radical polymerization and ionic polymerization. Polymers of versatile structures and well controlled molecular weight can be obtained. An alternative synthetic strategy is the use of polymer homologous reactions,[96] which is based on grafting side chains to preformed polymer backbones. These various strategies liberated the design of functional azobenzene-containing polymers. Thus, one can quite conveniently compare the properties of azobenzene, aminoazobenzene and pseudostilbene type moieties. It is impossible to summarize all of the work in this area. Instead, by means of selected examples, we will

indicate how the variation of the backbone, of the spacer (or tail), and of the type of azobenzene moiety affect the LC character.

Backbone effects. In most cases, polymer backbones tend to adopt a random-coil conformation.[96] This opposes the alignment tendency of side chains in LC mesophases. In order to overcome this opposition, Finkelmann et al. introduced the concept of using flexible alkyl chain spacers between the backbone and mesogenic core to partially decouple their interactions, and thus allow LC phases to form.[94] Unless the backbone and mesogen core are completely decoupled, the nature of the polymer backbone affects the LC properties. Mesophase stability is greater for SCLCPs with flexible backbones, such as polysiloxane, than for those with less flexible backbones.[96] On the other hand, backbones that are too flexible can lead to crystalline phases.[96] For example, for the same p-cyanoazobenzene side chain, a polymethacrylate backbone shows a smectic phase, whereas a much more flexible polyester backbone results in a crystalline phase.[97] In this case, the more flexible backbone shows more evidence of cooperative orientation of the azo side chains during photoorientation. Flexible backbone can also decrease the T_g while enhancing the isotropization temperature, as found in a biphenyl SCLCP.[98]

Spacer effects. Most polymers with mesogenic cores directly attached to the backbone are amorphous.[96] But in some cases, such as PBA mentioned above,[91,99-102] a smectic phase occurs for spacer-free SCLCPs, which could be due to the strong ordering tendency of the side groups.[96] Usually, when short spacers exist, the nematic phase appears. With increasing spacer length, the tendency for smectic phases increases.[96] For example, a polymer with a methacrylate backbone and a cyanoazobenzene mesogenic core shows a nematic phase for a butylene spacer, but smectic A phases for spacers of six and eight CH_2 groups, respectively.[103] For an acrylate backbone and a nitroazobenzene mesogen, a nematic mesophase was found for a spacer length of six CH_2, but no mesophase was found for spacer lengths of three and four CH_2.[104] A polystyrene-based SCLCP with a methoxy substituent terminating the azobenzene mesogen was amorphous with a spacer length of three and smectic A for spacer length of 4-12 CH_2.[105]

Mixed spacer lengths can also affect LC behaviour. In a series of random polystyrene-based copolymers with the same azo mesogen, but two different spacer lengths,[105] it was found that when the spacer length of one component is fixed at eight CH_2,

while the other varies from three to twelve CH_2, the two components being equimolar, all of the copolymers show a smectic A phase. The transition temperatures and entropies are weighted averages of the values for the homopolymers, except when there is a large disparity (3-4 CH_2) in the spacer length. A similar deviation was found in a biphenyl copolymer series.[106] This effect suggests an unfavourable interaction between the mesogenic core and the spacers.[105] Unfortunately, no X-ray analysis of the mesophase structure was done, which could have given more detailed information on the molecular packing.

Mesogen effects. The focus here is on azobenzene-based mesogens. Different substituents on this moiety give different polarities and isomerization properties. Imrie and coll. studied various SCLCPs with a fixed spacer length of four CH_2 and where the azobenzene moiety is terminated with nitro, cyano, methoxy and fluoro substituents.[107] They all give smectic A phases. However, X-ray diffraction and calorimetric investigations suggested that there is a significant difference in packing between the nitro- and cyano-substituented azo SCLCP's on the one hand and the methoxy and fluoro-substituted ones on the other hand (discussed further in Chapter 2.

Again, a polystyrene-based copolymer series was investigated, this time with two different azobenzene mesogens (one with varying spacer length), specifically involving nitroazobenzene (electron deficient) and methoxyazobenzene (electron rich).[108-111] The nitro homopolymer[112] (for spacers ranging from three to twelve CH_2) shows a smectic A phase while the methoxy one[105,111] shows an amorphous structure for a spacer of three CH_2, and a smectic A phase for spacers from four to twelve CH_2 (as already mentioned above). In the copolymers, where the spacer for the methoxy mesogen was fixed at eight and that for the nitro mesogen varied from three to twelve, only a smectic A phase was found.[110] The clearing temperatures (same as isotropization temperature) are significantly higher than the average values from both homopolymers. In another copolymer system with the same two mesogens and fixed spacer lengths (six CH_2) but varying relative content of the two co-units, a smectic phase was observed for both homopolymers and copolymers,[109] but the clearing temperature was enhanced in the copolymers.[109] A similar phenomenon was found in a hydrogen bonding SCLCP system.[113] It was attributed to the specific interaction between the two types of mesogens.[109,110] This idea was reinforced by the investigation of

a blend of a cyano-substituted biphenyl and a methoxy substituted azobenzene SCLCP.[111] The homopolymers, with a spacer length of three CH_2, were all amorphous, but their blends all gave a smectic A phase. Similar studies in other systems suggested specifically charge transfer interactions[114,115] or dipolar interactions.[116]

1.7.2.3 Azobenzene-containing block copolymers

Azo moieties can be found in many block copolymers thanks to the well developed living polymerization methods.[34,117-125] Two-block azo-containing copolymers (AB) are the most widely studied. Three-block copolymers of the type ABA and ABC have also been investigated, as well as a star-shaped copolymer.[118] One of the prominent characteristics of block copolymers is their self-assembly into well-defined microdomain structures in bulk or in selective solvents.[126] These novel structures are the basis for diverse applications, such as in the fields of drug delivery, information storage, or photonic and electronic applications.[126] Studies of azobenzene-containing block copolymers, including ones with LC character, have been reviewed recently.[32] It has been found that the orientation and growth of LC structure starts at the block interfaces, called "inter-material dividing surfaces" (IMDS).[127] Molecular properties, such as spacer length, are also important.[127,128] The confinement effects between domains can affect the phase transition temperature and photoinduced orientation of azobenzene moieties.[127,129,130]

An interesting phenomenon with azo-containing block copolymers is light-induced domain morphology change. A cylindrical morphology perpendicular to the surface can be reoriented parallel to the surface simply with laser irradiation,[122] as shown schematically in Figure 1.14. SRG formation can be highly dependent on the nanophase separation in block copolymers.[131,132] For example, mass transport is strongly depressed when the azo block is a discontinuous minority phase such as in a spherical morphology.[132]

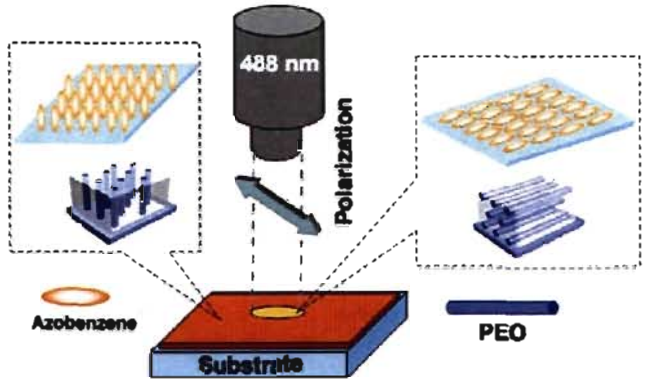

Figure 1.14 Photoinduced alignment switch with an azobenzene-containing block copolymer.[122]

1.7.3 Supramolecular azo-containing LCPs

1.7.3.1 Hydrogen-bonded systems

Hydrogen bonds exist between highly electronegative elements, such as oxygen and nitrogen, and a hydrogen attached to highly electronegative elements.[23] Its interaction strength is on the order of 20 kJ/mol.[23] They can play an important role in LC formation[133] and can help stabilize mesophases by increasing the phase transition temperature.[134] Azopyridine is a frequently used azo mesogen, due to the pyridine moiety being a good ligand for coordination with metals[134-138] or as a hydrogen bond acceptor.[135,139-144] Figure 1.15a shows an example of an azopyridine side chain homopolymer, to which acid-functionalized small molecules are H-bonded to modify LC mesophases.[135,140] This strategy was also applied to block copolymers (Figure 1.15b).[135] The block copolymer, which has a lamellar microdomain structure, is amorphous on its own. However, the addition of hydrogen bonding small molecules resulted in either a nematic or smectic phase, especially with higher azopyridine content. Very recently, Toh et al. developed a MCLCP hydrogen-bonding azopyridine system from bifunctional small molecules (Figure 1.15c).[144] The materials mainly showed a nematic phase, depending on the combination of spacer lengths in the azopyridine and benzoic acid parts.[144] A fibrous supramolecular main-chain polymer can be prepared from a single type of small molecule that contains both azopyridine and carboxylic acid.[139,145]

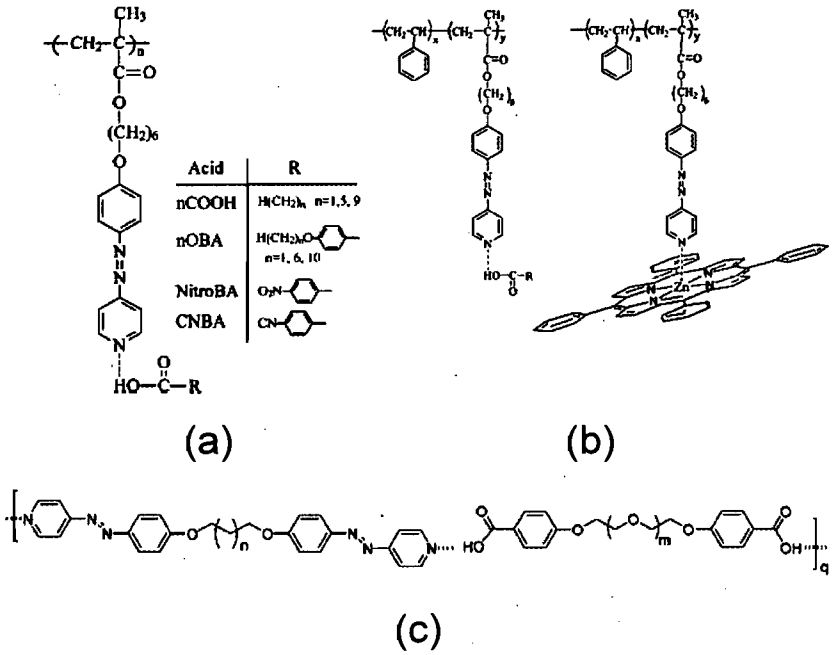

Figure 1.15 Examples of hydrogen bond formation with azopyridine groups, in (a) homopolymer,[140] (b) a block copolymer[135] and (c) a main-chain LC polymer.[144]

Hydrogen bonded LCPs involving pyridine (not azopyridine) derivatives have also been widely studied.[63,65,66,146-151] Imidazole is another choice as hydrogen bond acceptor in LCs.[113,152-157] For example, a siloxane polymer with carboxylic acid-terminated side chains mixed with imidazole-functionalized azobenzene-containing mesogens gives a nematic phase (Figure 1.16).[113,155] The formation of the mesophase is subject to the terminal group R (Figure 1.16) and the electron-donor and –acceptor property of the azobenzene.[113,155] Very recently, Zettsu et al. reported the efficient formation of SRG on an imidazole-functionalized hydrogen-bonded azobenzene-containing polymer.[157]

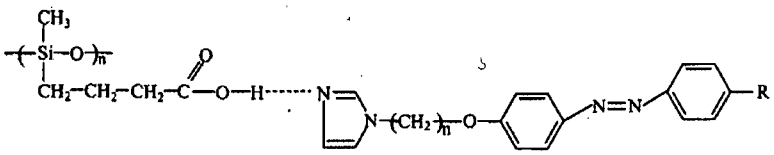

Figure 1.16 Example of a hydrogen-bonding LCP with an imidazole group.[113,155]

Azophenol has also been used recently for constructing hydrogen-bonded LCPs. A study on LC complexes between P4VP and a series of azophenol mesogens with different alkyl tail lengths by ten Brinke and coll. revealed an interesting counter-intuitive effect of increased T_g with increasing alkyl tail length.[158] A series of hydrogen-bonded complexes of phenol-functionalized azo molecules with pyridyl pyridinium-terminated side-chain polymers were prepared by Bazuin and coll.[159] The increased viscosity due to the ionic interactions as well as high polarity of the terminal group on the azophenol mesogen were found to retard the appearance of LC phases on cooling.[159]

1.7.3.2 Ionically bonded systems

Compared to the hydrogen bond (5-65 kJ/mol),[73] the ionic bond is generally stronger (50-250 kJ/mol)[73] and more suitable for materials with thermal stability requirements. Ionic self-assembly is easy, reliable and very efficient for obtaining stoichiometric complexes, especially in dye-surfactant systems.[73] Polyelectrolyte-surfactant[160-162] and dye-surfactant[163-165] systems, studied and reviewed by Faul and Antonietti among others,[73,163-166] show ordered morphologies and high mesophase stability (some are stable until degradation[162,164,165]). It may be mentioned that photoinduced anisotropy in a complex of a commercial azo-dye and a surfactant was found to be much larger than in conventional azobenzene polymers, and it was successfully used for the fabrication of optical gratings.[165] Here, we will examine mainly liquid crystals.[167] The emphasis is on azo-containing LCPs investigated in recent years (mainly since 2005), and their structural and photoresponsive properties.

The ionic bond was first introduced as a linkage element into LCPs by Ujiie and Iimura[70] in 1992, when they reported on a complex between poly(vinyl sulfonate) (PVS)

and an azobenzene surfactomesogen (shown in Figure 1.17). The surfactomesogen (with I^- counterion) is itself LC with a smectic A phase. Its complexation with PVS increases the stability of the mesophase by about 65 °C.

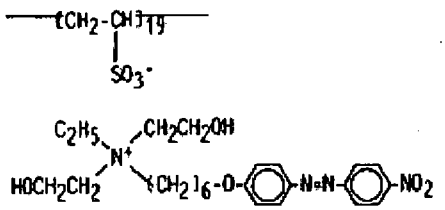

Figure 1.17 The first SCLCP complex formed by an ionic linkage.[70]

Tibirna and Bazuin[71] studied the complexation of a non-liquid crystalline triethylammonium-functionalized nitro azobenzene surfactomesogen with a variety of polyelectrolytes; namely, PVS, carboxymethyl cellulose, cellulose sulfate, polymethacrylate and polyacrylate. All of the complexes were found to exhibit the smectic A phase over a wide temperature range. A similar system was investigated recently by Xiao and Lu, based on the polyacrylate backbone and a methoxyazobenzene surfactomesogen with varying spacer length.[168] Photoinduced anisotropy was observed. Unfortunately, no convincing evidence was shown to confirm a LC mesophase.

Ionic interactions can also help in effectively crosslinking the molecular structure. Qi and Zhao[169] prepared an ionomer by random copolymerization of an azobenzene-containing monomer and methyl methacrylic acid. The addition of cations such as Cu^{2+}, Zn^{2+} and Mn^{2+} introduces ionic crosslinking. The clearing temperature as well as the photoinduced birefringence and SRG were modified by the addition of different cations.

Ionic bonds can also be obtained by proton transfer from an acid to a base, as obtained, for example, by mixing a polymer such as poly(acrylic acid) with a diethyl amine-functionalized surfactomesogen.[72] A smectic A phase was observed in an azo-containing system studied by Tibirna and Diouf.[170] Recently, Marcos et al.[171] prepared a stoichiometric dendrimer-like complex by proton transfer. The dendrimer core was amine-functionalized and the azobenzene mesogen was carboxylic acid-functionalized, and neither

are LC when not complexed. The complex forms a nematic phase instead of the usually observed smectic A phase in the presence of ionic interactions.[167] This discovery also applied to hyperbranched polyethyleneimine.[171] Another very interesting proton transfer complex with an unusual mesophase was reported by Zhu et al.[172] In this case, as shown in Figure 1.18, proton transfer from a sulfonic acid-functionalized wedge-shaped azobenzene mesogen to P4VP results in a complex with a hexagonal columnar phase for degrees of sidechain substitution above 80%, whereas a lamellar structure forms at low sidechain loading.[172]

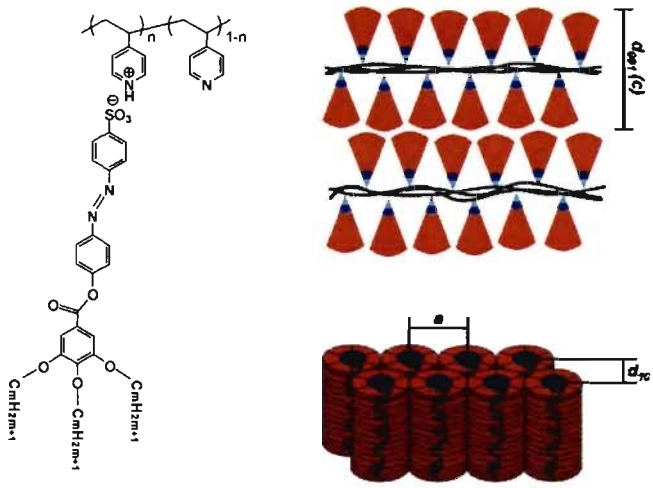

Figure 1.18 Example of a proton transfer complex involving a wedge-shaped mesogen and the columnar mesophase structure formed at high mesogen content.[172]

This section has summarized studies related to LC aspects of azo-containing polymer materials. Many other aspects of these materials are under active investigation, in particular their usefulness for producing molecular machines,[59,173-179] in photomechanics,[180-191] and in life[192-197] and surface[198-206] sciences.

1.8 Objective and scope of this thesis

This thesis will focus on polymeric azo-containing liquid crystals with ionic bonds. An important goal is to understand the properties of polymer liquid crystals in the presence of ionic interactions, namely the phase properties, packing structures, and responses to

external factors, such as the addition of small molecules, including moisture and solvent vapour. A second goal is to investigate photoinduced birefringence and SRG inscription in these materials, to obtain knowledge on how the ionic interactions, the presence of LC order and other molecular parameters may affect optical properties.

In Chapter 2, a series of stoichiometric side chain polymer complexes consisting of a polystyrene sulfonate (PSS) backbone and ammonium-functionalized azobenzene surfactomesogens (SMs), shown in Figure 1.19, were investigated very carefully (high purity and rigorous dry conditions). This work represents a continuation of previous studies in the Bazuin group on ionic surfactomesogen/polyelectrolyte complexes. These kinds of SCLCP complexes have been much less investigated than H-bonded SCLCPs and simple surfactant/polyelectrolyte SCLCPs. In fact, very few studies of SCLCPs have been made that compare so many different mesogen cores, whether in all-covalent or supramolecular systems. Furthermore, insufficient attention has been paid to the need for rigorous drying due to the hygroscopic nature of the ionic bond. However, it will be shown that rigorously dried samples are also highly viscous, even well above the T_g, which tends to give a frozen-in amorphous structure instead of LC phases. In several cases, this difficulty could sometimes be overcome by annealing at high temperatures.

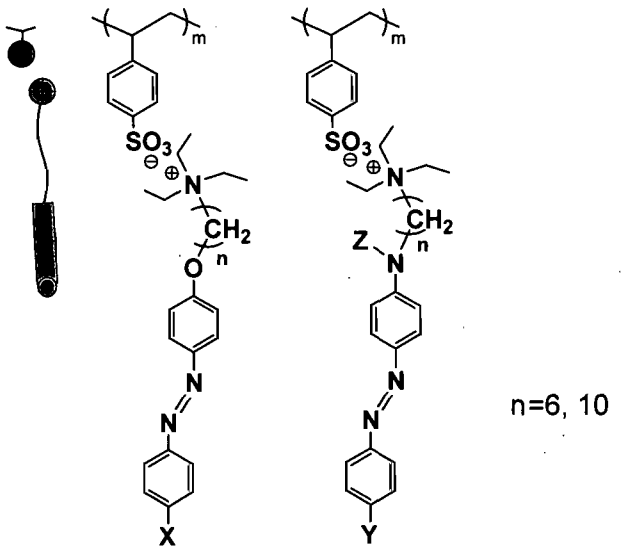

Figure 1.19 Complexes studied in Chapter 2. X, Y and Z are substituents (details given in Chapter 2).

An alternative to reduce high viscosity and increase molecular mobility is to use small molecules as plasticizers (solvent-assisted procedure). Furthermore, given the hygroscopic nature of the complexes, it is of interest to investigate the effect of controlled humidity atmospheres on the LC properties of the surfactomesogen/polyelectrolyte complexes. This humidity exposure, as well as exposure to organic solvent atmospheres of some of the complexes studied in dry form in Chapter 2, is the subject in Chapter 3.

A brief study of PIB behaviour in the SM/PSS complexes in Chapter 2 indicated no superior property to other covalently bonded side-chain polymers. This was thought to be related to the presence of flexible components in the chemical structure that induced too much relaxation. Therefore, flexible components were eliminated in an investigation of a commercially available dye, methyl orange (MO), complexed with methylated poly(4-vinyl pyridine) (P4VPMe) (Figure 1.20a). The LC structure and PIB behaviour of this novel spacer and tail-free LC complex will be described in Chapter 4. It shows high PIB values with very good thermal and temporal stability, and can be inscribed with SRGs. This impressive performance led to a detailed follow-up study, described in Chapter 5, of a series of spacer-free complexes with different terminal substituents on the dye, as well as a polyelectrolyte backbone with a short spacer, all shown in Figure 1.20. The goal was to determine the effect of variable degrees of flexibility on the LC structure and on the optical responses (PIB, SRG inscription).

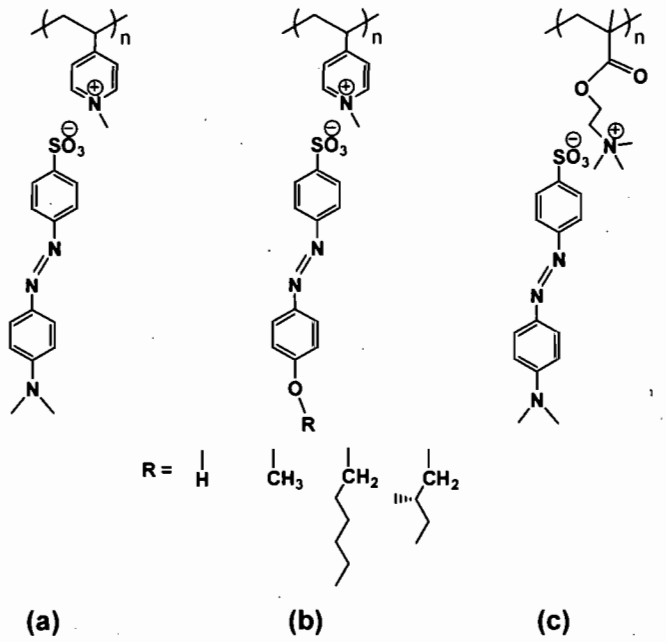

Figure 1.20 Spacer-free LC complexes studied in Chapter 5. Complex (a) is also the subject of Chapter 4.

Chapter 6 is the result of an accidental discovery of a one-pot synthesis of small molecule dye-surfactant complexes, which may also be considered to be thermotropic ionic liquid crystals, shown in Figure 1.21. This discovery was made during the synthesis of the mesogens shown in Figure 1.20b when using DMF as the solvent. The one-pot synthesis includes the simultaneous synthesis of the two components (dye and surfactant) and their ionic complexation. Their thermal and structural properties were investigated. One complex, characterized by a SmT-like mesophase, was also tested for photoisotropization.

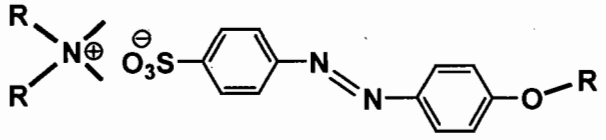

R = C_nH_{2n+1}, n= 6-12, 16

Figure 1.21 Ionic dye-surfactant complexes, obtained in a one-pot synthesis, studied in Chapter 6.

Chapters 7 and 8 are exploratory investigations on two possible uses for the complex of Chapter 4. In Chapter 7, the moisture sensitivity of the complex was exploited in an attempt to modify prefabricated SRGs, in combination with partial protection of the SRG profile by selective shadowing with gold. In this sense, an azopolymer SRG can be considered as a unique soft work bench for nanofabrication.

Chapter 8 investigates the possibility of making light-sensitive fibres with the MO/P4VPMe complex by the electrospinning technique. It has already been shown that azo films can have the very interesting property of bending in light.[187] This is extremely important in the application of converting light into mechanical energy.[183,188] It can be anticipated that when the 2D film is transformed into a 1D fibre, this photomechanical property may be amplified and more practical to control – for example, by alternate stretching and shrinkage. Manipulation of these fibres by light is the ultimate goal of this project, although only the initial step – the feasibility of making electrospun fibres from our complex – is shown in this chapter. In future work, photoinduced orientation and photomechanical properties will be investigated.

The final chapter, Chapter 9, summarizes and discusses the overall results obtained from the studies described in Chapters 2-8, and gives a perspective for future directions.

1.9 Composition of thesis

Chapters 2, 3, 4 and 5 constitute the chapters required for a thesis in the form of articles that are published, accepted or submitted. The remaining chapters are normal thesis chapters. For the sake of uniformity, they have been written in the same format as the chapters based on articles. The work described in Chapters 2, 3, 6 and 7 was done entirely by myself under the supervision of Prof. Bazuin. The optical experiments in Chapters 4, 5 and 7 were done by myself (unless otherwise noted) in the laboratory of Prof. Christopher Barrett (Dept. of Chemistry, McGill University). Ph.D. student, Xin Wang, in the Bazuin group prepared and characterized one of the six complexes studied in Chapter 3, under my supervision and with my help. The gold shadowing in Chapter 7 was done in the laboratory of Prof. Jean-François Masson (Chemistry Department, University of Montreal). The work described in Chapter 8 was performed in collaboration with Prof. Christian Pellerin (Chemistry Department, University of Montreal) and Ph.D. student, Xiaoxiao Wang. It

describes a method that I developed to prepare photoresponsive fibers using the electrospinning technique available in the Pellerin laboratories, and which will be further developed by Wang.

1.10 References

1. Griess, P. *Liebigs Ann. Chem.* **1858,** 106, 123.
2. Allen, R. L. M., *Color chemistry*. Thomas Nelson and Sons (Canada): 1971.
3. Pavia, D. L.; Lampman, G. M.; Kriz, G. S., *Introduction to spectroscopy: a guide for students of organic chemistry*. 3rd ed.; Harcourt college publishers: Montreal, 2001.
4. Rau, H., Photoisomerization of azobenzenes. In *Photochemistry and photophysics*, Rabek, J. K., Ed.; CRC Press: Boca Raton, FL., 1990; Vol. 2, pp. 119-141.
5. Schulze, F. W.; Petrick, H. J.; Cammenga, H. K.; Klinge, H. *Zeitschrift fuer Physikalische Chemie* **1977,** 107, 1-19.
6. Fischer, E.; Frankel, M.; Wolovsky, R. *J. Chem. Phys.* **1955,** 23, 1367.
7. Kumar, G. S.; Neckers, D. C. *Chem. Rev.* **1989,** 89, 1915-1925.
8. Yager, K. G.; Barrett, C. J., Light-induced nanostructure formation using azobenzene polymers. In *Polymeric Nanostructures and Their Applications*, Nalwa, H. S., Ed.; American Scientific Publishers: Los Angeles, 2007; Vol. 2, pp. 243-280.
9. Hartley, G. S. *Nature* **1937,** 140, 281.
10. Barrett, C.; Natansohn, A.; Rochon, P. *Macromolecules* **1994,** 27, 4781-4786.
11. Rau, H. *J. Photochem.* **1984,** 26, 221-225.
12. Eisenbach, C. D. *Makromol. Chem.* **1978,** 179, 2489-2506.
13. Chen, D. T. L.; Morawetz, H. *Macromolecules* **1976,** 9, 463-468.
14. Spoerlein, S.; Carstens, H.; Satzger, H.; Renner, C.; Behrendt, R.; Morader, L.; Tavan, P.; Zinth, W.; Wachtveitl, J. *Proc. Natl. Acad. Sci. U. S. A.* **2002,** 99, 7998-8002.
15. Stolow, A.; Jonas, D. M. *Science* **2004,** 305, 1575-1577.
16. Irie, M.; Hirano, Y.; Hashimoto, S.; Hayashi, K. *Macromolecules* **1981,** 14, 262-267.
17. Irie, M.; Menju, A.; Hayashi, K. *Macromolecules* **1979,** 12, 1176-1180.
18. Eisenbach, C. D. *Polymer* **1980,** 21, 1175-1179.
19. Irie, M.; Tanaka, H. *Macromolecules* **1983,** 16, 210-214.
20. Peters, M. V.; Stoll, R. S.; Kuehn, A.; Hecht, S. *Angew. Chem., Int. Ed.* **2008,** 47, 5968-5972, S5968/1-S5968/32.
21. Yu, X.; Xiong, C.; You, Y.; Dong, L.; Yao, J. *Synth. Met.* **2008,** 158, 375-378.
22. Natansohn, A.; Rochon, P. *Chem. Rev.* **2002,** 102, 4139-4175.
23. Atkins, P. W., *Physical Chemistry*. 8th ed.; W. H. Freeman: New York, 1994.
24. Henneberg, O.; Geue, T.; Pietsch, U.; Saphiannikova, M.; Winter, B. *Appl. Phys. Lett.* **2004,** 84, 1561-1563.
25. Petrova, S. S.; Shaverdova, V. G. *Opt. Spectrosc.* **2006,** 101, 549-554.
26. Sekkat, Z.; Wood, J.; Aust, E. F.; Knoll, W.; Volksen, W.; Miller, R. D. *J. Opt. Soc. Am. B* **1996,** 13, 1713-1724.

27. Sekkat, Z.; Wood, J.; Knoll, W.; Volksen, W.; Miller, R. D.; Knoesen, A. *J. Opt. Soc. Am. B* **1997,** 14, 829-833.
28. Okano, K.; Shishido, A.; Ikeda, T.; Shiono, T. *Mol. Cryst. Liq. Cryst.* **2005,** 441, 275-285.
29. Okano, K.; Shishido, A.; Tsutsumi, O.; Shiono, T.; Ikeda, T. *J. Mater. Chem.* **2005,** 15, 3395-3401.
30. Okano, K.; Tsutsumi, O.; Shishido, A.; Ikeda, T. *J. Am. Chem. Soc.* **2006,** 128, 15368-15369.
31. Okano, K.; Shishido, A.; Ikeda, T. *Macromolecules* **2006,** 39, 145-152.
32. Zhao, Y., Azo-benzene-containing block copolymers. In *Polymeric Nanostructures and Their Applications*, Nalwa, H. S., Ed.; American Scientific Publishers: Los Angeles, 2007; Vol. 2, pp. 281-311.
33. Yavrian, A.; Galstian, T. V.; Piche, M. *Opt. Eng.* **2002,** 41, 852-855.
34. Yu, H.; Asaoka, S.; Shishido, A.; Iyoda, T.; Ikeda, T. *Small* **2007,** 3, 768-771.
35. Naydenova, I.; Nikolova, L.; Ramanujam, P. S.; Hvilsted, S. *J. Opt. A: Pure Appl. Opt.* **1999,** 1, 438-441.
36. Wu, Y.; Ikeda, T.; Zhang, Q. *Adv. Mater.* **1999,** 11, 300-302.
37. Choi, S.-W.; Kawauchi, S.; Ha, N. Y.; Takezoe, H. *Phys. Chem. Chem. Phys.* **2007,** 9, 3671-3681.
38. Nikolova, L.; Nedelchev, L.; Todorov, T.; Petrova, T.; Tomova, N.; Dragostinova, V.; Ramanujam, P. S.; Hvilsted, S. *Appl. Phys. Lett.* **2000,** 77, 657-659.
39. Nikolova, L.; Todorov, T.; Ivanov, M.; Andruzzi, F.; Hvilsted, S.; Ramanujam, P. S. *Opt. Mater.* **1997,** 8, 255-258.
40. Iftime, G.; Labarthet, F. L.; Natansohn, A.; Rochon, P. *J. Am. Chem. Soc.* **2000,** 122, 12646-12650.
41. Kim, M.-J.; Shin, B.-G.; Kim, J.-J.; Kim, D.-Y. *J. Am. Chem. Soc.* **2002,** 124, 3504-3505.
42. Tejedor, R. M.; Oriol, L.; Serrano, J. L.; Urena, F. P.; Gonzalez, J. J. L. *Adv. Funct. Mater.* **2007,** 17, 3486-3492.
43. Hore, D. K.; Natansohn, A. L.; Rochon, P. L. *J. Phys. Chem. B* **2003,** 107, 2506-2518.
44. Teitel, A. *Naturwissenschaften* **1957,** 44, 370.
45. Neporent, B. S.; Stolbova, O. V. *Opt. Spektrosk.* **1961,** 10, 287-288.
46. Todorov, T.; Nikolova, L.; Tomova, N. *Appl. Opt.* **1984,** 23, 4309-4312.
47. Kim, D. Y.; Tripathy, S. K.; Li, L.; Kumar, J. *Appl. Phys. Lett.* **1995,** 66, 1166-1168.
48. Rochon, P.; Batalla, E.; Natansohn, A. *Appl. Phys. Lett.* **1995,** 66, 136-138.
49. Luc, J.; Bouchouit, K.; Czaplicki, R.; Fillaut, J. L.; Sahraoui, B. *Optics Express* **2008,** 16, 15633-15639.
50. Zhang, Q.; Bazuin, C. G.; Barrett, C. J. *Chem. Mater.* **2008,** 20, 29-31.
51. You, F.; Paik, M. Y.; Hackel, M.; Kador, L.; Kropp, D.; Schmidt, H.-W.; Ober, C. K. *Adv. Funct. Mater.* **2006,** 16, 1577-1581.
52. Collings, P. J., *Liquid Crystals, Nature's Delicate Phase of Matter*. 2nd ed.; Prinston University Press: Woodstock, Oxfordshire, 2002.
53. Kumar, S., *Liquid crystals, experimental study of physical properties and phase transitions*. Cambridge University press: Cambridge, 2001.
54. Baron, M. *Pure Appl. Chem.* **2001,** 73, 845-895.

55. Collings, P. J.; Hird, M., *Introduction to liquid crystals-chemistry and physics*. Taylor & Francis ltd: London, 1997.
56. Demus, D., *Handbook of liquid crystals*. Wiley-VCH: Toronto, 1998.
57. Lehn, J.-M., *Supramolecular Chemistry: Concepts and Perspectives*. Wiley-VCH: New York, 1995.
58. Cragg, P. J., *A Practical Guide to Supramolecular Chemistry*. John Wiley & Sons: 2005.
59. Steed, J. W.; Turner, D. R.; Wallace, K. J., *Core Concepts in Supramolecular Chemistry and Nanochemistry*. John Willey & Sons: 2007.
60. Alexander, C.; Jariwala, C. P.; Lee, C. M.; Griffin, A. C. *Polym. Prepr.* **1993,** 34, 168-169.
61. Griffin, A. C.; Lee, C. M.; St Pourcain, C. B. *Polym. Mater. Sci. Eng.* **1995,** 72, 172.
62. Lee, C. M.; Griffin, A. C. *Macromol. Symp.* **1997,** 117, 281-290.
63. Kato, T.; Frechet, J. M. J. *Macromolecules* **1989,** 22, 3818-3819.
64. Bazuin, C. G., Design of polymer liquid crystals with non-covalent bonds. In *Mechanical and Thermophysical Properties of Polymer Liquid Crystals*, Brostow, W., Ed.; Chapman and Hall: London, 1998; pp. 59-100.
65. Bazuin, C. G.; Brandys, F. A. *Chem. Mater.* **1992,** 4, 970-972.
66. Brandys, F. A.; Bazuin, C. G. *Chem. Mater.* **1996,** 8, 83-92.
67. Stewart, D.; Imrie, C. T. *J. Mater. Chem.* **1995,** 5, 223-228.
68. Ten, B. G.; Ruokolainen, J.; Okkala, O. *Europhys. Lett.* **1996,** 35, 91-95.
69. Ruokolainen, J.; ten Brinke, G.; Ikkala, O.; Torkkeli, M.; Serimaa, R. *Macromolecules* **1996,** 29, 3409-3415.
70. Ujiie, S.; Iimura, K. *Macromolecules* **1992,** 25, 3174-3178.
71. Tibirna, C. M.; Bazuin, C. G. *J. Polym. Sci., Part B: Polym. Phys.* **2005,** 43, 3421-3431.
72. Bazuin, C. G.; Tork, A. *Macromolecules* **1995,** 28, 8877-8880.
73. Faul, C. F. J.; Antonietti, M. *Adv. Mater.* **2003,** 15, 673-683.
74. Imrie, C. T. *Trends Polym. Sci.* **1995,** 3, 22-29.
75. Kato, T. *Structure and Bonding* **2000,** 96, 95-146.
76. Kato, T.; Mizoshita, N.; Kishimoto, K. *Angew. Chem., Int. Ed.* **2006,** 45, 38-68.
77. Hsiao, V. K. S.; Zheng, Y. B.; Juluri, B. K.; Huang, T. J. *Adv. Mater.* **2008,** 20, 3528-3532.
78. Matczyszyn, K.; Chwialkowska, A.; Sworakowski, J. *Thin Solid Films* **2008,** 516, 8899-8904.
79. Baldovino-Pantaleon, O.; Porras-Aguilar, R.; Sanchez-Castillo, A.; Ramirez-San-Juan, J. C.; Ramos-Garcia, R.; Gonzalez, E. A. *Mol. Cryst. Liq. Cryst.* **2008,** 488, 1-10.
80. Zolot'ko, A. S.; Budagovsky, I. A.; Ochkin, V. N.; Smayev, M. P.; Bobrovsky, A. Y.; Shibaev, V. P.; Boiko, N. I.; Lysachkov, A. I.; Barnik, M. I. *Mol. Cryst. Liq. Cryst.* **2008,** 488, 265-278.
81. Medvedev, A. V.; Barmatov, E. B.; Medvedev, A. S.; Shibaev, V. P.; Ivanov, S. A.; Kozlovsky, M.; Stumpe, J. *Macromolecules* **2005,** 38, 2223-2229.
82. Sandhya, K. Y.; Pillai, C. K. S.; Sato, M.; Tsutsumi, N. *J. Polym. Sci., Part A: Polym. Chem.* **2003,** 41, 1527-1535.

83. Yesodha, S. K.; Sadashiva Pillai, C. K.; Tsutsumi, N. *Prog. Polym. Sci.* **2004,** 29, 45-74.
84. Bahulayan, D.; Sreekumar, K. *J. Mater. Chem.* **1999,** 9, 1425-1429.
85. Sandhya, K. Y.; Pillai, C. K. S. *J. Appl. Polym. Sci.* **2004,** 91, 1976-1982.
86. Acierno, D.; Amendola, E.; Bugatti, V.; Concilio, S.; Giorgini, L.; Iannelli, P.; Piotto, S. P. *Macromolecules* **2004,** 37, 6418-6423.
87. Heldmann, C.; Warner, M. *Macromolecules* **1998,** 31, 3519-3531.
88. Vix, A.; Stocker, W.; Stamm, M.; Wilbert, G.; Zentel, R.; Rabe, J. P. *Macromolecules* **1998,** 31, 9154-9159.
89. Kumaresan, S.; Kannan, P. *J. Polym. Sci., Part A: Polym. Chem.* **2003,** 41, 3188-3196.
90. Jayalatha, D.; Balamurugan, R.; Kannan, P. *Liq. Cryst.* **2008,** 35, 275-285.
91. Baccaredda, M.; Magagnini, P.; Pizzirani, G.; Giusti, P. *J. Polym. Sci., Polym. Lett. Ed.* **1971,** 9, 303-310.
92. Newman, B. A.; Frosini, V.; Magagnini, P. L. *J. Polym. Sci., Polym. Phys. Ed.* **1975,** 13, 87-93.
93. Frosini, V.; Levita, G.; Lupinacci, D.; Magagnini, P. L. *Mol. Cryst. Liq. Cryst.* **1981,** 66, 341-356.
94. Finkelmann, H.; Ringsdorf, H.; Wendorff, J. H. *Makromol. Chem.* **1978,** 179, 273-276.
95. Finkelmann, H.; Wendorff, H. J., *Polymeric Liquid Crystals*. Plenum Press: New York and London, 1985; p 295-302.
96. Percec, V.; Pugh, C., Molecular engineering of predominantly hydrocarbon-based LCPs. In *Side Chain Liquid Crystal Polymers*, McArdle, C. B., Ed.; Blackie and Son Ltd: New York, 1989.
97. Han, M.; Kidowaki, M.; Ichimura, K.; Ramanujam, P. S.; Hvilsted, S. *Macromolecules* **2001,** 34, 4256-4262.
98. Imrie, C. T.; Karasz, F. E.; Attard, G. S. *Macromolecules* **1993,** 26, 3803-3810.
99. Frosini, V.; Magagnini, P. L.; Newman, B. A. *J. Polym. Sci., Polym. Phys. Ed.* **1974,** 12, 23-34.
100. Frosini, V.; Magagnini, P. L.; Newman, B. A. *J. Polym. Sci., Polym. Phys. Ed.* **1977,** 15, 2239-2254.
101. Magagnini, P. L. *Macromol. Chem. and Phys., Suppl.* **1981,** 4, 223-240.
102. Magagnini, P. L.; Marchetti, A.; Matera, F.; Pizzirani, G.; Turchi, G. *Eur. Polym. J.* **1974,** 10, 585-591.
103. Altomare, A.; Andruzzi, L.; Ciardelli, F.; Gallot, B.; Solaro, R. *Polym. Int.* **1998,** 47, 419-427.
104. Li, M.; Zhou, E.; Xu, J.; Chen, X. *J. Appl. Polym. Sci.* **1996,** 60, 2185-2190.
105. Imrie, C. T.; Karasz, F. E.; Attard, G. S. *Macromolecules* **1992,** 25, 1278-1283.
106. Percec, V.; Lee, M. *Polym. Bull.* **1991,** 25, 131-137.
107. Imrie, C. T.; Schleeh, T.; Karasz, F. E.; Attard, G. S. *Macromolecules* **1993,** 26, 539-544.
108. Schleeh, T.; Imrie, C. T.; Rice, D. M.; Karasz, F. E.; Attard, G. S. *J. Polym. Sci., Part A: Polym. Chem.* **1993,** 31, 1859-1869.
109. Imrie, C. T.; Karasz, F. E.; Attard, G. S. *Liq. Cryst.* **1991,** 9, 47-57.
110. Imrie, C. T.; Attard, G. S.; Karasz, F. E. *Macromolecules* **1996,** 29, 1031-1035.

111. Imrie, C. T.; Paterson, B. J. A. *Macromolecules* **1994,** 27, 6673-6676.
112. Imrie, C. T.; Karasz, F. E.; Attard, G. S. *Macromolecules* **1993,** 26, 545-550.
113. Li, X.; Goh, S. H.; Lai, Y. H. *Liq. Cryst.* **2002,** 29, 675-685.
114. Demus, D.; Pelzl, G.; Sharma, N. K.; Weissflog, W. *Mol. Cryst. Liq. Cryst.* **1981,** 76, 241-251.
115. Sharma, N. K.; Pelzl, G.; Demus, D.; Weissflog, W. *Zeitschrift fuer Physikalische Chemie (Leipzig)* **1980,** 261, 579-584.
116. Takenaka, S.; Hirohata, T.; Shimohara, I.; Kusabayashi, S. *J. Chem. Soc., Perkin Trans. 2* **1986**, 1121-1125.
117. Yu, H.; Shishido, A.; Iyoda, T.; Ikeda, T. *Macromol. Rapid Commun.* **2007,** 28, 927-931.
118. Zhang, Y.; Zhang, W.; Chen, X.; Cheng, Z.; Wu, J.; Zhu, J.; Zhu, X. *J. Polym. Sci., Part A: Polym. Chem.* **2008,** 46, 777-789.
119. Cui, L.; Tong, X.; Yan, X.; Liu, G.; Zhao, Y. *Macromolecules* **2004,** 37, 7097-7104.
120. Cui, L.; Zhao, Y.; Yavrian, A.; Galstian, T. *Macromolecules* **2003,** 36, 8246-8252.
121. Forcen, P.; Oriol, L.; Sanchez, C.; Alcala, R.; Hvilsted, S.; Jankova, K.; Loos, J. *J. Polym. Sci., Part A: Polym. Chem.* **2007,** 45, 1899-1910.
122. Yu, H.; Iyoda, T.; Ikeda, T. *J. Am. Chem. Soc.* **2006,** 128, 11010-11011.
123. Yu, H.; Li, J.; Shishido, A.; Iyoda, T.; Ikeda, T. *Mol. Cryst. Liq. Cryst.* **2007,** 478, 1027-1037.
124. Yu, H.; Shishido, A.; Ikeda, T.; Iyoda, T. *Macromol. Rapid Commun.* **2005,** 26, 1594-1598.
125. Zhao, Y.; Qi, B.; Tong, X.; Zhao, Y. *Macromolecules* **2008,** 41, 3823-3831.
126. Hadjichristidis, N.; Pitsikalis, M.; Iatrou, H., Synthesis of Block Copolymers. In *Adv. Polym. Sci.*, Springer Berlin: Berlin, 2005; pp. 1-124.
127. Osuji, C. O.; Chen, J. T.; Mao, G.; Ober, C. K.; Thomas, E. L. *Polymer* **2000,** 41, 8897-8907.
128. Anthamatten, M.; Zheng, W. Y.; Hammond, P. T. *Macromolecules* **1999,** 32, 4838-4848.
129. Mao, G.; Wang, J.; Clingman, S. R.; Ober, C. K.; Chen, J. T.; Thomas, E. L. *Macromolecules* **1997,** 30, 2556-2567.
130. Tong, X.; Cui, L.; Zhao, Y. *Macromolecules* **2004,** 37, 3101-3112.
131. Yu, H.; Okano, K.; Shishido, A.; Ikeda, T.; Kamata, K.; Komura, M.; Iyoda, T. *Adv. Mater.* **2005,** 17, 2184-2188.
132. Yu, H.; Naka, Y.; Shishido, A.; Ikeda, T. *Macromolecules* **2008,** 41, 7959-7966.
133. Prajapati, A. K.; Vora, R. A.; Pandya, H. M. *Mol. Cryst. Liq. Cryst. Sci. Technol., Sect. A* **2001,** 369, 37-46.
134. Vora, R. A.; Prajapati, A. K.; Kevat, J. B.; Raina, K. K. *Liq. Cryst.* **2001,** 28, 983-989.
135. Cui, L.; Dahmane, S.; Tong, X.; Zhu, L.; Zhao, Y. *Macromolecules* **2005,** 38, 2076-2084.
136. Halder, G. J.; Kepert, C. J. *Aust. J. Chem.* **2005,** 58, 311-314.
137. Sun, S.-S.; Anspach, J. A.; Lees, A. J. *Inorg. Chem.* **2002,** 41, 1862-1869.
138. Sun, S.-S.; Lees, A. J. *J. Am. Chem. Soc.* **2000,** 122, 8956-8967.
139. Aoki, K. i.; Nakagawa, M.; Seki, T.; Ichimura, K. *Bull. Chem. Soc. Jpn.* **2002,** 75, 2533-2539.

140. Cui, L.; Zhao, Y. *Chem. Mater.* **2004,** 16, 2076-2082.
141. Ishii, D.; Udatsu, M.; Nakagawa, M.; Iyoda, T. *Trans. Mater. Res. Soc. Jpn.* **2004,** 29, 889-892.
142. Mallia, V. A.; Antharjanam, P. K. S.; Das, S. *Chem. Lett.* **2001,** 752-753.
143. Mallia, V. A.; Das, S. *Liq. Cryst.* **2001,** 28, 259-264.
144. Toh, C. L.; Xu, J.; Lu, X.; He, C. *Liq. Cryst.* **2008,** 35, 241-251.
145. Nakagawa, M.; Ishii, D.; Aoki, K. i.; Seki, T.; Iyoda, T. *Adv. Mater.* **2005,** 17, 200-205.
146. Fouquey, C.; Lehn, J. M.; Levelut, A. M. *Adv. Mater.* **1990,** 2, 254-257.
147. St.Pourcain, C. B.; Griffin, A. C. *Macromolecules* **1995,** 28, 4116-4121.
148. Wilson, L. M. *Macromolecules* **1994,** 27, 6683-6686.
149. Wilson, L. M. *Liq. Cryst.* **1995,** 18, 381-385.
150. Vera, F.; Almuzara, C.; Orera, I.; Barbera, J.; Oriol, L.; Serrano, J. L.; Sierra, T. *J. Polym. Sci., Part A: Polym. Chem.* **2008,** 46, 5528-5541.
151. Kato, T.; Hirota, N.; Fujishima, A.; Frechet, J. M. J. *J. Polym. Sci., Part A: Polym. Chem.* **1996,** 34, 57-62.
152. Kato, T.; Kawakami, T. *Chem. Lett.* **1997,** 211-212.
153. Kawakami, T.; Kato, T. *Macromolecules* **1998,** 31, 4475-4479.
154. Lee, H.-K.; Lee, K.; Ko, Y. H.; Chang, Y. J.; Oh, N.-K.; Zin, W.-C.; Kim, K. *Angew. Chem., Int. Ed.* **2001,** 40, 2669-2671.
155. Li, X.; Goh, S. H.; Lai, Y. H.; Cheng, S. X. *Liq. Cryst.* **2001,** 28, 1527-1538.
156. Osuji, C. O.; Chao, C.-Y.; Ober, C. K.; Thomas, E. L. *Macromolecules* **2006,** 39, 3114-3117.
157. Zettsu, N.; Ogasawara, T.; Mizoshita, N.; Nagano, S.; Seki, T. *Adv. Mater.* **2008,** 20, 516-521.
158. de Wit, J.; van Ekenstein, G. A.; Polushkin, E.; Kvashnina, K.; Bras, W.; Ikkala, O.; ten Brinke, G. *Macromolecules* **2008,** 41, 4200-4204.
159. Sallenave, X.; Bazuin, C. G. *Macromolecules* **2007,** 40, 5326-5336.
160. Antonietti, M.; Burger, C.; Thunemann, A. *Trends Polym. Sci.* **1997,** 5, 262-267.
161. Antonietti, M.; Conrad, J. *Angew. Chem. Int. Ed.* **1994,** 106, 1927-1929.
162. Antonietti, M.; Conrad, J.; Thuenemann, A. *Macromolecules* **1994,** 27, 6007-6011.
163. Faul, C. F. J.; Antonietti, M. *Chem.-Eur. J.* **2002,** 8, 2764-2768.
164. Guan, Y.; Antonietti, M.; Faul, C. F. J. *Langmuir* **2002,** 18, 5939-5945.
165. Zakrevskyy, Y.; Stumpe, J.; Faul, C. F. J. *Adv. Mater.* **2006,** 18, 2133-2136.
166. Faul, C. F. J. *Mol. Cryst. Liq. Cryst.* **2006,** 450, 55-65.
167. Binnemans, K. *Chem. Rev.* **2005,** 105, 4148-4204.
168. Xiao, S.; Lu, X.; Lu, Q.; Su, B. *Macromolecules* **2008,** 41, 3884-3892.
169. Bo, Q.; Yavrian, A.; Galstian, T.; Zhao, Y. *Macromolecules* **2005,** 38, 3079-3086.
170. Tibirna, C. M.; Diouf, P. N. *Polymer* **2008,** 49, 241-253.
171. Marcos, M.; Alcala, R.; Barbera, J.; Romero, P.; Sanchez, C.; Serrano, J. L. *Chem. Mater.* **2008,** 20, 5209-5217.
172. Zhu, X.; Beginn, U.; Moeller, M.; Gearba, R. I.; Anokhin, D. V.; Ivanov, D. A. *J. Am. Chem. Soc.* **2006,** 128, 16928-16937.
173. Nepogodiev, S. A.; Stoddart, J. F. *Chem. Rev.* **1998,** 98, 1959-1976.
174. Bortolus, P.; Monti, S. *J. Phys. Chem.* **1987,** 91, 5046-5050.

175. Anderson, S.; Claridge, T. D. W.; Anderson, H. L. *Angew. Chem., Int. Ed.* **1997,** 36, 1310-1313.
176. Craig, M. R.; Hutchings, M. G.; Claridge, T. D. W.; Anderson, H. L. *Angew. Chem., Int. Ed.* **2001,** 40, 1071-1074.
177. Cheetham, A. G.; Hutchings, M. G.; Claridge, T. D. W.; Anderson, H. L. *Angew. Chem., Int. Ed.* **2006,** 45, 1596-1599.
178. Murakami, H.; Kawabuchi, A.; Matsumoto, R.; Ido, T.; Nakashima, N. *J. Am. Chem. Soc.* **2005,** 127, 15891-15899.
179. Balzani, V.; Credi, A.; Marchioni, F.; Stoddart, J. F. *Chem. Commun.* **2001**, 1860-1861.
180. Merian, E. *Text. Res. J.* **1966,** 36, 612-618.
181. Barrett, C. J.; Mamiya, J.-i.; Yager, K. G.; Ikeda, T. *Soft Matter* **2007,** 3, 1249-1261.
182. Camacho-Lopez, M.; Finkelmann, H.; Palffy-Muhoray, P.; Shelley, M. *Nat. Mater.* **2004,** 3, 307-310.
183. Ikeda, T.; Mamiya, J.-i.; Yu, Y. *Angew. Chem., Int. Ed.* **2007,** 46, 506-528.
184. Tanchak, O. M.; Barrett, C. J. *Macromolecules* **2005,** 38, 10566-10570.
185. Yager, K. G.; Tanchak, O. M.; Godbout, C.; Fritzsche, H.; Barrett, C. J. *Macromolecules* **2006,** 39, 9311-9319.
186. Naciri, J.; Srinivasan, A.; Jeon, H.; Nikolov, N.; Keller, P.; Ratna, B. R. *Macromolecules* **2003,** 36, 8499-8505.
187. Yu, Y.; Nakano, M.; Ikeda, T. *Nature* **2003,** 425, 145.
188. Yamada, M.; Kondo, M.; Mamiya, J.-i.; Yu, Y.; Kinoshita, M.; Barrett, C. J.; Ikeda, T. *Angew. Chem., Int. Ed.* **2008,** 47, 4986-4988.
189. Mamiya, J.-i.; Yoshitake, A.; Kondo, M.; Yu, Y.; Ikeda, T. *J. Mater. Chem.* **2008,** 18, 63-65.
190. Holland, N. B.; Hugel, T.; Neuert, G.; Cattani-Scholz, A.; Renner, C.; Oesterhelt, D.; Moroder, L.; Seitz, M.; Gaub, H. E. *Macromolecules* **2003,** 36, 2015-2023.
191. Hugel, T.; Holland Nolan, B.; Cattani, A.; Moroder, L.; Seitz, M.; Gaub Hermann, E. *Science* **2002,** 296, 1103-1106.
192. Gorostiza, P.; Isacoff, E. Y. *Science* **2008,** 322, 395-399.
193. Liu, X.-M.; Yang, B.; Wang, Y.-L.; Wang, J.-Y. *Chem. Mater.* **2005,** 17, 2792-2795.
194. Zou, J.; Tao, F.; Jiang, M. *Langmuir* **2007,** 23, 12791-12794.
195. Wang, Y.; Ma, N.; Wang, Z.; Zhang, X. *Angew. Chem., Int. Ed.* **2007,** 46, 2823-2826.
196. Zhao, Y. *Chem. Rec.* **2007,** 7, 286-294.
197. Zhu, Y.; Fujiwara, M. *Angew. Chem., Int. Ed.* **2007,** 46, 2241-2244.
198. Ichimura, K.; Suzuki, Y.; Seki, T.; Hosoki, A.; Aoki, K. *Langmuir* **1988,** 4, 1214-1216.
199. Aoki, K.; Seki, T.; Suzuki, Y.; Tamaki, T.; Hosoki, A.; Ichimura, K. *Langmuir* **1992,** 8, 1007-1013.
200. Feng, C. L.; Qu, G.; Song, Y.; Jiang, L.; Zhu, D. *Surf. Interface Anal.* **2006,** 38, 1343-1347.
201. Moeller, G.; Harke, M.; Motschmann, H.; Prescher, D. *Langmuir* **1998,** 14, 4955-4957.
202. Paik, M. Y.; Krishnan, S.; You, F.; Li, X.; Hexemer, A.; Ando, Y.; Kang, S. H.; Fischer, D. A.; Kramer, E. J.; Ober, C. K. *Langmuir* **2007,** 23, 5110-5119.

203. Haro, M.; del Barrio, J.; Villares, A.; Oriol, L.; Cea, P.; Lopez, M. C. *Langmuir* **2008,** 24, 10196-10203.
204. Haruta, O.; Matsuo, Y.; Hashimoto, Y.; Niikura, K.; Ijiro, K. *Langmuir* **2008,** 24, 2618-2624.
205. Kumar, B.; Prajapati, A. K.; Varia, M. C.; Suresh, K. A. *Langmuir* **2009,** 25, 839-844.
206. Goncalves, V. C.; Ferreira, M.; Olivati, C. A.; Cardoso, M. R.; Mendonca, C. R.; Balogh, D. T. *Colloid Polym. Sci.* **2008,** 286, 1395-1401.

Chapter 2. Liquid Crystallinity and Other Properties in Complexes of Cationic Azo-containing Surfactomesogens with Poly(styrene sulfonate)

Qian Zhang and C. Geraldine Bazuin*

Centre de recherche sur les matériaux auto-assemblés (CRMAA/CSACS),
Département de chimie, Université de Montréal, C.P. 6128, succursale Centre-Ville,
Montréal (QC), Canada H3C 3J7

Macromolecules **2009**, 42, 4775-4786

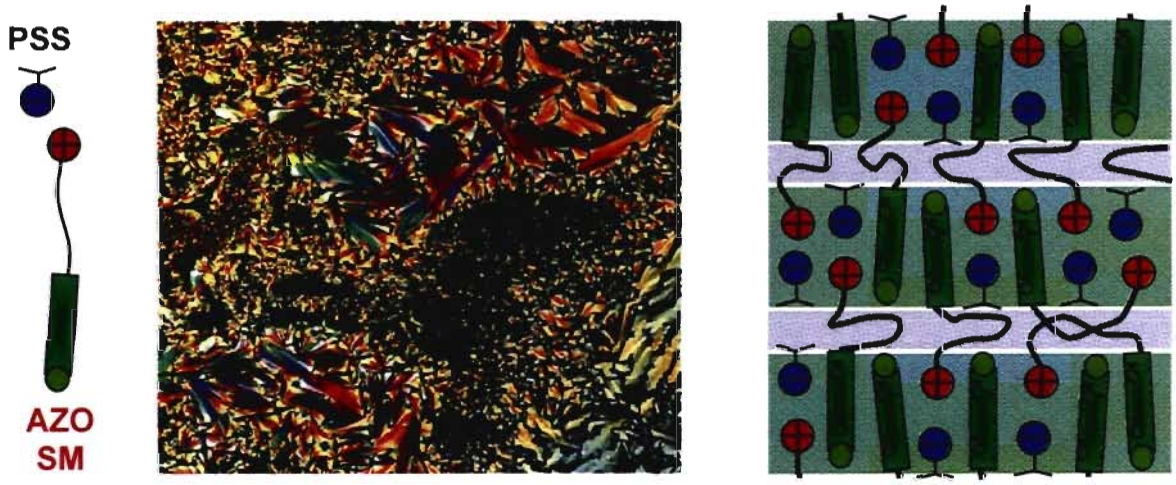

Abstract

A series of stoichiometric ionically bonded side-chain polymer complexes, constructed from poly(styrene sulfonate) (PSS) and quaternary ammonium-functionalized azo-containing surfactomesogens (SMs) with hexyl and decyl spacers, were prepared under rigorous conditions and thoroughly dried, and their potential thermotropic liquid crystal (LC) properties investigated. The SM series consists of eight differently substituted azobenzene cores with a range of polarities. In their Br-neutralized form, they are generally crystalline to high temperatures (those with an ethyl amine linking group having very slow recrystallization kinetics). Only some of the complexes showed LC properties in their as-prepared form, while several others required exceedingly long annealing times (hours to days) at appropriate temperatures to reveal LC character, attributed to the semi-rigid PS backbone, relatively high molecular weight, and strong ionic interactions that greatly retard the kinetics of chain reorganization towards equilibrium. Among the decyl-spacer complexes, only the two with an ethyl amine linking group appear intrinsically isotropic, whereas, among the hexyl-spacer complexes, just two revealed LC character. X-ray diffraction (XRD) indicated that the LC structure is generally of an effectively single-layer SmA type; but while the complexes based on SMs with nonpolar tails produce a classical SmA XRD pattern, those with polar tails produce one with a quasi-extinct or reduced intensity first-order diffraction peak. The former also have lamellar thicknesses that are ca. 5 Å less than the latter, in agreement with literature data for all-covalent polystyrene-based analogues and explained by greater mesogen interdigitation for those with nonpolar tails that thus lie in the alkyl spacer subplane. A model proposed to rationalize the apparent extinction of the first-order XRD peak relies on dipole-dipole interactions between the polar mesogens and the ion pairs that allow them to share the same subplane, thus halving the effective lamellar thickness. A study of photoinduced birefringence (PIB) in selected complexes, compared with a spacer-free complex, shows that the flexible spacer plays a significant role in reducing PIB stability.

2.1 Introduction

Azo-containing polymers continue to be an active area of interest because of their many potential applications as optically driven functional materials, based on the reversible trans-cis photoisomerisation of the azo bond (see, for example, reviews 1-6). When combined with liquid crystal (LC) character, optical control can be further enhanced by exploiting the inherent anisotropy of LC materials.[2] Elegant illustrations of the latter are based on the photomechanical effect, such as observed in directed light-induced bending of azo-based LC polymer films[7] and a light-driven plastic motor.[8]

To simplify what are often tedious and costly synthetic procedures and yet avoid the instabilities of simple doped systems, supramolecular means to obtaining azo-containing and LC polymers (LCPs) with desired optical responses are attractive.[9-14] Supramolecular thermotropic LCPs, some of which are azo-containing, have been investigated extensively for more than a decade (see, e.g., reviews 15-22), and continue to be studied (see, e.g., refs. 23-27, to mention only homopolymer systems). The majority utilize hydrogen bonds as supramolecular links, in both main-chain and side-chain architectures. Ionic bond systems most frequently involve alkyl surfactants complexed to oppositely charged polyelectrolytes, leading to supramolecular side-chain LCPs (SCLCPs). There are few papers that have investigated the thermotropic LC properties of ionically complexed SCLCPs derived from molecules that combine a surfactant-like structure (ionic head group and alkyl chain) with a thermotropic mesogen structure (elongated aromatic core and alkyl chain),[12,18,28-32] as shown schematically in Scheme 2.1, and that we term surfactomesogens.[32,33] Of these, none have compared the LC properties of such complexes that involve a series of different mesogenic motifs (even in all-covalent SCLCPs, this kind of comparison is limited). It should be mentioned, however, that a number of surfactomesogens have been studied in solution and in ultrathin films (Langmuir-Blodgett, layer-by-layer), often complexed with polyelectrolytes or surfactants, and also occasionally in the bulk state (see, e.g., refs. 6, 21, 34-42). Similar mesogenic molecules have been used to construct supramolecular SCLCP systems based on H-bonding,[15-17,43] but these interactions are sometimes too weak to lead to high complexation rates, in particular when the driving force for self-crystallization of the

mesogenic molecules is strong, which can compromise the ability to obtain LC properties in the complexes.[44,45]

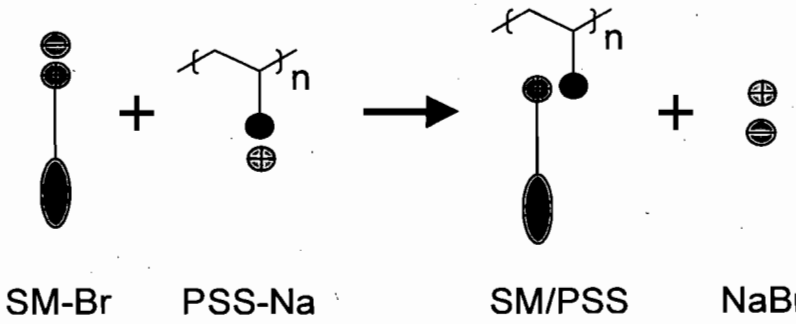

Scheme 2.1 Representation of the ionic complex, SM/PSS, obtained from a surfactomesogen (SM-Br) and an oppositely charged polyelectrolyte, poly(sodium styrene sulfonate) (PSS-Na), with elimination of the NaBr counterions.

Ionically complexed supramolecular LCPs present greater challenges than hydrogen-bonded systems. Ionic bonds are generally stronger and require higher temperatures to become labile compared to H-bonds, and hence lead to much more viscous solutions and melts. This can result in frozen-in structures far from equilibrium whose kinetics to reach equilibrium are much slower. The presence of other polar groups may give rise to additional electrostatic interactions that contribute further to this effect. Furthermore, as is well known for solid-state polyelectrolytes and ionomers, ion-containing systems are susceptible to the presence of (trace) amounts of water, and are often insufficiently dried or sometimes impossible to dry completely without causing some degradation.[46,47] Even if well-dried, they may be subject to rapid absorption of humidity from the atmosphere during sample preparation or transfer to the measuring device, particularly on humid days. On the other hand, strong ionic complexation is attractive for obtaining robust supramolecular systems,[18] for possibly mitigating the plasticizing effect of side chains,[48] and thus for designing higher performance materials.[20]

In the present study, we investigate the thermotropic properties of a series of triethyl ammonium-functionalized surfactomesogens with azo-containing mesogenic cores that are complexed to a readily available oppositely charged polyelectrolyte, poly(sodium styrene sulfonate) (PSS-Na), paying particular attention to the above influences. (In a follow-up paper, the direct influence of humidity and other solvent atmospheres on the LC structure

of selected complexes will be described.[49]) We also examine briefly the photoinduced birefringence response in selected complexes. The sulfonate functionality of PSS-Na provides strong interactions with cationic groups, and is well known to lead to strong cooperative binding in polyelectrolyte-surfactant solutions.[20,34] Furthermore, the polystyrene backbone may enhance the relative rigidity and increase the glass transition temperature (T_g) of the complexes,[50-52] an advantage for the long-term stability often required for electro-optical applications.[53-55] The alkyl chain spacer between the mesogenic core and ionic head group of the surfactomesogen is composed of 6 and 10 methylene units, as representative of two commonly used spacer lengths in all-covalent SCLCPs.[56,57]

The specific substituents chosen for the mesogenic azo core, along with the nomenclature used, are listed in Table 2.1. The dipole moments of the cores, calculated by Hyperchem (see Experimental Section) with the surfactant moiety replaced by a methyl group, are given for reference. As shown in Scheme 2.1, the complexes (SM/PSS) are achieved by simple ion exchange between SM-Br and PSS-Na, with elimination of the NaBr counterions by dialysis against deionized water. A number of analogous all-covalent azo-containing SCLCPs based on polystyrene, particularly with O_2N-O, H_3CO-O and NC-O mesogenic motifs with different spacer lengths, have been investigated in the past,[50,52,53,58-66] providing a convenient point of comparison for the present complexes.

Table 2.1 Nomenclature of the azo-containing surfactomesogens (SMs) synthesized, where the hyphen designates the azobenzene core, n refers to the linear spacer composed of n=6 and 10 CH_2 groups, and Q refers to the triethyl ammonium head group, as well as the calculated dipole moments of the mesogenic core in trans form with nQ replaced by CH_3. The SMs are neutralized by Br (SM-Br) or, when complexed, by PSS (SM/PSS). The azobenzene substituents X, Y and Z are indicated in Scheme 2.2.

Surfactomesogen (SM)	Phenol type X	Aniline type Y	Aniline type Z	Dipole moment [b] (D)
O_2N-N(Et)nQ		NO_2	CH_2CH_3	10.00
O_2N-N(Me)nQ		NO_2	CH_3	9.96 [c]
NC-N(Et)nQ [a]		CN	CH_2CH_3	8.74
O_2N-OnQ	NO_2			7.49
NC-OnQ	CN			5.57
H_3CO-OnQ	OCH_3			0-3 [d]
H_3C-OnQ	CH_3			2.00
H-OnQ	H			1.76

[a] Only n=10 was synthesized. [b] The dipole moments were calculated using Hyperchem 7. [c] In agreement with the value of 9.94 D in ref. 67. [d] Calculated values are subject to the molecular conformation: it is 0 D when the methoxy groups are on opposite sides of the azobenzene axis (symmetric conformation) and 3.42 D when the methoxy groups are on the same side of the azobenzene axis (antisymmetric conformation).

2.2 Experimental section

2.2.1 Instrumentation

^{1}H NMR (500 MHz) spectra were obtained using a Bruker Avance spectrometer and mass spectral data using an Agilent Technologies 6210 time-of-flight LC/MS spectrometer. CHNS elemental analysis was done using a Fisons AE1108 analyzer, Na^+ and Br^- analysis using a FEI Quanta 200 FEG environmental scanning electron microscope equipped with an energy dispersive spectrometer (EDS), and thermogravimetric analysis (TGA) using a TA Instruments Hi-Res TGA 2950 analyzer at a heating rate of 10 °C/min under nitrogen atmosphere. Differential scanning calorimetry (DSC) was performed using a TA instruments Q1000 DSC at heating and cooling rates of 10 °C/min and polarizing optical microscopy (POM) using a Zeiss Axioskop 40Pol microscope coupled with a Linkam Scientific Instrument THMS600 hot stage and a TMS94 temperature controller. X-ray

diffraction (XRD) analysis on powder-like samples packed in 1.0-mm diameter glass capillaries (Charles Supper) was performed with a Bruker D8 Discover system equipped with a 2D Bruker AXS wire-grid detector, using Cu Kα radiation; sample temperature was controlled by a modified Instec HCS410 heating stage and STC200 temperature controller. UV-visible spectra of well-dried films spin-coated from DMF for O_2N-OnQ/PSS and from DMSO for O_2N-N(Et)10Q/PSS were obtained using a Varian Cary 500 Scan UV-Vis-NIR spectrophotometer. Freeze-drying was effected using an FTS Systems FD-3-85A-MP freeze-dryer working at 1-3 mT with the condenser at -90 °C. The molecular dipole moment of the mesogenic core (with a methyl group replacing the ammonium-capped alkyl spacer) was calculated by HyperChem 7.0 (Hypercube), using the ab initio procedure with a small basis set (3-21G) and the conjugate gradient method with an RMS gradient of 0.1 kcal/Å·mol as the termination condition. The most extended molecular lengths (l_c) of the SMs and SM/PSS repeat units (with van der Waals' radii at the extremities included) were estimated by Hyperchem 7.0 energy minimization simulations. For the complexes, the ionic groups were placed in close proximity lying either along the molecular long axis or laterally relative to the long axis before applying minimization.

2.2.2 Synthesis of surfactomesogens

The SMs were synthesized using well-known procedures,[68,69] as indicated in Scheme 2.2 for (a) the phenol type and (b) the aniline type families. The synthesis of O_2N-OnQ was reported previously.[36] Those of the azophenol derivatives and several of the alkyl bromide-substituted precursors, in particular as intermediates in the synthesis of other azo molecules and SCLCPs, have also been reported elsewhere (see, e.g., refs. 25, 58-60, 70, 71 and many citations in refs. 1-21). The particular procedures followed by us for a representative phenol-type and a representative aniline-type SM, along with the elemental and molecular characterization of all of the SMs, are given in the Supporting Information of this chapter.

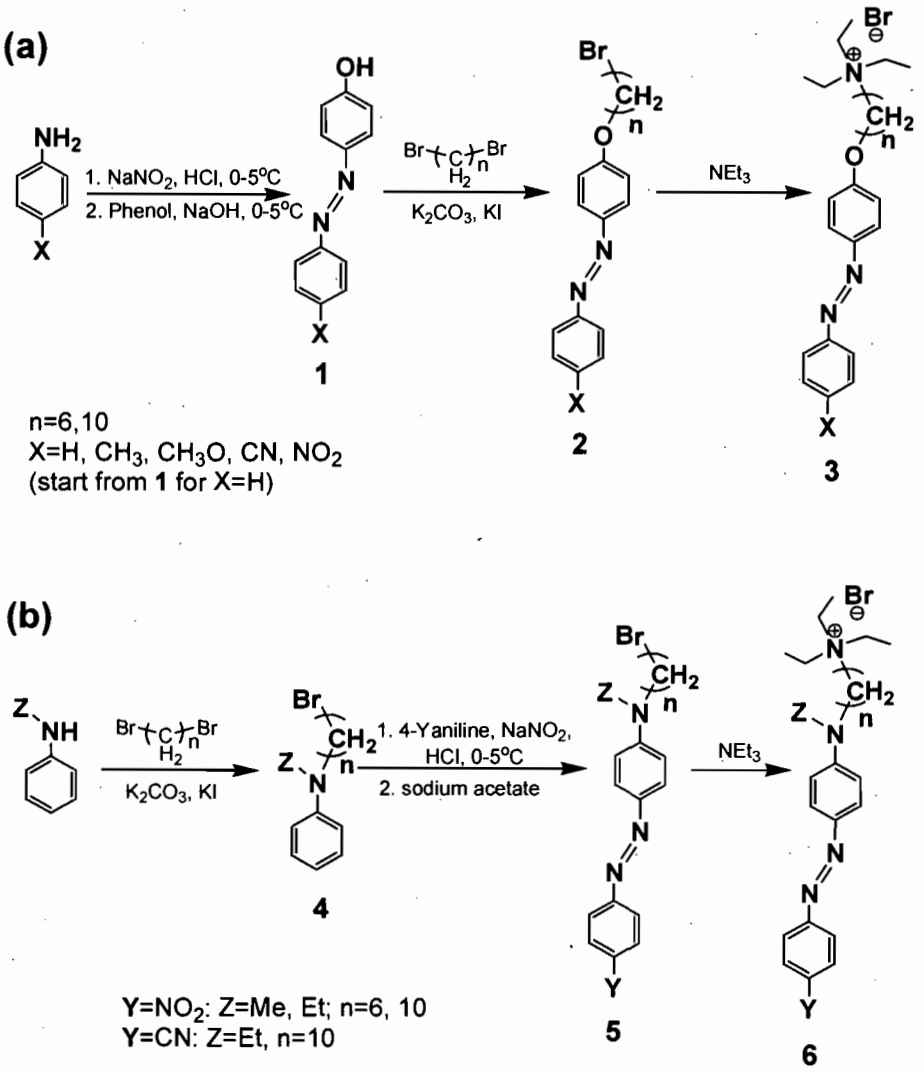

Scheme 2.2 General synthetic strategy of the azo surfactomesogens (SM-Br): (a) phenol type and (b) aniline type.

2.2.3 Preparation of the SM/PSS complexes

The polyelectrolyte used, poly(sodium 4-styrene-sulfonate) (PSS-Na) was obtained from Sigma-Aldrich [M.W.=70,000 and Brookfield viscosity 15,000-55,000 cps in 20% solution at 25 °C, reported by the supplier; M_n=45,000 (DP_n ca. 220) and M_w/M_n=2.0, determined in ref. 32]. The SM/PSS complexes were prepared by ion-exchange procedures (Scheme 2.1) as follows. The SM was dissolved in DMSO (spectrograde; Sigma-Aldrich) at a concentration of ca. 40 mg/mL. In parallel, PSS was dissolved in a minimal amount (a

few drops) of deionized water (Millipore) giving a clear gel-like solution, to which DMSO (ca. 1 mL per 20 mg of PSS) was then added. The amounts of PSS and SM used were calculated to have a small excess (2-5 mol %) of SM relative to the PSS repeat unit, to optimize for stoichiometric complexes, given that excess SM is easily eliminated during the subsequent dialysis procedure. The two separately prepared solutions were stirred in a 60 °C oil bath for ca. 15 min, and then the SM solution was added dropwise to the PSS solution (with DMSO rinsing). If precipitation occurred, enough DMSO was added until resolubilization occurred (to facilitate removal of counterions and excess SM during dialysis). The final concentration of the transparent, colored solution was typically ca. 35 mg/mL. It was stirred at 60 °C for 24 h, then transferred to a dialysis bag (Spectrapor, cutoff M.W. 3500; VWR) where it was dialyzed for a minimum of 4 days against deionized water (ca. 3 L) that was refreshed at least once a day. In the course of dialysis, the resulting complex formed a precipitate and/or a colloidal suspension inside the dialysis bag. The bag contents were transferred to a freeze-drying flask for several days of freeze-drying, followed by vacuum drying at ca. 60 °C for a week, and then storage in a desiccator containing drierite (Sigma-Aldrich). The elimination of all detectable sodium bromide counterions was verified by EDS. The elemental and molecular characterization of the complexes is given in the Supporting Information. For one complex, it was verified that ca. 3 days of dialysis is sufficient to obtain pure stoichiometric complexes and that this is unchanged by longer dialysis times.[72] Just before measurement, the samples were again vacuum dried overnight at ca. 60 °C. Many samples were annealed for POM and XRD studies; in this case, they were annealed in the microscope slides and sealed XRD capillaries, respectively, in a hot stage (Mettler FP5 or Linkam TMS94).

2.2.4 Photoinduced birefringence (PIB)

Photoinduced birefringence in spin-coated films of several complexes was examined using a 454-nm Ar ion writing laser at a power of ca. 700 mW/cm^2 using the same setup as in ref. 9. The O_2N-N(Et)10Q/PSS and O_2N-O10Q/PSS films were spin-coated from dichloromethane (6.6 and 11.6 wt % concentration, respectively) and the O_2N-O6Q/PSS film from nitromethane/dichloromethane (0.74/1 w/w, 11.6 wt % concentration). They were dried in a vacuum oven at 80 °C for at least one week. The films were estimated to

have a thickness of the order of 0.5 μm. The sample chamber was flushed with dry N_2 during PIB measurements.

2.3 Results and discussion

2.3.1 Characteristics of the surfactomesogens (SM-Br)

The SM-Br, having been subjected to rigorous column chromatography and crystallization purification procedures, are highly pure, as attested to by NMR and elemental analysis.[72] Their thermal properties determined by DSC and TGA are summarized in Table 2.2. Their 1% wt loss values ($T_d^{1\%}$) generally lie between ca. 175 and 200 °C (usually slightly higher for the 6-spacer than the 10-spacer ones), with only NC-N(Et)10Q significantly lower (at 155 °C).

Table 2.2 Thermal properties of the azo surfactomesogens, SM-Br, determined by DSC and TGA.[a]

Sample[b]	T_m / °C (ΔH / J·g^{-1})		T_{cr} / °C (ΔH / J·g^{-1})		$T_d^{1\%}$ / °C	
	6Q	10Q	6Q	10Q	6Q	10Q
O_2N-N(Et)	207 (>45[d]) 188 (48)	132 (88), 147 (2)[f] T_g=41[g]	(max 210) 144 (-50)	(max 153) T_g=30[g]	199	179
O_2N-N(Me)	188 (61) 184 (53)	163 (85) 132 (46)	(max 195) 166 (-60)	(max 175) 105 (-44)	192	184
NC-N(Et)		101, 108 (39)[h] T_g=38[g]		(max 118) T_g=27[g]		154
O_2N-O[c]	166 (86) 163 (71)	141 (62) 142 (28)	(max 185) 124 (-72)	(max 150) 115 (-25)	177	173
NC-O	171 (94), 182 (55)[e] 167 (75)	154 (86) 153 (84)	(max 190) 126 (-58)	(max 170) 114 (-76)	187	182
H_3CO-O	195 (148) 188 (112)	186 (185) 181 (119)	(max 205) 93 (-8)	(max 195) 140 (-124)	193	186
H_3C-O	163 (68) 163 (61)	174 (85) 173 (81)	(max 170) 122 (-59)	(max 180) 127 (-89)	184	182
H-O	157 (95) 157 (94)	178 (81) 176 (75)	(max 165) 109 (-82)	(max 185) 146 (-77)	190	188

[a] The DSC (first heating) and TGA thermograms are given in the Supporting Information. The melting points (T_m, peak values) and enthalpies (ΔH) are from the first (upper entry) and second (lower entry) DSC heating scans. The crystallization temperatures (T_{cr}), obtained from the intermediate DSC cooling scan, are accompanied by the maximum temperature (max) of the first heating scan. T_m and T_{cr} are the maxima/minima of the peaks. $T_d^{1\%}$ is the temperature of 1% weight loss relative to the weight at 80°C. [b] The sample identification indicates the terminal and linking groups on either side of the azobenzene core. [c] The O_2N-O10Q SM was synthesized three times, each batch giving identical DSC data. In subsequent heating scans, a transition appeared at 124 °C that increased in intensity at the expense of the peak at 141 °C with each scan (cooling scan unchanged). [d] Scan stopped before baseline reached. [e] Recrystallization appears to occur between the two sharp peaks (exothermic dip). [f] The two temperatures given are the most intense and the highest temperature peaks, respectively, of multiple peaks. [g] No crystallization was observed in subsequent scans following melting; the T_g's given are inflection point values. [h] Two partially overlapping peaks of similar intensities.

All but two of the surfactomesogens are crystalline to high temperature, ranging from ca. 140 to 210 °C, where they melt directly to the isotropic phase, and recrystallize with a supercooling of typically 30-50 °C (keeping in mind that the data obtained after melting may be affected by slight degradation in the cases where the maximum scan temperature was near or beyond $T_d^{1\%}$). Usually, the 6-spacer SM-Br has a higher melting point than the corresponding 10-spacer SM-Br. The two lower melting compounds, NC-N(Et)10Q (which has a double melting peak in the 100-110 °C range[72]) and O_2N-N(Et)10Q (which has a complex melting pattern in the 120-150 °C range[72]), do not recrystallize at all in the

DSC conditions after melting but instead show an apparent glass transition near 40 °C in subsequent heating scans (in these two cases, the maximum temperature scans were well below $T_d^{1\%}$). However, POM and XRD investigations showed that crystallization occurs very slowly in these compounds [more slowly for NC-N(Et)10Q than for O_2N-N(Et)10Q] during annealing, performed at ca. 95 °C for several hours. No evidence of a liquid crystal mesophase in this region could be found (as examined by POM and XRD). The lower melting point and slow crystallization kinetics may be a consequence of several additive factors, such as increased electrostatic interactions involving the polar tail and ionic groups that increase viscosity and perhaps result in greater crystalline imperfection, steric interference from the ethyl side group, and enhanced disorder in the long flexible spacer.

The ambient-temperature diffractograms of the SM-Br before melting[72] prove their crystalline character. The presence of two and sometimes three (most often for the 10Q SMs) lower-angle equidistant diffraction peaks for the majority of the compounds are indicative of lamellar stacking. The spacings deduced from the peaks are usually significantly smaller than the calculated molecular lengths of the surfactomesogens in extended conformation,[72] suggesting that these molecules are tilted relative to the layer normal. Single crystals were obtained for two of the SM-Br's, H_3CO-O6Q and O_2N-O10Q: the structural data obtained by XRD indicate a triclinic crystal system in both cases.[72]

2.3.2 General characteristics of the SM/PSS complexes

The complexes of the surfactomesogens with PSS were all ascertained to be stoichiometric with respect to the ionic moieties, according to elemental analysis (CHNS data; absence of Na and Br signals in EDS data) and NMR.[72] For some complexes, conductivity measurements of the dialyzed mixture were also effected: the very low values measured (< 10 uS/cm generally)[72] are consistent with the quasi-absence of mobile small counterions and with the insolubility – i.e. lack of mobility – of the complexes in H_2O. The complexes are not only molecularly insoluble in H_2O, like stoichiometric surfactant/polyelectrolyte complexes in general,[34,73,74] but also in most other common solvents including alcohols (except at low concentrations). DMSO and DMF are the only readily available solvents for all of the complexes. Pyridine dissolves O_2N-N(Et)10Q/PSS, O_2N-O10Q/PSS and O_2N-O6Q/PSS, whereas dichloromethane dissolves the first two but

not the last of these three complexes unless nitromethane is added (the other complexes were not tested in these solvents). Thus, the presence of the mesogenic core, which complicates the hydrophilic/hydrophobic balance, reduces the variety of solvents available for these complexes compared to surfactant/polyelectrolyte complexes.

2.3.3 Thermal and birefringence properties of the SM/PSS complexes

The 1% weight loss ($T_d^{1\%}$) values of the complexes measured by dynamic TGA lie, with one exception, between ca. 240 and 270 °C (Table 2.3). Thus, the complexes are 50-80 °C more stable thermally than the corresponding Br-neutralized surfactomesogens. The maximum temperatures reached in the different investigations of these complexes are well below the $T_d^{1\%}$ values.

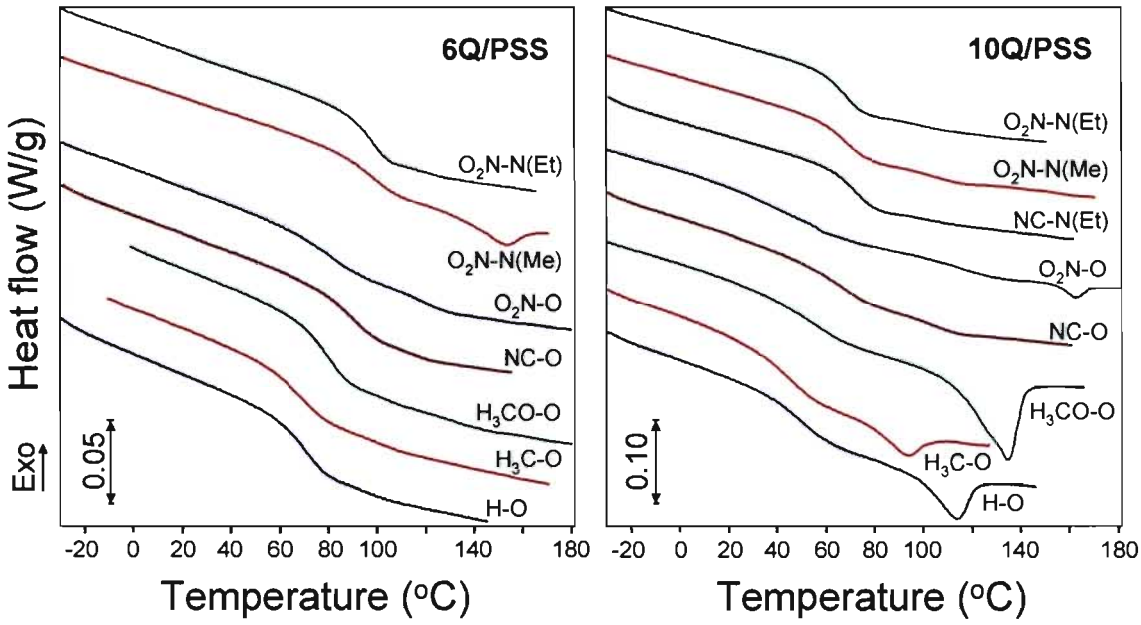

Figure 2.1 DSC thermograms (second heating curves, 10 °C/min) of the SM/PSS complexes.

Table 2.3 Thermal properties of the SM/PSS complexes, determined by DSC and TGA.

SM	T_g [a] °C		T_{cl} (ΔH) [b] °C ($J \cdot g^{-1}$)		$T_d^{1\%}$ [c] °C	
	6Q	10Q	6Q	10Q	6Q	10Q
O_2N-N(Et)nQ	97	69			240	225
O_2N-N(Me)nQ	95	70	155 (1) *140 (-1)*	~120	241	241
NC-N(Et)10Q		72				238
O_2N-OnQ	81	46		165 (1) *156 (-1)*	243	241
NC-OnQ	88	68		~120 (<<1)	253	252
H_3CO-OnQ	76	55		136 (9) *128 (-7)*	262	243
H_3C-OnQ	70	45		95 (2) *84 (-2)*	258	240
H-OnQ	71	51		113 (3) *105 (-3)*	267	253

[a] The T_g data (inflection points) are from the second and higher DSC heating scans (identical); the first heating scans generally show a very broad endotherm in this region. All ΔCp's lie in the 0.2-0.3 $J \cdot g^{-1} \cdot °C^{-1}$ range. [b] The T_{cl} data are max/min peak values (identical in multiple scans), obtained from the DSC heating and *cooling (in italics)* curves. [c] TGA data, relative to the weight at 80 °C.

DSC thermograms of the complexes are shown in Figure 2.1, with extracted data given in Table 2.3. Contrary to the SM-Br, none of the complexes display any crystallinity (as verified by XRD; see later); instead, a well-defined glass transition and, in some cases, a clear first-order transition peak are evident. A number of specific observations and trends can be pointed out.

First, the glass transition temperature (T_g) of the complexes lies between 45 and 100 °C, with that of the 6-spacer one being about 25±5 °C higher than that of the corresponding 10-spacer one. The internal plasticization effect of the alkyl spacers is thus about 6±1 $°C/CH_2$, the same rate as found for tail-end pyridinium alkyl polymethacrylate comb-like homopolymers.[48,75] For the same spacer length (6Q and 10Q, respectively), the aniline-type SM/PSS complexes, all with polar end groups, have almost identical T_g's, which thus appear to be independent of the nature of the lateral substituent on the amine (Me or Et) and of the polar end group (CN or NO_2 at least for 10Q, NC-N(Et)6Q not having been

synthesized). Furthermore, the T_g's of the aniline-type complexes are higher than or equal to those of the phenol-type complexes. The latter observation can be attributed to the higher polarity of the aniline-type mesogens and to the greater bulkiness (branched structure) of the laterally substituted amine compared to the ether linking group between the mesogenic core and alkyl spacer. Among the phenol-type complexes, the member with the cyano end group in both the 6Q and 10Q series has the highest T_g (higher than for the NO_2 end group), whereas the ones with a nonpolar end group (H, CH_3, OCH_3) have the lowest T_g's (with O_2N-O10Q/PSS also having an anomalously low T_g). Overall, except for O_2N-O10Q/PSS, the T_g tends to follow the dipole moment value of the SM azo groups, which is the highest and very similar for the three aniline-type SMs and the lowest and very similar for the three phenol-type SMs with a nonpolar end group (see Table 2.1). The coherency of the above data relative to their molecular characteristics concords with the quality of the complexes as established by their molecular and elemental characterization.

The T_g's of the complexes can be further compared with all-covalent PS-based analogues. For the H_3CO-O mesogen, the T_g's are 81 and 71 °C for covalently linked side chains with spacer lengths of 6 and 10 carbons,[61] respectively, compared to 76 and 55 °C, respectively, for the ionically linked side chains. For O_2N-O, the T_g's are 85 and 50 °C according to ref. 59, but 55 and 33 °C according to ref. 63, for spacer lengths of 6 and 10 carbons, respectively, the former being close to the T_g's of the analogous complexes. The different T_g's for O_2N-O could be due, in part, to differing molecular weights (average degrees of polymerization, DP, of ca. 250, 80 and 220 for refs. 59, ref. 63 and the ionic complexes, respectively). However, a study of the influence of molecular weight with covalently linked NC-O mesogens (n=4, 6) indicates an invariable T_g for DP=80-250 (T_g =73 °C for n=6, compared to 88 °C for the analogous complex).[65] Thus, the above comparative data do not allow any clear correlation to be made between the presence of ionic interactions and their effect on the T_g in these PS-based SCLCPs (which is not surprising in view of the variability observed in other comparisons involving SCLCPs – see, e.g. refs. 51 and 52). It is possibly of interest that, of the three mesogens for which comparative data are available, the ones with polar end groups (CN and NO_2) give a higher or similar T_g in the complexes than in the all-covalent analogues, whereas the one with the nonpolar end group (CH_3O) gives a lower T_g in the complexes than in the all-covalent

analogues (a point which will be brought up again later in connection with proposed models).

A distinct first-order transition, shown by POM (Figure 2.2) and XRD (see later) to be a clearing temperature (T_{cl}) from a birefringent liquid crystalline phase to the isotropic phase, is apparent in the heating and cooling DSC thermograms of only four out of the eight 10Q complexes (H-O10Q/PSS, H_3C-O10Q/PSS, H_3CO-O10Q/PSS, O_2N-O10Q/PSS; all in the phenol family) and one 6Q complex [O_2N-N(Me)6Q/PSS; in the aniline family]. Of the four 10Q complexes, the transition occurs at the highest temperature for the one with the polar NO_2 terminal group compared to the three with the nonpolar terminal groups, as observed also for the analogous PS-based SCLCPs (154[63] vs. 141[61] °C for NO_2 vs. CH_3O tails).

For the five as-prepared complexes showing a clear T_{cl} in DSC, reversible birefringence was observed by POM for the four 10Q complexes but, surprisingly, not for the 6Q complex. (Since the complexes are highly absorbing and also very difficult to spread by application of pressure even at high temperatures, it is generally restricted to thin parts of the samples.) Generally, the birefringence tends to brighten after some time of annealing above the T_g. Among the three phenol-type 10Q complexes with a nonpolar end group, birefringence becomes brighter and maximum birefringence reached with shorter annealing time in the end-group order, H_3CO>>H>H_3C, which may be related to the same order found for the ΔH and/or the T_{cl} values (Table 2.3). This relation may be intrinsic to the type of complex, but it may also reflect differing "degrees of liquid crystallinity" in the samples, as discussed later.

Revelatory POM textures were impossible to develop in these samples either by long-time annealing a little below T_{cl} (see several examples in Figure 2.2) or by very slow cooling ($\leq$ 0.2 °C/min) from the isotropic phase. By comparison, identifiable textures for all-covalent PS-based SCLCPs were also reported to be impossible to obtain by annealing,[58,60,61] in contrast to SCLCPs based on more flexible backbones.[76] Instead, the PS-based SCLCPs required very slow cooling from the isotropic phase to develop revealing textures.[50,60,61,63] Clearly, the rigid PS backbone must be a significant hindrance to texture formation in the complexes, but this is no doubt exacerbated by both the much higher DP of the present complexes compared to the PS-based SCLCPs as well as by the strong ionic

interactions, which are well known to retard, often drastically, the onset of flow in ionomers.[46]

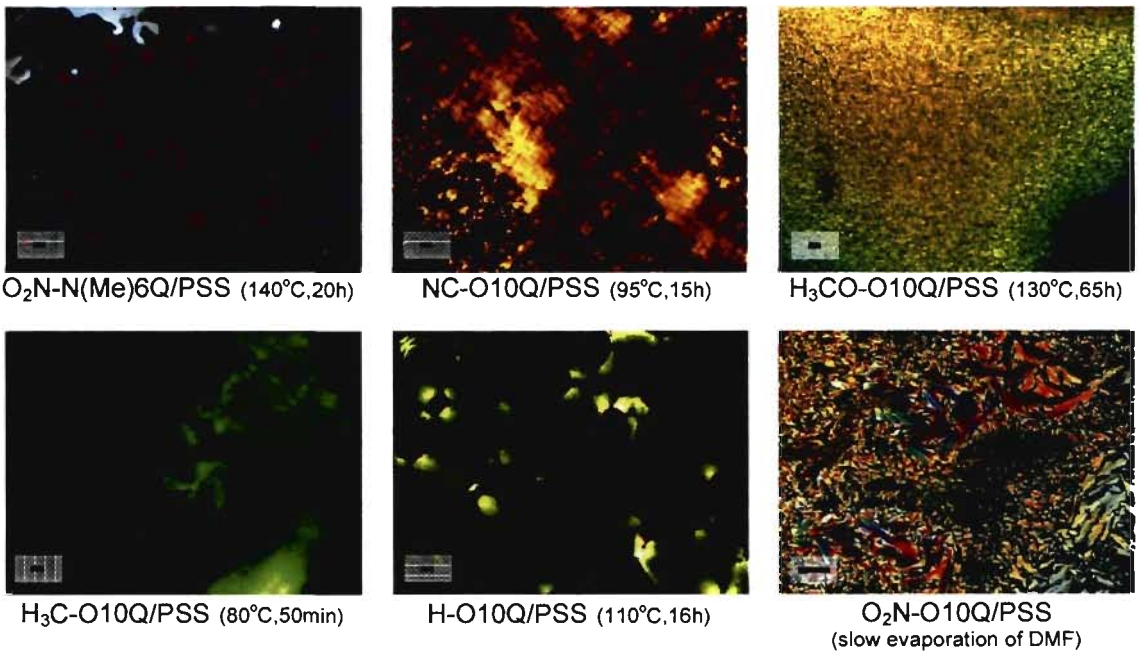

Figure 2.2 Polarizing optical micrographs of selected complexes taken after cooling from the isotropic phase at the temperatures and annealing times indicated. In the lower right picture, the complex was dissolved in DMF and the texture developed during slow solvent evaporation. The scale bar represents 20 μm.

The only way found to develop a revealing POM texture in the complexes, tested only on O_2N-O10Q/PSS, was by applying a solvent-assisted technique used to obtain LC textures in block copolymers[77] – notably, dissolution of the complex in dilute DMF (< 1 wt %), followed by solvent-casting on a glass slide, slow solvent evaporation over a period of two weeks at ambient temperature, and thorough drying in a vacuum oven at ca. 100 °C. This produced a focal-conic fan-shaped texture in a very small portion of the film, shown in Figure 2.2 (the rest of the film was birefringent, but with no specific texture). It may be argued, of course, that the focal-conic texture was formed and frozen in from a concentrated lyotropic solution. In this context, exposure to small amounts of selected solvents is being investigated separately.[48]

Although the other as-prepared 10Q complexes displayed no obvious birefringence in POM, some of them show hints of additional thermal events in the DSC curves above the

T_g (Figure 2.1): these events, which are reproducible in multiple scans, may be very weak broad peaks, may correspond to a second T_g-like event, as observed previously in some other comb-like polymer systems,[32,78-81] or may be baseline artefacts. The first possibility was tested by subjecting various samples to lengthy annealing at temperatures a little below weak DSC events. For the fifth phenol-type 10Q complex, NC-O10Q/PSS, weak birefringence was visible after 1-2 h of annealing a few degrees below the DSC event at ca. 120 °C, and was reversible on cycling above and below this event. Similarly, some weak birefringence developed in O_2N-N(Me)10Q/PSS after annealing for 1-2 days at ca. 100 °C; it vanished above the weak DSC event near 120 °C and again required lengthy annealing at 100 °C to reappear. These experiments indicate that the weak DSC event in these two complexes reflects a real transition, but involving a poorly or partially developed mesophase. In contrast, annealing of O_2N-N(Et)10Q/PSS and NC-N(Et)10Q/PSS at 100-105 °C (a little below slight hints of DSC events) for three days did not result in birefringence.

The only 6Q complex for which the as-prepared sample shows a clear DSC peak but no birefringence in POM, O_2N-N(Me)6Q/PSS, was also found to develop birefringence after annealing at 140 °C (weak after 2-3 h, more obvious after a day; again reversible on cycling around the DSC transition at 155 °C). The O_2N-O6Q/PSS complex, for which a slight hint of weak DSC events appear near 130 and 155 °C that are possibly very weak versions of the two events/peaks for the 10Q analogue, actually showed some very weak birefringence in the as-prepared sample, which disappeared at ca. 150 °C (reversible in some conditions), but we were unable to produce any clear birefringence by annealing (tested at several temperatures). Birefringence was not observed in O_2N-N(Et)6Q/PSS, NC-O6Q/PSS or H-O6Q/PSS after annealing at 120 °C for a day, 115 °C for a day, and 100 °C for 6 days, respectively, all at temperatures a little below slight hints of DSC events (annealing experiments were not conducted on H_3CO-O6Q/PSS and H_3C-O6Q/PSS). It is recognized, however, that annealing at another temperature and/or for longer times might perhaps develop birefringence in one or more of these samples.

To summarize the POM experiments, not only is it virtually impossible to obtain revelatory textures for the as-prepared complexes that show birefringence (without recourse to a solvent technique), but it can be difficult to obtain birefringence at all in other

complexes without considerable patience. This makes it somewhat problematic to distinguish complexes that are intrinsically isotropic from those that may be intrinsically liquid crystalline but have frozen-in isotropic morphology.

2.3.4 Molecular order in the SM/PSS complexes

More direct information about the state of order in the complexes can be obtained by XRD. The POM experiments described above indicate that annealing is necessary to favor an equilibrium state in these complexes. Imrie and coll. reported that (short) annealing was necessary to obtain reliable XRD data for all-covalent PS-based SCLCPs as well.[50] Figure 2.3 thus gives the diffractograms of the 6Q/PSS and 10Q/PSS complexes taken at ambient temperature after annealing at elevated temperatures for generally long times. The angles of the diffraction peak maxima and associated Bragg spacings are given in Table 2.4. A diffractogram of the parent PSS-Na is also shown in Figure 2.3 for comparison. It displays a fairly broad, distinct maximum centered at 4.7° corresponding to a Bragg spacing of 18.8 Å, which compares well with the calculated diameter of 19.6 Å for the PSS-Na chain (assuming random distribution of the styrene sulfonate moieties around the polymer backbone); this peak can therefore be ascribed to the average center-to-center distance of closest approach of neighboring PSS-Na chains in the amorphous state.

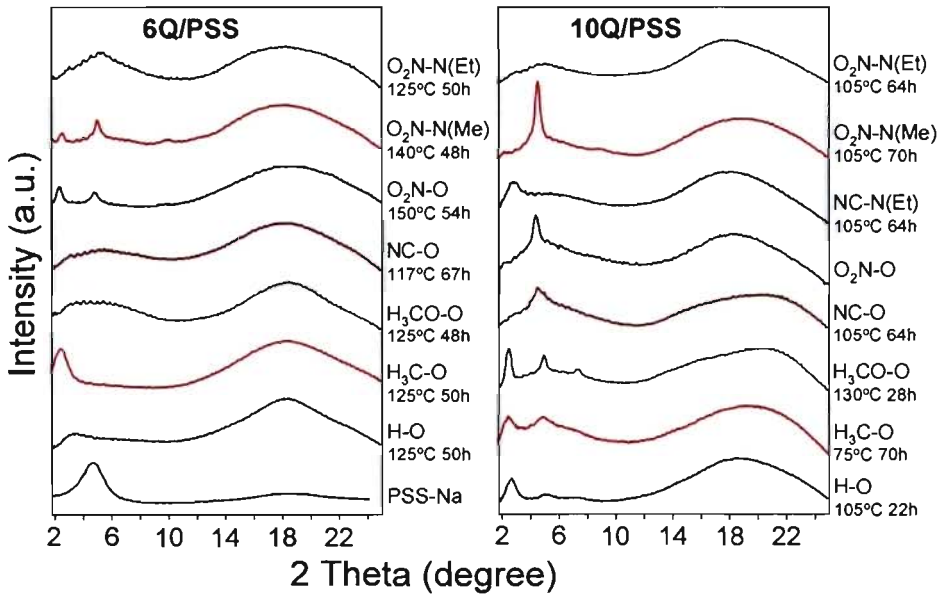

Figure 2.3 Ambient temperature X-ray diffractograms of the 6Q/PSS and 10Q/PSS complexes, with preceding annealing temperatures and times indicated. That for O_2N-O10Q was obtained after a heating and cooling cycle of diffractograms taken at various temperatures (maximum 195 °C; see Supporting Information for the complete cycle). A diffractogram of PSS-Na is included.

Before discussing the diffractograms of the annealed complexes, it should be mentioned that the four as-prepared 10Q/PSS complexes that were birefringent in POM and that showed a clear DSC peak also gave one or more XRD peaks in the lower-angle region (three for H_3CO-O10Q/PSS), shown in the Supporting Information for O_2N-O10Q/PSS. Annealing of these complexes tended to improve the order to some extent (somewhat sharper and more intense peaks) but did not change the nature of the order (unchanged peak positions). In contrast, O_2N-N(Me)6Q/PSS in as-prepared form, although it gave a clear DSC peak, did not show evidence of order by XRD until it was subjected to appropriate annealing (see below). Some other complexes, specified below, also developed long-range order after lengthy annealing, whereas others underwent little or no change. Simply obtaining a series of diffractograms of the complexes during a heating and cooling cycle up to isotropic (which amounts to effective annealing for short times at different temperatures) resulted in little or no change in order (see later for the particular case of O_2N-O10Q/PSS). Whether annealed or not, none of the complexes displayed any crystallinity, as indicated by the absence in the wide-angle region of features other than a broad halo, the latter being associated with the disordered nature of the ionically complexed side chains.

Table 2.4 Angles in 2θ and corresponding Bragg spacings, d, of the XRD diffraction peaks for the SM/PSS complexes and PSS-Na,[a] determined from the diffractograms in Figure 2.3, and calculated molecular lengths for the ion pairs in serial (l_A) and side-by-side (l_B) arrangement.

Complex	6Q/PSS				10Q/PSS			
	2θ (deg)	d (Å)	l_A (Å)	l_B (Å)	2θ (deg)	d (Å)	l_A (Å)	l_B (Å)
O_2N-N(Et)	(5.4)	(16.3)	34.1	29.4	(5.1)	(17.3)	38.3	34.5
O_2N-N(Me)	2.56 5.07 9.97	34.5 17.4 8.9	34.1	29.3	4.63 9.12	19.1 9.7	38.2	33.6
NC-N(Et)					(2.8)	(31.5)	38.4	33.3
O_2N-O	2.40 4.90	36.8 18.0	35.9	29.6	4.44	19.9	40.9	35.8
NC-O			36.1	32.0	4.66	19.0	41.1	36.5
H_3CO-O			36.5	31.8	2.51 5.01 7.41	35.1 17.6 11.9	41.5	35.9
H_3C-O	(2.5)	(35.3)	35.6	31.6	2.62 5.09	33.7 17.4	40.6	35.5
H-O	(3.4)	(26.0)	34.6	30.9	2.72 5.19 7.4	32.5 17.0 11.9	39.6	34.3
PSS-Na	4.64	19.0						

[a] Data in parenthesis are for broad peaks, considered to arise from short-range order in an otherwise isotropic state.

Regarding the XRD of the annealed samples in Figure 2.3 and focusing first on the 10Q/PSS series, two basic patterns can be observed in the low-angle region. The first one is shown by the three complexes with nonpolar terminal groups ("nonpolar-tailed complexes"). They all display three equidistant diffraction peaks in order of decreasing intensity, which, combined with the wide-angle halo, is a typical pattern observed for lamellar order of the SmA and SmC types. The peaks are the sharpest and best defined for H_3CO-O10Q/PSS, which also possesses the highest isotropization enthalpy in DSC and the most intense birefringence in POM. The corresponding Bragg distances indicate layer thicknesses of 35 Å for H_3CO-O10Q/PSS and ca. 34 Å for H_3C-O10Q/PSS and H-O10Q/PSS.

The second pattern is shown by the two phenol-type complexes, O_2N-O10Q/PSS and NC-O10Q/PSS, and the aniline-type complex with the smallest lateral substituent, O_2N-N(Me)10Q/PSS, all with polar terminal groups ("polar-tailed complexes"). These three complexes show a primary diffraction peak at ca. 4.5°, corresponding to a Bragg spacing of 19-20 Å. This peak is particularly intense for O_2N-N(Me)10Q/PSS (with a second peak at half the Bragg spacing weakly visible as well), but only after lengthy annealing. It is also relatively intense for O_2N-O10Q/PSS, which underwent limited effective annealing, whereas it is the weakest and broadest for NC-O10Q/PSS despite lengthy annealing. As discussed previously for O_2N-O10Q/PSS,[32] this peak may be a second-order diffraction from lamellar-type periodicity. In this case, the lamellar thickness for these complexes is 38-40 Å, larger than that for the nonpolar-tailed complexes above. It is noteworthy that Crivello et al. observed a weak first-order and sharp second-order peak for an NC-O azo mesogen covalently bound by an alkyl spacer (n=4, 6, 8, 10) to a poly(α-methyl styrene) backbone.[58] The extinction or reduction in intensity of the first-order peak is regularly reported in the literature – see, for example, refs. 25, 78, 82-84 – and is generally attributed to an additional plane of electron density within the layers.[82] The appearance of LC order in O_2N-N(Me)10Q/PSS and NC-O10Q/PSS supports the attribution of the weak peaks observed in their DSC thermograms to the clearing temperature of a poorly developed LC phase.

The diffractogram of O_2N-N(Et)10Q/PSS, which differs from O_2N-N(Me)10Q/PSS only by the lateral substituent (Et vs. Me) on the amine linking group, indicates short-range (isotropic) order only for this complex, including after lengthy annealing at the same temperature as led to the long-range order for the Me analogue. This can be ascribed at least in part to the lateral ethyl group, which, being more voluminous than the lateral methyl group, can sterically hinder ordered molecular packing of the mesogenic groups. Interestingly, the weak and broad small-angle peak that is present for the Et analogue occurs at about the same position as the sharp peak for the Me analogue, indicating a (weak) tendency towards similar packing. The diffractogram of the NC-terminated aniline-type complex, which also possesses an Et substituent, shows a single weak and broad peak at low angles (Bragg spacing ca. 31.5 Å). Its position, which is closer to that for the nonpolar-tailed complexes, makes it an exception to the otherwise general distinction in the

small-angle XRD pattern between the polar-tailed and nonpolar-tailed 10Q/PSS complexes investigated. However, the as-prepared form of the complex also shows this peak, and since neither POM nor DSC gives evidence of LC order in this complex, it can probably be ascribed to relatively short-range order in an otherwise isotropic state (observed also in some 6Q/PSS complexes and other systems; see below).

Of the 6Q/PSS complexes, only two were found to develop long-range order after appropriate annealing. We particularly investigated O_2N-N(Me)6Q/PSS, since it shows a DSC transition at 155 °C. First, it was found that 3 days of annealing at 130 °C resulted in little improvement in order compared to the as-prepared sample; however, annealing at 140 °C (close to the DSC transition) for two days finally led to well-defined order (this also illustrates that the choice of annealing temperature can be critical): as shown in Figure 2.3, the first, second and fourth (with a hint of the third) diffraction orders are apparent, with the second-order peak being the most intense, indicating a lamellar structure with a 35-Å periodicity. The periodicity and basic low-angle pattern are the same as for the polar-tailed 10Q/PSS complexes, taking into account the spacer-length difference.

The second 6Q complex for which long-range order was obtained is O_2N-O6Q/PSS. In this case, two sharp peaks were observed after 54 h of annealing at 150 °C. The XRD pattern indicates similar packing as for O_2N-N(Me)6Q/PSS (although the first-order peak appears a little more intense than the second-order peak in this case), with a Bragg spacing of 36 Å. No long-range order was found in the other 6Q complexes after long-time annealing, where the annealing temperatures were chosen to be a little below hints of DSC events when possible (arbitrary temperatures were chosen otherwise).

It may be noted that H_3C-O6Q/PSS shows a relatively intense and broad peak at 2.52 ° (35 Å), which is unchanged from what was observed for the as-prepared sample. This could be related to short-range order in the isotropic state, as was observed also for some other ion-containing SCLCP polymers with nonpolar side-chain terminal groups.[25,75] It may be added that the lowest small-angle peak in the smectic phase of H_3C-O10Q/PSS and H-O10Q/PSS remains present in the isotropic phase of these complexes. A possible reason is that in less polar mesogenic environments the ionic groups have a greater tendency to remain aggregated in the isotropic state, and thus to form short-range (possibly lamellar-like) structures; however, this explanation is probably simplistic since only some of the

nonpolar-tailed complexes and one polar-tailed complex [NC-N(Et)10Q/PSS] in the series studied show this effect.

Regarding the evolution of the XRD diffractograms with temperature, it was noted that, apart from the annealing effects described above, the type of molecular packing structure and the Bragg spacings are essentially constant up to isotropization. Generally, the wide-angle halo moves, as expected, to lower angles with increasing temperature, reflecting greater average lateral distances between the SM molecules due to increased thermal motion. A particular phenomenon, shown in Figure 2.4, was noted for O_2N-O10Q/PSS: the small-angle peak, which initially narrows in width and increases in intensity due to the annealing effect (three left-most curves in Figure 2.4), shows a partly *reversible* increase in intensity from ambient to 120 °C or more in the subsequent cooling-heating cycle (five rightmost curves in Figure 2.4; the decreased intensity at 150 °C is related to the proximity of T_{cl}). It is noteworthy that this intensity increase terminates in the temperature range of a weak and broad DSC event (ca. 120-140 °C), which had previously been hypothesized to be a second T_g-like transition;[32] however, its interpretation is not obvious. A technique such as dynamic mechanical analysis might allow a better understanding of this unusual behavior in O_2N-O10Q/PSS (with which its anomalously low T_g might also be associated).

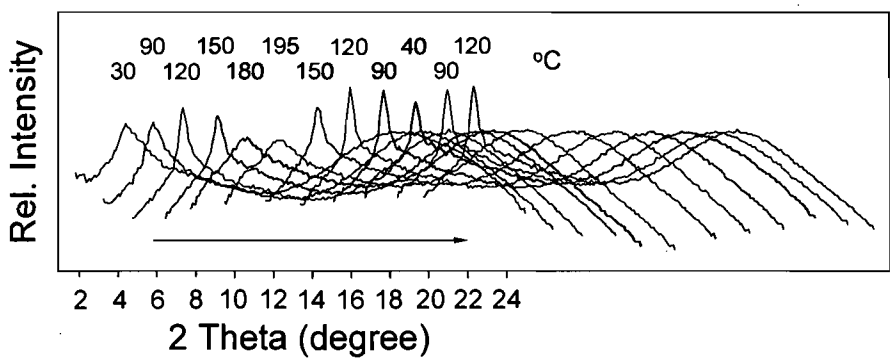

Figure 2.4 XRD of O_2N-O10Q/PSS at various temperatures, where the curves are normalized relative to the WAXS halo and progressively shifted to the right in order of sequence of measurement relative to the as-prepared sample (30 °C). The position of the small-angle peak is essentially constant (see Supporting Information).

To deduce additional information regarding the structural order of the complexes, the Bragg spacings corresponding to the low-angle XRD peaks can be compared with one

another and with the extended molecular lengths of the (complexed) mesogenic side chains. First, it is striking that, in the 10Q series, the nonpolar-tailed complexes, which all give a classic XRD pattern for disordered smectic phases (i.e. several diffraction orders with progressively decreasing intensity), have Bragg spacings (ca. 35 Å) that are ca. 5 Å shorter than those of the three polar-tailed complexes, for which the primary diffraction peak is considered to be second-order. The two polar-tailed 6Q complexes also give a Bragg spacing consistent with those of the 10Q polar-tailed complexes, considering the difference in spacer length.

A similar dependence of the Bragg spacing on the polarity of the mesogen tail was observed for analogous all-covalent polystyrene-based SCLCPs (with butyl and octyl spacers) studied by Imrie and coll.: specifically, they observed that the Bragg spacings for SCLCPs with a H_3CO-O azo core are smaller than those for SCLCPs with O_2N-O and NC-O azo cores.[50,62] (In addition, the enthalpy and entropy of the clearing transition are higher for the former than for the latter, as observed also in our complexes.) Assuming antiparallel side-by-side packing of the mesogens, these data were attributed to greater interdigitation of the rigid mesogenic cores with a nonpolar tail compared to those with a polar tail. This allows the nonpolar tail to lie in the same subplane as the alkyl spacer with which it is more miscible, whereas the polar tail lies in the same subplane as the rigid core with which it is more miscible (see further discussion below in relation to Figure 2.5). (This greater mesogenic overlap was also considered to account for the higher transition enthalpies/entropies in the SCLCPs with nonpolar tails compared to polar tails.[50,62])

In comparing the all-covalent PS-based SCLCP Bragg spacings (d) to calculated molecular lengths (l) with and without the backbone moiety included (d being a little lower and a little higher than l for the nonpolar- and polar-tailed SCLCPs, respectively, when the backbone moiety is included), Imrie and coll. concluded that the polystyrene backbone was confined between the lamellar planes for the polar-tailed SCLCPs, but was miscible with the side chains ("isotropic conformation" of the backbone) for the nonpolar-tailed SCLCPs.[50,62] In the present complexes, significant three-dimensional meandering of the backbone seems unlikely, since the driving force for nanophase separation between the ionic groups (directly connected to the PS backbone) and the neighboring alkyl spacers must be very strong. On the other hand, the ionic bonds in the complexes, being non-

directional bonds (although subject to the steric constraints imposed by the neighboring moieties), allow consideration of another possibility. Namely, there may be two distinct arrangements of the oppositely charged ionic groups within the molecular packing order: one where they are positioned approximately serially along the molecular long axis and another where they are positioned approximately side-by-side relative to the molecular long axis (Figure 2.5a). The all-trans molecular lengths given by the two arrangements were determined by Hyperchem to be ca. 40 and 35 Å, respectively, for the 10Q complexes and 35 and 30 Å, respectively, for the 6Q complexes (Table 2.4). Comparison of these lengths with the experimental spacings (Table 2.4) suggests that this packing consideration is another way to rationalize the difference in Bragg spacings between the polar- and nonpolar-tailed complexes.

In light of the above discussion, various molecular models can be proposed for the apparently single-layer SmA packing structure of the SM/PSS complexes. Among the most straightforward models are the two illustrated in Figure 2.5b and 2.5c, where the mesogenic cores are interdigitated in antiparallel fashion. This arrangement is frequently proposed for SCLCPs in general, supposing that the side chains orient non-preferentially on either side of the polymer backbone. The two groups of complexes are distinguished by greater interdigitation of the nonpolar-tailed mesogens (Figure 2.5c) than of the polar-tailed ones (Figure 2.5b), in line with what was proposed by Imrie and coll.[50,62] With the side-by-side overlapping of the mesogenic cores (and matching side-by-side alignment of the ionic groups), the alkyl chains fill in a lateral space equivalent to about two mesogenic molecular areas, thereby accounting for a lamellar thickness equivalent to a single effective side-chain length (see also refs. 32 and 84). It is less clear how these models can account for the quasi-extinction of the first-order diffraction peak in one group of complexes and not in the other, unless it is related to the changes in the electron density profile of the mesogenic core region caused by the polar tails that are "just right" to result in extinction or partial extinction.

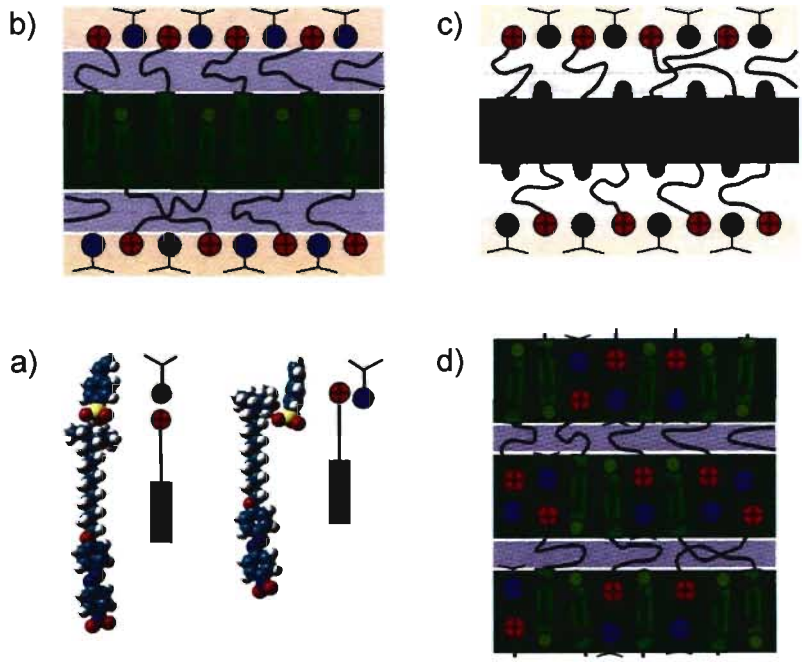

Figure 2.5 Schematics of possible packing models for the SM/PSS complexes with a SmA mesophase (see text for details).

There is another possible source of extinction, as follows. The azo mesogens with higher dipole moments (those with polar end groups; Table 2.1) may be subject to electrostatic interactions with the ion pairs, which also form dipoles, with the result that ion pairs and mesogenic cores may be located in the same subplanes. Such an arrangement would reduce the effective lamellar thickness by half, and thus rationalize the "second-order" diffraction peak, which, in this situation, is actually a first-order peak. A model illustrating the proposed arrangement is shown in Figure 2.5d. For adequate dipole-dipole interactions between ion pairs and mesogens, the ion pairs should be arranged serially relative to the molecular long axis. Within a subplane, the ion pairs may appear in sequences of variable lengths ranging from single to multiple ion pairs, which in turn are laterally interspersed between single to multiple sequences of mesogenic cores. In this case, and compared to the model in Figure 2.5c, the 5-Å difference in lamellar spacing between the polar- and nonpolar-tailed mesogens would appear to be related to the difference in ion pair arrangement rather than to the extent of mesogen interdigitation. However, the neat

single or double rows of ion pairs in the idealized models may not reflect the true situation, especially considering the atactic nature of the polymer backbone combined with the disordered nature of SmA mesophases. Instead, the ion pairs may be arranged with variable local orientations (along with the mesogen cores), with the alkyl spacers allowing the necessary flexibility for the adoption of lamellar order. From this perspective, the difference in mesogen interdigitation can once again be proffered as the best explanation for the approximately 5-Å difference in lamellar spacing between the polar- and nonpolar-tailed complexes. This is also consistent with the similar observation in the analogous all-covalent PS-based SCLCPs, for which the model of Figure 2.5d seems less applicable, and, indeed, only a single diffraction peak (assumed to be first order) is reported for these SCLCPs. On the other hand, Figure 2.5d may be applicable to ion-containing SCLCP polymers described by Guillon and coll.,[84] where biphenyl mesogenic groups are covalently attached through alkyl spacers to quaternized backbones. These polymers similarly organize as a single-layer smectic A mesophase, and give a second-order X-ray diffraction peak similar in intensity to the first-order. The presence of both peaks in these cases, observed also in the two 6Q/PSS complexes showing LC order, might be explained by a higher proportion of longer sequences of ion pairs and mesogens within the sublayers.

It may be remarked that SCLCP polymers can be thought of as trimer block molecules, where the three blocks correspond to (a) the rigid mesogenic core, (b) the alkyl spacer and (c) the directly connected polymer backbone and ionic groups.[51,63,85] From this point of view, the nonpolar-tailed complexes modeled essentially by Figure 2.5c can be described as a lamellar structure where the three blocks are segregated into three distinct subplanes, whereas the polar-tailed complexes modeled by Figure 2.5d can be described as a lamellar structure where block (a) and block (c) are located in the same subplanes. To investigate the validity of the proposed models, small-angle neutron scattering on appropriately deuterated samples or spectroscopic techniques that are sufficiently sensitive to local environments of specific atoms or groups (e.g. solid-state NMR, EXAFS, fluorescence) might be envisaged.

Finally, in comparing the T_g's of the complexes with all-covalent PS-based analogues (data available for three types of mesogens only), it was noted that the T_g's of the polar-tailed complexes were higher than or similar to those of the all-covalent analogues, whereas

those of the nonpolar-tailed complexes were significantly lower than for the all-covalent analogues. These observations might be at least partly correlated with the above models. In particular, if both the complexes and all-covalent analogues are represented by the model in Figure 2.5c for the nonpolar-tailed mesogens, and it is accepted that the former have lower T_g's than the latter (for the same mesogen), then the comparatively high T_g's in the polar-tailed complexes, represented by the model in Figure 2.5d, relative to their all-covalent analogues, represented by the model in Figure 2.5b, might be rationalized by the presence of strong ionic interactions in both of the subplanes in Figure 2.5d.

2.3.5 Photoinduced birefringence (PIB) in selected SM/PSS complexes

Azo-containing materials are of great interest for their photosensitivity. Photoinduced birefringence is one often studied photonic property in these kinds of materials. Our group reported recently on the high and thermally stable photoinduced birefringence observed in a film composed of an equimolar ionic polymer complex of readily available methyl orange (MO) with methylated poly(4-vinyl pyridine) (P4VPMe).[9] This impressive birefringence was attributed, at least in part, to the absence of flexible components – in particular, a flexible spacer – combined with the ionic and polymeric nature of the complex and possibly its LC (smectic A) character. The effect of the flexible spacer can be qualitatively assessed by comparing the PIB of the spacer-free MO/P4VPMe complex with that of the present complexes.

The UV-visible spectra of spin-coated films of three SM/PSS complexes are shown in Figure 2.6a. The two O_2N-OnQ/PSS films both show a strong absorbance band centered at 360 (±1) nm (with a slight shoulder near 400 nm), compared to 372 nm in H_2O for O_2N-O10Q,[72] ca. 375 nm for a similar complex of O_2N-O12Q with carboxymethylcellulose in chloroform[36] and ca. 370 nm for this same complex in the form of ultrathin Langmuir-Blodgett films.[36] This band can be attributed to the azobenzene π-π^* transition, which in the spin-coated film undergoes a blue shift, generally attributed to H-aggregation (side-by-side alignment of transition dipoles),[86,87] which is consistent with lamellar-type packing.[88] The O_2N-N(Et)10Q/PSS film shows a symmetric π-π^* band at much higher wavelengths, centered at 497 nm, as is typical for azobenzenes substituted at the 4- and 4'-positions by an electron-donor and an electron-acceptor moiety, respectively (pseudo-stilbene type azo).[3]

The spacer-free complex has a maximum absorbance at 425 nm, with a distinct shoulder on the high wavenumber side.

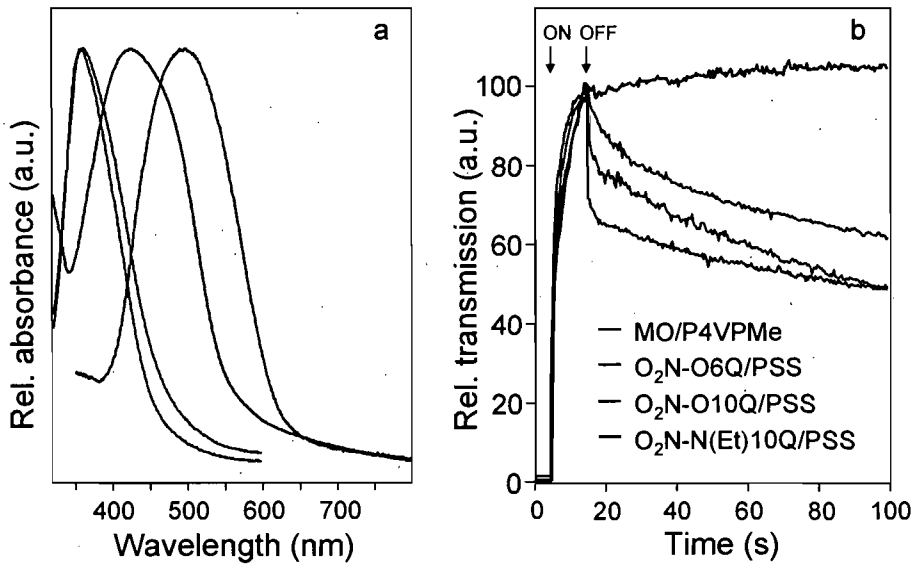

Figure 2.6 (a) UV-visible spectra and (b) photoinduced birefringence, relative to the maximum achieved at the end of the writing period, of spin-coated films of the complexes indicated in (b). The writing period in (b) takes place between the points marked as laser ON and laser OFF.

The room-temperature PIB curves of the three SM/PSS complexes compared with the spacer-free complex, normalized to the maximum PIB values obtained at the end of the writing period, are given in Figure 2.6b. It must be emphasized that all four complexes are stoichiometric, and they all involve similar ionic groups, in particular the strongly interacting sulfonate group, although the positive and negative moieties are inverted in the three SM/PSS complexes compared to MO/P4VPMe. Whilst the spacer-free complex shows no relaxation of the PIB at all in the time period sampled after the writing laser is removed, all three SM/PSS complexes show a significant amount of fast relaxation, more for the decyl spacer than for the hexyl spacer, followed by much slower relaxation. This indicates that the flexible spacer is an important source of PIB relaxation. It may be caused, in part, by its plasticizing effect on the T_g. However, this cannot be the only factor, since the fast relaxation becomes more pronounced in the order O_2N-O6Q/PSS < O_2N-O10Q/PSS < O_2N-N(Et)10Q/PSS whereas the T_g decreases in the order O_2N-O6Q/PSS (80 °C) > O_2N-N(Et)10Q/PSS (68 °C) >> O_2N-O10Q/PSS (46 °C). An additional factor may

be the molecular packing: as shown earlier, O_2N-N(Et)10Q/PSS is completely amorphous, whereas O_2N-O10Q/PSS (like MO/P4VPMe[9]) has smectic A packing (although it is not known to what extent this packing actually exists in the spin-coated film), suggesting that LC structure contributes to reducing fast relaxation. Finally, it is noted that significant PIB, despite the presence of a flexible spacer, is nevertheless maintained at longer times, which can be related to the ionic and polymeric nature of the complexes. Further investigations of PIB and other photoinduced properties that illustrate clearly the effect of the presence of flexible moieties are described in a forthcoming paper on a series of spacer-free complexes.[89]

2.4 Concluding remarks

The use of strongly interacting ionic functionalities of opposite charges constitutes an attractive means for constructing robust supramolecular SCLCPs that are stable to high temperatures. By contrast, hydrogen-bonding interactions are more attractive for supramolecular SCLCPs where greater temperature-dependent lability of the supramolecular bond is desired. However, the latter are more susceptible to partial complexation of the polymer backbone, even to the point of precluding the possibility of obtaining LC character in some cases.[44,45] Strong ionic bonding easily leads to equimolar complexation and thus to fully functionalized SCLCP homopolymers. Their downsides are a greater susceptibility to the effects of humidity and nonequilibrium morphologies that can be difficult to erase.

In this paper, we have taken great care to avoid contamination by humidity as much as possible. This care, coupled with the greater inherent rigidity of the PS backbone and its relatively high molecular weight, has resulted in highly viscous materials that typically require exceedingly long annealing times at well-chosen temperatures to attain equilibrium morphologies. That is, many of the as-prepared complexes are amorphous or show relatively short-range LC-type order only, with true LC character revealed only after appropriate annealing. This can be understood in relation to polymer viscoelastic properties. To achieve equilibrium morphologies, the polymer chains must undergo translational motion, which occurs only in the presence of flow. It is well known that

increasing molecular weight raises the onset temperature for flow and increases the (temperature-dependent) flow viscosity, and that ionic interactions exacerbate this effect drastically.[46] Thus annealing must take place at temperatures that are much higher than the T_g to be effective (the higher the temperature, the lower the viscosity, and therefore the faster the kinetics of chain movement), yet that are below any potential isotropization temperature. The slow kinetics of molecular reorganization furthermore suggests that these systems are subject to partial development of LC order. This partial LC order can be in the form of both paracrystalline and positional disorder (limited correlation lengths), but it might also be in the form of variability in the extent of order throughout the sample (microheterogeneity).[90] Frequent crossover of polymer chains between sublayers can contribute significantly to this disorder.

Despite the above difficulties, the present investigation has shown a number of correlations between molecular parameters and LC properties. The T_g's of the complexes are not only spacer-length dependent, but show an approximate correlation with the dipole moments of the mesogenic cores and, more specifically, with particular molecular aspects. In general, there are more 10Q than 6Q complexes that show LC order, as might be expected from longer side chains that can promote more effective nanophase separation. Only the aniline-type 10Q complexes with a lateral Et substituent on the amine linking group appear to be intrinsically amorphous, which can be attributed to steric hindrance to efficient molecular packing caused by the Et branch. The spacer length of the 6Q complexes may be at the limit of that required to satisfy at once the packing tendencies of the mesogenic cores, the association of the interacting ionic groups, and the conformational tendencies of the polymer backbone (as appeared to be the case also in some other ion-containing SCLCPs[48,75,91]). By comparison, many all-covalent (nonionic) SCLCPs with alkyl spacer lengths shorter than n=6 can resolve conflicting packing tendencies by adopting a nematic order, a state which seems unlikely for ion-containing side-chain polymers given the strong driving force for nanophase separation between ionic and nonpolar motifs, which therefore remain amorphous if smectic order is no longer favorable. On the other hand, the all-covalent PS-based SCLCPs (analogous to the present complexes), which do not contain ionic groups, are LC (SmA) for spacers as short as n-propyl with the O_2N-O mesogenic core and n-butyl with the H_3CO-O and NC-O mesogenic cores (but

amorphous for H_3CO-O with the n-propyl spacer).[50,61,63] It may therefore also be argued that, in the ionic complexes, the n-hexyl spacer has less internal plasticization power (higher T_g and presumably a higher onset of flow) than the n-decyl spacer, which may make it more difficult to find suitable annealing conditions (even impossible if the potential isotropization temperature is not sufficiently far from the T_g). Of the complexes for which some extent of LC order was achieved, there is no clear dependence of the clearing temperature on specific molecular parameters. However, this tends to be general for liquid crystals, where transitions between phases generally depend sensitively on a combination of steric and polar factors. In the present case, this transition may, in addition, decrease in temperature and enthalpy when the LC order is poorly developed.

Finally, it is striking to observe a systematic difference in the XRD pattern for the complexes with polar compared to nonpolar terminal groups on the mesogen, indicative of a systematic difference in the details of the lamellar packing. It was also noted that the accompanying difference in Bragg spacing matches a similar difference in analogous all-covalent PS-based SCLCPs, suggestive of a general phenomenon, and attributed to greater interdigitation of the mesogens with nonpolar tails than those with polar tails so that the nonpolar tails lie in the subplane of the alkyl spacers.[50] For the complexes, two different arrangements of the ionic groups were considered as another possible reason. To explain the difference in type of XRD pattern, it was proposed that dipole-dipole interactions between the polar mesogenic cores and the ion pairs can result in both moieties sharing the same subplanes to a greater or lesser extent, thus reducing the effective lamellar periodicity by about half.

2.5 Acknowledgments

The financial support of NSERC Canada and FQRNT Québec is gratefully acknowledged. Dr. Ximin Chen is thanked for participating in the synthesis of some of the SMs. Prof. Christopher J. Barrett (Chemistry Dept., McGill University, Montreal) is thanked for making available his laboratory for PIB measurements and Oleh Tanchak (former Ph.D. student in the Barrett laboratory) is thanked for training QZ in PIB investigations.

2.6 References

1. Natansohn, A.; Rochon, P. *Chem. Rev.* **2002,** 102, 4139-4175.
2. Ikeda, T.; Mamiya, J.-i.; Yu, Y. *Angew. Chem., Int. Ed.* **2007,** 46, 506-528. Ikeda, T. *J. Mater. Chem.* **2003,** 13, 2037-2057. Barrett, C. J.; Mamiya, J.-i.; Yager, K. G.; Ikeda, T. *Soft Matter* **2007,** 3, 1249-1261.
3. Yager, K. G.; Barrett, C. J., In *Polymeric Nanostructures and Their Applications*, Nalwa, H. S., Ed.; American Scientific Publishers: Los Angeles, 2007; Vol. 2, pp. 243-280.
4. Yesodha, S. K.; Sadashiva Pillai, C. K.; Tsutsumi, N. *Prog. Polym. Sci.* **2004,** 29, 45-74.
5. Kajzar, F.; Lee, K.-S.; Jen, A. K.-Y. *Adv. Polym. Sci.* **2003,** 161, 1-85.
6. Advincula, R. C., In *Handbook of Polyelectrolytes and Their Applications*, Tripathy, S. K.; Kumar, J.; Nalwa, H. S., Eds. American Scientific: Stevenson Ranch, CA, 2002; Vol. 1, pp. 65-97.
7. Yu, Y.; Nakano, M.; Ikeda, T. *Nature* **2003,** 425, 145.
8. Yamada, M.; Kondo, M.; Mamiya, J.-i.; Yu, Y.; Kinoshita, M.; Barrett, C. J.; Ikeda, T. *Angew. Chem., Int. Ed.* **2008,** 47, 4986-4988.
9. Zhang, Q.; Bazuin, C. G.; Barrett, C. J. *Chem. Mater.* **2008,** 20, 29-31.
10. Priimagi, A.; Kaivola, M.; Rodriguez, F. J.; Kauranen, M. *Appl. Phys. Lett.* **2007,** 90, 121103/1-121103/3. Priimagi, A.; Cattaneo, S.; Ras, R. H. A.; Valkama, S.; Ikkala, O.; Kauranen, M. *Chem. Mater.* **2005,** 17, 5798-5802. Priimagi, A.; Vapaavuori, J.; Rodriguez, F. J.; Faul, C. F. J.; Heino, M. T.; Ikkala, O.; Kauranen, M.; Kaivola, M. *Chem. Mater.* **2008,** 20, 6358-6363.
11. Stumpe, J.; Goldenberg, L.; Kulikovska, O. Film forming material and preparation of surface relief and optically anisotropic structures by irradiating a film of the said material. WO2006024500, 2006.
12. Xiao, S.; Lu, X.; Lu, Q.; Su, B. *Macromolecules* **2008,** 41, 3884-3892.
13. Lin, H.-C.; Tsai, C.-M.; Huang, G.-H.; Tao, Y.-T. *Macromolecules* **2006,** 39, 557-568.
14. Cui, L.; Zhao, Y. *Chem. Mater.* **2004,** 16, 2076-2082.
15. Imrie, C. T. *Trends Polym. Sci.* **1995,** 3, 22-29.
16. Bazuin, C. G., In *Mechanical and Thermophysical Properties of Polymer Liquid Crystals*, Brostow, W., Ed.; Chapman and Hall: London, 1998; Vol. 3, pp. 59-100.
17. Kato, T. *Struct. Bonding* **2000,** 96, 95-146. Kato, T.; Mizoshita, N.; Kishimoto, K. *Angew. Chem., Int. Ed.* **2006,** 45, 38-68.
18. Masson, P.; Guillon, D. *Mol. Cryst. Liq. Cryst.* **2001,** 362, 313-346.
19. Paleos, C. M.; Tsiourvas, D. *Liq. Cryst.* **2001,** 28, 1127-1161.
20. Faul, C. F. J.; Antonietti, M. *Adv. Mater.* **2003,** 15, 673-683.
21. Binnemans, K. *Chem. Rev.* **2005,** 105, 4148-4204.
22. Pollino, J. M.; Weck, M. *Chem. Soc. Rev.* **2005,** 34, 193-207.
23. de Wit, J.; van Ekenstein, G. A.; Polushkin, E.; Kvashnina, K.; Bras, W.; Ikkala, O.; ten Brinke, G. *Macromolecules* **2008,** 41, 4200-4204.
24. Canilho, N.; Kasëmi, E.; Mezzenga, R.; Schlüeter, A. D. *J. Am. Chem. Soc.* **2006,** 128, 13998-13999. Canilho, N.; Scholl, M.; Klok, H.-A.; Mezzenga, R. *Macromolecules* **2007,** 40, 8374-8383.
25. Sallenave, X.; Bazuin, C. G. *Macromolecules* **2007,** 40, 5326-5336.

26. Medvedev, A. V.; Barmatov, E. B.; Medvedev, A. S.; Shibaev, V. P.; Ivanov, S. A.; Kozlovsky, M.; Stumpe, J. *Macromolecules* **2005,** 38, 2223-2229.
27. Xu, J.; Toh, C. L.; Liu, X.; Wang, S.; He, C.; Lu, X. *Macromolecules* **2005,** 38, 1684-1690.
28. Ujiie, S.; Iimura, K. *Macromolecules* **1992,** 25, 3174-3178.
29. Bazuin, C. G.; Tork, A. *Macromolecules* **1995,** 28, 8877-80. Brandys, F. A.; Masson, P.; Guillon, D.; Bazuin, C. G. *Macromol. Chem. Phys.* **2001,** 202, 856-865. Tork, A.; Bazuin, C. G. *Macromolecules* **2001,** 34, 7699-7706. Bazuin, C. G.; Boivin, J.; Tork, A.; Tremblay, H.; Bravo-Grimaldo, E. *Macromolecules* **2002,** 35, 6893-6899.
30. Tal'roze, R. V.; Kuptsov, S. A.; Sycheva, T. I.; Bezborodov, V. S.; Platé, N. A. *Macromolecules* **1995,** 28, 8689-8691.
31. Gohy, J.-F.; Antoun, S.; Sobry, R.; Van den Bossche, G.; Jérôme, R. *Macromol. Chem. Phys.* **2000,** 201, 31-41.
32. Tibirna, C. M.; Bazuin, C. G. *J. Polym. Sci., Part B: Polym. Phys.* **2005,** 43, 3421-3431.
33. Benouazzane, M.; Bravo-Grimaldo, E.; Bissessur, R.; Bazuin, C. G. *Macromolecules* **2006,** 39, 5364-5370.
34. Goddard, E. D., In *Interactions of Surfactants with Polymers and Proteins*, Goddard, E. D.; Ananthapadmanabhan, K. P., Eds. CRC Press: Boca Raton, 1993; ch. 4. Lindman, B.; Thalberg, K., *ibid.*, ch. 5.
35. Abdallah, D.; Cully, M. J.; Li, Y.; Shipp, D. A. *Coll. Polym. Sci.* **2008,** 286, 739-745.
36. Panambur, G.; Robert, C.; Zhang, Y.; Bazuin, C. G.; Ritcey, A. M. *Langmuir* **2003,** 19, 8859-8866. Panambur, G.; Zhang, Y.; Yesayan, A.; Galstian, T.; Bazuin, C. G.; Ritcey, A. M. *Langmuir* **2004,** 20, 3606-3615.
37. Kunitake, T.; Okahata, Y.; Shimomura, M.; Yasunami, S.; Takarabe, K. *J. Am. Chem. Soc.* **1981,** 103, 5401-5413. Tian, Y.; Umemura, J.; Takenaka, T.; Kunitake, T. *Langmuir* **1988,** 4, 1064-1066. Kunitake, T. *Angew. Chem., Int. Ed.* **1992,** 31, 709-726.
38. Everaars, M. D.; Marcelis, A. T. M.; Sudhölter, E. J. R. *Liebigs Ann./Recl.* **1997,** 21-26. Nieuwkerk, A. C.; Marcelis, A. T. M.; Koudijs, A.; Sudhölter, E. J. R. *Liebigs Ann./Recl.* **1997,** 1719-1724.
39. Engelking, J.; Menzel, H. *Thin Solid Films* **1998,** 327-329, 90-95.
40. Caculitan, N. G.; Scudder, P. H.; Rodriguez, A.; Casson, J. L.; Wang, H.-L.; Robinson, J. M.; Johal, M. S. *Langmuir* **2004,** 20, 8735-8739.
41. Navarro-Rodriguez, D.; Frere, Y.; Gramain, P.; Guillon, D.; Skoulios, A. *Liq. Cryst.* **1991,** 9, 321-335. Bravo-Grimaldo, E.; Navarro-Rodriguez, D.; Skoulios, A.; Guillon, D. *Liq. Cryst.* **1996,** 20, 393-398.
42. Tschierske, C. *Prog. Polym. Sci.* **1996,** 21, 775-852.
43. Kawakami, T.; Kato, T. *Macromolecules* **1998,** 31, 4475-4479.
44. Brandys, F. A.; Bazuin, C. G. *Chem. Mater.* **1996,** 8, 83-92.
45. Stewart, D.; Imrie, C. T. *Macromolecules* **1997,** 30, 877-884. Stewart, D.; Paterson, B. J.; Imrie, C. T. *Eur. Poly. J.* **1997,** 33, 285-290. Stewart, D.; Imrie, C. T. *J. Mater. Chem.* **1995,** 5, 223-228.

46. Eisenberg, A.; King, M., *Ion-Containing Polymers*. Academic Press: New York, 1977. Eisenberg, A.; Kim, J.-S., *Introduction to ionomers*. John Wiley & Sons, Inc.: New York, 1998.
47. Zundel, G., *Hydration and Intermolecular Interaction*. Academic Press: New York, 1970.
48. Vuillaume, P. Y.; Bazuin, C. G.; Galin, J.-C. *Macromolecules* **2000,** 33, 781-790.
49. Zhang, Q.; Bazuin, C.G. Submitted.
50. Imrie, C. T.; Schleeh, T.; Karasz, F. E.; Attard, G. S. *Macromolecules* **1993,** 26, 539-544.
51. Imrie, C. T.; Karasz, F. E.; Attard, G. S. *Macromolecules* **1993,** 26, 3803-3810.
52. Craig, A. A.; Imrie, C. T. *Macromolecules* **1995,** 28, 3617-3624.
53. Hamley, I. W.; Imrie, C. T. *J. Mater. Sci. Lett.* **1998,** 17, 339-341.
54. Bosshard, C.; Sutter, K.; Prêtre, P.; Hulliger, J.; Flörsheimer, M.; Kaatz, P.; Günter, P., *Organic Nonlinear Optical Materials*. Gordon and Breach Publishers: Basel, 1995.
55. Prasad, P. N.; Williams, D. J., *Introduction to nonlinear optical effects in molecules and polymers*. Wiley: New York, 1991.
56. McArdle, C. B., *Side chain liquid crystal polymers*. Chapman and Hall: New York, 1989.
57. Demus, D.; Goodby, J.; Gray, G. W.; Spiess, H.-W.; Vill, V., *Handbook of liquid crystals*. Wiley-VCH: Toronto, 1998; Vol. III.
58. Crivello, J. V.; Deptolla, M.; Ringsdorf, H. *Liq. Cryst.* **1988,** 3, 235-247.
59. McCulloch, I. A.; Bailey, R. T. *Proc. SPIE-Int. Soc. Opt. Eng.* **1990,** 1147, 134-140. McCulloch, I. A.; Bailey, R. T. *Mol. Cryst. Liq. Cryst.* **1991,** 200, 157-165. Ref. 57, p. 258.
60. Imrie, C. T.; Karasz, F. E.; Attard, G. S. *Liq. Cryst.* **1991,** 9, 47-57.
61. Imrie, C. T.; Karasz, F. E.; Attard, G. S. *Macromolecules* **1992,** 25, 1278-1283.
62. Schleeh, T.; Imrie, C. T.; Rice, D. M.; Karasz, F. E.; Attard, G. S. *J. Polym. Sci., Part A: Polym. Chem.* **1993,** 31, 1859-1869.
63. Imrie, C. T.; Karasz, F. E.; Attard, G. S. *Macromolecules* **1993,** 26, 545-550.
64. Imrie, C. T.; Karasz, F. E.; Attard, G. S. *Makromol. Chem., Rapid Commun.* **1993,** 14, 351-357.
65. Imrie, C. T.; Karasz, F. E.; Attard, G. S. *J. Macromol. Sci., Pure Appl. Chem.* **1994,** A31, 1221-1232.
66. Imrie, C. T.; Karasz, F. E.; Attard, G. S. *Macromolecules* **1994,** 27, 1578-1581.
67. Ulman, A.; Willand, C. S.; Kohler, W.; Robello, D. R.; Williams, D. J.; Handley, L. *J. Am. Chem. Soc.* **1990,** 112, 7083-7090.
68. Vogel, A. I., *Vogel's textbook of practical organic chemistry, including qualitative organic analysis*. Longman: New York, 1978.
69. Zollinger, H., *Azo and diazo chemistry: Aliphatic and aromatic compounds*. Interscience: New York, 1961.
70. Heldmann, C.; Warner, M. *Macromolecules* **1998,** 31, 3519-3531.
71. Samyn, C.; Verbiest, T.; Kesters, E.; Van den Broeck, K.; Van Beylen, M.; Persoons, A. *Polymer* **2000,** 41, 6049-6054.
72. See Supporting Information.
73. Antonietti, M.; Conrad, J.; Thünemann, A. *Macromolecules* **1994,** 27, 6007-6011.

74. Ponomarenko, E. A.; Tirrell, D. A.; MacKnight, W. J. *Macromolecules* **1996,** 29, 8751-8758.
75. Vuillaume, P. Y.; Sallenave, X.; Bazuin, C. G. *Macromolecules* **2006,** 39, 8339-8346.
76. Noël, C., In Ref. 56.
77. Wang, W.; Hashimoto, T. *Macromolecules* **1999,** 32, 3163-3166.
78. Vuillaume, P. Y.; Bazuin, C. G. *Macromolecules* **2003,** 36, 6378-6388.
79. Percec, V.; Hahn, B.; Ebert, M.; Wendorff, J. H. *Macromolecules* **1990,** 23, 2092-2095.
80. Emmerling, U.; Lindau, J.; Diele, S.; Werner, J.; Kresse, H. *Liq. Cryst.* **2000,** 27, 1069-1073.
81. Hiller, S.; Pascui, O.; Budde, H.; Kabisch, O.; Reichert, D.; Beiner, M. *New J. Phys.* **2004,** 6, 10. Beiner, M.; Huth, H. *Nature Mater.* **2003,** 2, 595-599.
82. Davidson, P. *Prog. Polym. Sci.* **1996,** 21, 893-950.
83. Nieuwhof, R. P.; Marcelis, A. T. M.; Sudhölter, E. J. R. *Macromol. Chem. Phys.* **1999,** 200, 2494-2500.
84. Navarro-Rodriguez, D.; Guillon, D.; Skoulios, A.; Frère, Y.; Gramain, P. *Makromol. Chem.* **1992,** 193, 3117-3128. Masson, P.; Gramain, P.; Guillon, D. *Macromol. Chem. Phys.* **1995,** 196, 3677-3686. Masson, P.; Gramain, P.; Guillon, D. *Macromol. Chem. and Phys.* **1999,** 200, 616-620.
85. Tschierske, C. *J. Mater. Chem.* **2001,** 11, 2647-2671.
86. Kasha, M. *Radiat. Res.* **1963,** 20, 55-70.
87. Hirano, Y.; Tokuoka, Y.; Kawashima, N.; Ozaki, Y. *Vib. Spectrosc.* **2007,** 43, 86-96.
88. Nieuwkerk, A. C.; Marcelis, A. T. M.; Koudijs, A.; Sudhölter, E. J. R. *Liebigs Ann./Recl.* **1997**, 1719-1724.
89. Zhang, Q.; Wang, X. ; Barrett, C.J.; Bazuin, C.G. *Chem. Mater.* In press.
90. Tsukruk, V. V.; Shilov, V. V.; Lipatov, Y. S. *Acta Polym.* **1985,** 36, 403-412.
91. Köberle, P.; Laschewsky, A. *Macromolecules* **1994,** 27, 2165-2173.

2.7 Supporting information for Chapter 2

2.7.1 Surfactomesogens (SM-Br)

2.7.1.1 Synthesis

Materials. All reagents used were purchased from Sigma-Aldrich. 1,6-Dibromohexane (97%), 1,10-dibromodecane (97%), p-anisidine (99%), 4-nitroaniline (99+%), p-toluidine (99%), triethylamine (99.5%), 4-aminobenzonitrile (98%), phenol (99.0+%), anhydrous potassium carbonate (99.0+%), potassium iodide (99.0%), sodium nitrite (99.5%), sodium acetate (99.9+%), hydrochloric acid (36.5-38.0%), and 4-phenylazophenol (98%) were all used as received. N-ethylaniline (98%) and N-methylaniline (98%) were dried with KOH pellets and fractionally distilled under vacuum before use. Deionized water was obtained from a Millipore Gradient A10 Milli-Q system (resistivity 18.2 MΩ.cm at 25 °C). All other solvents (EMD, A&C) were used as received when of appropriate quality or passed through drying columns (Glass Contour system) before use. Column chromatography was performed with silica gel (60 Å, 70-230 mesh; Sigma-Aldrich).

Representative phenol type surfactomesogen (X=OCH_3, n=6). *4-Hydroxy-4'-methoxyazobenzene* (**1**). To a 500 mL three-necked flask were added 10.0 g (81.2 mmol) p-anisidine, then 60 mL deionized water, then 18.4 mL (37 wt %) HCl, cooled to 0-5 °C, and stirred mechanically for 20 min. Separately, 6.2 g (89.9 mmol) sodium nitrite were dissolved in 12 mL deionized water, cooled to 0-5 °C, and stirred for 20 min. Then the cold sodium nitrite solution was added dropwise to the cold p-anisidine solution, followed by stirring at 0-5 °C for 20 min, to obtain the diazonium solution. The resultant mixture was tested positive with KI starch paper. Then, a solution of 7.7 g (81.8 mmol) phenol dissolved in 58 mL (0.278 M) cold NaOH were added to the cold diazonium solution, giving an orange precipitate. The mixture was vigorously stirred for 10 min, followed by warming to room temperature. After ca. 1 h, the mixture was acidified with HCl, stirred vigorously for 15 min, then filtered and rinsed with deionized water. The product was purified by recrystallization in 50/50 ethanol/H_2O (v/v), and dried in vacuum. Orange powder (yield 15 g, 81%). ^{1}H NMR ($CDCl_3$, ppm): 7.89 (d, 2H, J=8.9 Hz, Ar-N=), 7.84 (d,

2H, J=8.8 Hz, Ar-N=), 7.02 (d, 2H, J=8.9 Hz, *Ar*-OCH_3), 6.94 (d, 2H, J=8.8 Hz, *Ar*-OCH_2), 5.96 (s, 1H, Ar-O*H*), 3.90 (s, 3H, Ar-OCH_3).

1-Bromo-6-(4-methoxyazobenzene-4'-oxy)hexane (**2**). In 50 mL anhydrous acetonitrile stirred under nitrogen atmosphere were dissolved 5.8 g (25.4 mmol) of **1**, to which were added 10.3 g (93.3 mmol) ground anhydrous potassium carbonate and 12.9 g (50.8 mmol) 1,6-dibromohexane. The mixture was refluxed for ca. 20 h with tracking by thin-layer chromatography (TLC) until the end of reaction. The acetonitrile was then removed by evaporation under reduced pressure. The mixture was redissolved in chloroform, filtered to remove insolubles, and extracted 3 times against deionized water. After removing the solvent by evaporation under reduced pressure, the product was recrystallized in ethanol and dried in vacuum. Orange crystalline powder (yield 6.8 g, 69%). ^{1}H NMR ($CDCl_3$, ppm): 7.90 (m, 4H, Ar-N=), 7.02 (m, 4H, Ar-O), 4.06 (t, 2H, J=6.4 Hz, Ar-OCH_2), 3.91 (s, 3H, Ar-OCH_3), 3.46 (t, 2H, J=6.8 Hz, $BrCH_2$), 1.98-1.83 (m, 4H, OCH_2CH_2 and $BrCH_2CH_2$), 1.50-1.60 (m, 4H, CH_2-$(CH_2)_2$-CH_2).

Triethyl-6-(4-methoxyazobenzene-4'-oxy)hexylammonium bromide (**3**) (H_3CO-O6Q). In 75 mL anhydrous ethanol were dissolved 4.2 g (10.7 mmol) of **2** and 60 mL (431 mmol) freshly distilled triethylamine. This solution was refluxed for 2 d while tracking by TLC until the end of reaction. Then the solvent and excess triethylamine were removed by evaporation under reduced pressure. The solid was purified by column chromatography with a 91/9 (v/v) dichloromethane/methanol eluent, followed by recrystallization in ethanol/hexane (yield 4.4 g).

Representative aniline type surfactomesogen (Y=NO_2, Z=Et, n=10). Synthesized by Dr. Ximin Chen. *N-(10-Bromodecyl), N-ethylaniline* (**4**). A mixture of N-ethyl aniline (6.06 g, 50 mmol), 1,10-dibromodecane (30 g, 100 mmol), K_2CO_3 (13.8 g, 100 mmol), KI (100 mg) and acetone (300 mL) was refluxed under nitrogen atmosphere for 4 d. After cooling to room temperature, the mixture was filtered to remove insolubles. Then the solvent was evaporated under reduced pressure and the residue purified by column chromatography using hexane as eluent to recover 12 g of 1,10-dibromodecane. Colorless liquid product (yield 5.55 g, 32%). ^{1}H NMR ($CDCl_3$, ppm): 7.30 (t, 2H, J=8.6 Hz, Ar protons and meta to amino group), 6.76 (d, 2H, J=9.0 Hz, Ar protons and orth to amino group), 6.73 (t, 1H, J=7.2 Hz, Ar proton and para to amino group), 3.47 (m, 4H, NCH_2);

3.33 (t, 2H, J=8.0 Hz, $BrCH_2$), 1.94 (m, 2H, $BrCH_2CH_2$), 1.68 (m, 2H, NCH_2CH_2), 1.52 (m, 2H, $BrCH_2CH_2CH_2$), 1.30-1.50 (m, 10H, CH_2-$(CH_2)_5$-CH_2), 1.24 (t, 3H, J=6.9 Hz, NCH_2CH_3). ^{13}C NMR ($CDCl_3$, ppm): 12.5, 27.4, 27.7, 28.3, 28.9, 29.6, 29.74, 29.76, 33.0, 34.2, 45.1, 50.6, 111.9 (2C), 115.4, 129.4 (2C), 148.1.

1-(4-(N-(10-Bromodecyl), N-ethylaniline)-2-(4-nitrophenyl)diazene (**5**). A stirred solution of 2.25 g (16.3 mmol) 4-nitroaniline, 10 mL (37 wt %) HCl and 20 mL water was added dropwise to a solution of sodium nitrite (1.24 g, 18 mmol) in 5 mL water kept at 0-5 °C. The resulting diazonium salt was stirred for 20 min, then added dropwise to a solution of **4** (5.55 g, 16.3 mmol) in 40 mL methanol, followed by stirring for 30 min, all at 0-5 °C. The product was precipitated by addition of sodium acetate and left at room temperature for 1 h. The precipitate was then recovered by filtration, washed with hexane followed by dilute Na_2CO_3 solution, and finally recrystallized from ether/hexane. Dark red solid (yield 5.19 g, 65%). ^1H NMR ($CDCl_3$, ppm): 8.33 (d, 2H, J=9.0 Hz, Ar-NO_2), 7.93 (d, 2H, J=9.0 Hz, Ar-N=), 7.90 (d, 2H, J=9.0 Hz, Ar-N=), 6.73 (d, 2H, J=9.0 Hz, *Ar*-N(Et)), 3.51 (q, 2H, J=7.0 Hz, NCH_2CH_3), 3.43 (t, 2H, J=7.0 Hz, NCH_2CH_2), 3.39 (t, 2H, J=8.0 Hz, $BrCH_2$), 1.90 (m, 2H, $BrCH_2CH_2$), 1.70 (m, 2H, NCH_2CH_2), 1.29-1.50 (m, 12H, CH_2-$(CH_2)_6$-CH_2), 1.26 (t, 3H, J=6.9 Hz, NCH_2CH_3).

Triethyl-(10-(N-ethyl,N'-4-(4-nitro-phenylazo)phenyl)aminodecyl)ammonium bromide (**6**) [O_2N-N(Et)10Q]. In 80 mL warm anhydrous ethanol were dissolved 3.5 g (7.16 mmol) of **5**, followed by addition of 30 mL dry triethylamine and refluxing for one day. Then ethanol and excess triethylamine were removed by evaporation under reduced pressure. The solid was washed with hexane and recrystallized twice from acetone/hexane (yield 3.9 g).

2.7.1.2 Characterization Data

O_2N-N(Et)6Q. Dark brown fine powder. Yield 78%. ^1H NMR ($CDCl_3$, ppm): δ = 8.34 (d, 2H, J=9.0 Hz, Ar-NO_2), 7.98-7.88 (m, 4H, Ar-N=), 6.74 (d, 2H, J=9.2 Hz, *Ar*-N(Et)), 3.60-3.48 (m, 8H, N^+CH_2), 3.48-3.38 (m, 4H, Ar-NCH_2), 1.86-1.76 (m, 2H, $N^+CH_2CH_2$), 1.76-1.68 (m, 2H, NCH_2CH_2), 1.60-1.48 (m, 4H, $NCH_2CH_2CH_2$ and $N^+CH_2CH_2CH_2$), 1.46-1.36 (m, 9H, $N^+CH_2CH_3$), 1.26 (t, 3H, J=6.1 Hz, NCH_2CH_3). ^{13}C

NMR ($CDCl_3$, ppm): 157.33, 151.85, 147.45, 143.66, 126.82, 125.05, 122.91, 111.62, 57.85, 53.89, 50.71, 45.85, 27.82, 26.98, 26.78, 22.51, 12.83, 8.48.

O_2N-N(Et)10Q. Dark brown fine powder. Yield 92%. ^1H NMR ($CDCl_3$, ppm): δ = 8.29 (d, 2H, J=9.0 Hz, Ar-NO_2), 7.89 (d, 2H, J=9.0 Hz, Ar-N=), 7.87 (d, 2H, J=9.0 Hz, Ar-N=), 6.70 (d, 2H, J=9.0 Hz, *Ar*-N(Et)), 3.51-3.40 (m, 8H, N^+CH_2), 3.36 (t, 2H, J=7.7 Hz, NCH_2CH_3), 3.28 (t, 2H, J=8.3 Hz, NCH_2CH_2), 1.70 (m, 4H, NCH_2CH_2 and $N^+CH_2CH_2$), 1.25-1.50 (m, 21H, CH_2-$(CH_2)_6$-CH_2 and N+CH_2CH_3), 1.23 (t, 3H, J=6.9 Hz, NCH_2CH_3). ^{13}C NMR (DMSO-d_6, ppm): 157.18, 152.41, 147.55, 143.30, 127.14, 125.85, 123.25, 112.23, 56.86, 52.82, 50.70, 45.64, 29.83, 29.76, 29.69, 29.38, 28.02, 27.23, 26.68, 21.81, 13.18, 8.04. Synthesized by Dr. Ximin Chen.

O_2N-N(Me)6Q. Dark brown fine powder. Yield 82%. ^1H NMR ($CDCl_3$, ppm): δ = 8.34 (d, 2H, J=9.0 Hz, Ar-NO_2), 7.96-7.88 (m, 4H, Ar-N=), 7.77 (d, 2H, J=9.2 Hz, *Ar*-N(Et)), 3.55-3.45 (m, 8H, N^+CH_2), 3.39 (t, 2H, J=8.7 Hz, NCH_2CH_2), 3.13 (s, 3H, NCH_3), 1.84-1.75 (m, 2H, $N^+CH_2CH_2$), 1.74-1.67 (m, 2H, NCH_2CH_2), 1.56-1.45 (m, 4H, $NCH_2CH_2CH_2$ and $N^+CH_2CH_2CH_2$), 1.43-1.36 (m, 9H, NCH_2CH_3).

O_2N-N(Me)10Q. Dark brown fine powder. Yield 65%. ^1H NMR ($CDCl_3$, ppm): δ = 8.23 (d, 2H, J=9.0 Hz, Ar-NO_2), 7.86-7.79 (m, 4H, Ar-N=), 6.66 (d, 2H, J=9.3 Hz, *Ar*-N(Et)), 3.43 (q, 6H, J=7.3 Hz, $N^+CH_2CH_3$), 3.37 (t, 2H, J=7.4 Hz, NCH_2), 3.22 (t, 2H, J=8.4 Hz, $N^+CH_2CH_2$), 3.03 (s, 3H, NCH_3), 1.54-1.50 (m, 4H, NCH_2CH_2 and $N^+CH_2CH_2$), 1.38-1.18 (m, 21H, CH_2-$(CH_2)_6$-CH_2 and N+CH_2CH_3). ^{13}C NMR ($CDCl_3$, ppm): 157.29, 152.95, 147.45, 143.76, 126.62, 125.01, 122.89, 111.67, 57.87, 53.87, 53.01, 39.12, 29.72 (2C), 29.66, 29.47, 27.42, 27.33, 26.80, 22.44, 8.46.

NC-N(Et)10Q. Red powder. Yield 94%. ^1H NMR ($CDCl_3$, ppm): δ = 7.86-7.77 (m, 4H, Ar-N=), 7.69 (d, 2H, J=8.4 Hz, Ar-CN), 6.66 (d, 2H, J=9.2 Hz, *Ar*-N(Et)), 3.50-3.40 (m, 8H, N^+CH_2), 3.32 (t, 2H, J=7.5 Hz, NCH_2CH_3), 3.24 (t, 2H, J=8.4 Hz, NCH_2CH_2), 1.70-1.55 (m, 4H, NCH_2CH_2 and $N^+CH_2CH_2$), 1.40-1.22 (m, 21H, CH_2-$(CH_2)_6$-CH_2 and N+CH_2CH_3), 1.19 (t, 3H, J=7.0 Hz, NCH_2CH_3). ^{13}C NMR ($CDCl_3$, ppm): 155.98, 151.70, 143.40, 133.40, 126.56, 122.99, 119.48, 111.75, 111.48, 57.90, 53.89, 51.03, 45.77, 29.76 (2C), 29.69, 29.50, 27.94, 27.40, 26.83, 22.48, 12.82, 8.49. HR-MS m/z: Calcd. $(SM\text{-}Br)^+$ 490.3904; Found 490.3888.

O_2N-O6Q. Dark orange fine powder. Yield 91%. ^{1}H NMR (DMSO-d_6, ppm): δ = 8.41 (d, 2H, J=8.9 Hz, Ar-NO_2), 8.02 (d, 2H, 9.1 Hz, Ar-N=), 7.96 (d, 2H, 9.1 Hz, Ar-N=), 7.17 (d, 2H, 8.1 Hz, Ar-O), 4.12 (t, 2H, 6.4 Hz, OCH_2), 3.25 (q, 6H, 7.2 Hz, $N^+CH_2CH_3$), 3.14 (t, 2H, 8.5 Hz, $N^+CH_2CH_2$), 1.84-1.75 (m, 2H, OCH_2CH_2), 1.68-1.58 (m, 2H, $N^+CH_2CH_2$), 1.56-1.46 (m, 2H, $OCH_2CH_2CH_2$), 1.44-.134 (m, 2H, $N^+CH_2CH_2CH_2$), 1.22-1.14 (m, 9H, $N^+CH_2CH_3$). ^{13}C NMR (DMSO-d_6, ppm): 163.45, 156.22, 148.82, 147.02, 126.35, 125.93, 124.01, 116.15, 68.92, 56.83, 52.85, 29.19, 26.40, 25.88, 21.78, 8.07. Synthesized by Dr. Ximin Chen.

O_2N-O10Q. Dark orange fine powder. Yield 92%. ^{1}H NMR ($CDCl_3$, ppm): δ = 8.32 (d, 2H, J=9.0 Hz, Ar-NO_2), 7.94 (t, 4H, J=9.0 Hz, Ar-N=), 7.00 (d, 2H, J=9.0 Hz, Ar-O), 4.03 (t, 2H, J=6.5 Hz, OCH_2), 3.50 (m, 6H, $N^+CH_2CH_3$), 3.28 (t, 2H, J=8.4 Hz, $N^+CH_2CH_2$), 1.80 (m, 2H, OCH_2CH_2), 1.69 (m, 2H, $N^+CH_2CH_2$), 1.30-1.50 (m, 21H, CH_2-$(CH_2)_6$-CH_2 and N+CH_2CH_3). ^{13}C NMR ($CDCl_3$, ppm): 163.33, 156.46, 148.54, 147.15, 126.03, 125.09, 123.49, 115.32, 68.87, 58.00, 53.98, 29.73 (2C), 29.65, 29.55, 29.49, 26.89, 26.34, 22.54, 8.54.

NC-O6Q. Orange fine powder. Yield 78%. ^{1}H NMR ($CDCl_3$, ppm): δ = 7.98-7.92 (m, 4H, Ar-N=), 7.80 (d, 2H, J=8.5 Hz, Ar-CN), 7.03 (d, 2H, 9.0 Hz, Ar-O), 4.10 (t, 2H, J=6.2 Hz, OCH_2), 3.54 (q, 6H, J=7.3 Hz, $N^+CH_2CH_3$), 3.43-3.36 (m, 2H, $N^+CH_2CH_2$), 1.94-1.76 (m, 4H, OCH_2CH_2 and $N^+CH_2CH_2$), 1.68-1.50 (m, 4H, $OCH_2CH_2CH_2$ and $N^+CH_2CH_2CH_2$), 1.42 (t, 9H, J=7.3 Hz, N+CH_2CH_3).

NC-O10Q. Orange fine powder. Yield 69%. ^{1}H NMR ($CDCl_3$, ppm): δ = 7.87 (d, 4H, J=8.3 Hz, Ar-N=), 7.72 (d, 2H, J=8.6 Hz, Ar-CN), 6.95 (d, 2H, 9.0 Hz, Ar-O), 3.99 (t, 2H, 6.5 Hz, OCH_2), 3.45 (q, 6H, 7.2 Hz, $N^+CH_2CH_3$), 3.23 (t, 2H, 8.5 Hz, $N^+CH_2CH_2$), 1.81-1.70 (m, 2H, OCH_2CH_2), 1.70-1.57 (m, 2H, $N^+CH_2CH_2$), 1.46-1.20 (m, 21H, CH_2-$(CH_2)_6$-CH_2 and N+CH_2CH_3). ^{13}C NMR (CDCl3, ppm): 163.11, 155.14, 146.99, 133.50, 125.83, 123.44, 119.06, 115.25, 113.32, 68.81, 57.88, 53.88, 29.68 (2C), 29.61, 29.49, 29.45, 26.83, 26.29, 22.46, 8.48.

H_3CO-O6Q. Brown crystals (yellow when ground to powder). Yield 83%. ^{1}H NMR ($CDCl_3$, ppm): δ = 7.88 (m, 4H, Ar-N=), 7.00 (m, 4H, Ar-O), 4.06 (t, 2H, J=6.1 Hz, OCH_2), 3.90 (s, 3H, OCH_3), 3.52 (q, 6H, J=7.2 Hz, $N^+CH_2CH_3$), 3.35 (t, 2H, J=8.5 Hz,

$N^+CH_2CH_2$), 1.90-1.72 (m, 4H, OCH_2CH_2 and $N^+CH_2CH_2$), 1.66-1.46 (m, 4H, $OCH_2CH_2CH_2$ and $N^+CH_2CH_2CH_2$), 1.42 (t, 9H, J=7.2 Hz, $N^+CH_2CH_3$).

H_3CO-O10Q. Yellow fine powder. Yield 91%. ^1H NMR ($CDCl_3$, ppm): δ = 7.91-7.85 (m, 4H, Ar-N=), 7.04-6.98 (m, 4H, Ar-O), 4.05 (t, 2H, J=6.5 Hz, OCH_2), 3.90 (s, 3H, OCH_3), 3.52 (q, 6H, J=7.2 Hz, $N^+CH_2CH_3$), 3.28 (t, 2H, 8.4Hz, $N^+CH_2CH_2$), 1.88-1.78 (m, 2H, OCH_2CH_2), 1.77-1.65 (m, 2H, $N^+CH_2CH_2$), 1.54-1.28 (m, 21H, CH_2-$(CH_2)_6$-CH_2 and $N+CH_2CH_3$).

H_3C-O6Q. Yellow fine powder. Yield 45%. ^1H NMR ($CDCl_3$, ppm): δ = 7.87 (d, 2H, J=8.9 Hz, Ar-N=), 7.76 (d, 2H, J=8.2 Hz, Ar-N=), 7.28 (d, 2H, 7.5 Hz, *Ar*-CH_3), 6.97 (d, 2H, 9.0 Hz, Ar-O), 4.02 (t, 2H, 6.2 Hz, OCH_2), 3.46 (q, 6H, J=7.2 Hz, $N^+CH_2CH_3$), 3.29 (t, 2H, 8.3 Hz, $N^+CH_2CH_2$), 2.41 (s, 3H, Ar-CH_3), 1.86-1.66 (m, 4H, OCH_2CH_2 and $N^+CH_2CH_2$), 1.61-1.41 (m, 4H, $OCH_2CH_2CH_2$ and $N^+CH_2CH_2CH_2$), 1.40-1.29 (m, 9H, $N^+CH_2CH_3$). ^{13}C NMR ($CDCl_3$, ppm): 161.66, 151.16, 147.30, 141.29, 130.11, 124.97, 122.91, 115.11, 68.24, 57.89, 53.94, 29.31, 26.59, 26.06, 22.49, 21.85, 8.53.

H_3C-O10Q. Yellow fine powder. Yield 52%. ^1H NMR ($CDCl_3$, ppm): δ = 7.84 (d, 2H, J=9.0 Hz, Ar-N=), 7.73 (d, 2H, J=8.3 Hz, Ar-N=), 7.24 (d, 2H, 8.1 Hz, *Ar*-CH_3), 6.94, (d, 2H, 9.0 Hz, Ar-O), 3.98 (t, 2H, 6.5 Hz, OCH_2), 3.42 (q, 6H, 7.3 Hz, $N^+CH_2CH_3$), 3.20 (t, 2H, 8.5 Hz, $N^+CH_2CH_2$), 2.37 (s, 3H, Ar-CH_3), 1.81-1.71 (m, 2H, OCH_2CH_2), 1.67-1.54 (m, 2H, $N^+CH_2CH_2$), 1.48-1.20 (m, 21H, CH_2-$(CH_2)_6$-CH_2 and $N^+CH_2CH_3$). ^{13}C NMR ($CDCl_3$, ppm): 161.86, 151.15, 147.18, 141.19, 130.07, 124.92, 122.86, 115.08, 68.66, 57.87, 53.89, 29.66 (2C), 29.59, 29.49, 29.38, 26.81, 26.29, 22.45, 21.82, 8.48.

H-O6Q. Light orange fine powder. Yield 84%. ^1H NMR ($CDCl_3$, ppm): δ = 7.92 (m, 4H, Ar-N=), 7.56-7.43 (m, 3H, Ar-N=N-), 7.00-7.05 (m, 2H, Ar-O), 4.09 (t, 2H, J=6.0 Hz, OCH_2), 3.55 (q, 6H, J=7.3 Hz, $N^+CH_2CH_3$), 3.39 (t, 2H, J=8.6 Hz, $N^+CH_2CH_2$), 1.75-1.95 (m, 4H, OCH_2CH_2 and $N^+CH_2CH_2$), 1.50-1.70 (m, 4H, $OCH_2CH_2CH_2$ and $N^+CH_2CH_2CH_2$), 1.46-1.39 (m, 9H, $N^+CH_2CH_3$).

H-O10Q. Light orange fine powder. Yield 85%. ^1H NMR ($CDCl_3$, ppm): δ = 7.91 (m, 4H, Ar-N=), 7.55-7.43 (m, 3H, Ar-N=N-), 7.00-7.05 (m, 2H, Ar-O), 4.06 (t, 2H, J=6.5 Hz, OCH_2), 3.53 (q, 6H, J=7.3 Hz, $N^+CH_2CH_3$), 3.29 (t, 2H, J=8.1 Hz, $N^+CH_2CH_2$), 1.84 (m, 2H, OCH_2CH_2), 1.70 (m, 4H, $N^+CH_2CH_2$ and $OCH_2CH_2CH_2$), 1.55-1.30 (m, 19H, CH_2-$(CH_2)_5$-CH_2 and $N+CH_2CH_3$).

Table 2.S1 CHN elemental analysis of the surfactomesogens, with the theoretical values adjusted as necessary by added water molecules.

Surfactomesogen	C%		H%		N%	
	Theor.	Found	Theor.	Found	Theor.	Found
O_2N-N(Et)10Q	61.01	60.75	8.19	8.21	11.86	11.70
NO_2-N(Et)6Q+0.5 H_2O	57.45	57.72	7.60	7.47	12.88	12.77
O_2N-N(Me)10Q	60.41	60.92	8.04	8.11	12.15	12.02
O_2N-N(Me)6Q+0.5 H_2O	56.71	56.59	7.42	7.45	13.23	12.99
NC-N(Et)10Q	65.25	66.19	8.48	8.35	12.27	12.20
O_2N-O10Q	59.67	59.97	7.69	7.97	9.94	10.01
O_2N-O6Q	56.80	56.74	6.95	6.95	11.04	10.99
NC-O10Q	64.08	63.57	7.97	8.22	10.31	10.19
NC-O6Q	61.60	61.28	7.24	7.79	11.49	11.21
H_3CO-O10Q	63.49	63.68	8.45	8.64	7.66	7.64
H_3CO-O6Q	60.97	60.89	7.78	7.94	8.53	8.59
H_3C-O10Q	65.40	66.49	8.71	9.53	7.89	8.10
H_3C-O6Q	63.02	63.12	8.04	8.29	8.82	8.91
H-O10Q	64.85	64.78	8.55	8.44	8.10	8.11
H-O6Q	62.33	62.41	7.85	7.92	9.09	9.07

Thermal Data

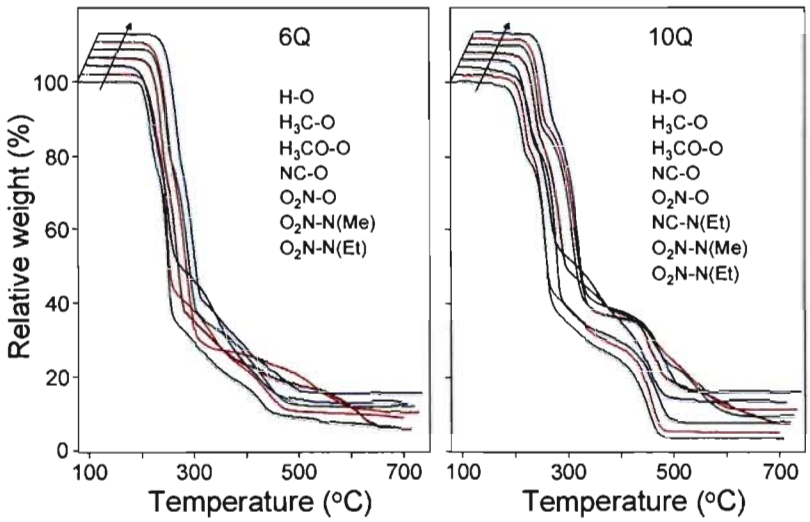

Figure 2.S1 TGA thermograms of the surfactomesogens. The curves are displaced along the diagonal indicated by the arrow, relative to the curves for O_2N-N(Et)nQ. They are identified in order from bottom to top as they appear along the arrow.

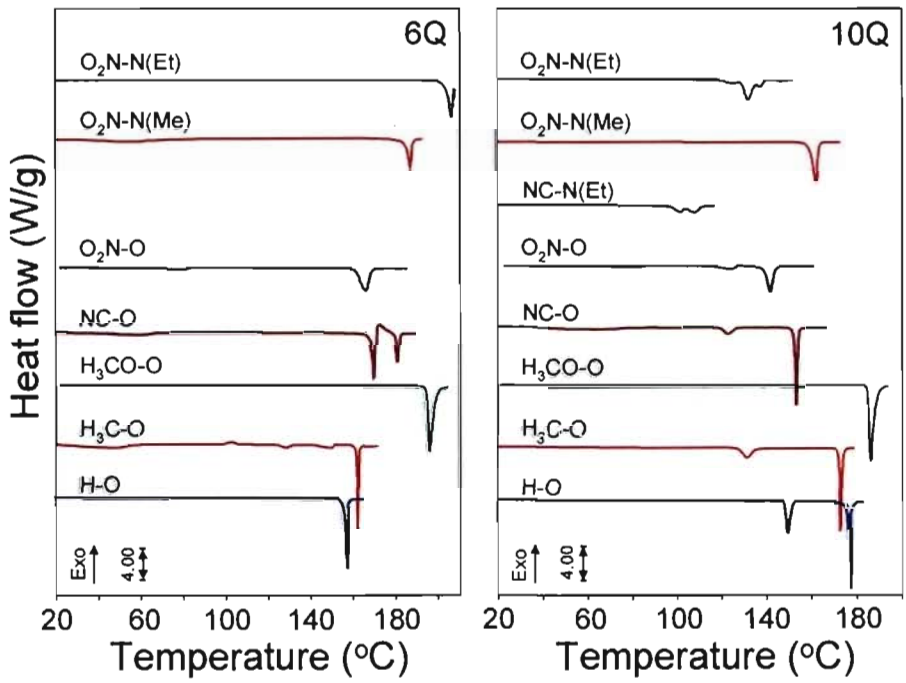

Figure 2.S2 DSC thermograms (first heating scans) of the SM-Br surfactomesogens.

X-Ray Data

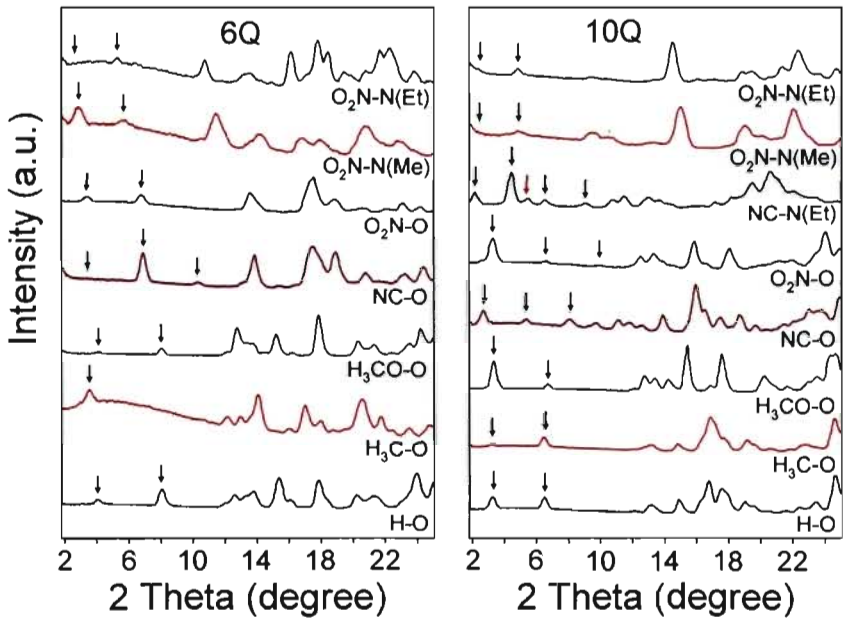

Figure 2.S3 Ambient temperature powder X-ray diffractograms of the as-prepared surfactomesogens. Black arrows identify lower angle peaks suggesting lamellar crystals, green arrows indicate the position of potential first-order peaks that appear extinct, and the red arrow indicates a peak not matching the lamellar pattern.

Table 2.S2 Bragg spacings determined from the small-angle peaks in Figure 2.S3 (black arrows) suggesting lamellar crystals. Calculated molecular lengths of the SM-Br's in their most extended conformation are 28±1 and 33±1 Å for the 6Q and 10Q SM-Br's, respectively.

SM-Br	Peak 1 (Å)	Peak 2 (Å)	Peak 3 (Å)	Peak 4 (Å)
O_2N-N(Et)6Q		16.8		
O_2N-N(Et)10Q	36.8	18.1		
O_2N-N(Me)6Q	30.4	15.4		
O_2N-N(Me)10Q		18.1		
NC-N(Et)10Q	40.0	19.8	13.4	9.7
O_2N-O6Q	25.9	13.0		
O_2N-O10Q	26.8	13.4	8.9	
NC-O6Q		12.8	8.5	
NC-O10Q	32.0	16.3	10.8	
H_3CO-O6Q	21.6	11.0		
H_3CO-O10Q	26.2	13.1	8.7	
H_3C-O6Q	24.8			
H_3C-O10Q	26.9	13.5		
H-O6Q	21.7	10.9		
H-O10Q	27.1	13.6	9.1	

Single Crystal Data

Table 2.S3 Single crystal data for H_3CO-O6Q and O_2N-O10Q.

	H_3CO-O6Q	O_2N-O10Q
Crystal system	Triclinic	Triclinic
Space group	P-1	P-1
Unit cell dimensions	a=7.9241(2) Å, α=88.1650(10)° b=8.1348(2) Å, β=86.1580(10)° c=21.7527(4) Å, γ=63.8090(10)°	a=12.2784(3) Å, α=96.7010(10)° b=12.6117 Å, β=91.7280(10)° c=33.4518(8) Å, γ=116.1840(10)°
Cell volume	1255.40(5) Å	4597.32(19) Å
Density (calculated)	1.303 g/cm^3	1.265 g/cm^3

Single crystals of H_3CO-O6Q were obtained in the synthesis of this compound, where the last step was recrystallization from ethanol/hexane. A single crystal of O_2N-O10Q was cultivated from acetone exposed to hexane atmosphere. Both were analyzed by single-crystal XRD (Bruker AXS Smart 6000-FR591 diffractometer). The main results are summarized in Table 2.S3. Both single crystals are triclinic. For H_3CO-O6Q, the value of c confirms that peak 1 and peak 2 in Table 2.S2 correspond to the (001) and (002) planes, respectively. The single crystal obtained for O_2N-O10Q clearly has a different crystal structure than that of the as-prepared sample above (see Table 2.S2). In this case, the positions of the Br ion and H_2O could not be determined with certainty.

2.7.2 Surfactomesogen/poly(styrene sulfonate) (SM/PSS) complexes

NMR Data

O_2N-N(Et)6Q/PSS. Dark red powder. ^{1}H NMR (DMSO-d_6, 60 °C, ppm): δ = 8.28 (d, 2H, J=9.0 Hz, Ar-NO_2), 7.88 (d, 2H, J=9.0 Hz, Ar-N=), 7.80 (d, 2H, J=9.2 Hz, Ar-N=), 7.70-7.25 (broad, 2H, Ar-SO_3^-), 6.83 (d, 2H, J=9.3 Hz, Ar-N=), 6.75-6.10 (broad, 2H, Ar-SO_3^-), 3.50 (q, 2H, J=7.1 Hz, N$CH_2$$CH_3$), 3.41 (t, 2H, J=7.5 Hz, N$CH_2$$CH_2$), 3.19 (q, 6H, J=7.2 Hz, $N^+CH_2CH_3$), 3.09 (t, 2H, J=8.1 Hz, $N^+CH_2CH_2$), 1.66-1.54 (m, 4H, $N^+CH_2CH_2$ and NCH_2CH_2), 1.45-1.30 (m, 4H, $NCH_2CH_2CH_2$ and $N^+CH_2CH_2CH_2$), 1.16 (t, 3H, J=7.0 Hz, NCH_2CH_3), 1.07 (t, 9H, J=7.0 Hz, $N^+CH_2CH_3$), 2.2-0.7 (broad, 3H, $CHCH_2$ in backbone).

O_2N-N(Et)10Q/PSS. Dark red powder. ^{1}H NMR (DMSO-d_6, 90 °C, ppm): δ = 8.29 (d, 2H, J=9.0 Hz, Ar-NO_2), 7.88 (d, 2H, J=9.0 Hz, Ar-N=), 7.80 (d, 2H, J=9.1 Hz, Ar-N=), 7.70-7.20 (broad, 2H, Ar-SO_3^-), 6.81 (d, 2H, J=9.3 Hz, Ar-N=), 6.70-6.00 (broad, 2H, Ar-SO_3^-), 3.49 (q, 2H, J=7.0 Hz, N$CH_2$$CH_3$), 3.40 (t, 2H, J=7.5 Hz, N$CH_2$$CH_2$), 3.19 (q, 6H, J=7.2 Hz, $N^+CH_2$$CH_3$), 3.08 (t, 2H, J=8.3 Hz, $N^+CH_2$$CH_2$), 1.55-1.50 (m, 4H, $N^+CH_2CH_2$ and NCH_2CH_2), 1.40-1.24 (m, 12H, CH_2-(CH_3)$_6$-CH_2), 1.17 (t, 3H, J=7.0 Hz, NCH_2CH_3), 1.07 (t, 9H, J=7.1 Hz, $N^+CH_2CH_3$), 2.2-0.7 (broad, 3H, $CHCH_2$ in backbone).

O_2N-N(Me)6Q/PSS. Dark red powder. ^{1}H NMR (DMSO-d_6, 90 °C, ppm): δ = 8.28 (d, 2H, J=9.0 Hz, Ar-NO_2), 7.88 (d, 2H, J=9.0 Hz, Ar-N=), 7.80 (d, 2H, J=9.2 Hz, Ar-N=), 7.70-7.24 (broad, 2H, Ar-SO_3^-), 6.85 (d, 2H, J=9.3 Hz, Ar-N=), 6.78-6.00 (broad, 2H, Ar-SO_3^-), 3.46 (t, 2H, J=7.3 Hz, NCH_2), 3.18 (q, 6H, J=7.3 Hz, $N^+CH_2$$CH_3$), 3.12-3.04 (m, 5H, NCH_3 and $N^+CH_2$$CH_2$), 1.65-1.54 (m, 4H, $N^+CH_2CH_2$ and NCH_2CH_2), 1.42-1.29 (m, 4H, $N^+CH_2CH_2CH_2$ and $NCH_2CH_2CH_2$), 1.08 (t, 9H, J=7.1 Hz, $N^+CH_2CH_3$), 2.3-0.7 (broad, 3H, $CHCH_2$ in backbone).

O_2N-N(Me)10Q/PSS. Dark red powder. ^{1}H NMR (DMSO-d_6, 90 °C, ppm): δ = 8.29 (d, 2H, J=9.0 Hz, Ar-NO_2), 7.88 (d, 2H, J=9.1 Hz, Ar-N=), 7.80 (d, 2H, J=9.2 Hz, Ar-N=), 7.70-7.20 (broad, 2H, Ar-SO_3^-), 6.83 (d, 2H, J=9.2 Hz, Ar-N=), 6.76-6.00 (broad, 2H, Ar-SO_3^-), 3.44 (t, 2H, J=7.3 Hz, NCH_2), 3.18 (q, 6H, J=7.2 Hz, $N^+CH_2$$CH_3$), 3.10-3.04 (m, 5H, NCH_3 and $N^+CH_2$$CH_2$), 1.64-1.50 (m, 4H, $N^+CH_2CH_2$ and NCH_2CH_2), 1.38-1.22 (m, 12H, CH_2-(CH_3)$_6$-CH_2), 1.07 (t, 9H, J=7.1 Hz, $N^+CH_2CH_3$), 2.2-0.7 (broad, 3H, $CHCH_2$ in backbone).

NC-N(Et)10Q/PSS. Red fluff-like powder. ^{1}H NMR (DMSO-d_6, 75 °C, ppm): δ = 7.89-7.81 (m, 4H, Ar-N=), 7.79 (d, 2H, J=9.2 Hz, Ar-CN), 7.65-7.20 (broad, 2H, Ar-SO_3^-), 6.80 (d, 2H, J=9.3 Hz, Ar-N=), 6.75-6.00 (broad, 2H, Ar-SO_3^-), 3.48 (q, 2H, J=7.0 Hz, N$CH_2$$CH_3$), 3.39 (t, 2H, 7.5 Hz, N$CH_2$$CH_2$), 3.18 (q, 6H, J=7.2 Hz, $N^+CH_2$$CH_3$), 3.08 (t, 2H, J=8.3 Hz, $N^+CH_2$$CH_2$), 1.65-1.50 (m, 4H, $N^+CH_2CH_2$ and NCH_2CH_2), 1.40-1.24 (m, 12H, CH_2-(CH_3)$_6$-CH_2), 1.16 (t, 3H, J=7.0 Hz, NCH_2CH_3), 1.07 (t, 9H, J=7.1 Hz, $N^+CH_2CH_3$), 2.2-0.7 (broad, 3H, $CHCH_2$ in backbone).

O_2N-O6Q/PSS. Dark orange powder. ^{1}H NMR (DMSO-d_6, 90 °C, ppm): δ = 8.33 (d, 2H, J=8.7 Hz, Ar-NO_2), 7.96 (d, 2H, J=8.7 Hz, Ar-N=), 7.89 (d, 2H, J=8.9 Hz, Ar-N=), 7.7-7.2 (broad, 2H, Ar-SO_3^-), 7.14 (d, 2H, J=8.9 Hz, Ar-O), 6.8-6.0 (broad, 2H, Ar-SO_3^-),

4.12 (t, 2H, J=6.5 Hz, OCH_2), 3.20 (q, 6H, J=7.2 Hz, $N^+CH_2CH_3$), 3.11 (t, 2H, J=8.3 Hz, $N^+CH_2CH_2$), 1.81-1.73 (m, 2H, OCH_2CH_2), 1.65-1.55 (m, 2H, $N^+CH_2CH_2$), 1.53-1.44 (m, 2H, $OCH_2CH_2CH_2$), 1.42-1.33 (m, 2H, $N^+CH_2CH_2CH_2$), 1.08 (t, 9H, J=7.1 Hz, $N^+CH_2CH_3$), 2.3-0.7 (broad, 3H, $CHCH_2$ in backbone).

O_2N-O10Q/PSS. Dark orange powder. ^1H NMR (DMSO-d_6, 80 °C, ppm): δ = 8.34 (d, 2H, J=8.8 Hz, Ar-NO_2), 7.97 (d, 2H, J=8.8 Hz, Ar-N=), 7.89 (d, 2H, J=8.9 Hz, Ar-N=), 7.70-7.20 (broad, 2H, Ar-SO_3^-), 7.12 (d, 2H, J=8.9 Hz, Ar-O), 6.90-6.00 (broad, 2H, Ar-SO_3^-), 4.09 (t, 2H, J=6.5 Hz, OCH_2), 3.19 (q, 6H, J=7.2 Hz, $N^+CH_2CH_3$), 3.12-3.05 (m, 2H, $N^+CH_2CH_2$), 1.78-1.71 (m, 2H, OCH_2CH_2), 1.61-1.52 (m, 2H, $N^+CH_2CH_2$), 1.47-1.38 (m, 2H, $OCH_2CH_2CH_2$), 1.38-1.25 (m, 10H, CH_2-$(CH_2)_5$-CH_2), 1.07 (t, 9H, J=7.0 Hz, $N^+CH_2CH_3$), 2.2-0.9 (broad, 3H, $CHCH_2$ in backbone).

NC-O6Q/PSS. Orange powder. ^1H NMR (DMSO-d_6, 90 °C, ppm): δ = 7.96-7.85 (m, 6H, Ar-N=), 7.7-7.25 (broad, 2H, Ar-SO_3^-), 7.13 (d, 2H, J=9.0 Hz, Ar-O), 6.90-6.00 (broad, 2H, Ar-SO_3^-), 4.11 (t, 2H, J=6.5 Hz, OCH_2), 3.19 (q, 6H, J=7.2 Hz, $N^+CH_2CH_3$), 3.10 (t, 2H, J=8.2 Hz, $N^+CH_2CH_2$), 1.80-.172 (m, 2H, OCH_2CH_2), 1.64-1.56 (m, 2H, $N^+CH_2CH_2$), 1.52-1.44 (m, 2H, $OCH_2CH_2CH_2$), 1.41-1.33 (m, 2H, $N^+CH_2CH_2$), 1.08 (t, 9H, J=7.1 Hz, $N^+CH_2CH_3$), 2.3-0.7 (broad, 3H, $CHCH_2$ in backbone).

NC-O10Q/PSS. Dark orange powder. ^1H NMR (DMSO-d_6, 90 °C, ppm): δ = 7.96-7.85 (m, 6H, Ar-N=), 7.66-7.22 (broad, 2H, Ar-SO_3^-), 7.11 (d, 2H, J=9.0 Hz, Ar-O), 6.80-6.00 (broad, 2H, Ar-SO_3^-), 4.09 (t, 2H, J=6.5 Hz, OCH_2), 3.19 (q, 6H, J=7.3 Hz, $N^+CH_2CH_3$), 3.08 (t, 2H, J=8.4 Hz, $N^+CH_2CH_2$), 1.78-1.71 (m, 2H, OCH_2CH_2), 1.60-1.52 (m, 2H, $N^+CH_2CH_2$), 1.48-1.40 (m, 2H, $OCH_2CH_2CH_2$), 1.39-1.22 (m, 10H, CH_2-$(CH_2)_5$-CH_2), 1.07 (t, 9H, J=7.1 Hz, $N^+CH_2CH_3$), 2.4-0.7 (broad, 3H, $CHCH_2$ in backbone).

H_3CO-O6Q/PSS. Orange condensed flakes and powder. ^1H NMR (DMSO-d_6, 90 °C, ppm): δ = 7.85-7.75 (m, 4H, Ar-N=), 7.7-7.2 (broad, 2H, Ar-SO_3^-), 7.15-7.05 (m, 4H, Ar-O), 6.85-6.05 (broad, 2H, Ar-SO_3^-), 4.08 (t, 2H, J=6.5 Hz, OCH_2), 3.85 (s, 3H, OCH_3), 3.19 (q, 6H, J=7.2 Hz, $N^+CH_2CH_3$), 3.09 (t, 2H, J=8.3 Hz, $N^+CH_2CH_2$), 1.80-1.72 (m, 2H, OCH_2CH_2), 1.64-1.55 (m, 2H, $N^+CH_2CH_2$), 1.52-1.44 (m, 2H, OCH_2CH_2), 1.41-1.33 (m, 2H, $N^+CH_2CH_2$), 1.07 (t, 9H, J=7.1 Hz, $N^+CH_2CH_3$), 2.2-0.7 (broad, 3H, $CHCH_2$ in backbone).

H_3CO-O10Q/PSS. Yellow powder. ^{1}H NMR (DMSO-d_6, 75 °C, ppm): δ = 7.83-7.77 (m, 4H, Ar-N=), 7.65-7.20 (broad, 2H, Ar-SO_3^-), 7.10-7.05 (m, 4H, Ar-O), 6.8-6.0 (broad, 2H, Ar-SO_3^-), 4.07 (t, 2H, J=6.5 Hz, OCH_2), 3.86 (s, 3H, OCH_3), 3.19 (q, 6H, J=7.2 Hz, $N^+CH_2CH_3$), 3.08 (t, 2H, J=8.2 Hz, $N^+CH_2CH_2$), 1.8-1.7 (m, 2H, OCH_2CH_2), 1.62-1.52 (m, 2H, $N^+CH_2CH_2$), 1.50-1.40 (m, 2H, $OCH_2CH_2CH_2$), 1.40-1.22 (m, 10H, CH_2-$(CH_3)_5$-CH_2), 1.08 (t, 9H, J=7.1 Hz, $N^+CH_2CH_3$), 2.2-0.7 (broad, 3H, $CHCH_2$ in backbone).

H_3C-O10Q/PSS. Yellow powder. ^{1}H NMR (DMSO-d_6, 75 °C, ppm): δ = 7.82 (d, 2H, J=8.8 Hz, Ar-N=), 7.72 (d, 2H, J=8.2 Hz, Ar-N=), 7.66-7.24 (broad, 2H, Ar-SO_3^-), 7.34 (d, 2H, J=8.3 Hz), 7.08 (d, 2H, J=8.9 Hz, Ar-O), 6.85-6.00 (broad, 2H, Ar-SO_3^-), 4.07 (t, 2H, J=6.5 Hz, OCH_2), 3.18 (q, 6H, J=7.2 Hz, $N^+CH_2CH_3$), 3.08 (t, 2H, J=8.3 Hz, $N^+CH_2CH_2$), 2.34 (s, 3H, Ar-CH_3), 1.80-1.70 (m, 2H, OCH_2CH_2), 1.62-1.52 (m, 2H, $N^+CH_2CH_2$), 1.50-1.40 (m, 2H, $OCH_2CH_2CH_2$), 1.40-1.22 (m, 10H, CH_2-$(CH_3)_5$-CH_2), 1.07 (t, 9H, J=7.1Hz, $N^+CH_2CH_3$), 2.4-0.7 (broad, 3H, $CHCH_2$ in backbone).

H_3C-O6Q/PSS. Yellow powder. ^{1}H NMR (DMSO-d_6, 90 °C, ppm): δ = 7.82 (d, 2H, J=8.9 Hz, Ar-N=), 7.72 (d, 2H, J=8.3 Hz, CH_3-*Ar*), 7.66-7.20 (broad, 2H, Ar-SO_3^-), 7.33 (d, 2H, J=8.2 Hz, Ar-N=), 7.10 (d, 2H, J=8.9 Hz, Ar-O), 6.90-6.00 (broad, 2H, Ar-SO_3^-), 4.09 (t, 2H, J=6.5 Hz, OCH_2), 3.19 (q, 6H, J=7.2 Hz, $N^+CH_2CH_3$), 3.09 (t, 2H, J=8.3 Hz, $N^+CH_2CH_2$), 2.38 (s, 3H, Ar-CH_3), 1.80-1.72 (m, 2H, OCH_2CH_2), 1.64-1.54 (m, 2H, $N^+CH_2CH_2$), 1.52-1.44 (m, 2H, $OCH_2CH_2CH_2$), 1.42-1.32 (m, 2H, $N^+CH_2CH_2CH_2$), 1.08 (t, 9H, J=7.0 Hz, $N^+CH_2CH_3$), 2.4-0.7 (broad, 3H, $CHCH_2$ in backbone).

H-O6Q/PSS. Yellow powder. ^{1}H NMR (DMSO-d_6, 90 °C, ppm): δ = 7.86-7.79 (m, 4H, Ar-N=), 7.56-7.44 (m, 3H, Ar-N=N), 7.70-7.20 (broad, 2H, Ar-SO_3^-), 7.11 (d, 2H, J=9.0 Hz, Ar-O), 6.90-6.00 (broad, 2H, Ar-SO_3^-), 4.10 (t, 2H, J=6.5 Hz, OCH_2), 3.18 (q, 6H, J=7.2 Hz, $N^+CH_2CH_3$), 3.09 (t, 2H, J=8.4 Hz, $N^+CH_2CH_2$), 1.80-1.73 (m, 2H, OCH_2CH_2), 1.64-1.55 (m, 2H, $N^+CH_2CH_2$), 1.52-1.44 (m, 2H, $OCH_2CH_2CH_2$), 1.41-1.33 (m, 2H, $N^+CH_2CH_2CH_2$), 1.07 (t, 9H, J=7.1 Hz, $N^+CH_2CH_3$), 2.3-0.6 (broad, 3H, $CHCH_2$ in backbone).

H-O10Q/PSS. Yellow powder. ^{1}H NMR (DMSO-d_6, 105 °C, ppm): δ = 7.86-7.78 (m, 4H, Ar-N=), 7.55-7.45 (m, 3H, Ar-N=N), 7.65-7.20 (broad, 2H, Ar-SO_3^-), 7.09 (d, 2H, J=8.9 Hz, Ar-O), 6.90-6.00 (broad, 2H, Ar-SO_3^-), 4.08 (t, 2H, J=6.5 Hz, OCH_2), 3.18 (q, 6H, 7.2 Hz, $N^+CH_2CH_3$), 3.10-3.05 (m, 2H, $N^+CH_2CH_2$), 1.78-1.71 (m, 2H, OCH_2CH_2), 1.60-

1.52 (m, 2H, $N^+CH_2CH_2$), 1.47-1.40 (m, 2H, $OCH_2CH_2CH_2$), 1.39-1.25 (m, 10H, CH_2-$(CH_3)_5$-CH_2), 1.06 (t, 9H, J=7.1 Hz, $N^+CH_2CH_3$), 2.3-0.7 (broad, 3H, $CHCH_2$ in backbone).

To calculate the stoichiometric ratio of surfactomesogen and polymer repeat unit, protons at the ortho position to the polymer sulfonate group (broad peak at 7.7-7.2 ppm) were used, except for NC-OnQ/PSS and H-OnQ/PSS where the protons at the meta position (broad peak at 6.8-6.0 ppm) were used instead because the ortho protons suffered from peak overlap. The integration of these protons was compared to that of the following isolated aromatic SM protons: the protons ortho to the nitro group for O_2N-OnQ/PSS (~9.34 ppm), O_2N-N(Et)nQ/PSS (~8.29 ppm) and O_2N-N(Me)nQ/PSS (~8.28 ppm); the protons ortho to the ether links for H_3CO-OnQ/PSS (~7.8 ppm) and H_3C-OnQ/PSS (~7.82 ppm); all protons other than the one at the ortho position to the aniline nitrogen for NC-N(Et)nQ/PSS (~7.9 ppm); the protons meta to the inner oxygen for NC-OnQ/PSS (~ 7.13 ppm) and H-OnQ/PSS (~7.10 ppm).

Elemental Analysis

The peak for S in the CHNS elemental analysis curves was weak and broad, and overlapped a long tail of the peak for H. By taking this into account and applying a uniform baseline and cut-off procedure in the same way as for the standard, as well as by including small amounts of water (indicated in Table 2.S4), the elemental analysis for S and H was generally satisfactory.

Table 2.S4 CHNS elemental analysis of the surfactomesogen/poly(styrene sulfonate) complexes, with the theoretical values adjusted as necessary by adding H_2O.

SM/PSS complex (repeat unit+molar H_2O)	C%		H%		N%		S%	
	Theor.	Found	Theor.	Found	Theor.	Found	Theor.	Found
O_2N-N(Et)10Q/PSS+0.33 H_2O	65.21	64.99	8.01	8.33	10.01	9.77	4.58	5.09
O_2N-N(Et)6Q/PSS+0.33 H_2O	63.43	63.36	7.46	7.68	10.88	10.72	4.98	4.42
O_2N-N(Me)10Q/PSS+0.25 H_2O	64.93	64.83	7.88	8.15	10.23	9.99	4.69	4.39
O_2N-N(Me)6Q/PSS+0.25 H_2O	63.08	62.72	7.30	7.60	11.15	10.82	5.10	4.86
NC-N(Et)10Q/PSS	69.50	69.29	8.23	8.40	10.39	10.12	4.76	4.94
O_2N-O10Q/PSS+1.5 H_2O	62.31	62.30	7.70	7.70	8.07	8.09	4.62	4.38
O_2N-O6Q/PSS+0.25 H_2O	62.47	62.43	6.96	7.11	9.11	9.27	5.21	5.29
NC-O10Q/PSS	68.70	68.61	7.79	8.17	8.66	8.47	4.96	4.66
NC-O6Q/PSS+0.25 H_2O	66.58	66.46	7.20	7.42	9.41	9.42	5.39	5.09
H_3CO-O10Q/PSS+0.25 H_2O	67.70	67.83	8.21	8.49	6.40	6.13	4.89	4.62
H_3CO-O6Q/PSS+0.5 H_2O	65.53	65.39	7.66	7.76	6.95	6.58	5.30	5.39
H_3C-O10Q/PSS+0.33 H_2O	69.23	68.96	8.43	8.71	6.55	6.60	5.00	4.37
H_3C-O6Q/PSS+0.25 H_2O	67.83	67.88	7.85	8.15	7.19	7.18	5.48	5.09
H-O10Q/PSS	69.53	69.27	8.27	8.08	6.76	6.63	5.16	5.17
H-O6Q/PSS	67.93	67.75	7.66	7.73	7.43	7.20	5.67	5.15

Conductivity at End of Dialysis

The conductivity of the complex solution at the end of dialysis was recorded for several of the complexes after pouring the contents of the dialysis bag into a beaker (see Table 2.S5). The measurements were obtained with an inoLab 740 system (WTW Inc.) equipped with TetraCon 325/Pt or 325/C probes and calibrated by 1.00×10^{-2} M KCl before use.

Table 2.S5 Conductivity of the contents of the dialysis bag for selected complexes, following the dialysis time and at the temperature indicated. The appearance of the complex in the solution measured is also noted.

Complex	Dialysis time (days)	Appearance	Temperature (°C)	Conductivity [a] (μS/cm)
O_2N-N(Et)10Q/PSS	4	Precipitate	20.7	1.6
NC-N(Et)10Q/PSS	18	Colloidal solution, some precipitate	18.7	6.0
O_2N-O10Q/PSS	3	Colloidal solution, some precipitate	24.3	3.0
H-O6Q/PSS	6	Colloidal solution, some precipitate	18.9	35.0
H-O10Q/PSS	6	Precipitate	19.0	5.6

[a] In comparison, a conductivity of 0.5 μS/cm (23.1 °C) was measured for freshly deionized water and 0.9 μS/cm (21.9 °C) for the same water after exposure to air for 8 h with gentle stirring.

Study of Effects of Dialysis Time

For one complex, O_2N-O10Q/PSS, various methods were used to track the dialysis procedure, notably NMR (via the N/S ratio) and CHNS elemental analysis (both of which indicate the complex stoichiometry and purity), EDS (which tracks the Na and Br counterions), UV-visible spectroscopy of the water outside the dialysis bag (which detects the chromophore), and conductivity inside and outside the dialysis bag (which measures ion mobility), the latter two being particularly sensitive methods. The different measurements indicated that 3 days of dialysis were sufficient to obtain stoichiometric complexes with elimination of detectable small counterions. No further change within experimental error occurred after longer dialysis times (up to 18 days for some measurements). Only UV absorbance continued to decrease slightly even after several days of dialysis, which can probably be attributed to the slow release of a low molecular weight fraction of complexed chains through the dialysis bag (slight coloration of the water could also be detected by eye). In connection with the UV-visible tracking, the molar absorptivity of O_2N-O10Q in water (λ_{max}=372 nm) was determined to be 2.14×10^4 $L \cdot mol^{-1} \cdot cm^{-1}$.

TGA Data

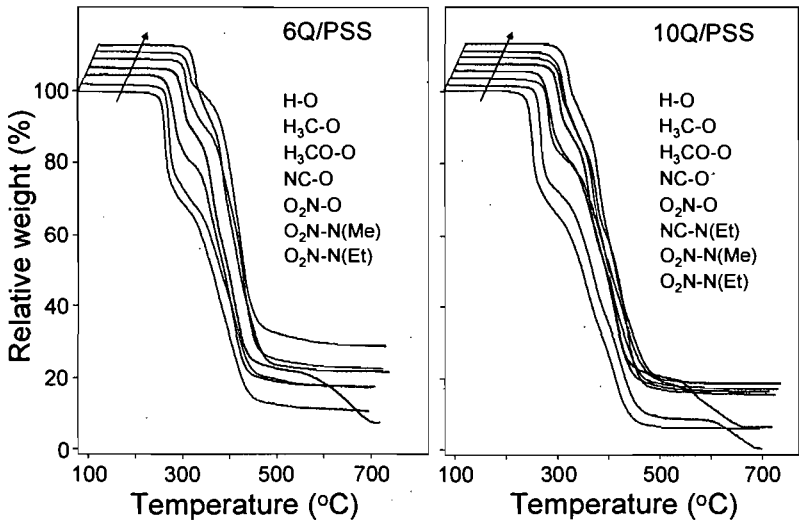

Figure 2.S5 TGA thermograms of the surfactomesogen/poly(styrene sulfonate) complexes. The curves are displaced along the diagonal indicated by the arrow, relative to the curves for O_2N-N(Et)nQ/PSS. They are identified in order from bottom to top as they appear along the arrow.

X-Ray Data for O_2N-O10Q/PSS

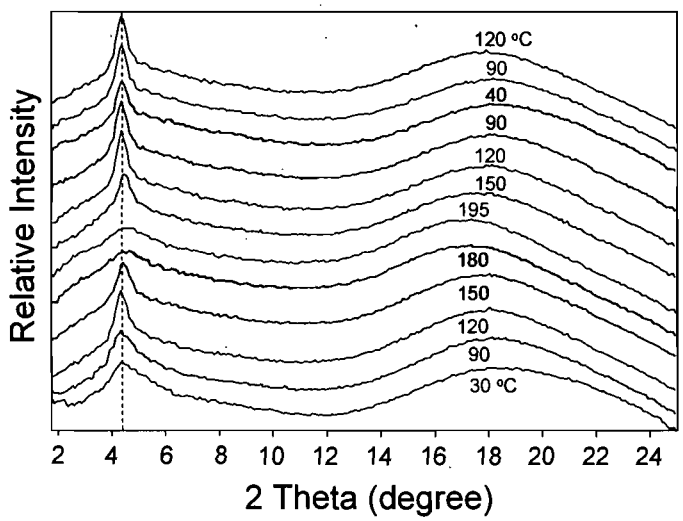

Figure 2.S6 XRD of O_2N-O10Q/PSS at various temperatures, beginning with the as-prepared sample and taken in order from bottom to top. The 40 °C curve is the one shown in Figure 2.3 of the main text.

Chapter 3. Solvent Manipulation of Liquid Crystal Order and Other Properties in Azo-Containing Surfactomesogen/Poly(styrene sulfonate) Complexes

Qian Zhang and C. Geraldine Bazuin*

Centre de recherche sur les matériaux auto-assemblés (CRMAA/CSACS),
Département de chimie, Université de Montréal, C.P. 6128, succursale Centre-Ville,
Montréal (QC), Canada H3C 3J7

Submitted

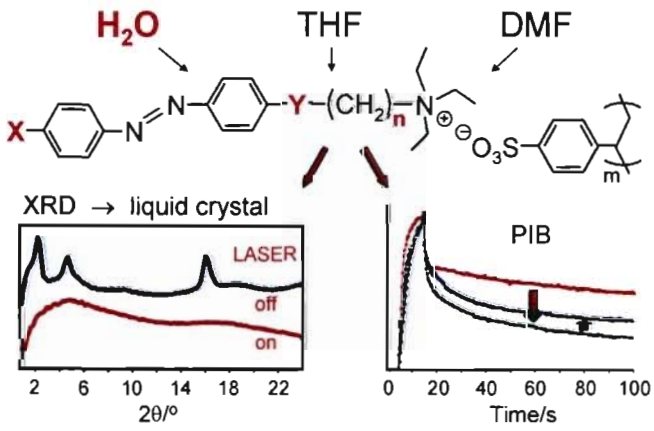

Abstract

Several stoichiometric ionically bonded side-chain polymer complexes, constructed from poly(styrene sulfonate) (PSS) and quaternary ammonium-functionalised azo-containing surfactomesogens (SMs), whose liquid crystalline characteristics in their well-dried form were previously investigated, were exposed to controlled humidity atmosphere, and one of them was exposed to atmospheres of different organic non-solvents (acetone, tetrahydrofuran, ethyl acetate) and one good solvent (dimethyl formamide) for the complex. Exposure to 100% RH atmosphere strongly modifies the molecular packing order of the complexes in a way that appears unique to each complex. Of those already ordered (as SmA) in the dry state, one appears to develop columnar order, whereas another maintains SmA order but with a significant difference in the lamellar electron density profile, upon exposure to 100% RH. Of the complexes that are isotropic in the dry state, humidity induces molecular order, with one showing a unique profile indicative of crystal-like structure, attributed to lamellar in-plane order at the level of the ionic groups. This structure was shown to be amenable to photoinduced isotropisation. The molecular order also appears to influence photoinduced birefringence relaxation in the humidity-exposed samples. Exposure to organic solvents improves the long-range order significantly in several cases, and otherwise modifies mainly the lamellar electron density profile. The latter suggests a method to resolve unanswered questions regarding variations of this profile that have been observed in these complexes and other (ionic) side-chain liquid crystal polymers. The conditions under which frozen-in morphologies may be obtained in dried samples are also discussed in the light of the data obtained for the humidity-exposed complexes.

3.1 Introduction

It is well known that the phase behaviour in thermotropic liquid crystals (LCs), both small molecule and polymeric, is highly sensitive to the presence of solvents and impurities. Ion-containing liquid crystals are especially susceptible to effects of humidity, due to the hygroscopic character of ionic groups. In supramolecular liquid crystals, ionic bonding is often used to bind together two oppositely charged components,[1-6] as an alternative to the very popular hydrogen-bonding interaction.[2-4,7,8] This is the case for the construction of supramolecular side-chain liquid crystal polymers achieved by the ionic complexation of polyelectrolytes with oppositely charged surfactants,[9-13] with surfactomesogens,[1,14-19] or with other ionic molecules such as ionic dyes.[6,20-23] The ionic bond is attractive, in part, for its more robust and thermally stable character compared to the hydrogen bond.[6,24] On the other hand, the materials can remain highly viscous up to elevated temperatures so that equilibrium states, including liquid crystal states, can be difficult to attain, especially when thoroughly dried, as we observed recently for a large series of azo-containing surfactomesogen/poly(styrene sulfonate) (SM/PSS) complexes.[25] Furthermore, the ionic character of the complexes decreases their solubility in conventional low-boiling solvents, making purification and drying a greater challenge..

Given the ubiquitous presence of ambient humidity and the possible traces of other solvents in these kinds of materials, or even the intentional retention of solvent to effect "solvent-annealing" (as used in block copolymer films for obtaining well ordered patterns[26,27]) or for other purposes, it is of interest to turn the problem around and investigate how controlled amounts of water and organic solvents can modify the liquid crystal and other properties in some of the SM/PSS complexes previously investigated in their rigorously dried state.[25] Up to now, this has been investigated to some extent mainly in surfactant/polyelectrolyte complexes (see, for example, refs. 13,28-30).

In this context, we have exposed several of the dry SM/PSS complexes studied previously to controlled humidity atmosphere and one of them to several organic solvent atmospheres, to investigate how the state of order in the complexes is affected, primarily at ambient temperature. The complexes chosen, with their nomenclature, are shown in Scheme 3.1. The O_2N-OnQ/PSS pair and the H_3CO-OnQ/PSS pair compare complexes –

all phenol-type – having two different spacer lengths (n=6 and 10 CH_2 units) as well as a polar (first pair) vs. nonpolar (second pair) SM end group (or tail). O_2N-N(Et)10Q/PSS allows comparison of behaviour in an aniline-type complex with the analogous phenol-type complex (O_2N-O10Q/PSS). All of them were exposed to controlled humidity atmospheres (100 and 58% RH). O_2N-O10Q/PSS was, in addition, exposed to saturated atmospheres of acetone, THF and ethyl acetate (all non-solvents for the complex, like H_2O) as well as to DMF (a solvent for the complex). In addition, taking advantage of the presence of the azo moiety in the surfactomesogens, which endows these materials with photoresponsive character based on reversible trans-cis photoisomerisation,[31] we examined photoinduced birefringence (PIB) behaviour in some of the humidity-exposed complexes and we observed photoinduced isotropisation in one of them.

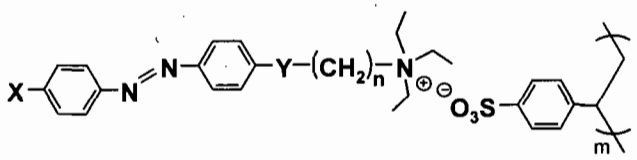

X=NO_2; Y=O; n=6,10	O_2N-OnQ/PSS
X=CH_3O; Y=O; n=6,10	H_3CO-OnQ/PSS
X=NO_2; Y=N(Et); n=10	O_2N-N(Et)10Q/PSS

Scheme 3.1 Surfactomesogen/poly(styrene sulfonate) (SM/PSS) complexes employed, with their nomenclature.

3.2 Experimental

3.2.1 Instrumentation

Polarising optical microscopy (POM) was performed using a Zeiss Axioskop 40Pol microscope coupled with a Linkam Scientific Instrument THMS600 hotstage and a TMS94 temperature controller. Differential scanning calorimetry (DSC) was performed with a TA Instruments Q1000 DSC using a high pressure, hermetic pan. X-ray diffraction (XRD) analysis was performed using a Bruker D8 Discover system equipped with 2D Bruker AXS wire-grid detector, with temperature controlled by a modified Instec HCS410 heating stage and a STC200 temperature controller. Powder samples (unless otherwise mentioned) packed in 1.0-mm diameter glass capillaries (Charles Supper) were irradiated with Cu Kα

radiation (λ=1.542 Å). Bragg spacings, d, were calculated from the diffraction peak positions, 2θ, using the Bragg equation, $\lambda=2d\cdot\sin\theta$. The calculated molecular lengths (l_c) of the repeat units of the complexes were estimated by Hyperchem 7.0, assuming most extended conformations and including van der Waals' radii at the extremities.

3.2.2 Materials

The synthesis of the surfactomesogens and the preparation of the complexes are described in ref. 25. Briefly, the complexes were obtained by dissolution of the two components in DMSO, followed by dialysis in deionised (Milli-Q) water for several days, then freeze-drying, and finally further drying in a vacuum oven at roughly 60 °C for a week. The 1:1 stoichiometry and purity of the complexes was verified by NMR, CHNS elemental analysis and energy dispersive spectrometry (EDS).[25] Sodium bromide (99.0%) and spectrograde DMSO, purchased from Sigma-Aldrich, and acetone and ethyl acetate, purchased from EMD Chemicals, were used as received. DMF and THF, purchased from EMD Chemicals, were passed through drying columns (Glass Contour system) before use. Deionised water was obtained from a Millipore Gradient A10 Milli-Q system (resistivity 18.2 MΩ.cm at 25 °C).

3.2.3 Solvent exposure

The dried complexes were exposed to non-solvents (H_2O, acetone, ethyl acetate, anhydrous THF) using the set-up illustrated in Scheme 3.2a. The bottom of a sealable chamber was covered with the desired solvent. The complex under investigation was put in a vial, the vial was covered with aluminum foil pierced with tiny holes and placed in the chamber, which was then sealed. Pure Milli-Q water was used for 100% RH atmosphere and a $NaBr\cdot 2H_2O$ saturated aqueous solution for 58% RH at 25 °C,[32] double checked with a hygrometer (Traceable, VWR). The complexes were exposed to the desired solvent atmosphere at ambient temperature for 5-7 days to achieve equilibrium saturation. The amount of solvent absorbed after different exposure times was determined gravimetrically. Some complexes (for PIB measurements) were also exposed to ambient humidity, measured as 45±5% RH, in an open container. For comparative purposes, samples exposed to 100% RH were redried for 7-10 days under high vacuum (1-3 mT, using a FTS Systems

FD-3-85A-MP freeze-dryer) at ambient temperature (room temperature was chosen to avoid entering another possible mesophase at higher temperature that might be frozen in during the drying process).

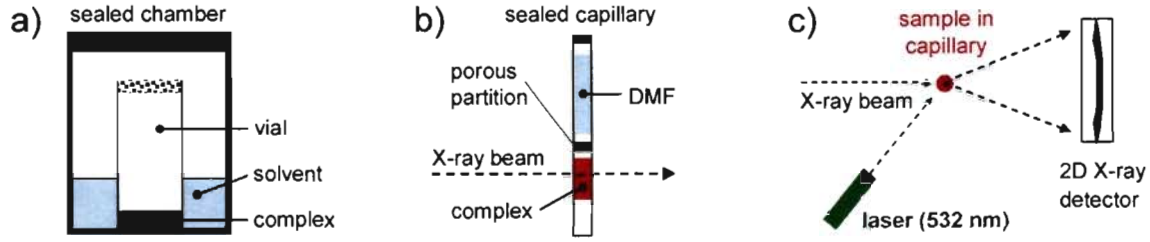

Scheme 3.2 Experimental setups for (a) solvent exposed complexes, (b) in situ XRD tracking of DMF into a sample, and (c) in-situ XRD tracking of photoinduced isotropisation.

Exposure to DMF, a good solvent for the complexes, was achieved using the set-up illustrated in Scheme 3.2b. The complex was first packed in the lower half of a 1.0-mm diameter glass capillary (Charles Supper), a small wad of cotton (VWR) was inserted (leaving a small space to avoid contact with the sample), and DMF was then added to the upper part of the capillary, followed by flame sealing of the capillary. In this setup, only DMF vapour diffuses through the cotton wad, which acts as a porous partition, to saturate the air space below, from which the DMF vapour diffuses into the sample. This diffusion was tracked *in situ* by XRD, as follows. A first diffractogram was taken immediately following preparation of the capillary, before the sample was affected by DMF (labelled 'Original' in Figure 3.7). Then, to accelerate diffusion of DMF vapour into the sample, the capillary was immersed in a 60 °C water bath. As soon as the top edge of the sample was contacted by DMF vapour, which was visually obvious by a small colour change, the capillary was remounted immediately on the sample stage such that the X-ray beam passed through the visually affected part of the sample, and an initial 30-min diffractogram (labelled "Initial contact" in Figure 3.6) was recorded. XRD data collection was then set to automatic mode, where a diffractogram was recorded every 30 min for 14.5 h. The capillary was demounted, and, 4 days later, a final diffractogram was acquired.

3.2.4 Photoinduced isotropisation

Photoinduced isotropisation in O_2N-N(Et)10Q/PSS mixed with excess H_2O was examined by combining XRD with *in situ* laser irradiation, using the set-up illustrated in Scheme 3.2c. In this experiment, the glass capillary was loaded with an H_2O-exposed complex along with a small amount of water. A 532-nm diode laser (B&W TEK; 21 mW) was used to illuminate the capillary from a distance of 30 cm. Several diffractograms, recorded for 15 min each with the laser alternately off or on per diffractogram, were taken sequentially.

3.2.5 Photoinduced birefringence

Photoinduced birefringence in spin-coated films of the nitro-azobenzene complexes, before and after exposure to 100% RH as well as to ambient humidity, was compared by applying a 454-nm Ar ion writing laser at a power of ca. 700 mW/cm^2 using the same setup as in ref. 23. The O_2N-N(Et)10Q/PSS and O_2N-O10Q/PSS films were spin-coated from dichloromethane (6.6 and 11.6 wt % concentration, respectively) and the O_2N-O6Q/PSS film from nitromethane/dichloromethane (0.74/1 w/w, 11.6 wt % concentration), and dried in a vacuum oven at 80 °C for at least one week. The films were estimated to have a thickness of the order of 0.5 μm. The sample chamber was flushed with dry N_2 during the PIB measurements for the dried samples, but not for the humidity-exposed samples. These measurements were all done on the same day.

3.3 Results and discussion

3.3.1 Complexes exposed to H_2O

Although the complexes are insoluble in water, their ion content can lead to absorption of water. The equilibrium absorption in the complexes exposed to 100% relative humidity (RH), measured gravimetrically over a period of two weeks and generally found to be constant within a day, was found to range from 15 to 25 wt %, corresponding to 7 to 10 H_2O molecules per repeat unit. Mechanically, all but one of these complexes are in a plasticised state at ambient temperature. The two phenol-type complexes with a polar

end-group, O_2N-OnQ/PSS, n = 6 and 10, are both soft (deformable) and sticky. In comparison, H_3CO-O10Q/PSS is somewhat less deformable and less sticky, whereas H_3CO-O6Q/PSS is deformable but not sticky (e.g. it slides on glass surfaces), and, interestingly, it flows over time like Silly Putty. The lesser stickiness of the latter two complexes compared to O_2N-OnQ/PSS can be related to the nonpolar end-group, which decreases the overall polarity of the material and which might also be preferentially exposed at the surface. In contrast, the aniline-type complex, O_2N-N(Et)10Q/PSS, remains powder-like at ambient temperature and cannot be made to coalesce by manual pressing until above ca. 120 °C (where it nevertheless remains highly viscous and difficult to spread).

POM observations indicate that the four phenol-type complexes exposed to 100% RH are all distinctly birefringent at ambient temperature, although less for H_3CO-OnQ/PSS, as shown by the representative micrographs in Figure 3.1. No revelatory liquid crystal textures were obtained. Nevertheless, together with the mechanical characteristics, the birefringence implies that these complexes must have some kind of liquid crystal character. O_2N-N(Et)10Q/PSS displays much less birefringence, probably due at least in part to its powder-like form that precludes thin film formation and therefore leads to high absorbance of light.

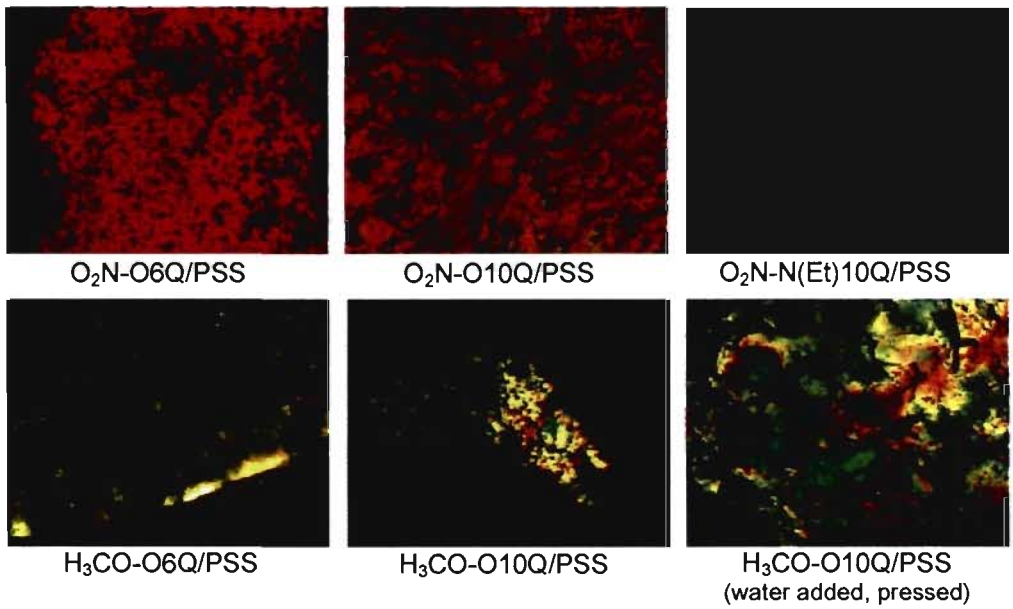

Figure 3.1 POM micrographs of the complexes equilibrated in 100% RH at ambient temperature (except where indicated otherwise).

Ambient temperature X-ray diffractograms of the 100% RH-exposed complexes are shown in Figure 3.2, where they are compared with diffractograms of the same samples redried at room temperature under high vacuum for 7-12 d, with diffractograms of the originally dried samples before exposure to humidity, and, in some cases, with diffractograms of samples exposed to 58% RH or mixed with liquid H_2O.[33] Among the original dried samples, only the O_2N-O10Q/PSS and H_3CO-O10Q/PSS complexes revealed liquid crystal order under normal thermal cycling conditions, assigned as an effectively single-layer SmA mesophase in both cases.[25,33] The same type of order could be observed in O_2N-O6Q/PSS (not shown in Figure 3.2) only after high-temperature annealing for long times; in contrast, no order could be produced in H_3CO-O6Q/PSS or O_2N-N(Et)10Q/PSS by similar annealing.[25] It is relevant for later discussion to specify that the small-angle peak in O_2N-O10Q/PSS has been considered as a second-order diffraction peak, whilst the first-order peak is essentially extinct due to an additional plane of symmetry in the electron density profile across the lamellar period.[18,25]

The X-ray diffractograms indicate the existence of some form of molecular packing order in all of the 100% RH-exposed complexes. Those that are essentially isotropic in the dry state become ordered in the H_2O-exposed state and those that show some order in the dry state undergo a change of order in the H_2O-exposed state, with the type of order depending on the sample. A generality is that all of the H_2O-exposed complexes, except one, conserve the presence of only a halo at wide angles in XRD, indicating the absence of crystallinity. The exception, O_2N-N(Et)10Q/PSS, shows evidence of crystal-type order, indicated by a sharp peak at 16.2° (2θ), and consistent with its solid, powder-like form.

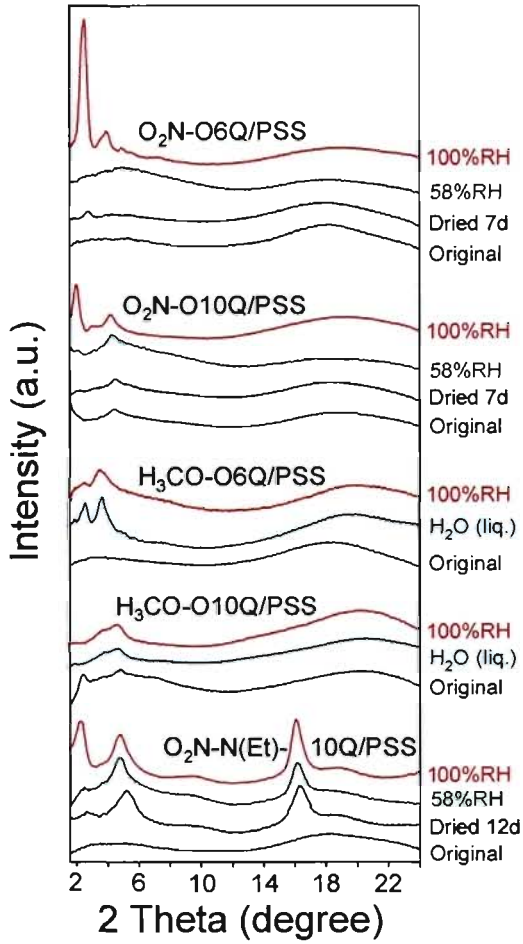

Figure 3.2 XRD diffractograms of SM/PSS complexes exposed to water [58%RH and 100%RH, 58 and 100% relative humidity atmospheres; H_2O (liq.), mixed with liquid water], compared with the original dry samples, and with the 100%RH-exposed samples subsequently redried at ambient temperature for the time (in days) indicated.[33]

The specific case of each sample will be addressed in the order from top to bottom in which they appear in Figure 3.2. The O_2N-O6Q/PSS complex, which shows no long-range order in the original dry state (unless subjected to high-temperature annealing) nor after exposure to 58% RH, develops an intense first-order diffraction peak at small angles, followed by at least two others of decreasing intensity, in the 100% RH-exposed sample, corresponding to Bragg spacings of 36, 22.5 and 18 Å, respectively (there also appears to be a fourth weak peak corresponding to 12 Å). Their reciprocal spacings are in a 1:1.6:2 ratio, which is fairly close to what a columnar phase would give, considering the

uncertainties in the peak values. The birefringence in POM rules out (purely) cubic phases. Another interpretation involves a lamellar structure (giving rise to the peaks with reciprocal spacing ratio 1:2:3:4) having a periodic undulation (giving rise to the 22.5-Å peak), as proposed by Antonietti, Thünemann and coll. for a number of surfactant/polyelectrolyte complexes.[34-36] After drying for a week under high vacuum at ambient temperature, the lowest-angle peak becomes very weak and the other two barely visible, indicating a tendency to return to the essentially isotropic structure of the well-dried sample. In addition, the peaks move to larger angles, corresponding to a difference in Bragg spacing of ca. 4 Å, consistent with contraction as the water evaporates.

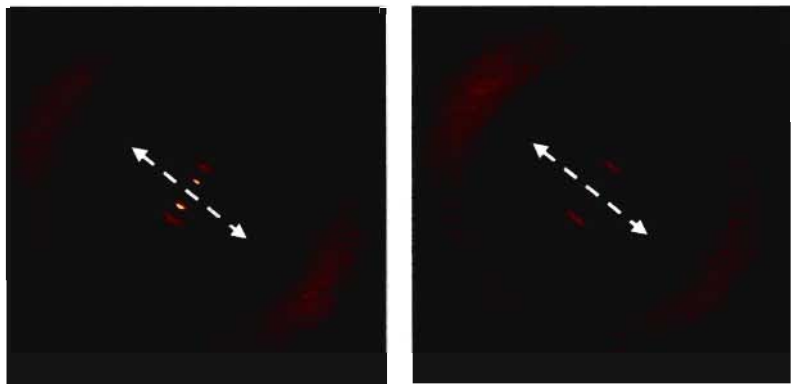

Figure 3.3 X-ray area diffractogram of (left) a sheared O_2N-O10Q/PSS sample previously equilibrated in 100% RH at ambient temperature and (right) the same sample redried at ambient temperature. The shear direction is indicated by the arrow.

The 10Q analogue of this complex, which when dry gives a weak, presumably second-order, small-angle X-ray peak of a single-layer lamellar mesophase with a 40-Å periodicity[25] (with little change in packing after exposure to 58% RH except for a small increase in periodicity by 2-3 Å, consistent with swelling by water), gives an additional peak at lower angles after exposure to 100% RH. This peak is more intense than the higher-angle one and the reciprocal spacings of the two peaks have a 1:2 ratio. (The corresponding Bragg spacing is the same as in the 58% RH-exposed sample.) It therefore seems reasonable to attribute them to the first and second-order peaks of the same lamellar phase as in the dry sample. When dried under vacuum at room temperature for a week, the XRD profile returns to that of the thoroughly dried sample. The 100% RH-exposed sample

was also subjected to manual unidirectional shearing, giving the diffractogram shown in Figure 3.3 (left). This diffractogram is consistent with an orthogonal lamellar mesophase, namely smectic A. After room temperature drying of this oriented sample, the lowest-angle peak disappears, in agreement with the XRD of the unoriented sample, while maintaining the oriented state that indicates an orthogonal mesophase (Figure 3.3, right). This suggests that the location of the H_2O molecules in the packing structure of the complex exposed to 100% RH, presumably primarily in the ionic plane, modifies the electron density profile such that the extinction condition for the first-order peak is lifted. A very weak peak between the two equidistant peaks in the wet sample (observed also in Figure 3.2) might again arise from a periodic ripple in the lamellae.

The XRD profiles of the two H_3CO-OnQ/PSS complexes exposed to 100% RH are relatively weak and broad, indicative of fairly short correlation lengths (consistent with the fairly weak birefringence observed in POM), and the second peak is more intense than the first in both cases. After putting the sample in direct contact with water, these two peaks become better defined (and the birefringence in POM more intense) for n=6, but undergo no significant change for n=10. The peak maxima correspond to Bragg spacings of ca. 34 and 24 Å, respectively, for n=6 and to roughly 25 and 19 Å, respectively, for n=10 (the latter being particularly imprecise given the broadness and overlap of the peaks), thus shorter for n=10 than for n=6. Their reciprocal spacings have a ratio near 1.3-1.4, which is suggestive of a cubic phase, although the observed birefringence in POM would seem to be in disagreement with this. The ill-defined nature of the XRD data, resulting from the poor packing order, does not allow a definitive assignment of the phase(s).

Finally, the profile of O_2N-N(Et)10Q/PSS, which is essentially isotropic when thoroughly dry, is characterised by relatively intense peaks after equilibration in 100% RH atmosphere, including one at 16.2°, indicative of crystal-like order. After drying (12 d), the profile is basically unchanged, except for the quasi-disappearance of the lowest-angle peak, discussed further below. The lowest-angle peak is hardly present either in the sample exposed to 58% RH. In the 100% RH-exposed complex, the two lowest-angle peaks and the much weaker one at 2θ=9-10° have reciprocal spacings of 1:2:4, indicating lamellar packing with a periodicity of ca. 38 Å. The peak at 16.2°, superimposed on the low-angle side of a weak halo, corresponds to a Bragg spacing of 5.46 Å. This peak is most likely

related to in-plane order at the level of the interacting sulfonate-ammonium ionic groups, which have larger diameters than alkyl or azobenzene segments. Ordered lamellar phases where the alkyl chains are disordered whilst the ionic groups self-assemble into two-dimensional sheets parallel to the lamellar planes have been observed regularly in low molecular weight ionic liquid crystals (see, for example, refs. 37-40). The nature of the in-plane order can be deduced when higher order reflections are present, not observed for the present complex (examined up to $2\theta=40^{\circ}$). We obtained a similar wide-angle profile in a SM/PE complex constructed from a sulfonated azo surfactomesogen and methylated poly(4-vinyl pyridine), which also forms a lamellar phase according to the smaller-angle profile.[41]

The fact that several complexes of the series studied previously,[25] including O_2N-O6Q/PSS, were found to reveal LC character only after annealing at high temperature (150 °C for O_2N-O6Q/PSS), where molecular mobility is presumably adequate for reorganisation to occur (albeit slowly due to very high viscosity), implies that these samples initially had frozen-in isotropic morphologies resulting from their preparation conditions. The last solvent with which they had contact was H_2O (during purification by dialysis), followed by drying at moderate temperature. In this context, it is of interest to know to what temperatures the morphologies noted above remain present. This was examined for three of the 100% RH-exposed complexes, keeping in mind that evaporation of H_2O can take place at higher temperature when using unsealed sample containers (glass microscope slides, common DSC capsules, poorly sealed XRD capillaries) and, even with hermetically sealed containers (XRD capillaries, special DSC capsules), the equilibrium state of H_2O in the complex is likely to change with temperature (and may not be reversible when air-space is also present).

For 100% RH-exposed O_2N-O6Q/PSS, the room temperature phase is maintained to ca. 80-90 °C, where isotropisation occurs, according to DSC and XRD, and is reversible as long as the sample is not heated to much higher temperatures. In contrast, 100% RH-exposed O_2N-O10Q/PSS shows no clear DSC transition and remains birefringent up to ca. 170 °C (where weak events appear, but the high temperature involved makes any interpretation unreliable). Interestingly, XRD shows that the lowest-angle diffraction peak decreases in intensity with increasing temperature, and is essentially absent by 90 °C. It

does not return after cooling from 90 °C, which may be a result of H_2O evaporation or H_2O expulsion from the sample due to the changing equilibrium at higher temperature that does not reverse itself since the air around the sample was not maintained at 100% RH. O_2N-O10Q/PSS could be more susceptible to this than O_2N-O6Q/PSS because of its longer alkyl spacer that increases hydrophobic character or because of its greater tendency to LC packing in the dry state. It is consistent that the XRD profiles of both of the 100% RH-exposed complexes at higher temperatures resemble the profiles of the originally dried samples.

The crystal-like XRD pattern of O_2N-N(Et)10Q/PSS is stable to ca. 65 °C, where a quite intense DSC peak (ΔH = 15 J/g) is observed, and is reversible when cycling between 25 and 80 °C. The 80 °C XRD pattern shows no sign of the diffraction peak at 16.2° that is present in the 25 °C pattern, and only shows the second of the two low-angle peaks, but more weakly and at slightly lower angles. Nevertheless, the sample remains powder-like mechanically and only begins to be slightly pressable near 120 °C, where the weak birefringence also disappears completely, indicating isotropisation (it is not reversible, possibly due to the high viscosity, but also most likely due to water evaporation). The mechanical rigidity of the complex can explain why redrying the 100% RH-exposed sample at ambient temperature does not modify the XRD pattern (resulting in a frozen-in structure), whereas the initial sample, dried at a temperature near the DSC transition, above which the XRD profile indicates only residual order (and irreversibly isotropic at 120 °C), shows an isotropic structure. According to previous annealing experiments, the isotropic structure is probably its equilibrium structure in the dry state, which can be related to the steric hindrance to ordered molecular alignment caused by the lateral ethyl substituent.[25]

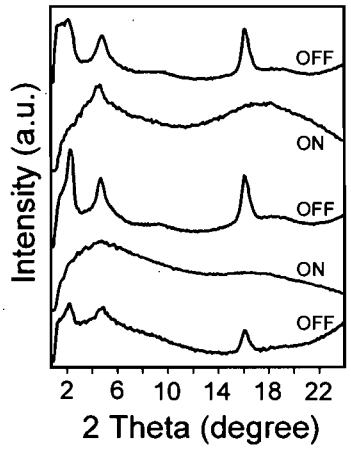

Figure 3.4 X-ray diffractograms illustrating photoinduced isotropisation in O_2N-N(Et)10Q/PSS mixed with water. The diffractograms were taken in situ in the order from top to bottom. OFF and ON refer to the state of the writing laser.

3.3.2 Photoinduced isotropisation in H2O-exposed O2N-N(Et)10Q/PSS

It was found that a photoinduced phase transition, notably photoinduced isotropisation,[31,42,43] can be induced in H_2O-exposed O_2N-N(Et)10Q/PSS. This is shown in Figure 3.4, where the XRD profiles of the complex mixed with water[44] and exposed to two cycles of laser on/laser off are given. Each time the laser is turned on, the diffraction peaks almost disappear [only the peak near 4.8° is still weakly visible the first time the laser is turned on (very similar to the 80 °C pattern mentioned above], and then reappear when the laser is turned off. This phenomenon is explained by the laser irradiation causing trans to cis isomerisation.[31,42,43] The non-linear cis form perturbs the molecular alignment thereby inducing an isotropic phase. When irradiation is arrested, the cis form returns quickly to trans (the lifetime of the cis form of pseudo-stilbene type azo moieties is on the scale of seconds[31,45]), thus restoring the ordered structure (although not completely reversibly when comparing the last cycle with the previous one). This is the first time, to our knowledge, that this phenomenon has been shown for an ionically bonded LC complex, but was observed before in a hydrogen-based supramolecular side-chain copolymer system.[46]

3.3.3 Photoinduced birefringence

Photoinduced birefringence (PIB) in well-dried spin-coated films of the three nitro-azobenzene complexes was compared previously (reproduced in Figure 3.5 for reference).[25] After turning off the writing laser, a significant amount of birefringence relaxation was observed in all three complexes, but more overall for the 10-spacer complexes than for the 6-spacer one, which was attributed mainly to the alkyl spacer in the surfactomesogen.[25,47] In comparing the 10-spacer complexes, it was also noted that the initial fast relaxation was less pronounced in the one with liquid crystal order (O_2N-O10Q/PSS) than in the isotropic one [O_2N-N(Et)10Q/PSS].

The comparative photoinduced birefringence for these same three complexes after exposure to 100% RH atmosphere as well as after exposure to ambient humidity (45±5% RH) is shown in Figure 3.5. For 100% RH exposure, the 6-spacer complex relaxes quickly, with complete disappearance of PIB within ca. 20 s, whereas the other two still show significant PIB at the end of the recording period. This could be related to the effectively higher ion content of the shorter-spacer complex that may allow the absorbed water to have a greater plasticising effect and/or to the differences in their liquid crystal packing structure. Interestingly, O_2N-N(Et)10Q/PSS has the highest PIB, which tends to a plateau value (ca. 35%), at the end of the recording period. This can be related to the fact that this complex, when exposed to 100% RH, is a rigid material with crystal-like structure, whilst the other two complexes are pliable materials under these conditions.

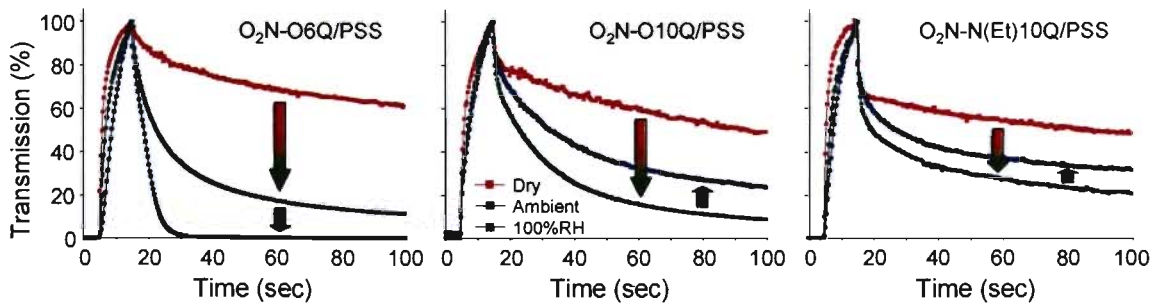

Figure 3.5 Photoinduced birefringence, relative to the maximum achieved at the end of the writing period, of spin-coated films of the complexes indicated, before and after exposure to 100% RH atmosphere.

Equally interesting is the counter-intuitive observation that, for the 10-spacer complexes, the samples exposed to ambient humidity show greater relaxation than the 100% RH-exposed samples (for the 6-spacer complex, by contrast, the relaxation follows the expected sequence of being more pronounced the higher the humidity). This can again be considered to be a consequence of the different liquid crystal structures in the 100% RH-exposed samples compared to those exposed to the much lower ambient humidity. It may be noted, in particular, first, that both 10-spacer complexes exposed to 100% RH have lamellar-type structure whereas the 6-spacer one may be columnar in nature, and, second, that the first-order diffraction peak in the 10-spacer complexes is intense for 100% RH exposure and very weak for 58% RH exposure (see Figure 3.2, keeping in mind that ambient humidity was less than 58%). These intriguing preliminary results should be followed up by a detailed study comparing the LC structure and PIB response of these three complexes exposed to a series of different highly controlled humidity conditions.

3.3.4 Complex exposed to organic solvents

A single complex, O_2N-O10Q/PSS, was exposed to selected organic solvents, notably ethyl acetate (EtAc; dipole moment dm=1.78 D), THF (dm=1.63 D), and acetone (dm=2.91 D), all non-solvents for the complex, as well as DMF dm=3.86 D), a good solvent for the complex. For the non-solvents, equilibrium absorption was achieved within 1-3 days (determined gravimetrically as 21, 30 and 13%, or 2, 4 and 1.7 molecules per repeat unit, for EtAc, THF and acetone, respectively; however, there is significant uncertainty due to solvent evaporation during measurement). Mechanically, the samples exposed to THF and acetone became sticky and deformable, whereas the one exposed to ethyl acetate changed little compared to the dry sample.

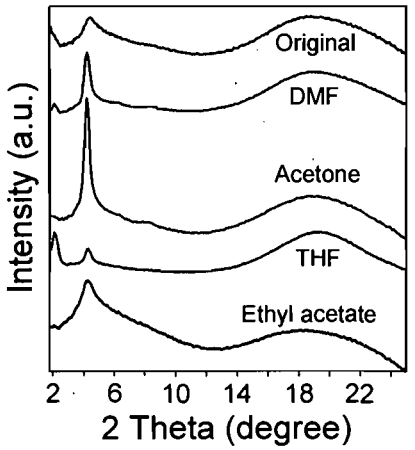

Figure 3.6 X-ray diffractograms of O_2N-O10Q/PSS exposed to selected organic solvents, all at ambient temperature: exposure time for DMF, 30 min total ('initial contact' in Figure 3.7); acetone, 7 d; THF, 5 d; ethyl acetate, 5 d. 'Original' indicates the dried sample before solvent exposure.

The ambient temperature X-ray diffractograms of O_2N-O10Q/PSS exposed to the various solvents are shown in Figure 3.6. In no case is any crystallinity induced, as indicated by the wide-angle region showing only a broad halo. At smaller angles, the dry complex, as described above, shows a single, relatively broad (presumably second-order) peak corresponding to a Bragg spacing of 20 Å. This peak remains present for all four solvent-exposed samples, with at most a slight increase in the Bragg spacing, measured as 20-21 Å. Exposure to DMF and especially to acetone narrows this peak and increases its intensity considerably, indicating significantly improved long-range order ("solvent-annealing"). Very weak higher order peaks also become apparent, in particular one at half the Bragg spacing of the intense peak. The DMF-exposed sample shows, in addition, a weak peak corresponding to a Bragg spacing of 42 Å, along with a third one corresponding to 14 Å (very slight hints of these two peaks also seem present for the acetone-exposed sample). The reciprocal spacings of these peaks are in a 1:2:3:4 ratio, confirming lamellar periodicity. For the THF-exposed sample, the 21-Å peak is much reduced in intensity and the 42-Å peak increased in intensity such that the latter is the more intense of the two small-angle peaks present, indicating a change in the electron density profile. The diffractogram of the ethyl acetate-exposed sample is similar to that of the original dry sample.

Since DMF is a solvent for the complex, it is of interest to track the effect of this solvent on the packing structure *in situ* during increasing solvent absorption. A representative selection of the diffractograms obtained during this process is shown in Figure 3.7 (left). The intensity and corresponding Bragg spacing of the most intense small-angle diffraction peak are plotted as a function of time in Figure 3.7 (right). Following the initial improvement in long-range order and increase in Bragg spacing (19.6 Å in the original sample shown), the intensity and position of the peak are approximately constant during the first 2-3 h, then both gradually decrease accompanied by a gradual increase in peak width (the intensity decreases throughout the 15-h recording period, whereas the Bragg spacing becomes constant after ca. 10 h). Four days later, the peak is much weaker and broader than even in the dry sample (but little changed in position). This evolution indicates that DMF initially intersperses itself within the LC structure to permit more efficient and long-range packing. Then, as DMF continues to diffuse into the sample, the smectic packing gradually deteriorates, which can be visualised as a gradual breakup of the originally large smectic domains into ever smaller ones. If any residual smectic packing remains 4 d later, it is short-range, and, clearly, there is no lyotropic liquid crystal phase at the concentration involved. A possible reason for the concomitant slight decrease in lamellar periodicity is that the gradual breakup of the lamellae induces somewhat greater disorder among the alkyl chains in SmA-type packing, as occurs upon exposure to increasing temperature. When this sample is redried at 60-80 °C for 10 d, the 20-A peak is restored, no doubt due to the reversibility of the packing structure as DMF is removed.

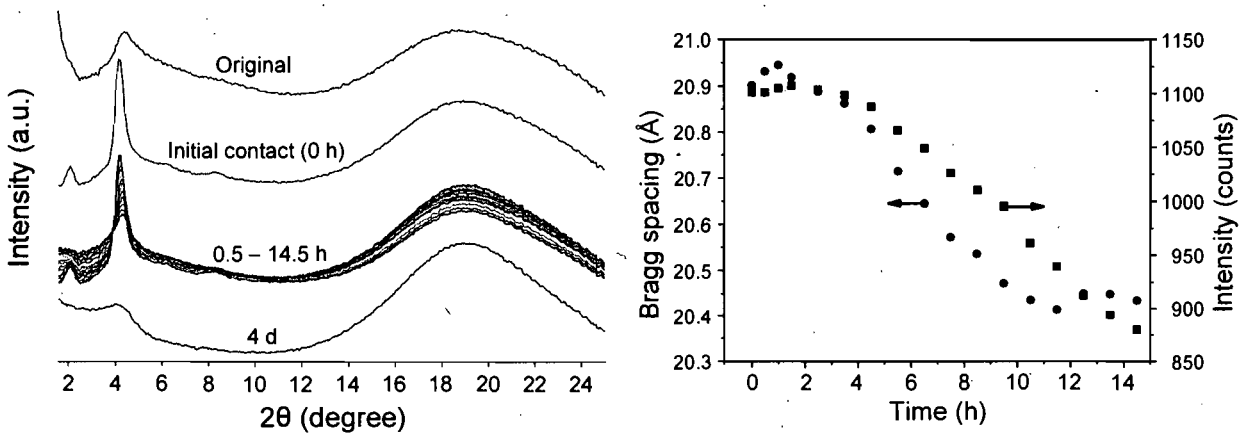

Figure 3.7 Left: XRD diffractograms of the O_2N-O10Q/PSS complex exposed to DMF vapour for various times, compared with the initially dried sample ('Original'). Right: Variation of the Bragg spacing and intensity of the most intense (second-order) small-angle peak as a function of time of exposure to DMF (times given are for the beginning of the 30-min recording period for each diffractogram; data from every other diffractogram only are shown after the first four points).

3.3.5 Discussion

In most cases, exposure of the SM/PSS complexes to H_2O and organic solvents modifies, sometimes strongly, their molecular packing and consequent liquid crystal order. H_2O may be expected to solvate the ionic groups in these complexes, such that it is the hydrophobic parts that prevent dissolution of the complexes by this solvent. The probable concentration of H_2O molecules in the vicinity of the ionic groups causes a volume expansion around these moieties. Possibly, a smaller fraction of H_2O molecules is adsorbed in the region of the polar NO_2 tail. For O_2N-O6Q/PSS, the final result appears to allow a columnar-type or undulated lamellar molecular packing structure. The longer alkyl chain in O_2N-O10Q/PSS may maintain the volume fractions of the immiscible sub-regions in the range where the structure remains simply lamellar. The much less polar azo group in the H_3CO-OnQ/PSS complexes probably minimises H_2O absorption anywhere but around the ionic groups. The resulting swelling of this subplane appears to perturb ordered packing in the 100% RH-exposed sample, although this packing might tend to have a cubic component. [Greater absorption of H_2O improves the order for n=6.] On the other hand, H_2O absorption in O_2N-N(Et)10Q/PSS exposed to 100% RH clearly allows for greater packing order, particularly in-plane order, making it a more solid (crystal-like) material.

The azo mesogenic core in this case is highly polar (dipole moment: 10.0 D[25]), and H_2O may be distributed around the ionic groups and mesogen core in such a way as to allow for in-plane order at the level of the ionic groups, not observed in any of the other complexes in the series investigated either in dry form[25] or when exposed to solvent. The interplay of volume fractions of immiscible moieties (along with other factors) and resulting LC structure was discussed also in relation to the simpler surfactant-polyelectrolyte complexes.[48]

The organic non-solvents for the complexes are insufficiently polar to solvate the ionic groups, which are probably largely responsible for holding the complexes together when exposed to those solvents. Although it is difficult to know if these solvents absorb preferentially in particular sub-regions of the complex structure, they clearly have distinctive effects on the packing details. The overall packing into effectively single-layer smectic A structure appears to remain intact, however. This is true also for absorption of small amounts of DMF, which is more polar and which is the only solvent that can actually solubilise the complexes.

We previously discussed possible packing models for the complexes in their dry form, in particular to try to rationalise the apparent extinction of the first-order diffraction peak in the complexes with polar tails, like the present O_2N-O10Q/PSS.[25] Usually, extinction of the first-order peak is attributed to an additional plane of symmetry in the electron density profile, as mentioned above. We proposed, for the complexes with polar tails, that another possible explanation is that the ionic groups and polar tails may be located in the same subplane, which effectively halves the expected lamellar thickness.[25] In this context, DMF (in small amounts) and especially acetone strongly accentuate the (almost) exclusive appearance of the "second-order" peak, whereas THF promotes the appearance of the first-order peak. The difference between acetone and DMF on the one hand and THF on the other may be related to a difference in their preferential absorption sites, which can change the electron density profile normal to the lamellar plane, or they may modify differently the subplane distribution of the polar and ionic groups. Regarding the latter, it may be speculated that the more polar DMF and acetone molecules (noting that DMF also has an ionic resonance form) may facilitate dipolar interactions with and among the ion pairs and polar tails, thus promoting their co-existence in the same subplanes.

Although the present data do not allow an evaluation or further development of the models discussed in ref. 25 (and which are therefore not reproduced and further discussed in the present paper), they suggest that the O_2N-O10Q/PSS complex exposed to THF and to acetone may be an ideal system to investigate further in order to resolve the uncertainty regarding the detailed packing structure. In particular, these solvents may be used in deuterated form, and possibly allow useful small-angle neutron scattering investigations of these complexes, which may moreover be oriented more easily when plasticised by solvents than is possible with the intractable dry samples. Similarly, the use of deuterated H_2O in conjunction with SANS may allow better precision of the molecular packing in the H_2O-plasticised complexes.

Finally, the presence of the azo chromophoric moiety allows these materials to be manipulated by light. Modification of their properties and structure by solvent is a relatively straightforward way to also modify and fine-tune their photonic behaviour. Thus, photoisotropisation of an H_2O-induced crystal-like phase was demonstrated. In addition, preliminary data of photoinduced birefringence in H_2O-exposed complexes suggests that, while plasticisation may affect PIB relaxation in proportion to the water content as expected, induced changes to the liquid crystal order can make the PIB response much more complex, which may be of much interest to investigate in greater depth in a dedicated future study.

3.4 Conclusions

The investigations undertaken have shown that exposure of azo-containing surfactomesogen/polyelectrolyte complexes to different humidity atmospheres can change their properties (mechanical, photoinduced birefringence) and molecular packing structure drastically, but in ways that are specific to each type of complex. This can be related, in part, to preferential solvation of the ionic groups that change the relative volumes of the nanophase-separated moieties, thereby modifying their packing space requirements. Most of the complexes are highly plasticised by humidity, but one complex develops instead a crystal-like packing, attributed to in-plane order at the level of the ionic groups. This order was shown, moreover, to be susceptible to photoisotropisation. Exposure to organic

solvent atmospheres appears to affect mainly the electron density profile normal to the lamellar planes, while also permitting improved long-range order. Thus, the properties of the complexes can be modified, even exploited, by solvent manipulation (or solvent annealing), particularly under conditions where desired solvent-induced properties can be frozen into dried samples. In addition, it is proposed that solvent effects may be used to understand the nature of molecular packing in more detail (e.g. using deuterated solvents in conjunction with SANS experiments) as well as the influence of packing order on photoinduced birefringence behaviour.

3.5 Acknowledgements

The financial support of NSERC Canada and FQRNT Québec is gratefully acknowledged. QZ thanks Université de Montréal for a final year graduate scholarship. Prof. Christopher J. Barrett (Chemistry Dept., McGill University, Montreal) is thanked for making his laboratory available for the photoinduced birefringence experiments and for lending the laser used for the photoinduced isotropisation experiment.

3.6 References and notes

1. P. Masson and D. Guillon. *Mol. Cryst. Liq. Cryst.* 2001, **362**, 313-346.
2. C. T. Imrie. *Trends Polym. Sci.* 1995, **3**, 22-29.
3. C. G. Bazuin, in *Mechanical and Thermophysical Properties of Polymer Liquid Crystals*, ed. W. Brostow, Chapman and Hall, London, 1998, ch. 3, pp. 59-100.
4. J. M. Pollino and M. Weck. *Chem. Soc. Rev.* 2005, **34**, 193-207.
5. K. Binnemans. *Chem. Rev.* 2005, **105**, 4148-4204.
6. C. F. J. Faul and M. Antonietti. *Adv. Mater.* 2003, **15**, 673-683.
7. T. Kato. *Struct. Bonding* 2000, **96**, 95-146. T. Kato, N. Mizoshita and K. Kishimoto. *Angew. Chem., Int. Ed.* 2006, **45**, 38-68.
8. C. M. Paleos and D. Tsiourvas. *Liq. Cryst.* 2001, **28**, 1127-1161.
9. W. J. MacKnight, E. A. Ponomarenko and D. A. Tirrell. *Acc. Chem. Res.* 1998, **31**, 781-788.
10. M. Antonietti and A. Thünemann. *Curr. Opin. Colloid Interface Sci.* 1996, **1**, 667-671.
11. S. Zhou and B. Chu. *Adv. Mater.* 2000, **12**, 545-556.
12. D. Tsiourvas, C. M. Paleos and A. Skoulios. *Macromolecules* 1999, **32**, 8059-8065.
13. C. K. Ober and G. Wegner. *Adv. Mater.* 1997, **9**, 17-31.

14. S. Ujiie and K. Iimura. *Macromolecules* 1992, **25**, 3174-3178.
15. C. G. Bazuin and A. Tork. *Macromolecules* 1995, **28**, 8877-8880. F. A. Brandys, P. Masson, D. Guillon and C. G. Bazuin. *Macromol. Chem. Phys.* 2001, **202**, 856-865. A. Tork and C. G. Bazuin. *Macromolecules* 2001, **34**, 7699-7706. C. G. Bazuin, J. Boivin, A. Tork, H. Tremblay and E. Bravo-Grimaldo. *Macromolecules* 2002, **35**, 6893-6899.
16. R. V. Tal'roze, S. A. Kuptsov, T. I. Sycheva, V. S. Bezborodov and N. A. Platé. *Macromolecules* 1995, **28**, 8689-8691.
17. J.-F. Gohy, S. Antoun, R. Sobry, G. Van den Bossche and R. Jérôme. *Macromol. Chem. Phys.* 2000, **201**, 31-41.
18. C. M. Tibirna and C. G. Bazuin. *J. Polym. Sci., Part B: Polym. Phys.* 2005, **43**, 3421-3431.
19. A. F. Thünemann, D. Ruppelt, S. Ito and K. Mullen. *J. Mater. Chem.* 1999, **9**, 1055-1057.
20. A. Priimagi, S. Cattaneo, R. H. A. Ras, S. Valkama, O. Ikkala and M. Kauranen. *Chem. Mater.* 2005, **17**, 5798-5802.
21. S. Xiao, X. Lu and Q. Lu. *Macromolecules* 2007, **40**, 7944-7950.
22. X. Pan, S. Xiao, C. Wang, P. Cai, X. Lu and Q. Lu. *Opt. Commun.* 2009, **282**, 763-768.
23. Q. Zhang, C. G. Bazuin and C. J. Barrett. *Chem. Mater.* 2008, **20**, 29-31.
24. Y. Zakrevskyy, J. Stumpe and C. F. J. Faul. *Adv. Mater.* 2006, **18**, 2133-2136. Y. Guan, M. Antonietti and C. F. J. Faul. *Langmuir* 2002, **18**, 5939-5945.
25. Q. Zhang and C. G. Bazuin. *Macromolecules* 2009, **42**, 4775-4786.
26. K. Fukunaga, H. Elbs, R. Magerle and G. Krausch. *Macromolecules* 2000, **33**, 947-953. K. Fukunaga, T. Hashimoto, H. Elbs and G. Krausch. *Macromolecules* 2002, **35**, 4406-4413.
27. S. H. Kim, M. J. Misner, T. Xu, M. Kimura and T. P. Russell. *Adv. Mater.* 2004, **16**, 226-231. S. Park, B. Kim, J.-Y. Wang and T. P. Russell. *Adv. Mater.* 2008, **20**, 681-685.
28. M. Antonietti and M. Maskos. *Macromolecules* 1996, **29**, 4199-4205.
29. A. F. Thünemann and K. H. Lochhaas. *Langmuir* 1999, **15**, 4867-4874.
30. S. Zhou, H. Hu, C. Burger and B. Chu. *Macromolecules* 2001, **34**, 1772-1778.
31. A. Natansohn and P. Rochon. *Chem. Rev.* 2002, **102**, 4139-4175.
32. D. R. Lide, *CRC Handbook of Chemistry and Physics*. Taylor & Francis, New York, 86th edn., 2006.
33. It should be specified that the signal at angles lower than those shown in Figure 3.2 simply decreases in value in most cases, with a drastic decrease due to the beamstop occurring below ca. $2\theta=1.5^{\circ}$. Only the originally dried samples often show a strong small-angle upturn, which disappears on heating above the glass transition temperature and which we believe is a result of sample porosity that gives rise to a kind of correlation hole effect. For H_3CO-O10Q/PSS, the liquid crystal order shown by Figure 3.2 actually appears only after heating above the Tg during a normal heating cycle. For O_2N-O10Q/PSS under the same conditions, the small-angle peak, as shown in Figure 3.2, simply becomes better defined.
34. M. Antonietti, J. Conrad and A. Thünemann. *Macromolecules* 1994, **27**, 6007-6011.
35. A. F. Thünemann. *Prog. Polym. Sci.* 2002, **27**, 1473–1572.

36. M. Antonietti, A. Wenzel and A. Thünemann. *Langmuir* 1996, **12**, 2111-2114.
37. F. Mathevet, P. Masson, J.-F. Nicoud and A. Skoulios. *J. Am. Chem. Soc.* 2005, **127**, 9053-9061. F. Mathevet, P. Masson, J.-F. Nicoud and A. Skoulios. *Chem.--Eur. J.* 2002, **8**, 2248-2254. F. Tittarelli, P. Masson and A. Skoulios. *Liq. Cryst.* 1997, **22**, 721-726. E. Alami, H. Levy, R. Zana, P. Weber and A. Skoulios. *Liq. Cryst.* 1993, **13**, 201-212.
38. A. Nikokavoura, D. Tsiourvas, M. Arkas, Z. Sideratou and C. M. Paleos. *Liq. Cryst.* 2002, **29**, 1547-1553.
39. K. Ohta, T. Sugiyama and T. Nogami. *J. Mater. Chem.* 2000, **10**, 613-616.
40. C. G. Bazuin, D. Guillon, A. Skoulios and R. Zana. *J. Physique (Paris)* 1986, **47**, 927-930.
41. X. Sallenave, M. Kryuchkov and C. G. Bazuin. unpublished work.
42. T. Ikeda, S. Horiuchi, D. B. Karanjit, S. Kurihara and S. Tazuke. *Macromolecules* 1990, **23**, 42-48.
43. T. Ikeda and O. Tsutsumi. *Science* 1995, **268**, 1873-1875.
44. The complex was mixed with water in order to "dilute" it for sufficient penetration of the laser light.
45. H. Rau, *In Photochemistry and Photophysics*. CRC Press, Boca Raton, FL., 1990; Vol. 2, p 119.
46. T. Kato, N. Hirota, A. Fujishima and J. M. J. Fréchet. *J. Polym. Sci., Part A: Polym. Chem.* 1996, **34**, 57-62.
47. Q. Zhang, X. Wang, C. J. Barrett and C. G. Bazuin. *Chem. Mater.*, **2009,** 21, 3216-3227.
48. M. Antonietti, C. Burger, J. Conrad and A. Kaul. *Macromol. Symp.* 1996, **106**, 1-8.

Chapter 4. Simple Spacer-Free Dye-Polyelectrolyte Ionic Complex: Side-Chain Liquid Crystal Order with High and Stable Photoinduced Birefringence

Qian Zhang, C. Geraldine Bazuin*[1], and Christopher J. Barrett[2]

Centre de recherche sur les matériaux auto-assemblés (CRMAA/CSACS)

[1]Département de chimie, Université de Montréal, C. P. 6128, succ. Centre-ville, Montréal (QC), Canada H3C 3J7

[2] Department of Chemistry, McGill University, 801 Sherbrooke St. W., Montréal (QC), Canada H3A 2K6

Communication to *Chem. Mater.* **2008**, 20, 29-31.

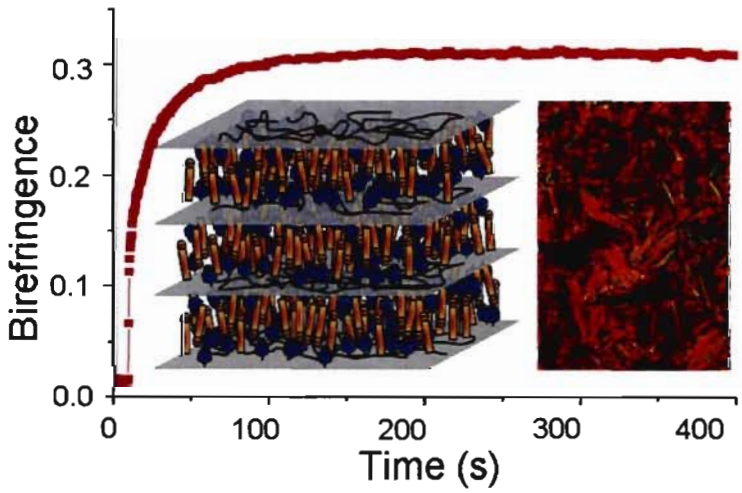

Abstract

A supramolecular ionic complex of methyl orange and methylated poly(4-vinyl pyridine) in equimolar proportions, prepared by ion-exchange procedures, is shown to be structurally organized like a smectic A side-chain liquid crystal polymer (SCLCP) from ambient to degradation (above 230 °C). This is the first report of an ionically complexed SCLCP-like material that is free of both flexible spacers and tails. Furthermore, this complex, easily obtained from readily available components, is shown to provide exceptionally high and, even more importantly, temporally stable and erasable photoinduced birefringence, even at 180 °C. This material is thus competitive, if not superior, in this respect to the best previously reported azo polymers, both amorphous and liquid crystalline. Surface relief gratings can also be inscribed.

4.1 Communication

Azo-containing polymer materials are of immense interest for their potential in various optical and opto-electronic applications, and a host of them have been synthesized and investigated.[1] One of the simplest and least expensive means to obtain such materials is by mixing available azo dyes in common polymers.[1,2] To achieve high loading of the dye molecules without phase separation, as is essential for many applications, recourse is made to strong noncovalent[1e,3] or synthetically more onerous covalent[1a-d] bonding of the dye to the polymer. The former has the advantage that the materials are relatively easily assembled from readily available components;[3,4] e.g., the ionic complex formed from poly(styrene sulfonic acid) and Disperse Red 1 (DR1) via proton transfer.[3a] This dye, like many others, is rod-shaped. Thus, such motifs are also used as calamitic rigid cores in thermotropic side-chain liquid crystal polymers (SCLCP's).[1,2] Here, we will show that a similar dye/polyelectrolyte ionic complex (1) has liquid crystal (LC) smectic A (SmA) order, despite the absence of flexible spacer and tail; and (2) exhibits high photoinduced birefringence (PIB) that is both temporally and thermally stable.

A side-chain flexible spacer is commonly present in thermotropic SCLCP's, following its pioneering introduction by Finkelmann and coll.[5] It serves to decouple antagonistic tendencies of the polymer backbone and the mesogenic moiety sufficiently to allow LC order to appear.[5,6] However, the first SCLCP's reported in the literature, and occasional later ones, incorporated neither a flexible spacer nor a flexible tail.[7-11] A notable example is poly(4-biphenyl acrylate) (PBA),[9] the first SCLCP with an equilibrium mesophase to have been discovered; the structural model proposed corresponds to what we now identify as a bilayer SmA mesophase. Thermotropic LC's of low molar mass also generally possess one or more flexible moieties in addition to a rigid core. But recent work[12] including revival of very old work[12c,13] has emphasized that rigid molecules free of flexible chains can be liquid crystalline. The present contribution will show that *ionically complexed* side-chain polymers free of flexible spacer and tail can likewise generate liquid crystal order.

Such complexes are part of a large class of *supramolecular* SCLCP's investigated over the past decade and more, based mainly on hydrogen or ionic bonding of small-molecule "side chains" or amphiphiles (including with azo moieties) to polymers.[14] Almost all such materials to date incorporate a flexible spacer between the polymer backbone and

mesogenic core, or otherwise only a flexible side chain (as in polyelectrolyte-surfactant complexes[15]). One exception is an H-bonded complex of phenol derivatives (e.g., 4'-methoxy-4-hydroxyazobenzene) with a random copolymer of 4-vinyl pyridine and butyl acrylate, reported to be nematic.[16] However, the use of a copolymer with a flexible co-unit and the thermal lability of the H-bond make this system less rigid than what can be expected from equimolar ionic complexation to a homopolymer.[17]

Specifically, we study the ionic complex, obtained by ion-exchange procedures,[18] of methyl orange (MO) – a commercially available azo-containing rod-shaped dye possessing a terminal anionic group, no flexible spacer and a short bulky tail – to methylated poly(4-vinyl pyridine) (P4VPMe) (Figure 4.1), P4VP also being commercially available and easily quaternized. Energy dispersive analysis indicated the absence of Na and I ions; NMR in DMSO-d_6 and elemental analysis indicated 100% complexation.[18]

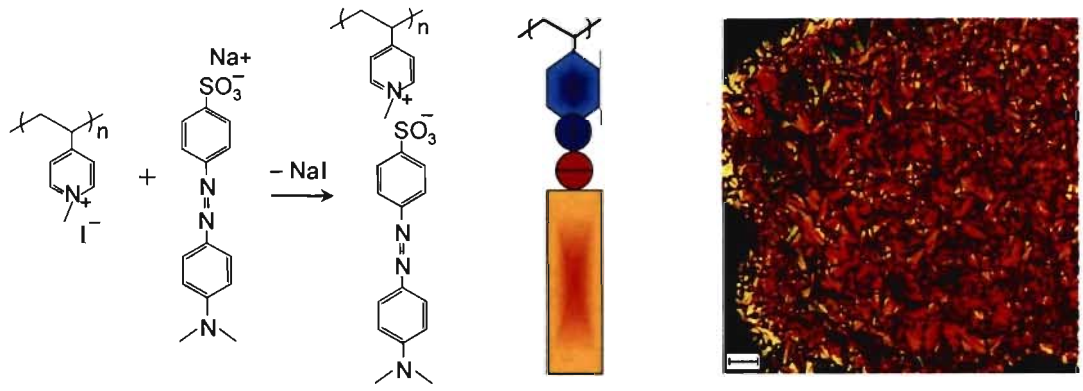

Figure 4.1 Left, "synthesis" of the supramolecular ionic complex of methylated P4VP (P4VPMe) and methyl orange (MO). Center, schema-tic representation of the complex. Right, polarizing optical micrograph of a solution-cast film of the MO/P4VPMe complex (scale bar: 2 μm).

The dried MO/P4VPMe complex is essentially intractable up to high temperature, becoming liquid-like with almost simultaneous onset of degradation at ca. 240 °C according to thermogravimetric analysis and differential scanning calorimetry (DSC).[18] In polarized optical microscopy (POM), the initially opaque powder momentarily shows strong birefringence as it liquefies, suggesting anisotropy before degradation (after which it is permanently isotropic). These properties resemble what was described for PBA, except that the latter has a reversible SmA-isotropic transition near 270 °C.[9] To obtain an

identifiable POM texture, a thin film was prepared by solvent casting from DMF.[18] As shown in Figure 4.1, this provides a well-defined focal-conic and fan-shaped texture, stable up to degradation, that is typical for LC order like SmA.

X-ray diffraction (XRD) provides direct information on the molecular packing structure (Figure 4.2). The ambient-temperature diffractogram of the complex shows, at wide angles, a broad halo and, at low angles, a sharp first-order reflection, for a Bragg spacing of 24.2 Å, accompanied by a much weaker reflection corresponding to 12.1 Å. The 2:1 ratio suggests lamellar order with a periodicity comparable to a single molecular length of the MO/4VPMe repeat unit. This data is consistent with a single-layer or a fully interdigitated bilayer SmA structure. The XRD pattern, and hence molecular packing, is invariant up to degradation.

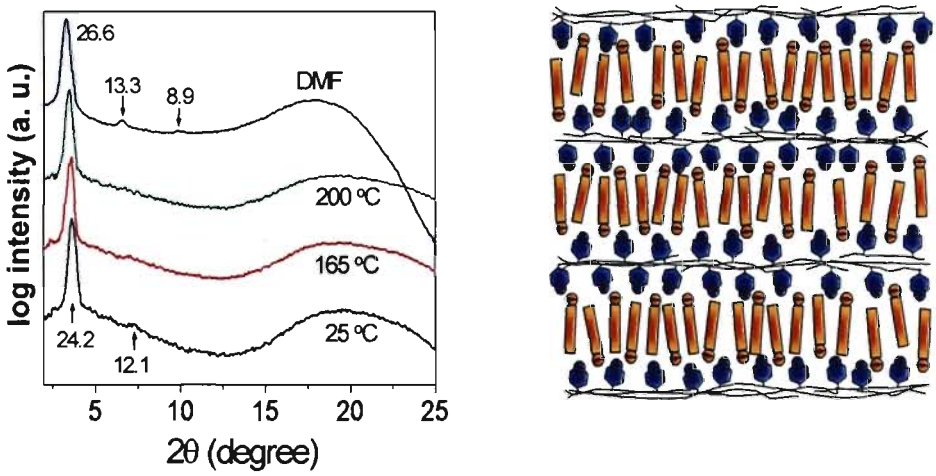

Figure 4.2 Left, X-ray diffractograms of the MO/P4VPMe complex at the temperatures indicated, and at room temperature in concentrated DMF solution (ca. 60 wt %), with Bragg spacings given in Å. Right, possible molecular packing model for the MO/P4VPMe complex.

The SmA structure is indirectly confirmed by the XRD of a DMF solution of the complex (ca. 60 wt %), where a third diffraction order is visible (Figure 4.2). The somewhat larger lamellar thickness (26.6 Å) compared to the dried sample is consistent with swelling by DMF. It may be argued that the LC structure in the dried film is non-equilibrium, frozen in from the lyotropic state. Because of quasi-simultaneous

isotropization and degradation, this cannot be ruled out; however, the similarity in molecular architecture and properties to PBA, which is a thermotropic LC, argues for the present complex having an equilibrium LC structure. Surfactant/polyelectrolyte complexes involving sulfonate groups also typically exhibit LC order up to degradation.[15]

A structural packing model for the complex mesophase is illustrated in Figure 4.2. The fully interdigitated bilayer structure, with laterally alternating oppositely charged ionic groups, permits efficient packing of the MO molecules while accommodating the complexed polymer backbones that meander two-dimensionally between the MO subplanes. Since MO itself is crystalline up to degradation, the disordered LC state of the complex mesophase must be attributed to the constraints on the MO packing imposed by the 4VPMe counterions combined with their (atactic) polymer chain connectivity.

Photoinduced birefringence (PIB) curves of a spin-coated MO/P4VPMe film in N2 atmosphere[18] are shown in Figure 4.3. Application of a 488-nm Ar writing laser (1 W/cm^2 power) for 10 s at room temperature gives a PIB value of about 0.18.[18,19] The saturation value was determined to be 0.31.[18] After removal of the 10-s excitation, there is very little thermal relaxation (about 5%, mainly within the first 10 s). The curves obtained at 70 (not shown) and 100 °C are essentially identical, giving enhanced PIB values that approach 0.20 after 10 s of writing; relaxation after cessation of writing reaches the same plateau value of 0.17 as at room temperature. At 150 °C, the 10-s PIB still approaches 0.20, but after removal of the laser there is noticeably more relaxation that, however, stabilizes at above 0.15. It is only at 180 °C that a decrease in the 10-s PIB is observed, followed by relaxation over the entire 30-s off period; nevertheless, the end PIB value remains quite high at 0.12. These observations are reversible on cooling, as illustrated in Figure 4.3 by the curve obtained at 30 °C. In addition, at all temperatures the PIB can be completely removed by optical erasure within a few seconds. The sequence of write-erase cycles shown in Figure 4.3 indicates excellent reproducibility with no degradation of signal. The above performance may be attributed to the absence of flexible components combined with the ionic character of the complex, giving a quite rigid (and therefore high Tg) material, as well as to the high dye content and possibly the LC order.[1a] It is also worth mentioning that it is possible to inscribe a surface relief grating (SRG) on a film of this complex.[18]

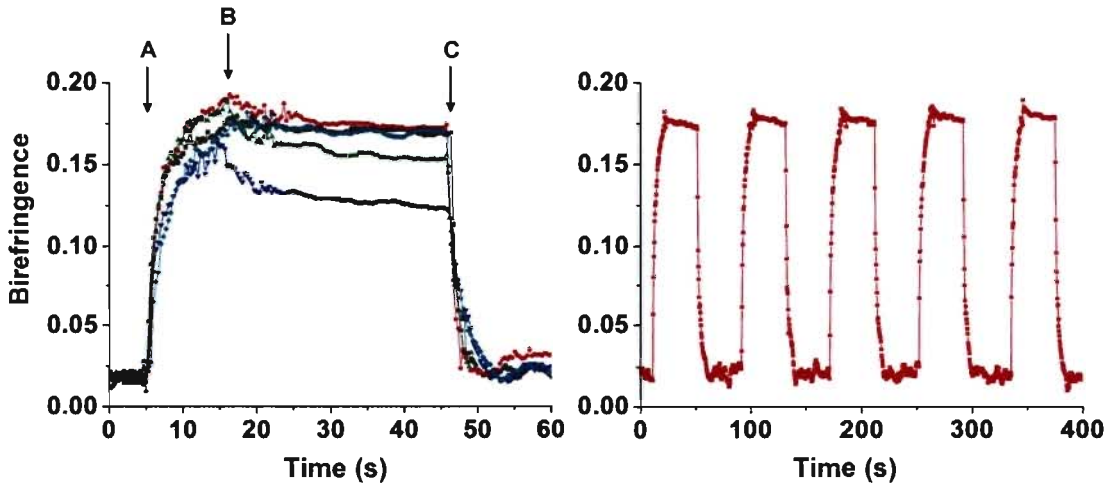

Figure 4.3 Photoinduced birefringence (PIB) in a spin-coated film (200 nm thick) of the MO/P4VPMe complex. Left, PIB curves (A, write ON 10 s; B, write OFF 30 s; C, erasure ON) taken at the same spot in the order: black, freshly prepared film at 20 °C; red, 100 °C; green, 150 °C; blue, 180 °C; cyan, cooled back to 30 °C. Right, multiple write-erase cycles (25 °C; write ON 10 s, write OFF 30 s, erase ON 30 s, erase OFF 10 s); only the first five of eight identical cycles are shown.

At comparable exposure doses,[20] previously studied amorphous azo polymers generally give much lower PIB values than the present complex.[21,22] However, higher values, similar to ours or less, are obtained when the azo group is attached to the polymer backbone via a rigid moiety (attributed to a high Tg)[23] or when the polymer is semi-crystalline.[21b] SCLCP's using highly anisotropic azo-tolane moieties can also provide high PIB's.[24,25] However, none of these polymers have the advantage of relatively easy synthesis and preparation. In some cases, little or no relaxation occurs after cessation of excitation,[21b,26] but good performance is not maintained at the high temperatures observed for the MO/P4VPMe complex (in the cases where this was investigated). Just recently, Priimagi *et al.* showed that H-bonding of DR1 to polymers also enhances PIB values and stability, but again much less than in the present ionic complex.[27]

In summary, we have shown that ionic complexation of crystalline MO to amorphous P4VPMe generates a solid material with smectic A order stable to degradation. This is the first published example, to our knowledge, of an *ionically complexed* side-chain polymer *free of flexible spacer and tail* that shows LC order. It provides exception-ally high and reversibly erasable PIB with excellent temporal and thermal stability, competitive with if

not superior to those of the best (all-covalent) azo polymers reported to date, yet much simpler to synthesize.[3,4] The properties can be easily tailored and optimized, in particular through choice and ratio of chromophore(s) and (co)polymer.

4.2 Acknowledgments

NSERC (Canada) is acknowledged for their financial support. The authors are members of the multi-university Centre for Self-Assembled Chemical Structures (CSACS), supported by FQRNT (Quebec).

4.3 References and Notes

1. Some recent reviews: (a) Natansohn, A.; Rochon, P. *Chem. Rev.* **2002**, 102, 4139. (b) Ikeda, T. J. *Mater. Chem.* **2003**, 13, 2037. (c) Yesodha, S. K.; Pillai, C. K. S.; Tsutsumi, N. *Prog. Polym. Sci.* **2004**, 29, 45. (d) Ikeda, T.; Mamiya, J.; Yu, Y. *Angew. Chem. Int. Ed.* **2007**, 46, 506. (e) Advincula, R. "Polyelectrolyte Layer-by-Layer Self-Assembled Multilayers Containing Azobenzene Dyes" in *Handbook of Polyelectrolytes and Their Applications*; Tripathy, S.K., Kumar, J., Nalwa, H.S., Eds; American Scientific: Stevenson Ranch, CA, **2002**; Vol. 1, Ch. 3, p.65.
2. See, e.g., Bosshard, C. *et al. Organic Nonlinear Optical Materials*; Gordon and Breach Science Publishers: Basel, **1995**. Marks, T. J.; Ratner, M. A. *Angew. Chem. Int. Ed. Engl.* **1995**, 34, 155. Todorov, T.; Nikolova, L.; Tomova, N. *Appl. Optics* **1984**, 23, 4309.
3. See, e.g., (a) Priimagi, A.; Cattaneo, S.; Ras, R. H. A.; Valkama, S.; Ikkala, O.; Kauranen, M. *Chem. Mater.* **2005**, 17, 5798. (b) Vishalakshi, B. *J. Polym. Sci.: Part A: Polym. Chem.*, **1995**, 33, 365. (c) Buruiana, T.; Buruiana, E. C.; Airinei, A.; Greco, I. *Eur. Polym. J.* **2001**, 37, 343. (d) Stumpe, J.; Goldenberg, L. E.C. Patent Appl. EP20040020997, **2006**.
4. In terms of ease of synthesis, mention may be made as well of the ionic self-assembly of charged azo-dyes with oppositely charged small molecules (generally with flexible alkyl chains present), some of which also show LC behavior along with high dichroic ratios: Zakrevskyy, Y.; Stumpe, J.; Faul, C. F. J. *Adv. Mater.* **2006**, 18, 2133. Zakrevskyy, Y.; Stumpe, J.; Smarsly, B.; Faul, C. F. J. *Phys. Rev. E* **2007**, 75, 031703.
5. Finkelmann, H; Ringsdorf, H.; Wendorff, J. H. *Makromol. Chem.* **1978**, 179, 273.
6. (a) Percec, V.; Pugh, C. in *Side Chain Liquid Crystal Polymers*; McArdle, C. B., ed. New York: Chapman and Hall, **1989**; Ch. 3. (b) Demus, D.; Goodby, J. W.; Gray, G. W.; Spiess, H. W.; Vill, V.; Eds. *Handbook of Liquid Crystals*, Vol. 4; Wiley-VCH: Weinheim, **1998**.
7. Ref. 6a, pp. 49-53; and references therein.
8. Blumstein, A.; Hsu, E. C. in *Liquid Crystalline Order in Polymers*; Blumstein, A., ed. New York: Academic Press, **1978**; Ch. 3.

9. Baccaredda, M.; Magagnini, P. L.; Pizzirani, G.; Giusti, P. *J. Polym. Sci., Polym. Lett.* **1971**, 9, 303. Newman, B. A.; Frosini, V.; Magagnini, P.L. *J. Polym. Sci., Polym. Phys. Ed.* **1975**, 13, 87. Frosini, V.; Levita, G.; Lupinacci, D.; Magagnini, P. L. *Mol. Cryst. Liq. Cryst.* **1981**, 66, 21.
10. Âlimoglu, A. K.; Ledwith, A.; Gemmell, P. A.; Gray, G. W.; Lacy, F. R. S. and D. *Polymer* **1984**, 25, 1342. Blumstein, A.; Blumstein, R. B.; Clough, S. B.; Hsu, E. C. *Macromolecules* **1975**, 8, 73. Duran, R.; Gramain, P.; Guillon, D.; Skoulios, A. *Mol. Cryst. Liq. Cryst. Lett.* **1986**, 3, 23. Duran, R.; Guillon, D.; Gramain, Ph.; Skoulios, A. *Makromol. Chem., Rapid Comm.* **1987**, 8, 321. Zhou, Q.-F.; Zhu, X.; Wen, Z.- *Macromolecules* **1989**, 22, 493. Yu, Z.; Tu, H.; Wan, X.; Chen, X.; Zhou, Q.-F. *J. Polym. Sci.: Part A: Polym. Chem.* **2003**, 41, 1454.
11. It is long known that a sufficiently long flexible tail in the side chain can also allow LC order to appear, as observed for comb polymers having simple alkyl side chains (see, e.g., Platé, N. A.; Shibaev, V. P. *J. Polym. Sci., Macromol. Rev.* **1974**, 8, 117). In this context, many early SCLCP's consisted also of directly attached side-chain rigid groups with long alkyl tails (see, e.g., refs. 7-10).
12. (a) Barberá, J.; Rakitin, O. A.; Ros, M. B.; Torroba, T. *Angew. Chem. Int. Ed.* **1998**, 37, 296. (b) Kölbel, M.; Beyersdorff, T.; Tschierske, C.; Diele, S.; Kain, J. *Chem. Eur. J.* **2000**, 6, 3821. (c) Van Deun, R.; Ramaekers, J.; Nockemann, P.; Van Hecke, K.; Van Meervelt, L.; Binnemans, K. *Eur. J. Inorg. Chem.* **2005**, 563. (d) Ohta, K.; Shibuya, T.; Ando, M. *J. Mater. Chem.* **2006**, 16, 3635.
13. Vorländer, D. *Ber. Dtsch. Chem. Ges.* **1910**, 43, 3120. Demus, D.; Sackmann, H.; Seibert, K. *Wiss. Z. Univ. Halle* **1970**, 19, 47. Dyer, D. J.; Lee, V. Y.; Twieg, R. J. *Liq. Cryst.* **1997**, 23, 551.
14. Some recent reviews: Binnemans, K. *Chem. Rev.* **2005**, 105, 4148. Faul, C. F. J.; Antonietti, M. *Adv. Mater.* **2003**, 15, 673. Paleos, C. M.; Tsiourvas, D. *Liq. Cryst.* **2001**, 28, 1127. Kato, T. *Struct. Bond.* **2000**, 96, 95. Bazuin, C. G. in *Mechanical and Thermophysical Properties of Polymer Liquid Crystals*; Brostow, W., ed. London: Chapman and Hall, **1998**; Vol. 3, Ch. 3.
15. See, e.g., Antonietti, M.; Conrad, J.; Thünemann, A. *Macromolecules* **1994**, 27, 6007. Chen, H.-L.; Hsaio, M.-S. *Macromolecules* **1999**, 32, 2967. Tsiourvas, D.; Paleos, C. M.; Skoulios, A. *Macromolecules* **1999**, 32, 8059. Kharas, G. B.; Heiskell, J. R.; Herrman, J.; Kasudia, P. T.; Schreiber, P. J.; Passe, L. B.; Bravo-Grimaldo, E.; Bazuin, C. G.; Romanowski, P. T.; Schueller, R. M. *J. Macromol. Sci., Part A: Pure Appl. Chem.* **2006**, 43, 213.
16. Wu, X.; Zhang, G.; Zhang, H. *Macromol. Chem. Phys.* **1998**, 199, 2101.
17. Similar H-bond complexes of phenol and pyridyl derivatives to poly(2-dimethylaminoethyl methacrylate) and poly(2-hydroxyethyl methacrylate), respectively, reported to be nematic, involve a short spacer in the pendant group of the polymer and less than equimolar complexation: Malik, S.; Dhal, K.; Mashelkar, R. A. *Macromolecules* **1995**, 28, 2159.
18. See Supporting Information for details.
19. A thermal cis-trans relaxation rate of 0.4 s-1 was determined for this system, orders of magnitude faster than typical rates for other MO-based azo dyes (see Barrett, C.; Natansohn, A.; Rochon, P. *Chem. Mater.* **1995**, 7, 899, and ref. 3c), suggesting that the ionic interactions alter the electronic structure of the chromophore significantly.

20. The PIB depends on the exposure dose (power of writing laser multiplied by writing time) and the intrinsic response of the chromophore at the writing wavelength used (photoisomerization quantum yield, cis-trans isomerization rate, etc.). Thus, comparisons possible depend on the information avaliable, and, in some cases, are extrapolated. A high exposure dose may also cause irreversible changes in the exposed region that affect potential relaxation processes.
21. (a) Shi, Y.; Steier, W. H.; Yu, L.; Chen, M.; Dalton, L. R. *Appl. Phys. Lett.* **1991**, 59, 2935. (b) Natansohn, A.; Rochon, P.; Pezolet, M.; Audet, P.; Brown, D.; To, S. *Macromolecules* **1994**, 27, 2580.
22. Polyelectrolyte layer-by-layer assemblies involving covalently or noncovalently bound dyes can also show interesting photoinduced align-ment (see, e.g., ref. 1e); however, to our knowledge there are no reports of high PIB, only high dichroic ratios, which are not easily compared.
23. Angiolini, L.; Bozio, R.; Giorgini, L.; Pedron, D.; Turco, G.; Daurù, A. *Chem. Eur. J.* **2002**, 8, 4241. Angiolini, L.; Benelli, T.; Giorgini, L.; Salatelli, E.; Bozio, R.; Daurù, A.; Pedron, D. *Macromolecules* **2006**, 39, 489.
24. Fukuda, T.; Kim, J. Y.; Barada, D.; Senzaki, T.; Yase, K. J. *Photochem. Photobiol., A: Chem.* **2006**, 182, 262.
25. In a novel approach to obtain high birefringence changes, an azo-tolane film was pre-aligned, providing extremely high birefringence, which could then be erased by applying a laser beam: Okano, K.; Shishido, A.; Tsutsumi, O.; Shiono, T.; Ikeda, T. *J. Mater. Chem.* **2005**, 15, 3395. Okano, K.; Tsutsumi, O.; Shishido, A.; Ikeda, T. *J. Amer. Chem. Soc.* **2006**, 128, 15368. Okano, K.; Shishido, A.; Ikeda, T. *Adv. Mater.* **2006**, 18, 523
26. Holme, N. C. R.; Ramanujam, P. S.; Hvilsted, S. *Appl. Optics* **1996**, 35, 4622.
27. Priimagi, A.; Kaivola, M.; Rodriguez, F. J.; Kauranen, M. *Appl. Phys. Lett.* **2007**, 90, 121103.

4.4 Supporting information for Chapter 4

4.4.1 Materials and synthesis of complexes

Methyl orange (MO) was obtained from Aldrich and used as received. Poly(4-vinyl pyridine) (P4VP), obtained from Scientific Polymer Products (viscosity M.W. = 200,000), was quaternized by CH_3I in nitromethane to give P4VPMe, following literature procedures;[1] methylation was verified to be 100% by ^1H NMR in D_2O. Complexation between MO and P4VPMe was achieved by first dissolving 1.14 eq of MO in warm spectrograde DMSO and 1 eq of P4VPMe in Milli-Q H_2O (20-30 mg/mL concentrations), then adding the MO solution to the polymer solution. Sufficient DMSO was added to the mixture to redissolve the precipitate that formed. This solution was stirred at 45 °C for 1 h, and then dialyzed (SpectraPor dialysis membrane, M.W. cutoff 3500; Spectrum Laboratories) against Milli-Q water, which was refreshed twice a day for 4 days, to eliminate the Na and I counterions, DMSO and excess MO. The resulting opaque, dark-red, fine precipitate was freeze-dried for 5 days, and then dried under vacuum at 60 °C for 3 days followed by 100 °C for 1 day. The absence of Na and I counterions as indicated by energy dispersive analysis (EDS), the ^1H NMR spectrum in DMSO-d (Figure 4.S1), and CHNS elemental analysis (Table 4.S1 shows excellent agreement between the experimental and calculated values when 1/2 H_2O per repeat unit is included in the latter) all show that full complexation of MO to P4VPMe (1:1 VPMe:MO molar ratio) was achieved in the final product.[2]

4.4.2 Instrumentation and sample preparation

EDS was carried out with a FEI Quanta 200 FEG environmental scanning electron microscope attachment; CHNS elemental analysis with a Fisons AE1108 analyzer (Table 4.S1); ^1H NMR with a Bruker Avance 400 MHz spectrometer (Figure 4.S1); thermogravimetric analysis (TGA) with a TA Instruments Hi-Res TGA 2950 analyzer, under nitrogen atmosphere and using a heating rate of 10 °C/min; differential scanning calorimetry (DSC) with a TA instruments Q1000 DSC, using heating and cooling rates of 10 °C/min; polarizing optical microscopy (POM) with a Zeiss Axioskop 40Pol microscope coupled with a Linkam Scientific Instrument THMS600 hot stage and a TMS94

temperature controller; X-ray diffraction (XRD) analysis with a Bruker D8 Discover system equipped with a 2D Bruker AXS wire-grid detector, using Cu Kα radiation, with the powder sample packed in a 1.0-mm diameter capillary (Charles Supper) and temperature controlled by a HCS410 heating stage and a STC200 temperature controller from Instec; UV-visible spectra with a Varian Cary 500 Scan UV-Vis-NIR spectrophotometer; and atomic force microscopy (AFM) with a Digital Instruments Dimension 3100 instrument, used in tapping mode. Unless otherwise specified, the analyses were performed on dialyzed samples after thorough drying.

Films of the MO/P4VPMe complex were prepared for certain experiments. To obtain an identifiable POM texture, a film was solvent-cast onto a glass slide from a dilute DMF solution (< 5 wt %), subjected to very slow evaporation in a covered beaker over a period of many days, followed by drying under vacuum at ca. 80 °C for several days (and months with no change).[3] This (translucent) film also served to obtain the UV-visible spectrum shown in Figure 4.S2. For photoinduced birefringence measurements, (slightly translucent) films were prepared by spin-coating (20 s at 2350 rpm; spin-coater model EC101, Headway Research) onto a glass slide from a 7.1 wt % solution of DMF/CH_2Cl_2 (60/40 w/w), followed by drying under vacuum at 60-80 °C for about a month. A thicker solvent-cast film (5-10 μm; quite opaque), dried for several weeks under vacuum at ca. 80 °C, was used for inscribing a surface relief grating (SRG).

The thickness of the first film used for photoinduced birefringence measurements was determined to be 250±50 nm by AFM, as measured at six representative points along two parallel scratches, or 270±5 nm based on four points (lowest point and highest point eliminated). Using the average thickness of 250 nm and the UV-vis absorbance of this film at 400 nm, the thickness of subsequent films was determined by their UV-vis absorbance at 400 nm, averaged from four readings at different spots.

Photoinduced birefringence was tested via the setup described elsewhere.[4] The film was placed between two crossed polarizers in a temperature-controlled sample chamber flushed with dry N_2. An Ar ion laser (Spectra-Physics, Model 2030) operated at 488 nm and 1.0 W/cm^2, set at a polarization angle of 45° with respect to the polarizer orientation, was used as the pump laser. A strongly attenuated He-Ne laser (model 1125P; JDS Uniphase) operated at 633 nm and 5.0 mW was used as the probe laser. Optical erasure

was effected using a quarter-wave plate inserted in the path of the pump laser to convert linearly polarized light into circularly polarized light. The different temperature scans, of which a selection is shown in Figure 4.3 in the main text (maximum temperature, 180 °C), and the write-erase cycles in Figure 4.3 were performed at the same spot in the film, with no evidence of photo-bleaching found. The photoinduced birefringence values (Δn) were calculated using the equation,

$$\frac{I}{I_o} = \sin^2\left(\frac{\pi|\Delta n|d}{\lambda}\right)$$

where I is the photodiode transmission signal, I_o the photodiode signal in the absence of the sample (parallel polarizer/analyzer orientation), d the film thickness and λ the probe wavelength. The raw data in the plateau regions in Figure 4.3 were smoothed by manually averaging each point using the four preceding and four following points (no smoothing was effected on the data in Figure 4.S5).

Surface relief gratings (SRGs), as shown in Figure 4.S6, were inscribed using a one-beam setup with a quarter-wave plate,[5] an Ar laser operating at 488 nm (beam diameter enlarged to 15 mm, power density 65 mW/cm^2), and the angle between the propagation axis and mirror plane set near 15°. Recording was done at ambient for 2.25 h.

4.4.3 Supporting data

Table 4.S1 Elemental analysis of the MO/P4VPMe complex, assuming 100% complexation.

MO/P4VPMe	% N	% C	% H	% S
Found	12.49	61.21	5.89	7.41
Calcd.	13.20	62.24	5.70	7.55
Calcd. (0.5 H_2O [a])	12.92	60.95	5.81	7.40

[a] per repeat unit

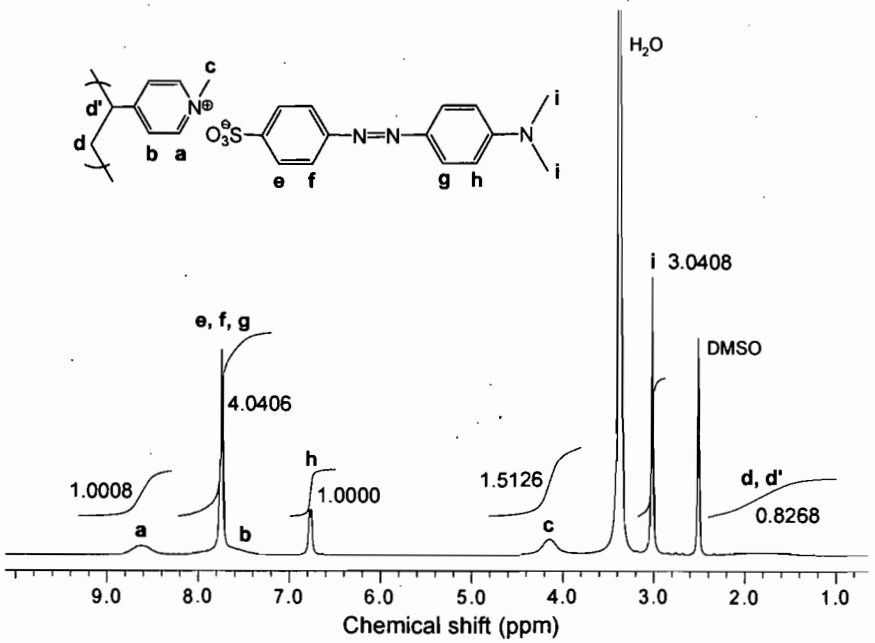

Figure 4.S1 ^{1}**H NMR spectrum of the MO/P4VPMe complex in DMSO-d6. The numbers associated with the signals specify the integration values. Signals a and c for P4VPMe compared to signals h and i for MO (as well as the sum of e+f+g+b) show that the two components are in exactly equimolar proportion with respect to the polymer repeat unit.**

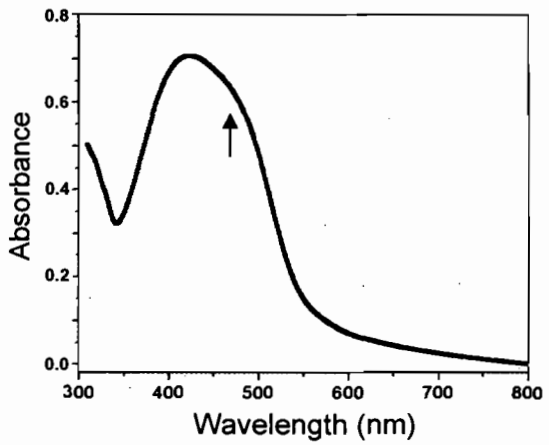

Figure 4.S2 UV-visible spectrum of the MO/P4VPMe film, solvent cast from DMF and thoroughly dried. The arrow indicates the wavelength of the writing laser used.

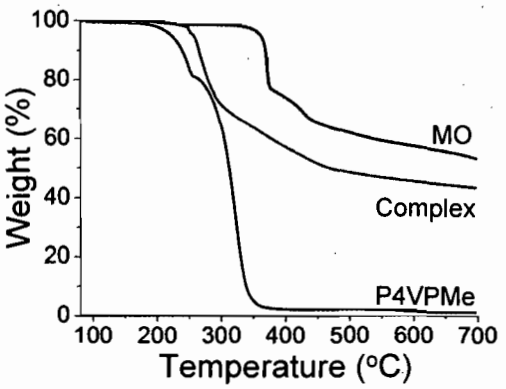

Figure 4.S3 Thermogravimetric analysis of MO, P4VPMe and the MO/P4VPMe complex.

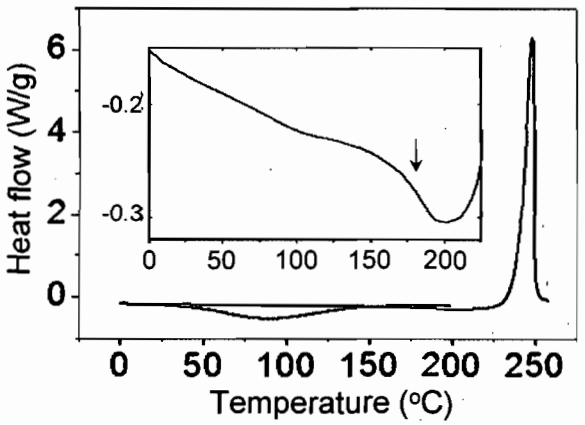

Figure 4.S4 Differential scanning calorimetry (10 °C/min) of the MO/P4VPMe complex (black line, initial heat to 200 °C; red line, second heat; inset, y-axis expansion of second heat). The arrow points to a possible glass transition. ***Note that the peak near 250 °C in the heating curve is exothermic.*** **See Additional Comments for details.**

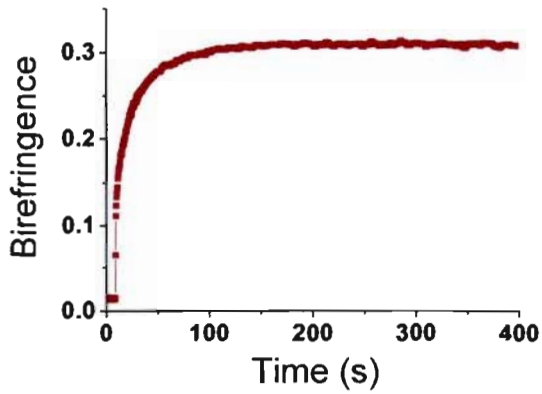

Figure 4.S5 Saturation PIB of a spin-coated MO/P4VPMe film (previously heated to 200 °C; see Additional Comments for more detail).

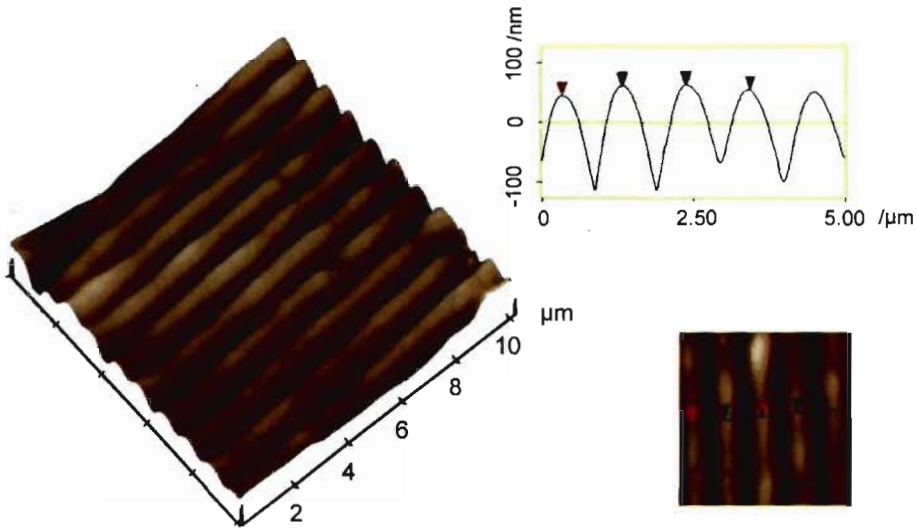

Figure 4.S6 AFM height image of the surface relief grating (SRG) inscribed on a thick solvent-cast film. Left: three-dimensional image. Right: cross-sectional height profile (uncorrected for the tip profile) of a portion of the image (as shown). The period of the SRG is about 1 µm and the amplitude approaches 200 nm.

4.4.4 Additional comments

The DSC thermogram obtained on heating to high temperatures shows a sharp, intense *exo*thermic peak (maximum 249 °C, enthalpy –290 J/g; Figure 4.S4), which occurs near the onset of degradation as indicated by TGA (Figure 4.S3). Such an exothermic peak on heating was also noted for protonated P4VP complexes with sulfonic acid derivatives.[6,7] No other clear transitions are apparent in DSC, although there is a very broad endotherm spanning 100 °C (first heating only, possibly related to slow loss of bound H_2O or to slight softening of the material) and perhaps a T_g at about 180 °C (second heating scan; inset in Figure 4.S4). Techniques such as dynamic mechanical thermal analysis, dielectric analysis and solid-state NMR spectroscopy could help clarify these very weak DSC events. The T_g may also occur above degradation, as reported for strongly complexed surfactant-polyelectrolyte materials (involving sulfonate or sulfate anionic moieties).[8]

The PIB curve in Figure 4.S5, showing that saturation is reached in less than 200 s, was taken on a film previously heated to 200 °C. In another film, exposed to a maximum of 180 °C (used for the data in Figure 4.3 of the main text), the PIB first increased rapidly (ca. 50 s) to above 0.2, but continued to increase slowly reaching a value of 0.25 at the end of the 15-min testing period; nevertheless, it clearly tended towards a similar value as for the curve in Figure 4.S5. The difference in kinetics may be related to the higher-temperature exposure of the first film, which may, for example, have caused slight degradation. Another possible reason may be differences in humidity exposure; humidity cannot be altogether eliminated from the sample area, which although protected by dry N_2, is not air-tight.

4.4.5 References

1. Kawaguchi, D.; Satoh, M. *Macromolecules* **1999**, *32*, 7828.
2. A complex of MO with ethylated P4VP [as well as ethylated poly(dimethylaminoethyl methacrylate)] was previously reported, but the limited investigations did not permit observation of any potential LC character: Lin, X.; Zhong, A.; Chen, D.; Zhou, Z.; He, B. *J. Appl. Polym. Sci.* **2003**, *87*, 369 (same paper in *J. Appl. Polym. Sci.* **2002**, *85*, 638).
3. This technique was used to obtain LC-like POM textures of block copolymer thin films: Wang, W.; Hashimoto, T. *Macromolecules* **1999**, *32*, 3163.
4. Natansohn, A.; Rochon, P.; Gosselin, J.; Xie, S. *Macromolecules* **1992,** *25*, 2268.
5. Yager, K. G.; Barrett, C. J. *Current Opinion in Solid State and Materials Science* **2002**, *5*, 487.
6. Zhu, X.; Beginn, U.; Möller, M.; Gearba, R. I.; Anokhin, D. V.; Ivanov, D. A. *J. Am. Chem. Soc.* **2006**, *128*, 16928.
7. Shibata, M.; Kimura, Y.; Yaginuma, D. *Polymer* **2004**, *45*, 7571.
8. See, e.g., Antonietti, M.; Conrad, J.; Thünemann, A. *Macromolecules* **1994**, *27*, 6007.

Chapter 5. Spacer-Free Ionic Dye-Polyelectrolyte Complexes: Influence of Molecular Structure on Liquid Crystal Order and Photoinduced Motion

Qian Zhang,[1] Xin Wang,[1] Christopher J. Barrett[2] and C. Geraldine Bazuin*,[1]

Centre de Recherche sur les Matériaux Auto-Assemblés (CRMAA/CSACS),
[1]Département de chimie, Université de Montréal, C.P. 6128, succursale Centre-Ville, Montréal (QC), Canada H3C 3J7
[2]Department of Chemistry, McGill University, 801 Sherbrooke St. W., Montréal (QC), Canada H3A 2K6

Chem. Mater. **2009**, 21, 3216-3227

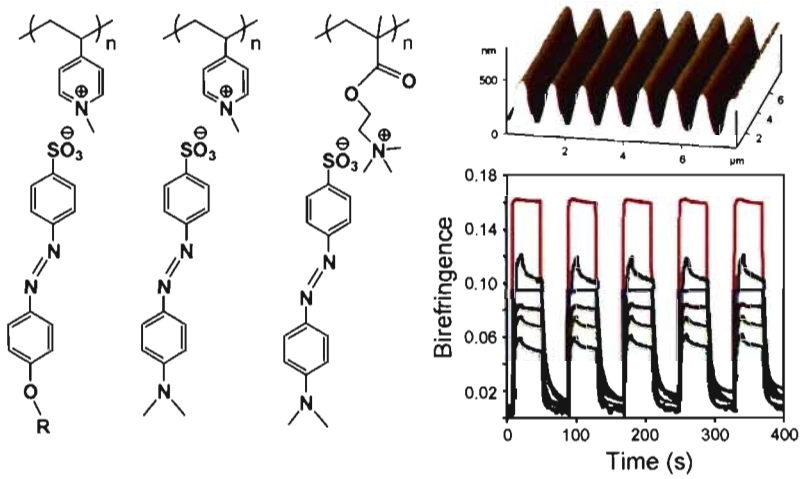

Abstract

A series of spacer-free ionic azobenzene-containing stoichiometric complexes was prepared from mono-sulfonated azo dyes and cationic polyelectrolytes [methylated poly(4-vinylpyridine) (PVP) and poly(dimethylaminoethyl methacrylate) (PDM)]. Their thermal and structural characteristics and optical responses, particularly photoinduced birefringence (PIB) and surface relief grating (SRG) inscription, were investigated as a function of selected molecular parameters. All of the complexes have high apparent T_gs, 180-210 °C, and show liquid crystal (LC) order of the single-layer SmA type from ambient to very high temperature, usually to degradation. The LC order appears most long-range for the chromophores with longer alkyl tails and the least long-range for the chromophore with a hydrogen-bonding OH terminal group and for the complex of methyl orange (MO) with PDM. PIB, SRG quality and diffraction efficiency were all shown to depend in a similar way on molecular structural features: the more rigid the molecular structure, the higher the PIB, the better its thermal and temporal stability, and the higher the SRG amplitude. Thus, a flexible alkyl unit in the polyelectrolyte component or in the chromophore tail or spacer reduces the optical performance, with a clear dependence on alkoxy tail length (e.g., no SRG formation was possible in the complex with a hexoxy tail), whereas the most rigid complex, MO/PVP, provides the best performance, contrasting with many previous literature reports that suggest a beneficial role for flexible spacers. The present paper shows that flexible moieties increase relaxation of photoinduced orientation. A simple hydroxyl tail also provides much improved PIB and SRG performance, which is attributed to a physical crosslinking effect of H-bonding interactions.

5.1 Introduction

Azo-containing materials continue to attract considerable interest, particularly in the field of photomechanics,[1] for optoelectronic[2-5] and photochemical[6] applications, as photosensitive molecular machines,[7,8] in life[9,10] and surface[11] sciences, etc. All of these areas take advantage of the well-known azobenzene photoisomerization phenomenon,[12] which allows orientation of the chromophores under irradiation, light triggered shape and polarity changes, etc.[2,5] Many of the azo-containing materials used are in the form of all-covalent polymers.[2] Elements of supramolecular chemistry have also been incorporated into polymeric photonic materials, which can simplify the synthesis and introduce novel properties. For example, Ikeda and coll. described photo-bendable films of an azopolymer where hydrogen-bond crosslinks replace conventional covalent crosslinks.[13] Besides simplifying the preparation of the material, this approach renders it recyclable due to its solubility in suitable solvents in contrast to the insolubility of chemically crosslinked polymers. In another supramolecular system, Ikkala and coll. demonstrated that enhanced stability and intensity of photoinduced birefringence can be achieved by using hydrogen bonds to bind the chromophore to the polymer chain allowing high doping levels.[14]

Ionic bonding is another interaction exploited in supramolecular systems for its high strength,[15] such as in dye-surfactant,[16-18] surfactant-polyelectrolyte,[19-22] and surfactomesogen-polyelectrolyte[23-27] complexes, which typically self-assemble into ordered mesomorphous structures. Dye-polyelectrolyte complexes that combine rigidity, liquid crystallinity and ionic polymer properties as well as high dye loading have been shown to be particularly promising for optical applications.[28-30] In fact, dye-polyelectrolyte systems have been a topic of interest for many years,[15,31] but mainly in solution form,[31-34] as Langmuir-Blodgett films,[35-37] and as layer-by-layer films.[38]

In this paper, we are following up on our communication concerning the simple spacer-free dye-polyelectrolyte complex composed of methyl orange (MO) and methylated poly(4-vinylpyridine) (PVP, where Me is omitted from the acronym for simplicity).[30] This easily prepared material is rigid and possesses liquid crystal (LC) structure up to degradation, and, in spin-coated films, it gives high and thermally stable photoinduced birefringence (PIB) and is amenable to surface relief grating (SRG) inscription.[30] Similar

properties were reported quasi-simultaneously for a complex of MO with ethylated poly(4-vinyl pyridine).[29a] The exceptional PIB properties were attributed in part to the absence of any flexible spacer or tail in these materials.[30] The role of flexible components in the optical responses of photonic polymers has not yet been well elucidated, and generally chromophores in sidechain polymers have been designed with a flexible spacer incorporated, in particular longer ones in order to promote LC structure that is thought to enhance photo-orientation.[2] The above study suggests that flexible spacers may be counterproductive to optical performances and, besides, shows that they are not always necessary for obtaining LC order. In this context, we investigate here a series of mainly spacer-free dye-polyelectrolyte complexes, to examine how certain molecular structural features, and especially the presence of flexible moieties, influence LC order and photoresponsive properties, specifically PIB and SRG inscription. The ease of preparing such complexes is a strong advantage for establishing structure-property relations.

The dye-polyelectrolyte complexes under study are shown, along with the nomenclature used, in Scheme 5.1. Complexes (a) to (e) have an identical polyelectrolyte backbone, PVP. The previously studied complex,[30] MO/PVP (e), serves as a reference. Complexes (a) to (d) differ from (e) by the linking atom (O vs. N) between mesogen core and tail and by the tail length and structure. They differ from one another by the tail length [(a) < (b) < (d) < (c)], as well as by a branched tail and therefore chiral center for (d) and by an OH terminal group and therefore hydrogen-bonding capacity for (a). Complex (f) involves MO and a different polyelectrolyte, methylated poly(dimethylaminoethyl methacrylate) (PDM), which is exempt of aromaticity and contains a short ethylene spacer, making it a more flexible backbone than PVP.

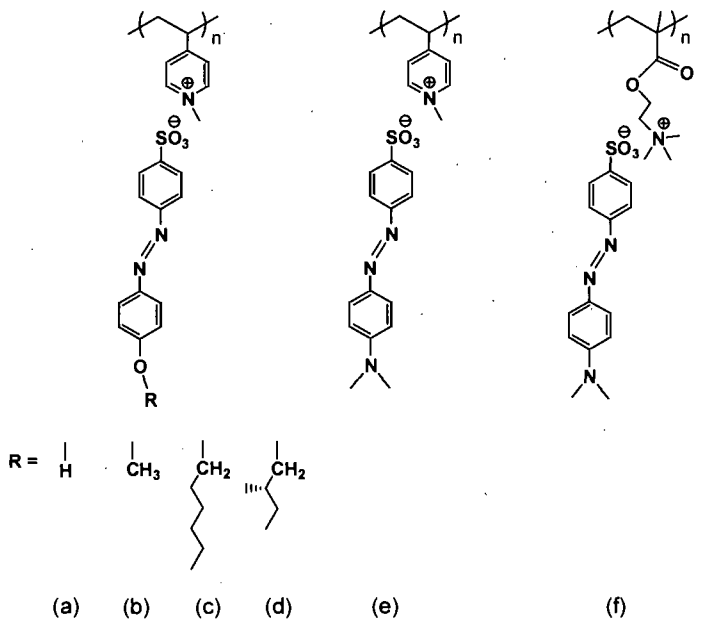

Scheme 5.1 Chemical structure of the complexes studied. Nomenclature: (a) H/PVP; (b) Me/PVP; (c) Hex/PVP; (d) Ch*/PVP; (e) MO/PVP; (f) MO/PDM. PVP and PDM refer to the polyelectrolyte components in methylated form (when not complexed, they are designated as PVP-I and PDM-I).

5.2 Experimental section

5.2.1 Materials

Methyl orange (MO) was obtained from Sigma-Aldrich and used as received. Poly(4-vinyl pyridine) was obtained from Scientific Polymer Products (viscosity M.W. = 200,000). Poly(N,N'-dimethylaminoethyl methacrylate) was donated by Prof. R. Jérôme and Dr. C. Detrembleur of the Centre d'Étude et de Recherche sur les Macromolécules (CERM) of Université de Liège, Belgium [SEC (DMF/LiBr; PS standards): M_n=16600, M_w/M_n=1.22; true mass estimated at ca. 8000].

Sulfanilic acid, sodium salt hydrate (97%), 1-bromohexane (98%), (S)-(+)-1-bromo-2-methylbutane (99%), iodomethane (99.5%), sodium nitrite (99.5%), phenol (99.0+%), hydrochloric acid (36.5-38.0%), sodium iodide (99+%), phenol (99.0+%), anhydrous sodium carbonate (99.5+%), and sodium hydroxide (97.0+%) were purchased from Sigma-Aldrich and used as received. Deionized water was obtained from a Millipore Gradient

A10 Milli-Q system (resistivity 18.2 MΩ.cm at 25 °C). Spectrograde DMSO (Sigma-Aldrich) was used in the preparation of the complexes. All other solvents (EMD, A&C) were used as received or dried by passing through drying columns (Glass Contour system).

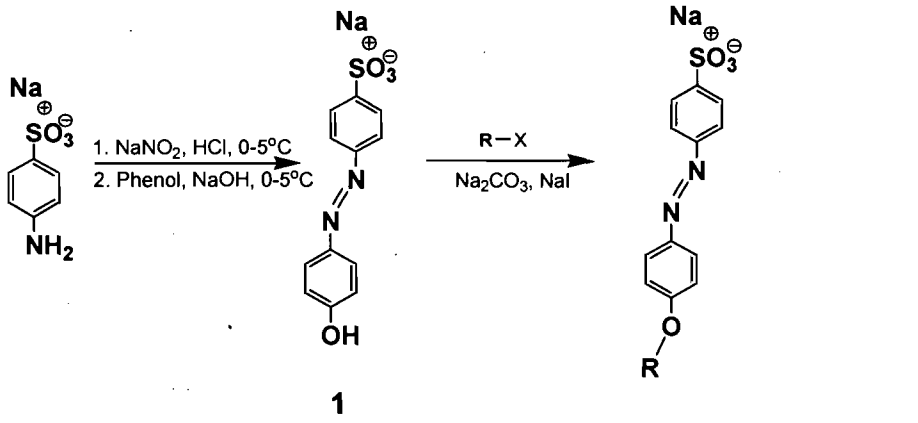

Scheme 5.2 Synthetic route for the chromophores. The chromophores are designated by their terminal group (tail) as follows: (1) H; (2) Me; (3) Hex; (4) Ch*.

5.2.2 Synthesis

Both polymers were quaternized by CH_3I in nitromethane, following literature procedures,[30,39,40] and, after precipitation into dichloromethane, were freeze-dried followed by vacuum drying at 40 °C for 3 d. Methylation was verified to be essentially 100% for both polymers by ^1H NMR.

The Na^+-neutralized chromophores (a) to (d) were synthesized according to Scheme 5.2. The H chromophore (**1**) is the precursor compound for the alkoxy-tailed chromophores (**2-4**). NMR (see below) and elemental analysis (Table 5.1) data indicate highly pure products.

Table 5.1 Elemental analysis of the Na^+-neutralized chromophores synthesized and of the chromophore/polyelectrolyte complexes.

Sample	C %		H %		N %		S %	
	Theor.	Found	Theor.	Found	Theor.	Found	Theor.	Found
Chromophore								
H	48.00	48.18	3.02	3.04	9.33	9.32	10.68	11.22
Me	49.68	50.22	3.53	3.48	8.91	8.95	10.20	10.53
Hex	56.24	56.37	5.51	5.46	7.29	7.35	8.34	8.69
Ch*	55.12	54.93	5.17	5.17	7.56	7.71	8.66	8.80
Complex (+ mol H_2O)								
H/PVP + 0.33 H_2O	59.54	59.74	4.91	5.13	10.42	10.36	7.95	8.21
Me/PVP + 0.33 H_2O	60.42	60.41	5.23	5.41	10.07	10.03	7.68	7.92
Hex/PVP + 0.5 H_2O	63.65	63.56	6.57	5.79	8.56	8.37	6.54	6.46
Ch*/PVP + 1.5 H_2O	60.71	60.45	6.52	6.59	8.50	8.36	6.48	6.02
MO/PDM +1.0 H_2O	55.85	55.88	6.93	6.77	11.33	11.28	6.48	7.16

4-(4-Hydroxyphenylazo)benzenesulfonic acid, sodium salt (1). In 20 mL deionized water while stirring at 0-5 °C were dissolved 3.38 g (15.4 mmol) of sulfanilic acid sodium salt, followed by 1.17 g (1.1 eq.) of sodium nitrite. Separately, to a 500 mL three-necked flask in an ice bath were added under stirring 10 g of crushed ice and 3.15 mL concentrated HCl (2.5 eq.), to which the solution of sulfanilic acid and sodium nitrite was then added, followed by vigorous stirring for 20 min, which yielded a cloudy solution of diazonium salt. This solution was poured into a solution of NaOH [1.27 g (2.0 eq.)] dissolved in 10 mL deionized water, to which had been added 1.45 g (1.0 eq.) phenol, all in a 500-mL three-necked flask under stirring at 0-5 °C, giving an orange precipitate. After stirring for 3 h at 0-5 °C and 1 h at ambient temperature, the mixture was heated to 80 °C to obtain an almost clear solution. Then 21 g of NaCl were added and the pH adjusted to 7, causing precipitation. After overnight refrigeration, the raw product was isolated by filtration, rinsed successively with deionized water, chloroform and acetone, crystallized in 10 mL deionized water, then dried under vacuum at 70 °C for 2 d, giving an orange needle-like product (4.0 g, yield 87 %). ^{1}H NMR (DMSO-d_6, ppm): 10.34 (broad, 1H, Ar-*OH*), 7.82 (d, 2H, J=8.7 Hz, Ar-SO_3^-), 7.77 (s, 4H, Ar-N=), 6.95 (d, 2H, J=8.7 Hz, Ar-O). ^{13}C NMR (DMSO-d_6, ppm): 161.9, 152.7, 150.7, 146.1, 127.5, 125.8, 122.5, 116.8.

4-(4-Methoxyphenylazo)benzenesulfonic acid, sodium salt (2). To a clear solution of **1** [1.0372 g (3.4542 mmol)] in 20 mL of anhydrous DMF in a 100 mL flask were added under stirring 1.0983 g (3 eq.) of anhydrous sodium carbonate and 2.155 mL (10 eq.) of iodomethane. After stirring for 5 d at 40 °C, solvent and excess iodomethane were removed by rotovaporation, a small amount of water was added to the remaining mixture, which was then heated and recooled. The final precipitate was recuperated by filtration, rinsed successively with water (small amount), acetone and chloroform, then dried in vacuum at 70 °C for 2 d, giving an orange powder (0.86 g, yield 79 %). ^{1}H NMR (DMSO-d_6, ppm): 7.92 (d, 2H, J=8.9 Hz, Ar-SO_3^-), 7.79 (q, 4H, J=5.7 Hz, Ar-N=), 7.15 (d, 2H, J=8.9 Hz, Ar-O), 3.88 (s, 3H, O-CH_3).

4-(4-Hexyloxyphenylazo)benzenesulfonic acid, sodium salt (3). To a clear solution of **1** [0.7136 g (2.377 mmol)] in 20 mL of anhydrous DMF in a 100 mL flask were added under stirring 0.3031 g (1.2 eq.) of anhydrous sodium carbonate, 0.3553 g (1 eq.) of sodium iodide and 1.4 mL (4 eq.) of 1-bromohexane. After stirring for 4 d at 60 °C, DMF was removed by rotovaporation. The recuperated solid was rinsed successively with water, ethyl acetate and DMF and dried in vacuum at 50 °C for 2 d, giving an orange powder (0.4849 g, yield 53%). ^{1}H NMR (DMSO-d_6, ppm): 7.90 (d, 2H, J=8.0 Hz, Ar-SO_3^-), 7.79 (m, 4H, Ar-N=), 7.13 (d, 2H, J=8.0Hz, Ar-O), 4.09 (t, 2H, J=5.5 Hz, O-CH_2), 1.76 (m, 2H, J=7.9 Hz, OCH_2-*CH_2*), 1.45 (m, 2H, J=7.3 Hz, $O(CH_2)_2$-*CH_2*), 1.33 (m, 4H, $O(CH_2)_3$-*CH_2CH_2*), 0.89 (t, 3H, J=7.1 Hz, -CH_3).

4-(4-((S)-2-methylbutoxy)phenylazo)benzenesulfonic acid, sodium salt (4). To a clear solution of **1** [0.5024 g (1.6732 mmol)] in 10 mL of anhydrous DMF in a 100 mL flask were added under stirring 0.5320 g (3 eq.) of anhydrous sodium carbonate and 0.0125 g (0.05 eq.) of sodium iodide and 0.268 mL (1.3 eq.) of (S)-(+)-1-bromo-2-methylbutane. After stirring for 4 d at 80 °C, DMF was removed by rotovaporation. The recuperated solid was then rinsed successively with water, acetone, chloroform and a small amount of DMF, then dried in vacuum at 70 °C for 2 d, giving an orange powder (0.2320 g, yield 37%). ^{1}H NMR (DMSO-d_6, ppm): 7.90 (d, 2H, J=8.9 Hz, Ar-SO_3^-), 7.79 (m, 4H, Ar-N=), 7.14 (d, 2H, J=8.9Hz, Ar-O), 3.93 (m, 2H, O-CH_2), 1.86 (m, 1H, *C*HCH_3), 1.55 (m, 1H, *CH_2*CH), 1.26 (m, 1H, *CH_2*CH), 1.00 (d, 3H, J=6.8 Hz, CH*CH_3*), 0.93 (t, 3H, J=7.5 Hz, CH_2*CH_3*).

5.2.3 Preparation of complexes

The procedure for obtaining complexes is similar to that described previously for MO/PVP,[30] except that only a small amount of excess chromophore (relative to stoichiometric) was used due to its poor solubility in water (especially **3** and **4**). A small amount of Milli-Q water was first added to a calculated amount of PVP-I or PDM-I, giving a very viscous solution (~300 mg/mL), to which DMSO (30~40 mg/mL) was then added. Separately, 1.02~1.04 eq. of chromophore were dissolved in DMSO (15 mg/mL). Then, the chromophore solution was added dropwise to the polyelectrolyte solution, giving a transparent orange solution, which was stirred at 55 °C for 6 h. The solution was then transferred to a dialysis bag (SpectraPor, M.W. cutoff 3500; Spectrum Laboratories) and dialysed against Milli-Q water (refreshed at least daily) for 1-3 wks to eliminate the Na and I counterions, DMSO and excess chromophore. The resulting colloidal and/or precipitated mixture was freeze-dried, followed by further drying under vacuum at 60 °C for 3 d followed by 100 °C for 1 d and then storage in a desiccator containing indicator drierite until use.

H/PVP. Orange powder. ^{1}H NMR (DMSO-d_6, ppm): 10.38 (s, 1H, Ar-OH), 9.00-8.30 (br, 2H, pyridinium in α position), 8.10-7.20 (br, 2H, pyridinium in β position), 7.76 (m, 6H, Ar-N=), 6.92 (d, 2H, J=8.4 Hz, Ar-O), 4.09 (br, 3H, CH_3-N^+), 2.20-0.60 (br, 3H, CH_2CH in backbone).

Me/PVP. Orange powder. ^{1}H NMR (DMSO-d_6, 90 °C, ppm): 8.74-8.40 (br, 2H, pyridinium in α position), 7.84-7.74 (m, 6H, Ar-N=), 7.70-7.45 (br, 2H, pyridinium in β position), 7.07 (d, 2H, J=8.9Hz, Ar-O), 4.40-4.00 (br, 3H, CH_3-N^+), 3.86 (s, 3H, OCH_3), 2.40-1.40 (br, 3H, CH_2CH in backbone).

Hex/PVP. Orange powder. ^{1}H NMR (DMSO-d_6, 90 °C, ppm): 8.80-8.40 (br, 2H, pyridinium in α position), 8.10-7.40 (br, 2H, pyridinium in β position), 7.90-7.70 (m, 6H, Ar-N=), 7.06 (d, 2H, J=9.0 Hz, Ar-O), 4.35-4.10 (br, 3H, CH_3-N^+), 4.06 (t, 2H, J=6.5 Hz, OCH_2), 2.40-1.55 (br, 3H, CH_2CH in backbone), 1.75 (m, 2H, J=6.8 Hz, OCH_2-*CH_2*), 1.44 (m, 2H, J=7.7 Hz, $O(CH_2)_2$-*CH_2*), 1.24 (m, 4H, $O(CH_2)_3$-*CH_2CH_2*)), 1.00 (t, 3H, J=7.1 Hz, -CH_3).

Ch*/PVP. Orange powder. ^{1}H NMR (DMSO-d_6, 90 °C, ppm): 8.90-8.40 (br, 2H, pyridinium in α position), 8.10-7.40 (br, 2H, pyridinium in β position), 7.90-7.70 (m, 6H,

Ar-N=), 7.09 (d, 2H, J=8.8 Hz, Ar-O), 4.40-4.05 (br, 3H, CH_3-N^+), 4.00-3.84 (m, 2H, OCH_2), 2.40-1.50 (br, 3H, CH_2CH in backbone), 1.86 (m, 1H, $CHCH_3$), 1.54 (m, 1H, CH_2CH), 1.32 (m, 1H, CH_2CH), 1.00 (d, 3H, J=6.8 Hz, $CHCH_3$), 0.94 (t, 3H, J=7.5 Hz, CH_2CH_3).

MO/PDM. Red powder. ^{1}H NMR (DMSO-d_6, 110 °C, ppm): 7.81 (d, 2H, J=7.8Hz, Ar-SO_3^-), 7.75 (d, 2H, J=8.8Hz, Ar-N=), 7.71 (d, 2H, J=8.2Hz, Ar-N=), 6.80 (d, 2H, J=9Hz, Ar-N), 4.44 (br, 2H, N^+-CH_2), 3.81 (br, 2H, CH_2CO), 3.03 (s, 9H, $N^+(CH_3)_3$), 2.91 (s, 6H, $N(CH_3)$-), 2.25-1.50 (br, 2H, CH_2 in backbone), 1.16-1.06 (br, 3H, CH_3 in backbone).

To calculate the stoichiometric ratio of chromophore to the polyelectrolyte repeat unit in the PVP complexes (see ref. 30 for MO/PVP), the integration of the protons at the ortho position to the ether link in the chromophores (7.07 ppm generally, 6.92 ppm for H/PVP) was compared to that of the protons at the ortho position to the PVP pyridinium group (broad peak at 9.0-8.3 ppm). For MO/PDM, the integration of the proton at the ortho position to the amino substituent in MO (6.80 ppm) was compared to that of the protons on the ethyl spacer carbon next to the ammonium moiety in PDM (3.81 ppm). The NMR data as well as the elemental analyses (Table 5.1) indicate highly pure stoichiometric complexes. This is confirmed by EDS which indicated complete elimination of the sodium and iodide counterions.

We verified with the MO/PVP complex that a conventional polymer precipitation technique into water – profiting from the insolubility of the complexes in water – can be employed in the place of dialysis to purify the complexes. This is an advantage for preparing larger quantities of complex. To do this, the complex was prepared in solution as for the dialysis procedure, and then the solution was precipitated by dropwise addition into a large quantity of vigorously stirred Milli-Q water. The precipitate was filtered, put in clean Milli-Q water under stirring for a few hours, then filtered again. This cycle was repeated three times. Finally, the filtered solid was freeze-dried and dried under the same conditions as above. The NMR, EDS and XRD results for this complex were identical to those of the dialysis-purified complex.

In attempts to obtain recognizable POM textures, thin films were solvent-cast from dilute solutions of the complexes in DMF (< 1 % wt) onto clean glass slides. The slides were then covered with a beaker for ca. 2 weeks to allow very slow solvent evaporation,

followed by further drying in vacuum at 80 °C for at least 3 d to eliminate any remaining DMF. Thin films for obtaining UV-visible spectra and for the optical experiments (PIB, SRG) were prepared by spin-coating from a 3/1 DMF/dichloromethane solution (concentration: 3.5 wt % for the films used to obtain UV-visible spectra and 10 wt % for the films used for the optical experiments) onto clean glass slides, which were then vacuum dried at 100 °C for at least 3 d. The films for the optical experiments were sealed in N_2-flushed polyethylene zipper bags and placed in a Fisher mini-desiccator containing indicator drierite along with a small amount of P_2O_5 for storage and transportation. It is worth mentioning that all of the optical measurements were done in winter months, when the ambient humidity is low.

5.2.4 Instrumentation

Freeze-drying was effected using an FTS Systems FD-3-85A-MP freeze-dryer working at 1-3 mT with the condenser at -90 °C. ^{1}H NMR (500 MHz) spectra were obtained using a Bruker Avance spectrometer. CHNS elemental analysis was performed using a Fisons AE1108 analyzer, Na^+ and Br^- analysis using a FEI Quanta 200 FEG environmental scanning electron microscope equipped with an energy dispersive spectrometer (EDS), and thermogravimetric analysis (TGA) using a TA Instruments Hi-Res TGA 2950 analyzer at a heating rate of 10 °C/min under nitrogen atmosphere. Differential scanning calorimetry (DSC) was performed using a TA Instruments Q2000 DSC at heating and cooling rates of 10 °C/min and polarizing optical microscopy (POM) using a Zeiss Axioskop 40Pol microscope coupled with a Linkam Scientific Instrument THMS600 hot stage and a TMS94 temperature controller. X-ray diffraction (XRD) analysis on powder-like samples packed in 1.0-mm diameter glass capillaries (Charles Supper) was performed with a Bruker D8 Discover system equipped with a 2D Bruker AXS wire-grid detector, using Cu Kα radiation; sample temperature was controlled by a modified Instec HCS410 heating stage and STC200 temperature controller. The acquisition time for each diffractogram was 20-30 min. UV-visible spectra were obtained using a Varian Cary 500 Scan UV-Vis-NIR spectrophotometer. A Digital Instruments Dimension 3100 AFM working in tapping mode was used to measure the film thicknesses and to characterize the SRGs. The molecular length was calculated by HyperChem 7.0 (Hypercube), using the

MM+ molecular mechanics method, assuming most extended conformations and including van der Waals' radii at the extremities.

The photoinduced birefringence (PIB) experiments were done with the same setup as described elsewhere, except that the pump laser power was much lower in the present experiments.[30,41] The film was placed between two crossed polarizers in an Instec HCS302 hotstage flushed with dry N_2. An Ar ion laser (Spectra-Physics, Model 2030), operated at 488 nm and 320 mW/cm^2 (at this power, no bleaching was observed visually during the experiments) and set at a polarization angle of 45° with respect to the polarizer orientation, was used as the pump laser. A strongly attenuated He-Ne laser (model 1125P; JDS Uniphase), operated at 633 nm and 5.0 mW, was used as the probe laser. Optical erasure was effected using a quarter-wave plate inserted in the path of the pump laser to convert linearly polarized light into circularly polarized light. Photoinduced birefringence values (Δn) were calculated using the equation,

$$\frac{I}{I_o} = \sin^2\left(\frac{\pi|\Delta n|d}{\lambda}\right) \qquad (1)$$

where I is the photodiode transmission signal, I_o the photodiode signal in the absence of the sample (parallel polarizer/analyzer orientation), d the film thickness and λ the probe wavelength.

To measure a series of PIB writing-relaxation-erasure cycles at ambient temperature, the linearly polarized pump laser was turned on for 10 s to obtain birefringence and then turned off for 30 s to observe PIB relaxation. During this relaxation period, a quarter-wave plate was inserted into the optical route of the pump laser to convert it into circular polarization. At the end of the relaxation period, the laser was turned on for 30 s to erase the previously induced birefringence, and then turned off for 10 s to allow removal of the quarter-wave plate, after which the next cycle was begun. One PIB writing-relaxation-erasure cycle per temperature was measured at different temperatures during stepwise heating and cooling, all on the same spot (different from the spot used for the room temperature cycles). All of these experiments were done on the same day for all of the complexes except MO/PDM, for which they were done a few days later.

Surface relief gratings (SRGs) were inscribed at ambient temperature using a one-beam setup with a quarter-wave plate, an Ar laser operating at 488 nm (beam diameter

enlarged to 15 mm), with the angle between the propagation axis and mirror plane set at ca. 15°. The first order diffraction was tracked with a 633-nm probe laser. This is the same setup as used previously,[30] except that a higher writing power was used in the present experiments, which is more efficient for obtaining high quality SRG patterns.

AFM characterization of the gratings and film thickness measurements were done the day following SRG inscription. The gratings were again examined by AFM about two months later, to check their stability (a mark had been made on the SRGs to ensure inspection of the same region). The same film was used for both PIB and SRG experiments, except for the two MO complexes, for which separate films were prepared. For the films used in PIB experiments, three representative places along scalpel scratches were measured and the average thickness was used to calculate absolute PIB values using Equation 1. For the MO complex films that were used only for SRG, a single place along a scratch very close to the SRG-inscribed area was measured.

5.3 Results and discussion

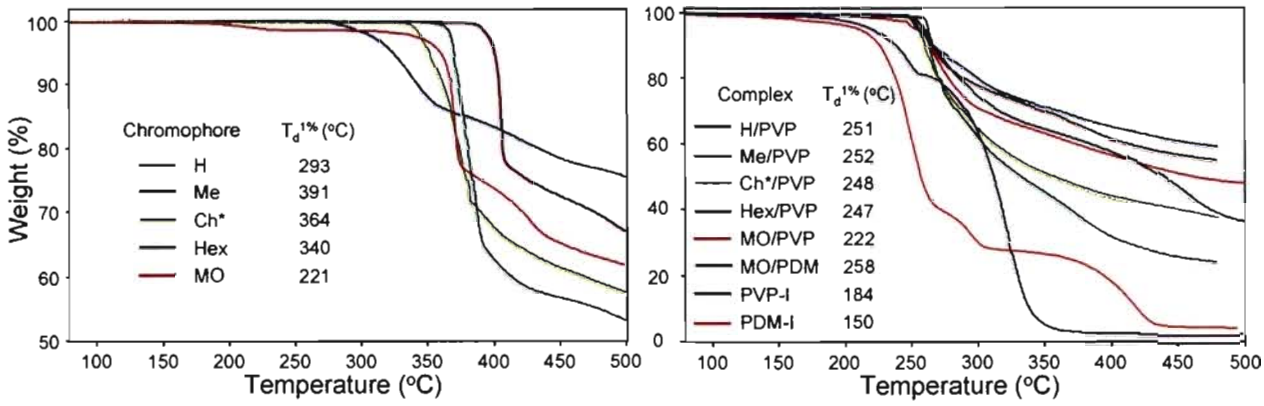

Figure 5.1 TGA thermograms (left) of the Na^+-neutralized chromophores and (right) of the complexes and I^--neutralized polyelectrolytes.

5.3.1 Thermal and structural analysis

The thermal stabilities of the chromophores and complexes were determined by dynamic TGA (Figure 5.1). The 1% weight loss ($T_d^{1\%}$) of all of the Na^+-neutralized

chromophores are above 200 °C, ranging from 220 °C to 390 °C in the order: MO < H < Ch* < Hex < Me. The lower $T_d^{1\%}$ for MO is a result of a small weight loss (2.7 %) well before the major loss occurs and that could be related to the dimethylamino terminal group, the only element in this chromophore that differs from the other chromophores. For the complexes, the beginning of major weight loss occurs in a much narrower temperature range (around 250 °C) than for the Na^+-neutralized chromophores and at significantly higher temperatures than for the two I^--neutralized polyelectrolytes.

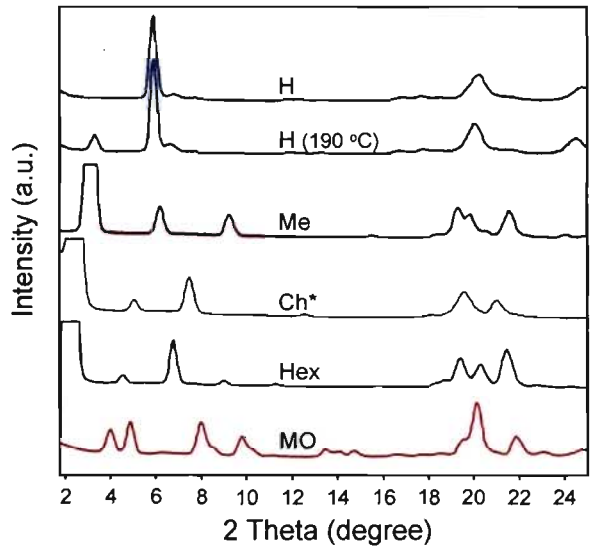

Figure 5.2 X-ray diffractograms of the Na^+-neutralized chromophores at room temperature (unless otherwise indicated).

The synthesized chromophores, like MO, are all crystalline up to decomposition as observed by POM. No peaks were observed in the DSC thermograms (scanned to about 40 °C below $T_d^{1\%}$), except for a broad low-enthalpy one at ca. 210 °C (ca. 200 °C on cooling) for chromophore H. The crystalline character of the chromophores at ambient temperature is confirmed by XRD (Figure 5.2 and Table 5.2). For the chromophores with alkoxy terminal groups, the three to four diffraction peaks at lower angles are equidistant, indicating lamellar-type crystalline structures, and their Bragg spacings indicate lamellar thicknesses that are between one and two calculated molecular lengths (Table 5.2). Chromophore H develops the lowest-angle peak only at high temperature (shown in Figure 5.2 at 190 °C), to which the low-enthalpy DSC transition may be related.

Table 5.2 Bragg spacings, $d_B(x)$ (x indicating the peak number in order of increasing 2θ), corresponding to the lower-angle X-ray diffraction peaks in Figure 5.2, and the calculated molecular lengths, L_{mol}, of the Na^+-neutralized chromophores.

Chromophore	$d_B(1)$ (Å)	$d_B(2)$ (Å)	$d_B(3)$ (Å)	$d_B(4)$ (Å)	L_{mol} [a] (Å)
H	26.8 [b]	14.9			18.5
Me	28.1	14.2	9.5		19.8
Ch*	35.4	17.4	11.8		23.5
Hex	38.8	19.3	13.0	9.8	26.1
MO	21.8	17.8	10.9		20.0

[a] Including sodium (ionic diameter of 1.9 Å). [b] This diffraction peak appeared at temperatures above 190 °C.

The complexes, unsurprisingly, have very different characteristics from the chromophores. Their DSC thermograms are given in Figure 5.3. In the first heating scan, the complexes show a very broad endotherm (as often observed in initial scans of polymeric materials), with a maximum at ca. 85 °C for Me/PVP and Ch*/PVP and at ca. 100 °C for all the others. Otherwise, transitions are observed only above 180 °C. These transitions are relatively broad and, in some cases, their appearance is similar to a glass transition. In others, they appear more like broad peaks, possibly superimposed on a glass-like transition. Because the temperatures above these transitions are fairly close to the onset of degradation (especially considering that the TGA determinations are dynamic, therefore underestimating degradation onset in conditions involving longer exposure times to high temperature), it is not easy to determine unequivocally the nature of these transitions.

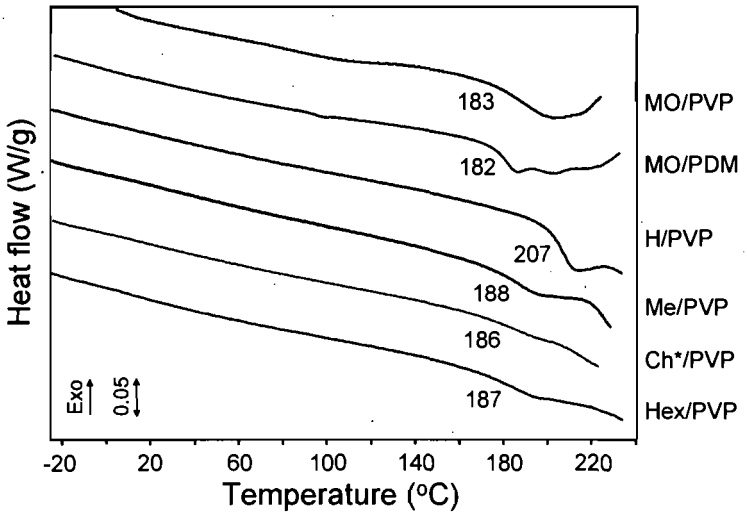

Figure 5.3 DSC thermograms of the complexes obtained during a second heating scan. The initial heating scan was to a maximum of 200 °C (180 °C for MO/PDM). The high temperature upturn in the MO/PVP thermogram is due to the onset of a sharp, intense exothermic peak related to the onset of degradation.[30] The numbers give the temperature in °C of the inflection point of the initial heat capacity change.[42]

Nevertheless, different pieces of information can be brought to bear in trying to identify them. First, X-ray diffractograms, given in Figure 5.4 for 160 °C and ambient temperature, show that there is no detectable crystallinity in the complexes (including in the as-prepared samples, for which the diffractograms are almost identical to those in Figure 5.4b except that the weak peaks marked with arrows are usually less or not at all visible); thus these transitions cannot be melting points. On the other hand, XRD indicates that the complexes have disordered liquid crystal (LC) structure (to be further discussed below), so that the transitions may be a glass transition (which can include an enthalpic peak), a LC-isotropic transition, or a LC-LC transition. POM observations indicate that the complexes with an alkoxy tail are birefringent to temperatures well above the transition (shown in Figure 5.5 for Hex/PVP), indeed until degradation becomes obvious. At the same time, it was noted that the samples remain powder-like, with no physical deformation possible, until the transition is passed. Above it, the powder-like grains begin to coalesce somewhat, although the material remains highly viscous and hardly spreads under manual pressure. This behavior strongly suggests that the transition is a glass transition in these cases. XRD at high temperature seems to support this assignment, at least for Hex/PVP and Ch*/PVP,

for which the small angle peak in the diffractograms acquired at 230 and 200 °C,[43] respectively, was essentially unchanged from the immediately preceding diffractograms obtained at 160 °C (for Me/PVP, in contrast, this peak in a diffractogram obtained at 210 °C was broadened and much reduced in intensity compared to the preceding 160 °C diffractogram). The resistance to spreading above the transition can be attributed to the strong ionic interactions and high molecular weight of the polymer resulting in a high-modulus rubbery plateau region with low deformability.[44]

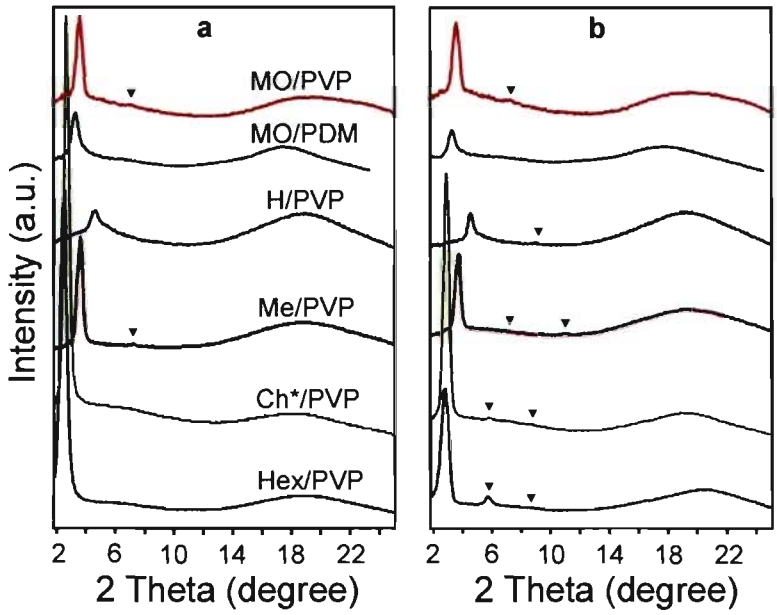

Figure 5.4 X-ray diffractograms of the complexes (a) at 160 °C (the maximum temperature in the heating-cooling cycle) and (b) at ambient temperature after cooling from 160 °C. Weak higher order diffraction peaks are indicated by arrows.

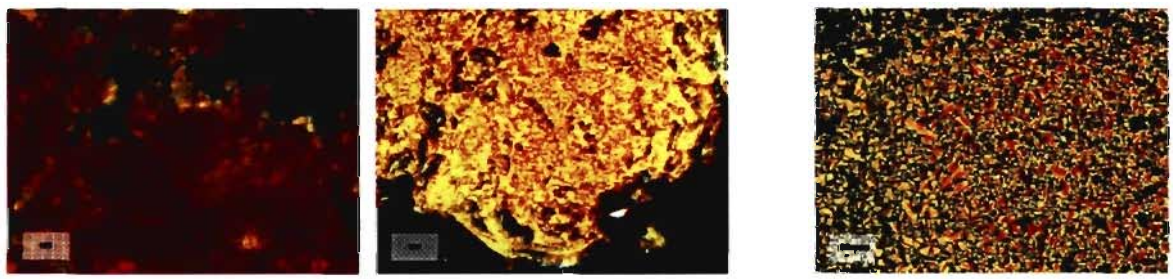

Figure 5.5 Polarizing optical micrographs for Hex/PVP in powder form at low and high temperature (left pair) and for a solution-cast film of Me/PVP (right). The scale bars represent 20 μm.

For MO/PVP, which is also intractable and birefringent until degradation, an apparent enthalpy change at ca. 185 °C in its DSC thermogram (reproduced in Figure 5.3) was assigned tentatively to a glass transition previously.[30] The parallel with the above complexes supports this assignment. The transition region in MO/PDM, which occurs in the same temperature range as MO/PVP, was more difficult to evaluate, particularly because this material had a fluffy rather than powdery aspect and appeared glassy in the microscope, which made any indication of coalescence impossible to see. Birefringence in this complex was much less pronounced than in the alkoxy-tailed complexes. It appeared to decrease slightly in the 190-200 °C region (without increasing again after cooling from that point), but otherwise remained to higher temperatures until degradation set in (as occurred, e.g., after a few minutes at 220 °C). In parallel, an XRD diffractogram obtained at 200 °C showed a broadened low-angle peak compared to lower temperature diffractograms. For H/PVP, clearer birefringence more obviously decreased, but very gradually, as the transition region was crossed (although some residual birefringence remained), and seemed to increase again to a small extent when decreasing the temperature (without any further development of birefringence after annealing, e.g. for a day at 160 °C). The observation that the birefringence is only partly reversible on cooling might be due to the high viscosity of this H-bonding material that restricts growth of mesophase domains (as observed in other ion-containing LC polymer complexes[27,45]), but possibly also to a beginning of degradation, especially considering that the transition region in this case is higher in temperature than for the other complexes (which can be attributed to H-bonding interactions). Although the exact nature of the transition region for H/PVP cannot be pinpointed with certainty, the decrease in birefringence suggests a combination of a glass transition and isotropization, which may account for its appearance as more like a peak compared to the alkoxy-tailed complexes. It is clear, in any case, that all of the complexes have liquid crystalline order up to high temperatures, even up to degradation temperature, as well as very high glass transition temperatures that are hardly affected by the incorporation of flexible tails.

The X-ray diffractograms in Figure 5.4 illustrate the essentially constant packing structure of the complexes between ambient and high temperature, except that weak higher order peaks are more visible at ambient for most of the complexes. The very high intensity

of the first-order peak relative to the wide-angle halo, combined with its narrowness, for Ch*/PVP, Hex/PVP and, to a lesser extent, for Me/PVP and MO/PVP, is consistent with the high birefringence observed (at high temperatures) in POM for these samples, and is indicative of well-developed, long-range LC order. In contrast, H/PVP and MO/PDM have a much weaker and somewhat broader low-angle peak, in accordance with weaker birefringence detected in POM.

As shown in Table 5.3, the different diffraction order peaks (up to three) are equidistant. This, combined with the absence of wide-angle peaks is indicative of lamellar packing of the smectic A or C type. The fact that the Bragg spacings determined from these peaks are similar to the calculated molecular lengths (Table 5.3) favors a single-layer or effective single-layer smectic A assignment, assuming side-by-side ordering of the ionic groups relative to the molecular long axis. This was also concluded previously for MO/PVP, for which a fully interdigitated bilayer structure, resulting in an effective single-layer periodicity, was proposed.[30] This same packing structure appears to apply to all of the complexes investigated.

Table 5.3 Bragg spacings, $d_B(x)$ (x indicating the peak number in order of increasing 2θ), corresponding to the lower-angle X-ray diffraction peaks in Figure 5.4b, and the calculated molecular lengths, L_{mol}, of the complexes investigated.

Complex	$d_B(1)$ (Å)	$d_B(2)$ (Å)	$d_B(3)$ (Å)	L_{mol} [a] (Å)
H/PVP	19.4	9.8		21.7
Me/PVP	24.0	11.7	8.0	23.9
Ch*/PVP	30.5	15.2	10.1	29.3
Hex/PVP	31.5	15.3	10.2	30.3
MO/PVP	24.2	12.1		23.3
MO/PDM	27.4			25.7

[a] Mesogen and backbone are assumed to be placed side by side relative to the molecular long axis.

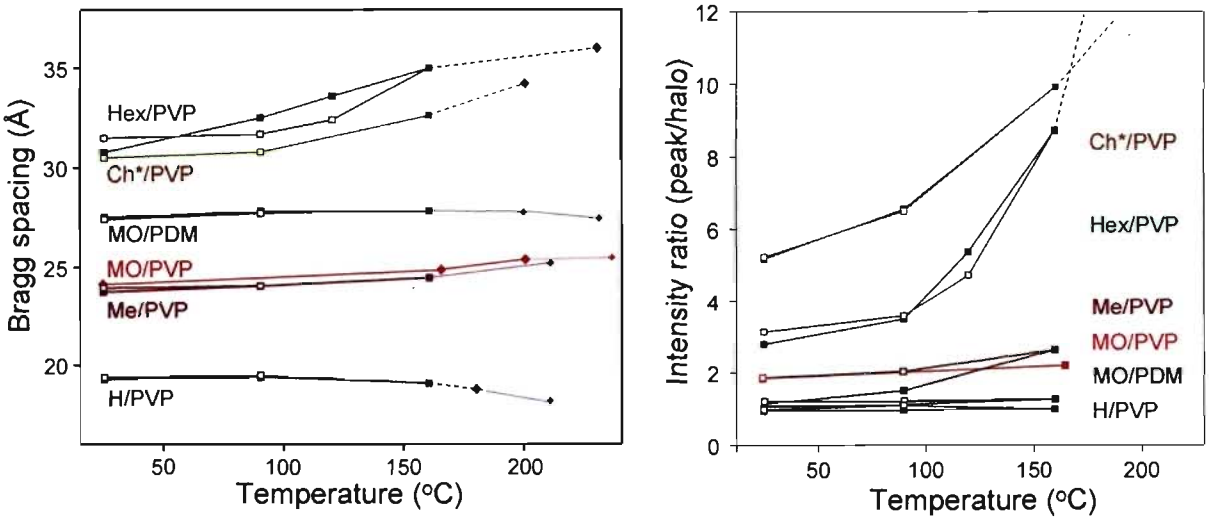

Figure 5.6 Bragg spacing and intensity (relative to the maximum intensity of the wide-angle halo) of the first order diffraction peak as a function of temperature for the complexes during heating (closed symbols) and subsequent cooling (open symbols). The temperatures below 160 °C for which only open symbols are visible have closed symbols coincident with the open ones. The points (lozenges) above 160 °C were obtained from a separate set of XRD experiments on samples heated up to degradation, with small lozenges indicating broadened, less intense peaks.

It is notable, however, that the Bragg spacings for Ch*/PVP and Hex/PVP increase reversibly with temperature (by 4-5 Å between ambient and the highest temperatures investigated), in contrast to the other complexes for which there is little or no evolution with temperature (see Figure 5.6). This is frequently associated with smectic C packing,[46] which, however, seems inconsistent with the similarity of the Bragg spacings to the calculated molecular lengths, unless a partially interdigitated tilted bilayer structure (e.g. interdigitated at the level of the alkoxy tails) has a tilt angle that fortuitously results in an apparent single-layer periodicity. It is also notable that, in parallel, the relative intensity of the low-angle peak for Hex/PVP and Ch*/PVP increases significantly (two- and three-fold, respectively) and reversibly with temperature between ambient and 160 °C (with still more increase at higher temperatures), whereas this effect is weak for Me/PVP and essentially nonexistent for the other three complexes (see Figure 5.6). Both phenomena thus appear to be related to the presence of a relatively long alkyl tail. Further clarification of the phase structure details might be obtained from oriented samples; however, the present complexes are not amenable to shearing due to their intractable character up to temperatures dangerously close to degradation onset.

It was previously found that solution-casting followed by slow evaporation of the solvent (DMF) yielded a well-defined focal conic texture for the MO/PVP complex, supporting the identification of its structural order as SmA-like.[30] This technique was also applied to the other complexes. Only Me/PVP gave a well-defined focal conic texture, shown in Figure 5.4. Unidentifiable textures (possibly ill-defined focal conics) were obtained for Hex/PVP and Ch*/PVP, whereas the texture surprisingly appeared more needle-like for H/PVP (micrographs shown in Supporting Information). MO/PDM showed no birefringence at all.

The thermal and structural order in these complexes may be compared with analogous all-covalent spacer-free side-chain (SC) polymers,[47] a number of which were among the first thermotropic SCLC polymers to be discovered[48,49] before the spacer concept was introduced by Finkelmann and coll.[50] in the late 1970s. In general, spacer-free SCLC polymers, many of them with biphenyl-based rigid cores, are characterized by high T_gs, usually in the 100-200 °C range (but not always detected), and smectic A mesophases that usually either become isotropic above 200 °C (sometimes well above) or are stable to degradation,[47,51] similar to the present complexes (whose apparent T_gs near 200 °C can be attributed to the strong ionic interactions). A study of such polymers based on the phenyl benzoate mesogen with variable length alkoxy tails indicates that both the T_g and clearing temperature decrease with increase in tail length up to 12 carbons, though both remain very high (180 to 130 and 254 to 208 °C, respectively).[52] The mesophases in the all-covalent polymers are typically bilayer or partially interdigitated bilayer phases,[48,51] in contrast to the effective single-layer phases of the present complexes. It is notable that the insertion of one or two methylene groups between a polyacrylate backbone and a biphenyl sidechain converts a smectic A polymer into an amorphous polymer.[53] This can be compared with the somewhat less well-ordered MO/PDM complex compared to the MO/PVP complex (as indicated by weaker birefringence and a less intense low-angle X-ray diffraction peak). It may also be mentioned that a nematic mesophase was reported for a spacer-free side-chain polymer with a carboxylic acid-terminated biphenyl mesogen,[54] which can be correlated perhaps with the weaker LC order observed in the hydrogen-bonding H/PVP complex.

A series of spacer-free hydrogen-bonded azo complexes with linear alkyl tails ranging from 6 to 10 carbons were similarly ordered into smectic A mesophases, in these

cases bilayered with some interdigitation of the alkyl tails.[55] However, the T_gs (ca. 35-60 °C) and isotropization temperatures (ca. 80-125 °C) are much lower than in the present spacer-free ionically-bonded azo complexes and in most of the spacer-free all-covalent polymers mentioned above. This illustrates the important role of the ionic interactions in the complexes for obtaining a high-T_g material, even when alkyl tails are present (e.g. Hex/PVP).

5.3.2 Photoinduced birefringence (PIB)

The UV-visible spectra of the spin-coated films are given in Figure 5.7. The MO complexes show a π-π* absorption maximum at 410 nm, along with a distinct shoulder near 480 nm. The maximum is close to that observed for MO in solvents like benzene, dioxane and acetone.[56] The complexes with the synthesized chromophores show a strong π-π* absorption maximum at ca. 345 nm and a very weak band at ca. 450 nm that may originate from the n→π* transition, as typical for azobenzene-type molecules.[12]

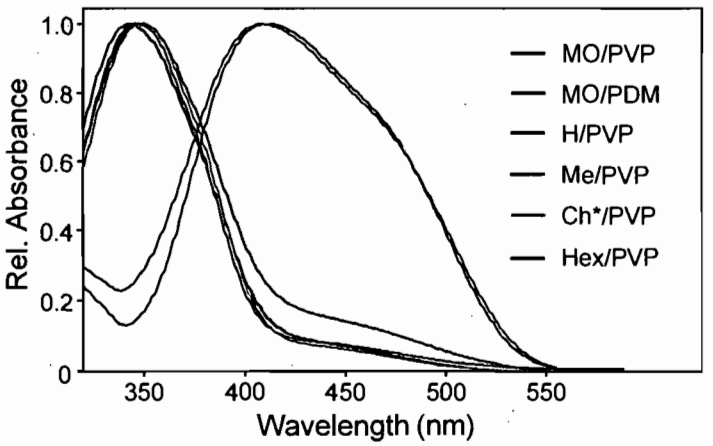

Figure 5.7 UV-visible spectra of spin-coated films of the complexes.

To evaluate the PIB properties of the complexes, a series of five or more consecutive cycles of writing (linearly polarized laser on for 10 s), relaxation (linearly polarized laser off for 30 s), and erasure (circularly polarized laser on for 30 s, then off for 10 s) were performed at room temperature for each complex. In addition, one writing-relaxation-erasure cycle was performed at each of several other temperatures during step-by-step

heating (maximum 180 °C) and cooling. Absolute PIB values were calculated from Equation 1 using the film thicknesses determined by AFM (given in Table 5.4).

Table 5.4 Thicknesses of the spin-coated films and amplitudes of the inscribed SRGs, as measured by AFM.

Complex	Film thickness (nm)	SRG amplitude (nm)
MO/PVP	360[a], 305[b]	360
MO/PDM	540[a], 650[b]	305
H/PVP	620[c]	235
Me/PVP	660[c]	75
Ch*/PVP	740[c]	30
Hex/PVP	710[c]	0

[a] Film used for PIB only (three points measured). [b] Film used for SRG only (single point measured). [c] Film used for both PIB and SRG (three points measured).

The room temperature cycles are shown in Figure 5.8. Both writing and erasure of PIB is efficient, with good reproducibility, for all of the complexes (except for a slight increase in residual birefringence after erasure, most pronounced for Me/PVP). PIB writing is particularly efficient for MO/PVP and H/PVP. On the other hand, the maximum value of birefringence achieved at the end of the writing period and the relaxation behavior after removal of the writing laser vary from chromophore to chromophore.

In order to compare directly the PIB performances of the different complexes both at ambient and as a function of temperature, the birefringence at the end of the 10-s writing period (B_1) and the % ratio of the birefringence at the end of the 30-s relaxation period (B_2) to B_1, i.e. B_2/B_1*100, are plotted against temperature in Figure 5.9. The maximum temperature tested was 180 °C for all of the complexes except Hex/PVP, which no longer displayed any PIB by 150 °C. The PIB values that were obtained during cooling reproduce those obtained during heating very well, showing excellent reversibility. This reversibility indicates that there is no annealing effect in these complexes, as has been reported for some other photosensitive liquid crystalline polymer films.[29b,57]

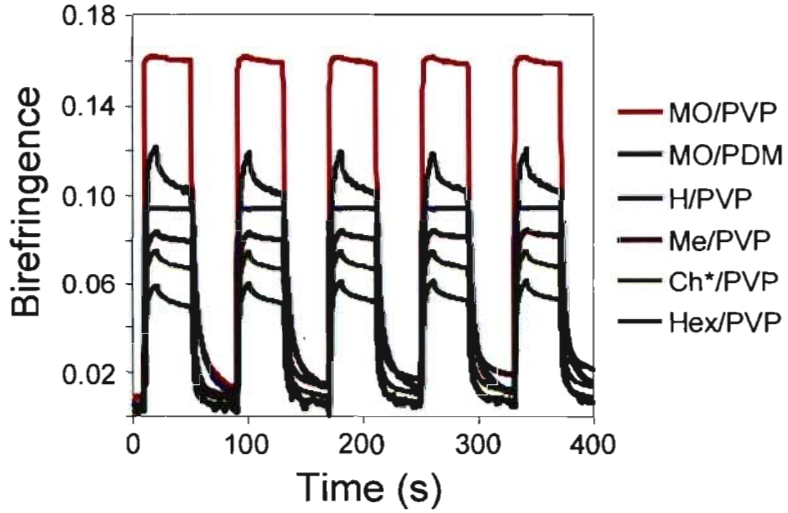

Figure 5.8 Inscription-relaxation-erasure cycles of photoinduced birefringence (PIB) in spin-coated films of the complexes.

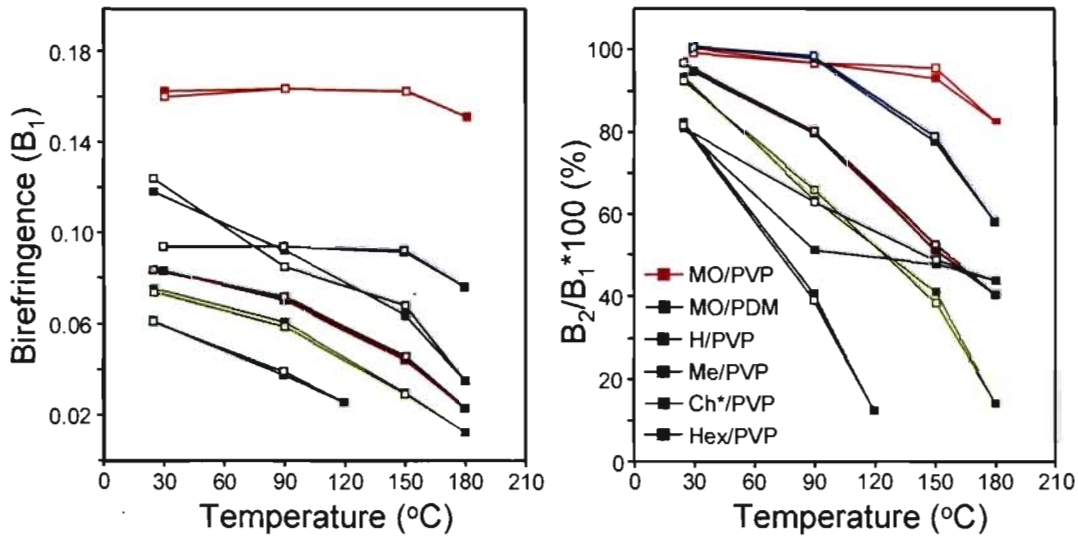

Figure 5.9 PIB of the different complexes as a function of temperature during heating (closed symbols) and cooling (open symbols): B_1 is the maximum PIB achieved at the end of the 10-s writing period, B_2 is the birefringence remaining at the end of the 30-s relaxation period. For temperatures where closed symbols are not visible, they are coincident with the open symbols.

In comparing the ambient temperature B_1 values, it is observed that MO/PVP has by far the highest B_1 at 0.16, followed by MO/PDM at 0.12, whereas the complexes with the synthesized chromophores all give a B_1 value of less than 0.1. This is first of all a consequence of the effect of the tail on the chromophore characteristics. In particular, the

stronger donor effect of the dimethylamino tail in MO compared to the alkoxy and hydroxyl tails influences B_1 both by modifying the wavelength of maximum absorption relative to that of the writing laser (they are much closer for the MO complexes) and by changing the molecular polarizability. Regarding the latter, high birefringence is related to a high degree of conjugation along the molecular length[58] and consequently a large anisotropy of polarizability.[59,60] For example, Ikeda and coll.[59] obtained extremely high PIB in an azotolane system, and Atwater and coll.[61] obtained high birefringence in a diazo system. Generally, stronger donor-acceptor substituents on the azo moiety increase the anisotropy of polarizability.[58] Thus, as indicated by the wavelength of maximum absorption (Figure 5.7), the two MO complexes can be directly compared to each other and, separately, the other four complexes can be compared among one another.

To do this, examination of the PIB behavior as a function of temperature is particularly revealing. Comparing the two MO complexes, it is observed that MO/PVP maintains its high B_1 to at least 150 °C with a very small decrease to 0.15 at 180 °C, whereas the B_1 value of MO/PDM decreases strongly with temperature. In parallel, the PIB in MO/PVP shows little or no relaxation, following removal of the writing laser, up to high temperature (B_2/B_1 decreases by only about 5% at 150 °C and less than 20% at 180 °C), whereas MO/PDM shows significant relaxation of PIB even at ambient (nearly 20%) up to more than 50% at 180 °C. Clearly, the more rigid PVP chain with its aromatic pyridine moiety compared to the more flexible PDM chain with its ethyl spacer and no aromatic unit is advantageous for obtaining high PIB that is stable to high temperatures (noting, however, that the PDM used has a much lower molecular weight than the PVP used, which can also have an effect). Significant PIB relaxation in MO/PDM undoubtedly takes place simultaneously with chromophore orientation during the writing period as well, which can explain its lower B_2 values compared to MO/PVP. This effect is exacerbated on increasing the temperature due to the increasing relaxation in MO/PDM.

The three complexes involving the chromophores with alkoxy tails also show decreasing B_1 values and increasing relaxation (decreasing B_2/B_1) with increase in temperature. The effects are more pronounced in the order Me < Ch* < Hex, which correlates very well with increasing length of the alkoxy moiety, clearly and unequivocally illustrating the deleterious effect of increasing flexibility, this time in the chromophore tail,

on high PIB. For Hex/PVP, the relaxation is so pronounced that no PIB at all can be inscribed at 150 °C. The fact that the PIB behavior in Ch*/PVP resembles that in Me/PVP more than that in Hex/PVP, despite its tail length being closer to that of Hex/PVP, can be attributed to the greater bulkiness of the Ch* tail due to the branching on the chiral carbon, which reduces its flexibility somewhat.

The H/PVP complex is an interesting case. The OH moiety composing the tail is well known to lead to hydrogen bonding, which can act as physical crosslinks. This effect is clearly observed in the B_1 values, which are constant to ca. 150 °C and decrease by ca. 0.02 units at 180 °C (very similar to MO/PVP). Furthermore, there is little PIB relaxation (B_2/B_1 is approximately constant) up to ca. 90 °C, above which it becomes quite pronounced, with a 40% reduction in B_2/B_1 at 180 °C. A possible reason for the much greater relaxation above 90 °C is that the H-bonds become labile at ca. 90 °C, thus allowing relaxation to take place, whereas at lower temperatures they prevent relaxation by acting as physical crosslinks. During the writing period, in contrast, the B_1 values are constant to a much higher temperature (until 180 °C), which could be related to the kinetics of H-bond exchange being slower than the writing process.

The above results illustrate the importance of minimizing flexible components in the materials in order to optimize the PIB response. On the other hand, a MO complex with n-butylated poly(4-vinyl pyridine) was shown as having no PIB relaxation following removal of the writing laser.[29b] Perhaps the fact that the n-butyl group is laterally positioned relative to the long molecular axis of the complex or that it is "isolated" by the rigid aromatic and ionic pyridine moiety that holds the complex together and to which it is attached minimizes its influence.

It is of interest to determine if liquid crystal order influences the PIB. In the series investigated, all of the complexes have LC order, but the extent of this order (correlation length, perfection) varies, as shown above. However, no relationship between the details of liquid crystal order and the PIB behavior is evident. For example, MO/PVP appears to have longer-range LC order and provides superior PIB performance than MO/PDM, whereas the complexes with the alkoxy-tailed chromophores have longer-range LC order but provide inferior PIB performance compared to the OH-tailed complex. Possibly, if LC order has a significant influence on PIB behavior, it is enough that this order is relatively

local such that the extent of order is not a significant factor. It must be kept in mind, also, that the state of order in the spin-coated films is not necessarily the same as in the powder products.

5.3.3 Surface relief gratings (SRGs)

Inscribed surface relief gratings were clearly visible by naked eye for most of the complexes, suggesting high quality gratings. For Ch*/PVP it was more weakly visible, whereas no evidence of a grating could be found for Hex/PVP. This correlates very well with the AFM observations of the gratings, as described below. An example of an SRG, inscribed on a film of MO/PVP and characterized by AFM, is illustrated in Figure 5.10. The grating is sinusoidal in nature, with a periodicity of 1 μm and an amplitude of 360 nm. The SRGs obtained in the other complexes were also all perfectly sinusoidal with a 1-μm periodicity; only their amplitudes varied, as indicated in Table 5.4. These amplitudes and the sinusoidal pattern were unchanged when checked again two months later, indicating their high temporal stability (at least at ambient temperature and in a dry atmosphere). No grating was found by AFM for Hex/PVP, consistent with the visual observation. The corresponding diffraction efficiencies for the SRG inscriptions are shown in Figure 5.11.

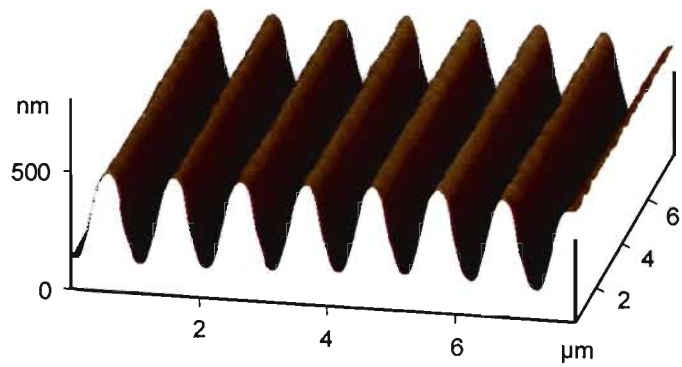

Figure 5.10 AFM surface profile of an optically inscribed SRG in a spin-coated film of MO/PVP exposed to a linearly polarized 488-nm Ar laser.

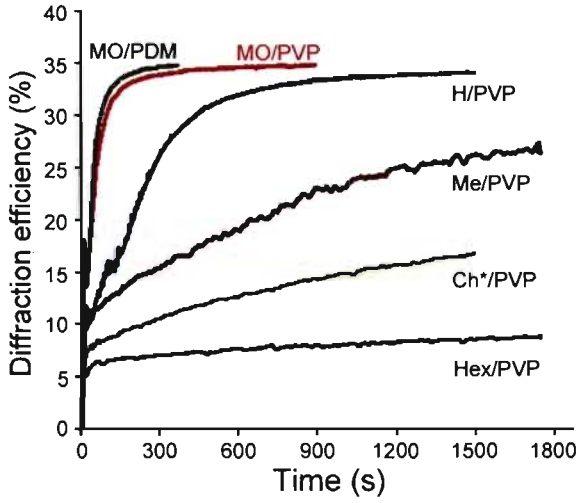

Figure 5.11 Diffraction efficiency during SRG inscription in spin-coated films of the complexes.

Table 5.4 indicates that the MO complexes have the highest SRG amplitudes and Figure 5.11 shows that they achieve higher diffraction efficiencies and reach a plateau value more quickly than the other complexes. This may be a consequence, in part, of the greater proximity of the pump laser wavelength (488 nm) to the wavelength of maximum absorption of the MO complex (450 nm) compared to that of the other complexes (~345 nm). However, the MO/PDM complex, whose maximum absorption wavelength is the same as for MO/PVP and whose diffraction efficiency behavior is also very similar, has a significantly lower-amplitude SRG, indicating a dependence on the molecular structure of the chromophore. This dependence can be associated in particular with the greater flexibility of PDM compared to PVP.

When the other complexes, all with a very similar wavelength of maximum absorption, are compared, it is observed that the diffraction efficiency curves and the SRG amplitudes follow the same order as the ambient temperature PIB values, thus showing the same dependence on the molecular characteristics of the chromophore tail. It is particularly striking that the hydrogen-bonding tail shows a diffraction efficiency and an SRG amplitude much higher than the alkoxy tail complexes. Indeed, its diffraction efficiency is similar to that of the MO complexes, except that the plateau value is attained more slowly (ca. 20 vs. 5 min). In contrast, Hex/PVP shows extremely low diffraction efficiency that may, in fact, be a result of a birefringence grating, since no SRG grating was found. For

comparison, it was reported that an octyl perfluorinated tail in a SCLC polymer also prevented SRG formation.[62] It may be added that we attempted to inscribe SRGs in a film of an azo-containing surfactomesogen/polyelectrolyte complex with a 6-carbon spacer [triethyl-6-(4-nitroazobenzene-4'-oxy)hexylammonium bromide complexed with poly(styrene sulfonate)], which is essentially amorphous and has a T_g of ca. 80 °C.[27] An SRG was visible by eye immediately after writing, but it faded within a few minutes (making this material useful, in fact, for optimizing the optical setup). All of these data indicate that flexible components in the molecular structure of these complexes, whether in the polyelectrolyte constituent or in the chromophore tail or spacer, detract from efficient diffraction and high quality SRGs.

5.4 Conclusions

We had previously shown that the ionic complexation (or ionic self-assembly, ISA[15]) of a commercially available spacer-free ionic dye, methyl orange (MO), with methylated poly(4-vinyl pyridine) (PVP) in stoichiometric proportion leads to a material that remains quite rigid up to degradation, that is characterized by SmA-like liquid crystal packing order, that gives impressively high and thermally stable photoinduced birefringence (PIB) and that is amenable to SRG inscription,[30] similar to a complex of MO with ethylated and n-butylated poly(4-vinyl pyridine).[29] Since these supramolecular polymers are quite easy to prepare [including purification by the classical polymer precipitation technique, notably in water (a "green solvent"), although we have preferred a dialysis procedure given the small amounts of sample prepared] and since systematic variants of small molecules like MO are easy to synthesize, they provide ideal systems to investigate the influence of different molecular parameters on their photonic properties. Although various photonic properties have been investigated in many all-covalent azo polymers, a good understanding of structure-property relations is far from complete, with the effect of flexible components and the role of liquid crystallinity being especially poorly circumscribed though some intriguing phenomena have been observed.[2]

In this paper, we have focused on the effect of introducing flexible elements in the ionic chromophore/polyelectrolyte molecular structure, particularly in the chromophore tail

but also in the polyelectrolyte. These modifications do not affect the overall thermal and structural properties of the complexes. The materials are all mechanically rigid, essentially to degradation, and what are concluded to be T_gs are all similar and very high (ca. 185 °C), with only an OH terminal group on the chromophore causing a mild increase of ca. 20 °C probably due to H-bonding. They also all display basically similar lamellar liquid crystal order (appearing to be of the single-layer SmA type) to at least the T_g and usually until degradation, just like MO/PVP. Only the degree of LC order varies somewhat, with longest-range order observed for the complexes with alkoxy tails and the shortest-range order for the complex with the OH tail as well as for the MO complex with methylated poly(dimethylaminoethyl methacrylate) (PDM), which has a short flexible spacer and lacks a rigid aromatic moiety. The lamellar thicknesses are generally invariant with temperature, except for some increase with temperature for the complexes with the longer alkoxy tails (possibly suggesting tilted lamellar phases), and the long-range order of the latter also reversibly increases with temperature.

On the other hand, the introduction of flexible and other elements in the molecular structure of the complexes strongly influences the photonic properties investigated, far outweighing any potential influence of the details of LC order. In general, both PIB writing and erasure is efficient in the complexes. The highest PIB and the highest amplitude SRGs are obtained with the MO/PVP complex, which is also the most molecularly rigid complex. Its high PIB is maintained to high temperature (with only a small decrease at 180 °C) and, in parallel, the PIB relaxation is minimal to more than 150 °C. The substitution of PVP by the more flexible PDM results in significant PIB relaxation that is exacerbated by increasing temperature, with the consequence that the PIB obtained is greatly reduced, along with a reduction in the SRG amplitude (the much lower molecular weight of PDM compared to PVP may also play a role, although this did not change the T_g). The influence of flexible elements is observed more systematically and very clearly in the series of the PVP complexes with the alkoxy tailed chromophores. The longer the alkoxy tail is, the greater the PIB relaxation, the lower the PIB attained, the lower the stability of the PIB with temperature, and the lower the SRG amplitude (with all PIB lost below 150 °C and no SRG at all observed for the complex with the hexoxy tail) – this despite similar, very high T_gs. In contrast, the hydroxyl tailed chromophore complex shows little PIB relaxation until at

least 90 °C and therefore a higher PIB than for the alkoxy-tailed complexes that is maintained to high temperature, as well as a much higher SRG amplitude than for the alkoxy-tailed complexes. The increasing PIB relaxation above 90 °C is postulated to be related to H-bond lability having set in. Since little or no PIB relaxation is observed for the MO and OH-tailed complexes with PVP (until high temperature), the PIB attained must reflect the maximum PIB possible in the absence of relaxation for the chromophore cores and optical set-up and conditions used.

5.5 Acknowledgments

The financial support of NSERC Canada and FQRNT Québec is gratefully acknowledged. QZ thanks Université de Montréal for a final year graduate scholarship.

5.6 References

1. Barrett, C. J.; Mamiya, J.-i.; Yager, K. G.; Ikeda, T. *Soft Matter* **2007**, 3, 1249-1261. Ikeda, T.; Mamiya, J.-i.; Yu, Y. *Angew. Chem., Int. Ed.* **2007**, 46, 506-528.
2. Natansohn, A.; Rochon, P. *Chem. Rev.* **2002**, 102, 4139-4175.
3. Yesodha, S. K.; Pillai, C. K. S.; Tsutsumi, N. *Prog. Polym. Sci.* **2004**, 29, 45-74.
4. Kucharski, S. H., In *New Research on Optical Materials*, Litchitika, S. J., Ed.; Nova Science Publishers: **2007**; pp. 119-156.
5. Kumar, G. S.; Neckers, D. C. *Chem. Rev.* **1989**, 89, 1915-25.
6. Peters, M. V.; Stoll, R. S.; Kühn, A.; Hecht, S. *Angew. Chem., Int. Ed.* **2008**, 47, 5968-5972.
7. Balzani, V.; Credi, A.; Marchioni, F.; Stoddart, J. F. *Chem. Commun.* **2001**, 1860-1861.
8. Cheetham, A. G.; Hutchings, M. G.; Claridge, T. D. W.; Anderson, H. L. *Angew. Chem., Int. Ed.* **2006**, 45, 1596-1599.
9. Gorostiza, P.; Isacoff, E. Y. *Science* **2008**, 322, 395-399.
10. Woolley, G. A. *Acc. Chem. Res.* **2005**, 38, 486-493.
11. Wang, S.; Song, Y.; Jiang, L. *J. Photochem. Photobiol., C* **2007**, 8, 18-29.
12. Rau, H., *Photoisomerization of azobenzenes. In Photochemistry and Photophysics*, Rabek, J. K., Ed.; CRC Press: Boca Raton, FL., **1990**; Vol. 2, pp. 119-141.
13. Mamiya, J.-i.; Yoshitake, A.; Kondo, M.; Yu, Y.; Ikeda, T. *J. Mater. Chem.* **2008**, 18, 63-65.
14. Priimagi, A.; Vapaavuori, J.; Rodriguez, F. J.; Faul, C. F. J.; Heino, M. T.; Ikkala, O.; Kauranen, M.; Kaivola, M. *Chem. Mater.* **2008**, 20, 6358-6363. Priimagi, A.; Kaivola, M.; Rodriguez, F. J.; Kauranen, M. *Appl. Phys. Lett.* **2007**, 90, 121103/1-121103/3.

15. Faul, C. F. J.; Antonietti, M. *Adv. Mater.* **2003**, 15, 673-683.
16. Everaars, M. D.; Marcelis, A. T. M.; Sudhölter, E. J. R. *Liebigs Ann./Recl.* **1997**, 21-26. Nieuwkerk, A. C.; Marcelis, A. T. M.; Koudijs, A.; Sudhölter, E. J. R. *Liebigs Ann./Recl.* **1997**, 1719-1724.
17. Stumpe, J.; Goldenberg, L.; Kulikovska, O. Film forming material and preparation of surface relief and optically anisotropic structures by irradiating a film of the said material. WO2006024500, **2006**.
18. Zakrevskyy, Y.; Stumpe, J.; Faul, C. F. J. *Adv. Mater.* **2006**, 18, 2133-2136. Guan, Y.; Antonietti, M.; Faul, C. F. J. *Langmuir* **2002**, 18, 5939-5945.
19. MacKnight, W. J.; Ponomarenko, E. A.; Tirrell, D. A. *Acc. Chem. Res.* **1998**, 31, 781-788.
20. Antonietti, M.; Thünemann, A. *Curr. Opin. Colloid Interface Sci.* **1996**, 1, 667-671.
21. Zhou, S.; Chu, B. *Adv. Mater.* **2000**, 12, 545-556.
22. Tsiourvas, D.; Paleos, C. M.; Skoulios, A. *Macromolecules* **1999**, 32, 8059-8065.
23. Ujiie, S.; Iimura, K. *Macromolecules* **1992**, 25, 3174-3178.
24. Masson, P.; Guillon, D. *Mol. Cryst. Liq. Cryst.* **2001**, 362, 313-346.
25. Tibirna, C. M.; Bazuin, C. G. *J. Polym. Sci., Part B: Polym. Phys.* **2005**, 43, 3421-3431. Bazuin, C. G.; Tork, A. *Macromolecules* **1995**, 28, 8877-8880.
26. Xiao, S.; Lu, X.; Lu, Q.; Su, B. *Macromolecules* **2008**, 41, 3884-3892.
27. Zhang, Q.; Bazuin, C. G. *Macromolecules*, submitted.
28. Priimagi, A.; Cattaneo, S.; Ras, R. H. A.; Valkama, S.; Ikkala, O.; Kauranen, M. *Chem. Mater.* **2005**, 17, 5798-5802.
29. (a) Xiao, S.; Lu, X.; Lu, Q. *Macromolecules* **2007**, 40, 7944-7950. (b) Pan, X.; Xiao, S.; Wang, C.; Cai, P.; Lu, X.; Lu, Q. *Opt. Commun.* **2009**, 282, 763-768.
30. Zhang, Q.; Bazuin, C. G.; Barrett, C. *J. Chem. Mater.* **2008**, 20, 29-31.
31. Horn, D. *Prog. Coll. Polym. Sci.* **1978**, 65, 251-64.
32. Goddard, E. D., In *Interactions of Surfactants with Polymers and Proteins*, Goddard, E. D.; Ananthapadmanabhan, K. P., Eds. CRC Press: Boca Raton, **1993**; ch. 4. Lindman, B.; Thalberg, K., *ibid.*, ch. 5.
33. Wang, G.-J.; Engberts, J. B. F. N. *Langmuir* **1994**, 10, 2583-2587.
34. Abdallah, D.; Cully, M. J.; Li, Y.; Shipp, D. A. *Colloid Polym. Sci.* **2008**, 286, 739-745.
35. Engelking, J.; Menzel, H. *Thin Solid Films* **1998**, 327-329, 90-95.
36. Kunitake, T.; Okahata, Y.; Shimomura, M.; Yasunami, S.; Takarabe, K. *J. Am. Chem. Soc.* **1981**, 103, 5401-5413. Tian, Y.; Umemura, J.; Takenaka, T.; Kunitake, T. *Langmuir* **1988**, 4, 1064-1066.
37. Panambur, G.; Robert, C.; Zhang, Y.; Bazuin, C. G.; Ritcey, A. M. *Langmuir* **2003**, 19, 8859-8866. Panambur, G.; Zhang, Y.; Yesayan, A.; Galstian, T.; Bazuin, C. G.; Ritcey, A. M. *Langmuir* **2004**, 20, 3606-3615.
38. Advincula, R. C., In *Handbook of Polyelectrolytes and Their Applications*, Tripathy, S. K.; Kumar, J.; Nalwa, H. S., Eds. American Scientific: Stevenson Ranch, CA, **2002**; Vol. 1, pp. 65-97.
39. Kawaguchi, D.; Satoh, M. *Macromolecules* **1999**, 32, 7828-7835.
40. Fang, Z.; Kennedy, J. P. *J. Polym. Sci., Part A: Polym. Chem.* **2002**, 40, 3679-3691.
41. Natansohn, A.; Rochon, P.; Gosselin, J.; Xie, S. *Macromolecules* **1992**, 25, 2268-2273.

42. The DSC transition region tends to decrease slightly on each subsequent heating scan, possibly due to a small amount of degradation in the upper temperature range.
43. In these two cases, a second diffractogram was acquired immediately after the first one at the same two temperatures (each acquisition lasting for 30 min), for which the peak was broadened considerably, reduced in intensity and displaced to lower angles, no doubt a result of degradation.
44. Ferry, J. D., *Viscoelastic Properties of Polymers.* 3rd ed.; John Wiley & Sons: New York, **1980**.
45. Vuillaume, P. Y.; Sallenave, X.; Bazuin, C. G. *Macromolecules* **2006**, 39, 8339-8346.
46. Heinrich, B.; Guillon, D. *Mol. Cryst. Liq. Cryst.* **1995**, 268, 21-43.
47. Percec, V.; Pugh, C., In *Side Chain Liquid Crystal Polymers*, McArdle, C. B., Ed.; Chapman and Hall: New York, **1989**; pp. 44-53 and references therein.
48. Baccaredda, M.; Magagnini, P.; Pizzirani, G.; Giusti, P. *J. Polym. Sci., Polym. Lett. Ed.* **1971**, 9, 303-310. Newman, B. A.; Frosini, V.; Magagnini, P. L. *J. Polym. Sci., Polym. Phys. Ed.* **1975**, 13, 87-93. Frosini, V.; Levita, G.; Lupinacci, D.; Magagnini, P. L. *Mol. Cryst. Liq. Cryst.* **1981**, 66, 341-356.
49. Blumstein, A.; Hsu, E. C., In *Liquid Crystalline Order in Polymers*, Blumstein, A., Ed.; Academic Press: New York, **1978**; Chapter 3.
50. Finkelmann, H.; Ringsdorf, H.; Wendorff, J. H. *Makromol. Chem.* **1978**, 179, 273-276.
51. Âlimoglu, A. K.; Ledwith, A.; Gemmell, P. A.; Gray, G. W.; Lacy, F. R. S. D. *Polymer* **1984**, 25, 1342-1346. Duran, R.; Gramain, P.; Guillon, D.; Skoulios, A. *Mol. Cryst. Liq. Cryst., Lett. Sect.* **1986**, 3, 23-31. Duran, R.; Guillon, D.; Gramain, P.; Skoulios, A. *Makromol. Chem., Rapid Commun.* **1987**, 8, 321-324.
52. Konstantinov, I. I.; Sitnov, A. A.; Grebneva, V. S.; Amerik, Y. B. *Eur. Polym. J.* **1983**, 19, 327-331.
53. Magagnini, P. L.; Marchetti, A.; Matera, F.; Pizzirani, G.; Turchi, G. *Eur. Polym. J.* **1974**, 10, 585-591. Bresci, B.; Frosini, V.; Lupinacci, D.; Magagnini, P. L. *Makromol. Chem., Rapid Commun.* **1980**, 1, 183-186. Frosini, V.; Levita, G.; Lupinacci, D.; Magagnini, P. L. *Mol. Cryst. Liq. Cryst.* **1981**, 66, 341-356 (21-36).
54. Blumstein, A.; Blumstein, R. B.; Clough, S. B.; Hsu, E. C. *Macromolecules* **1975**, 8, 73-76.
55. de Wit, J.; van Ekenstein, G. A.; Polushkin, E.; Kvashnina, K.; Bras, W.; Ikkala, O.; ten Brinke, G. *Macromolecules* **2008**, 41, 4200-4204.
56. Karukstis, K. K.; Savin, D. A.; Loftus, C. T.; D'Angelo, N. D. *J. Colloid Interface Sci.* **1998**, 203, 157-163.
57. Kidowaki, M.; Fujiwara, T.; Morino, S. y.; Ichimura, K.; Stumpe, J. *Appl. Phys. Lett.* **2000**, 76, 1377-1379.
58. Simpson, S. H.; Richardson, R. M.; Hanna, S. *J. Chem. Phys.* **2007**, 127, 104901/1-104901/14.
59. Okano, K.; Shishido, A.; Ikeda, T.; Shiono, T. *Mol. Cryst. Liq. Cryst.* **2005**, 441, 275-285. Okano, K.; Shishido, A.; Tsutsumi, O.; Shiono, T.; Ikeda, T. *J. Mater. Chem.* **2005**, 15, 3395-3401. Okano, K.; Shishido, A.; Ikeda, T. *Adv. Mater.* **2006**, 18, 523-527. Okano, K.; Tsutsumi, O.; Shishido, A.; Ikeda, T. *J. Am. Chem. Soc.* **2006**, 128, 15368-15369.

60. Sekine, C.; Iwakura, K.; Konya, N.; Minai, M.; Fujisawa, K. *Liq. Cryst.* **2001**, 28, 1375-1387.
61. Lachut, B. L.; Maier, S. A.; Atwater, H. A.; de Dood, M. J. A.; Polman, A.; Hagen, R.; Kostromine, S. *Adv. Mater.* **2004**, 16, 1746-1750.
62. Paik, M. Y.; Krishnan, S.; You, F.; Li, X.; Hexemer, A.; Ando, Y.; Kang, S. H.; Fischer, D. A.; Kramer, E. J.; Ober, C. K. *Langmuir* **2007**, 23, 5110-5119.

5.7 Supporting information for Chapter 5

Polarizing optical micrographs (POMs) of solution-cast films of the complexes specified (solvent: DMF). The scale bars shown are for 20 μm.

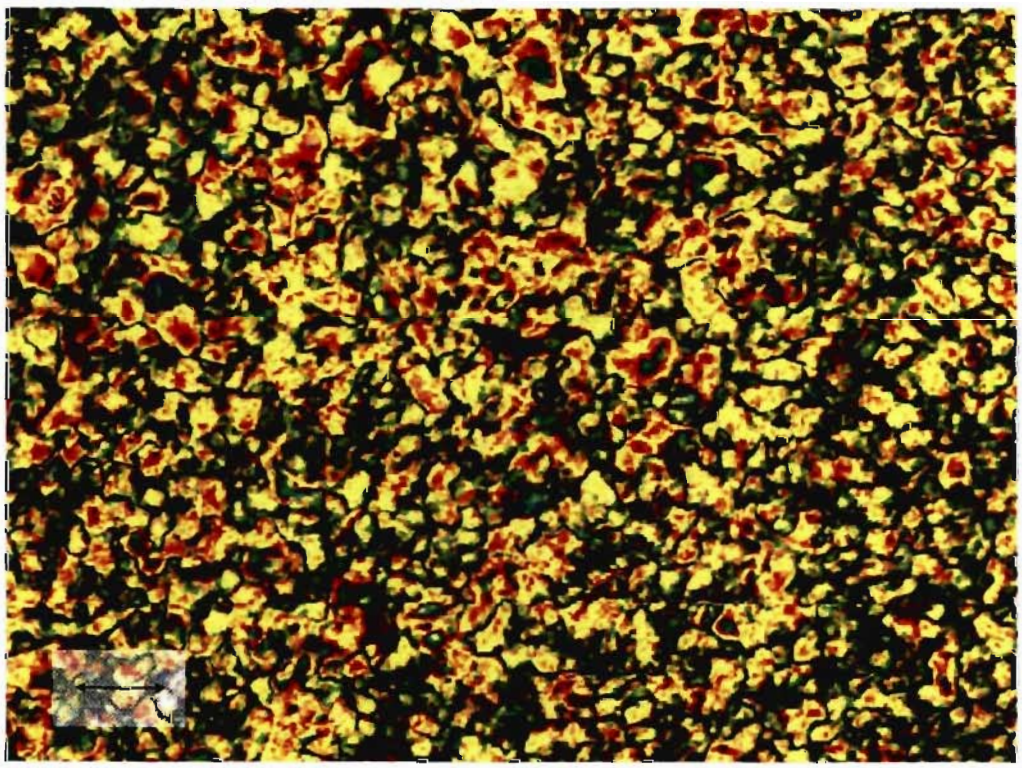

Figure 5.1S POM for Hex/PVP.

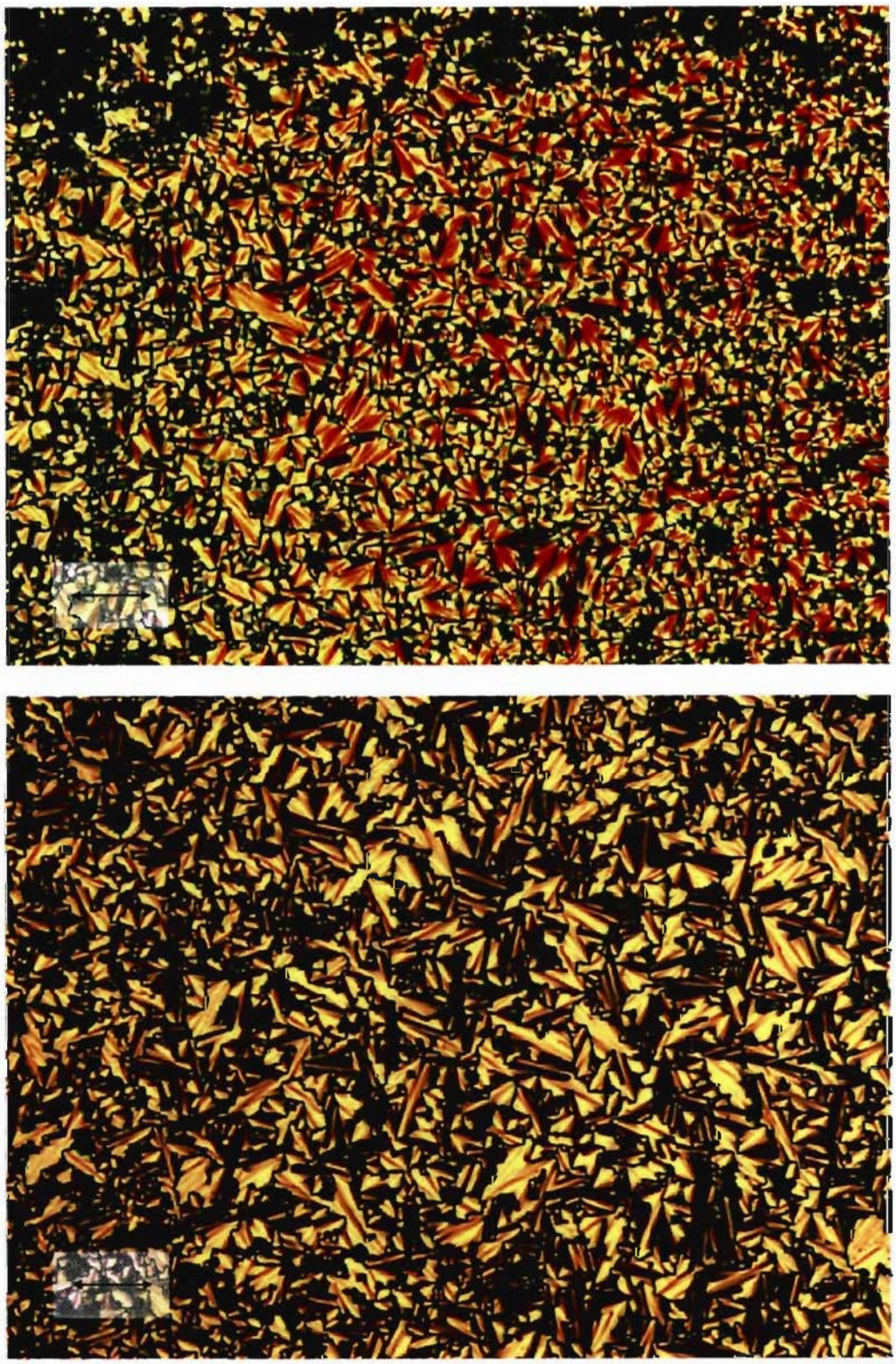

Figure 5.2S POM for Me/PVP (two images).

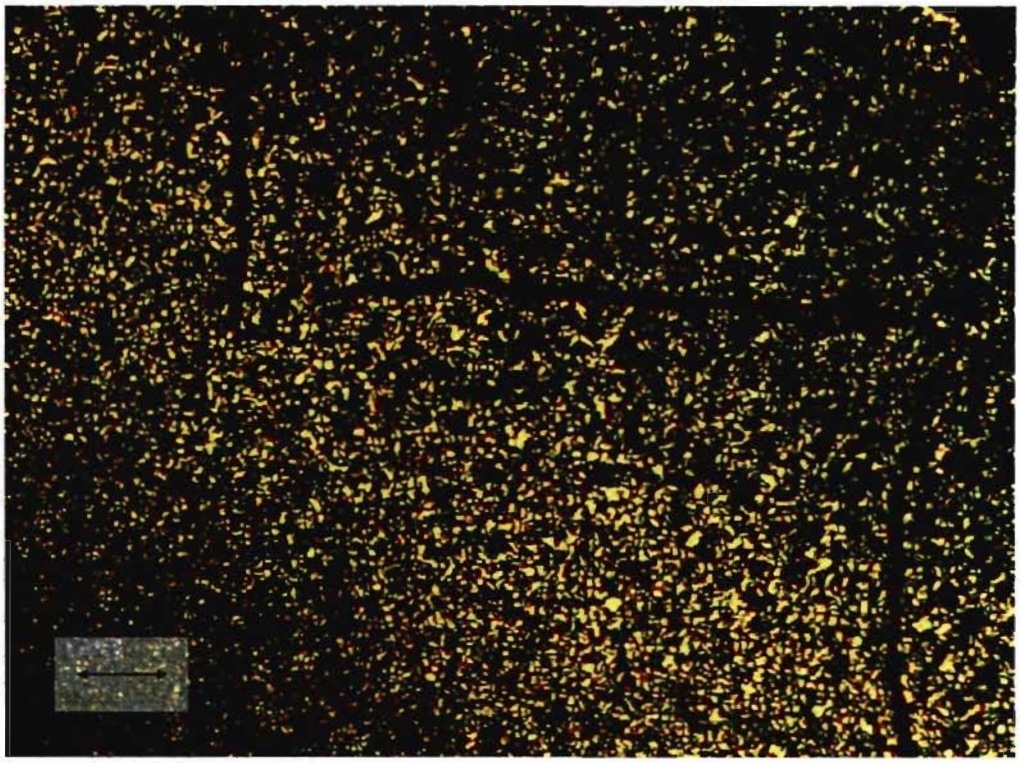

Figure 5.3S POM for Ch*/PVP.

Figure 5.4S POM for H/PVP.

Chapter 6: One-Pot Synthesis of Azo Dye/Surfactant Complexes and the Smectic T-like Mesophase

Abstract

A series of ionic complexes of an alkylated ionic azo dye and an oppositely charged surfactant were prepared from 1-bromoalkane and 4-hydroxyazobenzene sulfonate salt in DMF in a one-pot synthesis. The resulting complexes, with n-alkyl chains of 6-12 and 16 carbons, were all crystalline up to high temperature (136–156 °C). The complexes with n-dodecyl and n-hexadecyl chains formed a liquid crystalline mesophase with in-plane order of smectic T type at the level of the ionic groups. This phase was shown to undergo photoinduced isotropization on exposure to laser irradiation (488 nm) as detected by *in-situ* X-ray diffraction.

6.1 Introduction

Ionic liquid crystals have received much interest recently,[1] not only for their intrinsic high ion conductivity but also for their close relationship[2,3] to ionic liquids,[4] an environment-friendly medium for organic synthesis.[4] As one of the largest families of ionic liquid crystals, alkyl ammonium salts have been widely studied.[1] The simplest such salts are n-alkyl salts where the ionic group is a protonated primary amine.[1,5-7] Ionic liquid crystals with anionic moieties, like carboxylates, aromatic acid salts[8,9] or more complex carboxylates, have also been studied.[10-12]

In addition to the protonated amine salt, more stable quaternary ammonium salts have been investigated.[1] Alkyl trimethyl ammonium salts only show crystal-crystal phase transitions at high temperature (> 350 °C),[13] and decompose before melting.[14] This disadvantage can be addressed by replacing one of the methyl groups by n-propyl or 3-hydroxypropyl groups, leading to a smectic phase that becomes isotropic below 200 °C.[14] Thus, the introduction of a second bulky chain disturbs the crystalline packing and lowers the isotropization temperature. An interesting example is dialkyldimethylammonium bromide investigated by Skoulios and coll.[15] It was discovered that when the length of the alkyl chains is 12 to 18 carbons, and not necessarily the same for both, a smectic phase with in-plane tetragonal order (named the SmT phase) is formed.[15] It also appears to show a SmB phase below the isotropic phase.[16] A reinvestigation of the ammonium halide salt of diazabicyclo[2.2.2] alkane[17] revealed the same SmT structure.[18]

The chemical structures of dialkyl[19] dimethylammonium salts studied usually have halogens as counterions, especially bromide.[15,20-23] More complex counterions with multifunctional cores to bind dialkyldimethylammonium salts in disk-like form have also been employed.[24,25] They were expected to form columnar phases; however, surprisingly, only smectic phases were found.

Additional functionality can be introduced into ionic liquid crystals in view of specific applications. In particular, the azobenzene moiety, which is well-known for its photoisomerization process, is of particular interest for fabricating light-sensitive materials.[26-29] There have been a number of studies of the photo-response of small ionic molecules containing the azobenzene moiety.[30-33] An easy way to prepare such materials is

to combine alkyl chain salts with azobenzene-containing salts to obtain complexes of oppositely charged salts. Faul, Antonietti and coworkers synthesized a series of chromophoric ionic complexes composed of an azobenzene dye (e.g. ethyl orange) and dialkyldimethylammonium (and other) salts.[34,35] These complexes form crystalline or liquid crystalline phases (smectic and columnar LC phases were identified), and can show very good photoinduced performance.[36] It is of interest here to note that there is a change from the SmT mesophase to various more usual LC phases (stable up to degradation) when the bromide anion is replaced by the bigger ethyl orange anion.[15]

To our knowledge, none of the dye (or other) anions used so far with dialkyl ammonium salts contain long flexible tails,[34,35] in contrast to the short (forked) N,N-diethyl amino tail of ethyl orange.[36] In this study, we investigate a series of dye-surfactant complexes where long alkyl tails are present in the dye molecule as well as in the surfactant molecule (see Scheme 6.1). We anticipate that the incorporation of alkyl tails in the dye could increase (at least partly) the miscibility of dye and surfactant. This will possibly perturbsthe strong π-π interactions between dye molecules and hence lower the melting temperature (assuming that strong π-π interactions are the reason for their high values), and thus allow the appearance of thermotropic mesophases. In fact, as will be shown, a SmT-like phase is formed in the longest-chain compounds.

We previously reported on the synthesis of the sulfonated azo dye shown in Scheme 6.1.[37] We found serendipitously that it is possible to simultaneously alkylate this dye, synthesize a dialkyl ammonium cation, and complex the two components (Scheme 6.1). In this paper, we describe here this one-pot synthesis, and investigate the thermal and structural characteristics of the series of resulting complexes (indicated in Scheme 6.1, along with the nomenclature). Since many commercial sulfonate azo dyes have phenol groups[34,35] and are soluble in highly polar DMF, it is expected that they can form analogous complexes using the one-pot synthesis described here.[38]

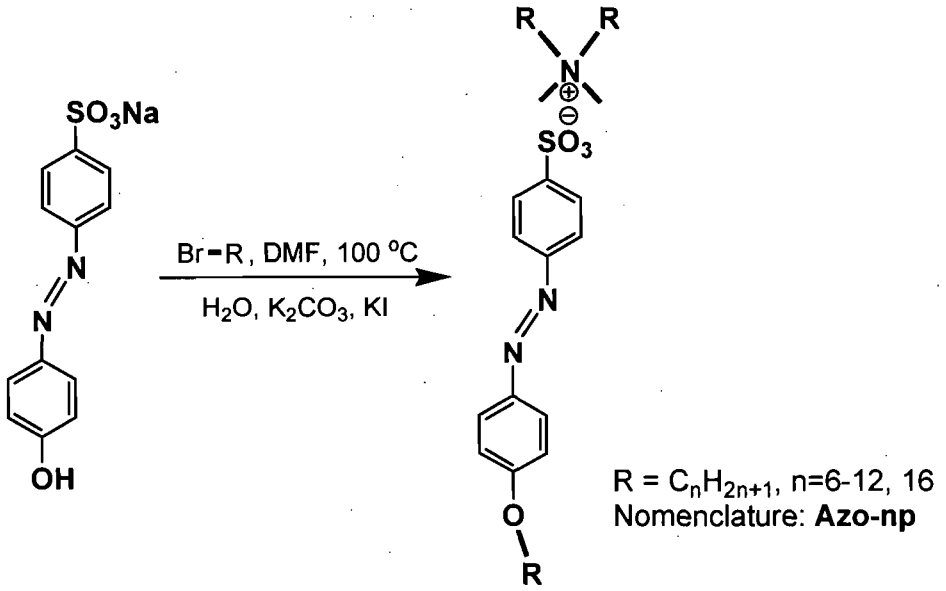

Scheme 6.1 One-pot synthesis of alkylated azo dye/dialkyldimethylammonium complexes. Some reactants and reaction sites are highlighted in red and blue, respectively.

6.2 Experimental section

6.2.1 Materials

The synthesis of 4-(4-hydroxyphenylazo)benzenesulfonic acid, sodium salt is reported elsewhere.[37] 1-Bromobutane (99%), 1-bromopentane (99%), 1-bromohexane (98%), 1-bromoheptane (99%), 1-bromooctane (99%), 1-bromononane (98%), 1-bromodecane (98%), 1-bromoundecane (98%), 1-bromododecane (97%), 1-bromohexdecane (97%), 1-bromodocosane (96%), anhydrous potassium carbonate (99.0+%) and potassium iodide (99.0%) were obtained from Sigma-Aldrich, and used as received. DMF (ACS grade) was obtained from EMD, and passed through drying columns (Glass Contour system). Other solvents for purification purposes were from EMD and A&C, and were used as received. Deionized water was obtained from a Millipore Gradient A10 Milli-Q system (resistivity 18.2 MΩ.cm at 25 °C).

6.2.2 Instruments

^{1}H NMR (400 MHz) spectra were obtained using a Bruker Avance spectrometer; CHNS elemental analysis using a Fisons AE1108 analyzer; energy dispersive analysis (EDS) of one sample with a FEI Quanta 200 FEG environmental scanning electron microscope (ESEM) attachment; thermogravimetric analysis (TGA) using a TA Instruments TGA Q500 analyzer at a heating rate of 10 °C/min under nitrogen atmosphere; differential scanning calorimetry (DSC) using a TA instruments Q1000 DSC at heating and cooling rates of 10 °C/min; and polarizing optical microscopy (POM) using a Zeiss Axioskop 40Pol microscope coupled with a Linkam Scientific Instrument THMS600 hot stage and a TMS94 temperature controller. X-ray diffraction (XRD) analysis with Cu Kα radiation was performed on powder samples packed in a 1.0-mm diameter glass capillary (Charles Supper), using a Bruker D8 Discover system equipped with a 2D Bruker AXS wire-grid detector, with sample temperature controlled by a modified Instec HCS410 heating stage and STC200 temperature controller. Each scan took 10-30 min. For a 2D diffractogram of an oriented sample, the exposure time was 4 h. The azimuthal distribution was smoothed by the Savitzky-Golay method[39,40] (polynomial 2, points 21-51) in GRAMS/AI 7.02 (Thermal Galactic). Single crystal X-ray data were obtained using a Bruker AXS Smart 6000-FR591 diffractometer. Molecular simulation was done by HyperChem 7.0 (Hypercube), using MM+ molecular mechanics and the conjugate gradient method with an RMS gradient of 0.2 kcal/Å·mol as the termination condition.

Light induced isotropization was studied by XRD coupled with a JDSU FCD488 solid state laser working at 488 nm with a power of 20 mW, using the same setup as reported elsewhere.[37] The laser impinged on the sample at an angle of about 30° relative to the X-ray beam. A hotstage was used to heat the sample (Azo-16p) to enter the lower temperature part of the mesophase, and held there. Then the laser was turned on. After 10-60 s, the X-ray beam was switched on and the diffractogram recorded for 10 min. Then, the laser was switched off, and a second diffractogram was recorded immediately. This procedure was repeated for two additional cycles.

6.2.3 Synthesis

All of the complexes were synthesized in the same way, unless otherwise specified. We described a representative synthesis procedure here for Azo-9p. To 170.5 mg of 4-(4-hydroxyphenylazo)benzenesulfonic acid, sodium salt (0.5678 mmol) were added 5 mL anhydrous DMF, giving a transparent solution. To this solution were added 313.9 mg (4 eq.) of anhydrous potassium carbonate and 94.3 mg (1 eq.) of potassium iodide. The mixture was heated to 100 °C with magnetic stirring for 5-10 min. Then, 0.649 mL (6 eq.) 1-bromononane were added all at once. The mixture was maintained at 100 °C for 24 h, cooled naturally to room temperature, and then poured into a large amount of deionized water. The precipitate was filtered and rinsed with more deionized water. Finally, the product was dissolved in chloroform, precipitated with ether, filtered, and then crystallized in acetone, yielding orange flake crystals. The flakes were dried in vacuum at 40 °C. In slight modifications, Azo-6p, 7p and 8p were not crystallized in acetone since the purity was already good after precipitation in H_2O. The reaction for Azo-10p took place at 80 °C for 5 d and in DMF. The product was not precipitated by chloroform/ether, but was crystallized from acetone. NMR (see below) and elemental analysis (Table 6.1) results are in agreement with the structure for all of the complexes prepared. A representative NMR spectrum (Azo-7p) is shown in Figure 6.1; the peaks assigned to the surfactant part match very well the spectrum for the same surfactant, but neutralized by bromine, provided by Sigma Aldrich. EDS was verified on Azo-6p, and it showed no evidence of any remaining inorganic ions. The yield for complexes with short alkyl tails ($n \leq 5$) was very low, possibly due to increasing solubility in H_2O, and thus were not studied. Azo-22p could not be prepared successfully because of the lesser reactivity of 1-bromodocosane with the phenol group in the azo dye.

A single crystal of Azo-6p was obtained successfully by diffusion of hexanes into an Azo-6p chloroform solution (3 wt%). Very thin single crystal flakes were obtained after about two weeks. A single crystal of Azo-16p obtained in the same way did not yield a satisfactory X-ray diffractogram.

Azo-6p. Orange powder. Yield 82%. ^{1}H NMR ($CDCl_3$, ppm): δ=8.04 (d, 2H, J=8.6 Hz, Ar-SO_3^-), 7.92 (d, 2H, J=9.0 Hz, Ar-N=), 7.88 (d, 2H, J=8.5 Hz, Ar-N=), 7.01 (d, 2H,

J=9.0 Hz, Ar-O), 4.06 (t, 2H, J=6.6 Hz, OCH_2), 3.40 (s, 4H, $CH_2N^+CH_2$), 3.32 (s, 6H, $N^+(CH_3)_2$), 1.84 (m, 2H, OCH_2CH_2), 1.68 (m, 4H, $CH_2CH_2N^+CH_2CH_2$), 1.51 (m, 2H, $OCH_2CH_2CH_2$), 1.42-1.26 (m, 16H, CH_2-$(CH_2)_n$-CH_3), 0.94 (t, 3H, J=7.0 Hz, CH_3 *in* hexyl group to O), 0.89 (t, 6H, J=6.9 Hz, CH_3 in hexyl group to N^+).

Azo-7p. Orange powder. Yield 60%. ^{1}H NMR ($CDCl_3$, ppm): δ=8.06 (d, 2H, J=8.3 Hz, Ar-SO_3^-), 7.93 (d, 2H, J=8.8 Hz, Ar-N=), 7.88 (d, 2H, J=8.4 Hz, Ar-N=), 7.01 (d, 2H, J=8.6 Hz, Ar-O), 4.06 (t, 2H, J=6.4 Hz, OCH_2), 3.41 (s, 4H, $CH_2N^+CH_2$), 3.32 (s, 6H, $N^+(CH_3)_2$), 1.84 (m, 2H, OCH_2CH_2), 1.70 (m, 4H, $CH_2CH_2N^+CH_2CH_2$), 1.50 (m, 2H, $OCH_2CH_2CH_2$), 1.44-1.20 (m, 22H, CH_2-$(CH_2)_n$-CH_3), 0.89 (t, 9H, CH_3).

Azo-8p. Orange powder. Yield 64%. ^{1}H NMR ($CDCl_3$, ppm): δ=8.06 (d, 2H, J=8.3 Hz, Ar-SO_3^-), 7.92 (d, 2H, J=8.8 Hz, Ar-N=), 7.88 (d, 2H, J=8.3 Hz, Ar-N=), 7.01 (d, 2H, J=8.8 Hz, Ar-O), 4.06 (t, 2H, J=6.6 Hz, OCH_2), 3.41 (s, 4H, $CH_2N^+CH_2$), 3.32 (s, 6H, $N^+(CH_3)_2$), 1.84 (m, 2H, OCH_2CH_2), 1.70 (m, 4H, $CH_2CH_2N^+CH_2CH_2$), 1.50 (m, 2H, $OCH_2CH_2CH_2$), 1.44-1.18 (m, 28H, CH_2-$(CH_2)_n$-CH_3), 0.89 (t, 9H, CH_3).

Azo-9p. Orange crystalline flakes. Yield 65%. ^{1}H NMR ($CDCl_3$, ppm): δ=8.06 (d, 2H, J=8.4 Hz, Ar-SO_3^-), 7.92 (d, 2H, J=8.9 Hz, Ar-N=), 7.88 (d, 2H, J=8.4 Hz, Ar-N=), 7.01 (d, 2H, J=8.9 Hz, Ar-O), 4.06 (t, 2H, J=6.5 Hz, OCH_2), 3.41 (s, 4H, $CH_2N^+CH_2$), 3.32 (s, 6H, $N^+(CH_3)_2$), 1.84 (m, 2H, OCH_2CH_2), 1.70 (m, 4H, $CH_2CH_2N^+CH_2CH_2$), 1.50 (m, 2H, $OCH_2CH_2CH_2$), 1.44-1.20 (m, 34H, CH_2-$(CH_2)_n$-CH_3), 0.89 (t, 9H, CH_3).

Azo-10p. Orange crystalline flakes. Yield 65%. ^{1}H NMR ($CDCl_3$, ppm): δ=8.04 (d, 2H, J=8.3 Hz, Ar-SO_3^-), 7.92 (d, 2H, J=8.8 Hz, Ar-N=), 7.88 (d, 2H, J=8.4 Hz, Ar-N=), 7.01 (d, 2H, J=8.9 Hz, Ar-O), 4.06 (t, 2H, J=6.5 Hz, OCH_2), 3.38 (m, 4H, $CH_2N^+CH_2$), 3.31 (s, 6H, $N^+(CH_3)_2$), 1.84 (m, 2H, OCH_2CH_2), 1.67 (m, 4H, $CH_2CH_2N^+CH_2CH_2$), 1.50 (m, 2H, $OCH_2CH_2CH_2$), 1.43-1.16 (m, 40H, CH_2-$(CH_2)_n$-CH_3), 0.88 (m, 9H, CH_3).

Azo-11p. Orange crystalline flakes. Yield 59%. ^{1}H NMR ($CDCl_3$, ppm): δ=8.06 (d, 2H, J=8.4 Hz, Ar-SO_3^-), 7.92 (d, 2H, J=8.9 Hz, Ar-N=), 7.88 (d, 2H, J=8.4 Hz, Ar-N=), 7.01 (d, 2H, J=8.9 Hz, Ar-O), 4.06 (t, 2H, J=6.6 Hz, OCH_2), 3.41 (m, 4H, $CH_2N^+CH_2$), 3.32 (s, 6H, $N^+(CH_3)_2$), 1.84 (m, 2H, OCH_2CH_2), 1.71 (m, 4H, $CH_2CH_2N^+CH_2CH_2$), 1.50 (m, 2H, $OCH_2CH_2CH_2$), 1.44-1.20 (m, 46H, CH_2-$(CH_2)_n$-CH_3), 0.89 (m, 9H, CH_3).

Azo-12p. Orange crystalline flakes. Yield 56%. ^{1}H NMR ($CDCl_3$, ppm): δ=8.05 (d, 2H, J=8.3 Hz, Ar-SO_3^-), 7.92 (d, 2H, J=8.7 Hz, Ar-N=), 7.88 (d, 2H, J=8.3 Hz, Ar-N=),

7.01 (d, 2H, J=8.8 Hz, Ar-O), 4.05 (t, 2H, J=6.5 Hz, OCH_2), 3.40 (m, 4H, $CH_2N^+CH_2$), 3.32 (s, 6H, $N^+(CH_3)_2$), 1.84 (m, 2H, OCH_2CH_2), 1.68 (m, 4H, $CH_2CH_2N^+CH_2CH_2$), 1.50 (m, 2H, $OCH_2CH_2CH_2$), 1.44-1.16 (m, 52H, CH_2-$(CH_2)_n$-CH_3), 0.89 (m, 9H, CH_3).

Azo-16p. Orange crystalline flakes. Yield 51%. ^{1}H NMR ($CDCl_3$, ppm): δ=8.05 (d, 2H, J=8.5 Hz, Ar-SO_3^-), 7.92 (d, 2H, J=9.0 Hz, Ar-N=), 7.88 (d, 2H, J=8.5 Hz, Ar-N=), 7.01 (d, 2H, J=9.0 Hz, Ar-O), 4.05 (t, 2H, J=6.6 Hz, OCH_2), 3.41 (m, 4H, $CH_2N^+CH_2$), 3.32 (s, 6H, $N^+(CH_3)_2$), 1.84 (m, 2H, OCH_2CH_2), 1.70 (m, 4H, $CH_2CH_2N^+CH_2CH_2$), 1.50 (m, 2H, $OCH_2CH_2CH_2$), 1.44-1.20 (m, 76H, CH_2-$(CH_2)_n$-CH_3), 0.90 (t, 9H, J=6.8 Hz, CH_3).

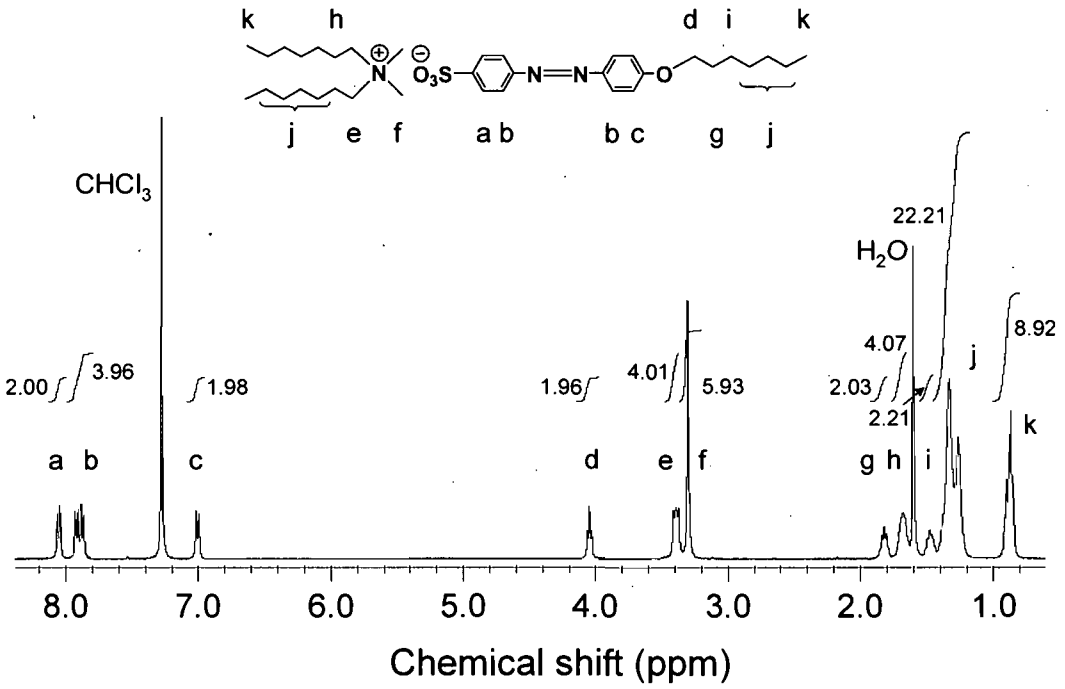

Figure 6.1 The NMR spectrum of Azo-7p.

Table 6.1 CHNS elemental analysis of the complexes.

Complex	C%		H%		N%		S%	
	Theor.	Found	Theor.	Found	Theor.	Found	Theor.	Found
Azo-6p	66.74	66.80	9.28	9.31	7.30	7.30	5.57	5.16
Azo-7p	68.03	67.83	9.62	9.71	6.80	6.76	5.19	5.11
Azo-8p	69.15	69.19	9.93	9.94	6.37	6.35	4.86	4.64
Azo-9p	70.14	70.81	10.19	10.28	5.99	6.09	4.57	4.38
Azo-10p	71.02	71.00	10.43	10.71	5.65	5.66	4.31	4.01
Azo-11p	71.80	71.87	10.64	10.77	5.34	5.54	4.08	4.32
Azo-12p	72.50	72.59	10.83	10.94	5.07	5.17	3.87	3.86
Azo-16p	74.72	74.72	11.43	11.48	4.22	4.33	3.22	3.17

6.3 Results and discussions

6.3.1 One-pot synthesis

The basis of the one-pot synthesis is that DMF, used as a solvent for the phenol azobenzene sulfonate salt, also acts as a reactant in the presence of excess 1-bromoalkane (6 eq. relative to the azo compound), potassium carbonate (a base), and a small amount of potassium iodide (a catalyst). The reaction mechanism is shown in Scheme 6.2. The base and traces of water (possibly present in one or more of the chemicals used) are hydrolysis agents for the formation of dimethylamine from N,N-dimethylformamide (DMF), following the same mechanism as usual amide hydrolysis in basic conditions.[41] The dimethylamine then reacts with 1-bromoalkane to form the dialkyldimethylammonium bromide surfactant. Simultaneously, the phenol group in the azo compound reacts with 1-bromoalkane to form the alkoxy tail. The resulting surfactant and azo mesogen form a complex that precipitates at lower temperature. In this way, dye-surfactant complexes were conveniently prepared with high purity and good yield.

6.3.2 Thermal characterization

The thermal stability of all the complexes was determined by dynamic TGA (Figure 6.2). The 1% weight loss temperature ($T_d^{1\%}$) of the complexes are all at 255±5 °C (Table

6.2), which is somewhat lower than that of the starting material, (4-hydroxyphenylazo)benzenesulfonic acid, sodium salt, at 293 °C.[37]

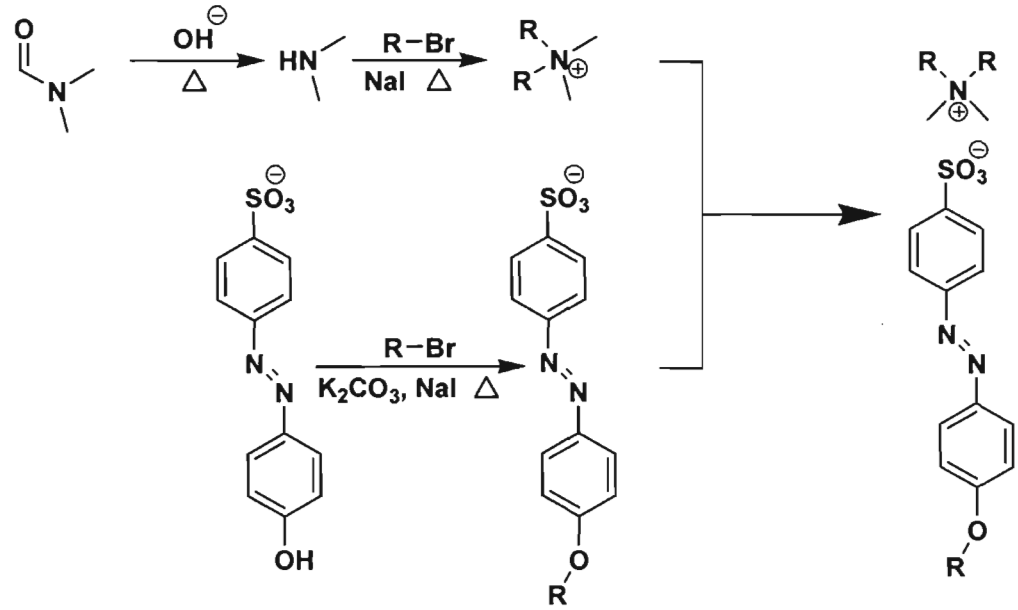

Scheme 6.2 Reaction mechanism for the one-pot synthesis of the dye/surfactant complex.

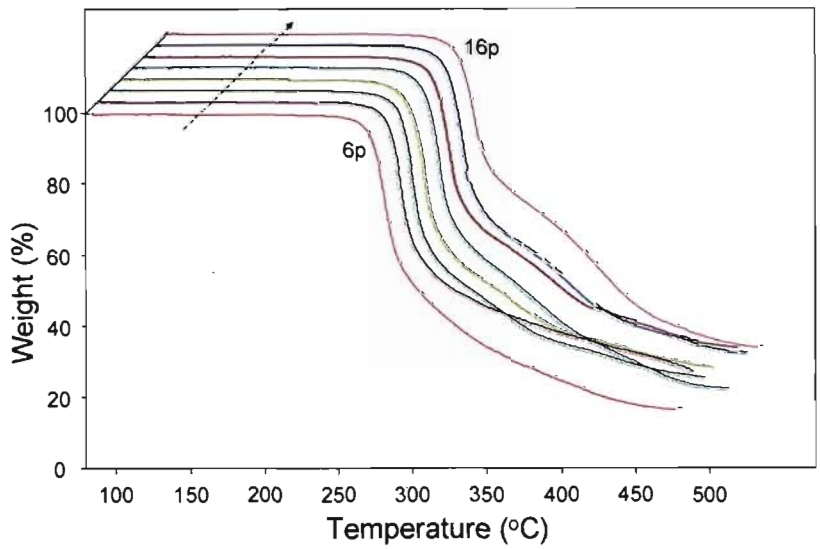

Figure 6.2 TGA thermograms of the Azo-np complexes, displaced relative to Azo-6p in the direction of the arrow in the order of increasing n.

Table 6.2 Thermal properties of the Azo-np complexes, determined by DSC and TGA.

Complex	$T_{tr(h)}$ [a] / °C (ΔH / J·g^{-1})	$T_{tr(c)}$ [a] / °C (ΔH / J·g^{-1})	Super-Cooling[b] (°C)	$T_d^{1\%}$ / °C
Azo-6p	134 (90)	114 (92)	20	255
Azo-7p	146 (108)	135 (108)	11	255
Azo-8p	150 (100)	137 (100)	13	251
Azo-9p	156 (104)	146 (102)	10	254
Azo-10p	145 (92)	138 (91)	7	259
Azo-11p	140 (85)	135 (84)	5	257
Azo-12p	110, 112 (12)	108 (1.7)	2	257
	134, 136 (79)	127 (64)	7	
		134 (14)	2	
Azo-16p	124 (52)	119 (53)	5	257
	137 (17)	135 (17)	2	

[a] $T_{tr(h)}$: transition peaks in heating thermograms. $T_{tr(c)}$: transition peaks in cooling thermograms.
[b] calculated by the temperature difference between the heating and cooling transitions.

Polarizing optical microscopy indicated that all of the complexes become isotropic (complete disappearance of birefringence) and liquid in the 136 - 155 °C range. Since ionic LC compounds can be prone to orient normal to the glass surface in liquid phases (homeotropic alignment), the samples were mechnically pressed at temperatures above the transitions to perturb any such alignment, which confirmed that the phase is truly isotropic.

The transition temperatures were confirmed by DSC (Figure 6.3 and Table 6.2). The thermograms shown in Figure 6.3 are second heating curves, but the subsequent and initial heating curves are essentially identical to them (the end of the scanning temperature for each complex was set to around 20 °C higher than the isotropization temperature found by POM). A single transition peak is found for the n=6-11 Azo-np compounds, on both heating and cooling, with that on heating corresponding to the isotropization temperature observed by POM within ±2 °C. Azo-12p and Azo-16p show more than one peak in heating. Their very high enthalpies (≥85 J/g), listed in Table 6.2, indicate a transition between a highly ordered (crystalline) phase and what has been identified as the isotropic phase by POM. There is no odd-even alternation of the melting point with n, as frequently observed in liquid crystals;[42] however, it is interesting to observe that the melting point

increases from Azo-6p to 9p and then decreases again from Azo-9p to 11p. It is also interesting to note that supercooling (peak difference between melting and crystallization temperatures) tends to decrease monotonously from 20 °C for Azo-6p to 5 °C for Azo-11p (Table 6.2).

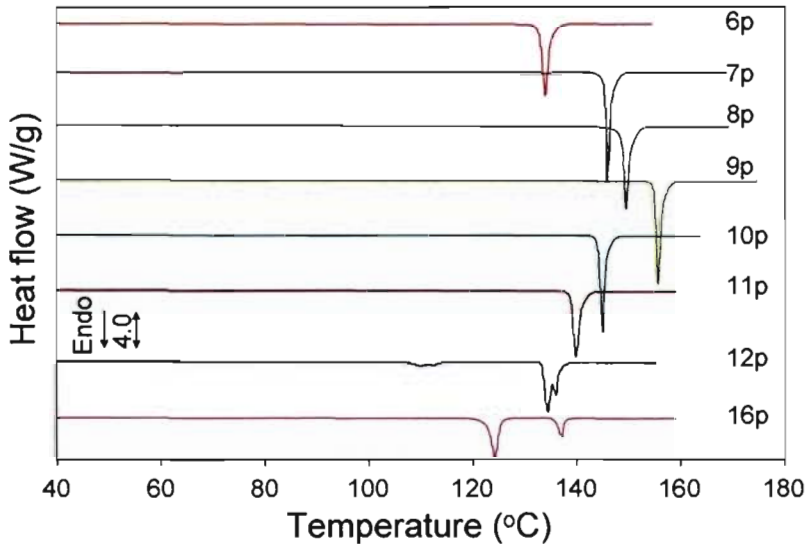

Figure 6.3 Second heating DSC thermograms of the Azo-np complexes.

Azo-12p and 16p show two prominent DSC transitions in heating and cooling. The lower temperature transition has the highest enthalpy, and therefore is probably a melting/crystallization point from/to the crystalline phase. It also continues the tendency of the melting point to decrease in temperature with increasing n starting from Azo-9p. The higher temperature transition, at 136-137 °C, has a lower enthalpy (ca. 15 J/g) and a small supercooling (ca. 2 °C), which indicate a transition between a less ordered phase and the isotropic phase. For Azo-12p, the two transitions partially overlap in the heating curve, but are well separated in cooling due to the greater supercooling for the lower-temperature transition. For Azo-16p, the two transitions are well separated in both the heating and cooling curves, due to the decrease in melting/crystallization point with increase in n. The fact that the clearing point is almost identical for Azo-12p and 16p, but below the melting/crystallization points for Azo-7p to 11p suggests that the mesophase involved shows up in these two complexes due to the decrease in the temperature stability of the crystalline phase. It should be added that Azo-12p shows, in addition, two weak transitions

on heating (one on cooling) near 110 °C, which are probably crystal-crystal (solid-solid) transitions, which are frequently observed in LC materials. Azo-11p shows such a transition just before melting only on the first heating scan.

In POM, the higher-temperature mesophase for Azo-12p and -16p gives the textures shown in Figure 6.4, obtained by slow cooling from the isotropic phase. The lancet-like texture, which coexists with a homeotropic texture, grows relatively slowly. In comparison, a nondescript, highly birefringent texture grows very quickly when cooling Azo-6p to 11p from the isotropic to the crystalline phase. This same nondescript texture fills in the homeotropic regions of the mesophase upon further cooling to the crystalline phase (shown in Figure 6.4 for Azo-16p). This lancet-like texture was observed previously for SmB[16] (or CrB) and SmT[15] phases.

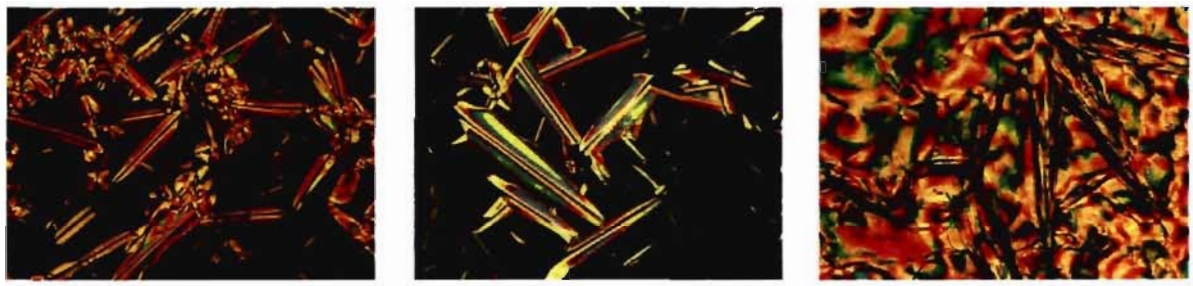

Figure 6.4 POM micrographs for Azo-12p and 16p after cooling from the isotropic phase into the high temperature mesophase, and then, for Azo-16p, into the crystalline phase.

6.3.3 Structural investigations

X-ray diffraction was used to investigate the packing structure of the complexes at room temperature, as well as in the high temperatures after cooling from the isotropic phase for Azo-11p, 12p and 16p. The results are shown in Figure 6.5 and summarized in Table 6.3.

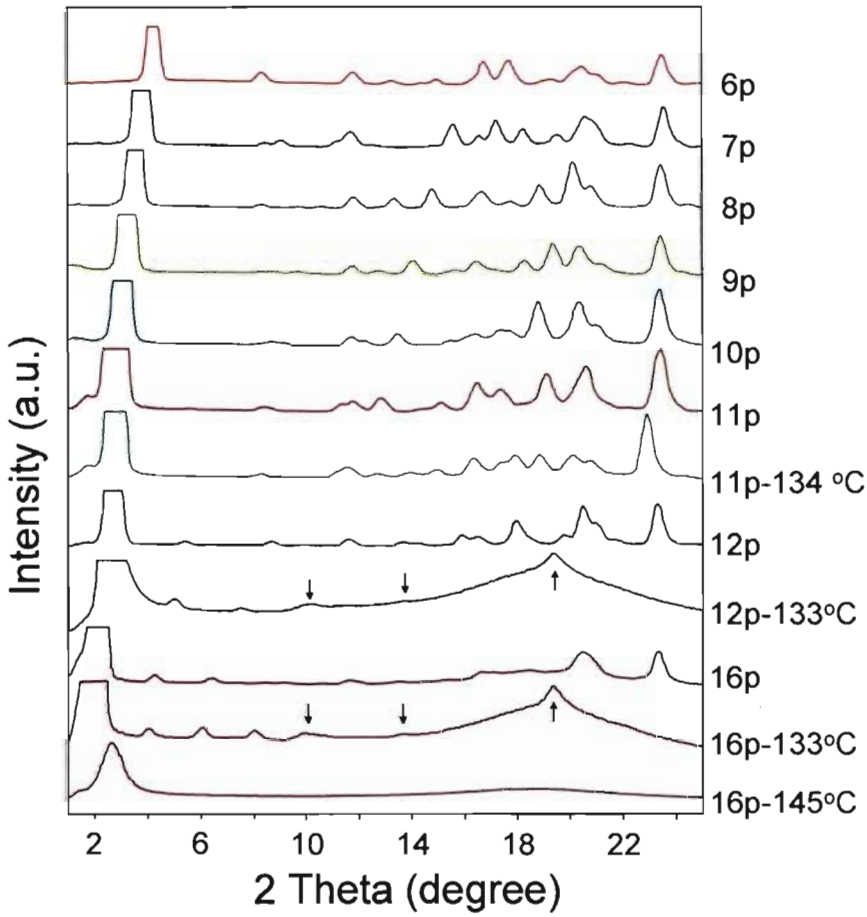

Figure 6.5 X-ray diffractograms of the complexes at room temperature (when unspecified) after cooling from the melt, and at a temperature (specified) just below the clearing point after slowly cooling from the isotropic phase for Azo-11p, 12p and 16p. The diffractogram for Azo-16p in the isotropic phase (145 °C) is also shown. The arrows indicate peaks related to in-plane order (see text).

Table 6.3 Bragg spacings of the lower angle X-ray diffraction peaks of Azo-np complexes in the crystalline phase.

Complex n		(001) 1st peak/Å	(002) 2nd peak/Å	(003) 3rd peak/Å
6	[a]	20.9	10.5	7.4
	[b]	20.9	10.5	7.5
7	[a]	23.3	-	-
	[b]	23.3	-	-
8	[a]	25.2	12.7[c]	-
	[b]	24.9	12.5[c]	-
9	[a]	26.9	13.5[c]	-
	[b]	26.9	13.5[c]	-
10	[a]	28.7	-	-
	[b]	28.8	-	-
11	[a]	30.4	15.1[c]	10.2
	[b]	31.2	15.6[c]	10.4
	[d]	31.3	15.5[c]	10.6
12	[a]	32.7	16.2	-
	[b]	32.6	16.2	-
16	[a]	39.9	20.0	13.3
	[b]	41.1	20.4	13.6

[a] for unmelted sample.
[b] after cooling from the isotropic phase.
[c] very weak.
[d] at 134 °C, after cooling from isotropic phase.

Table 6.4 XRD results for the complexes, Azo-12p and 16p, in the high temperature mesophase.

Complex n		Peaks at lower angles (Å)				Peaks at higher angles (Å)		
		1st (001)	2nd (002)	3rd (003)	4th (004)	(101) (011)	(110)	(020) (200)
12	133 °C	34.9	17.6	11.7	-	8.80	6.47	4.57
	Calcd.[a]	35.1	17.6	11.7	-	8.85	6.46	4.57
16	133 °C	43.5	21.5	14.4	10.9	8.81	6.44	4.56
	Calcd.[b]	43.3	21.7	14.4	10.8	8.92	6.45	4.56

[a] calculated assuming the tetragonal cell: a=b=9.14, c=35.1 Å.
[b] calculated assuming the tetragonal cell: a=b=9.12, c=43.3 Å.

6.3.3.1 Crystalline phase

Figure 6.5, which shows that there are multiple peaks in the wide-angle region of the diffractograms, confirms the crystalline nature of the complexes at room temperature. Before and after melting, the X-ray diffractograms are almost identical for Azo-6p, 9p, 10p

and 12p, and are similar for Azo-7p, 8p and 16p. Azo-11p shows a more significant difference in crystal structure before and after melting. Azo-11p and 16p also show a slight 1-Å change in the low-angle Bragg spacing (see Table 6.3). The lowest angle diffraction peak has very high intensity, and shifts to lower angles with increasing length of the alkyl chain, indicating crystalline cell expansion with increasing molecular size. In most cases, the intense low-angle peak is accompanied by a weak second-order peak and, in some cases, by a weak third-order peak. Their reciprocal spacings are in the ratio 1:2:3, which indicates lamellar packing of the crystalline planes along the longest axis.

To better understand the crystalline packing structure, it is often useful to plot the experimental Bragg spacings calculated from the lowest angle diffraction peak (Table 6.3, after cooling back from isotropic phase) versus the alkyl chain length, n. This is shown in Figure 6.6, indicating a linear dependence, whose least-squares fit is described by equation (1):

$$l = 9.00 + 2.00n \qquad (1)$$

Correlation coefficient: R=0.999

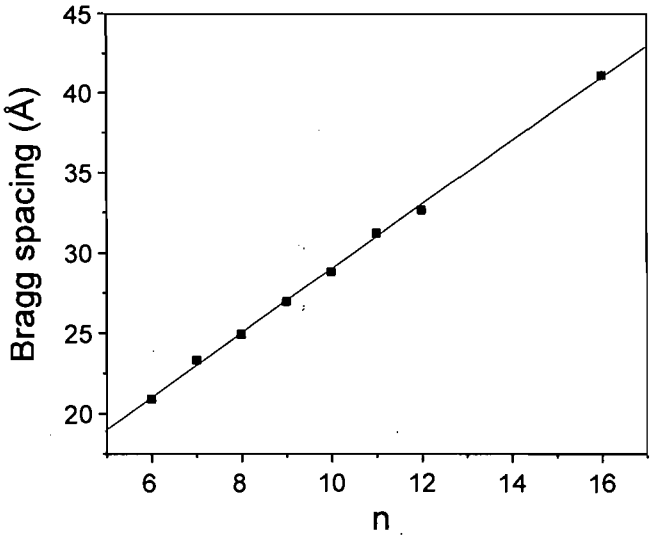

Figure 6.6 Bragg spacing calculated from the smallest angle (first-order) peak in Table 6.3 (after cooling from isotropic phase) as a function of the alkyl chain length, n.

The almost perfect linearity in Figure 6.6 suggests that all the complexes may have very similar, or the same, crystalline packing structure. The slope of 2.00 is much larger

than the known elongation of alkyl chains in their fully extended, all-trans conformation (1.27 Å[22]). This indicates that the lamellar normal is composed of more than one, probably two, alkyl chains. However, the fact that the slope is less than 2.54 Å (twice 1.27 Å) suggests that, if two alkyl chains are involved, they are tilted relative to the layer normal and/or overlap partially. In addition, the intercept of 9 Å, which gives the projection of the nonalkyl component along the lamellar normal is much less than the calculated length of the azobenzene moiety, 14.8 Å, implying tilting and/or overlap of this moiety relative to the lamellar normal as well.

A single crystal structure was obtained for Azo-6p, which may help in clarifying the general crystal structure for the complexes. In the single crystal analysis of Azo-6p, some disorder was found in the sulfonate group and in the alkyl chain of the azosulfonate moiety. The crystal structure with the highest probability, 62%, is shown in Figure 6.7, and the main results are summarized in Table 6.5. It indicates a monoclinic system. The longest axis, b, is very close to twice the lamellar thickness of Azo-6p (Table 6.3). Simulation of the single crystal structure indeed gives the very similar low-angle diffraction peak, but the overall diffractogram does not correspond to the powder diffractogram. Furthermore, the alkyl chain disposition in Figure 6.7 should give a slope of 2.3, which is larger than observed from the powder diffractograms, and the azobenzene moiety should provide a contribution of 8.1 Å, which is smaller than the calculated intercept. This may imply that the alkyl chains are more tilted or overlapped, whereas the azobenzene moiety is somewhat less tilted in the powder crystal structure than in the single crystal structure shown in Figure 6.7.

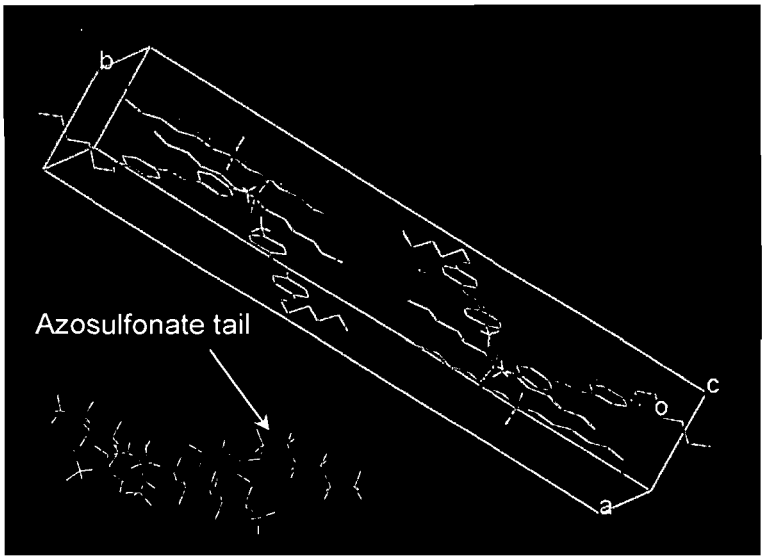

Figure 6.7 Single crystal structure of Azo-6p with a probability of 62%. For clarity, the hydrogens are omitted from the chemical structure in the unit cell.

Table 6.5 Summary of the results of the single crystal analysis of Azo-6p.

Complex	Azo-6p
Crystal system	Monoclinic
Space group	$P2_1/c$
Number of molecules per unit cell	4
Unit cell dimensions	a = 7.3989(3) Å $\alpha = 90^\circ$ b = 42.0789(15) Å $\beta = 91.383(2)^\circ$ c = 10.8058(5) Å $\gamma = 90^\circ$
Cell volume	3363.3(2) $Å^3$
Density calculated	1.137 g/cm^3

The following points about the single crystal structure in Figure 6.7 are noteworthy: (a) the two hexyl chains are fully extended in opposite directions relative to the ammonium cation, forming an angle of 163° [as measured by (terminal C)–N–(terminal C)], very close to the simulated value of 165° (see Figure 6.9); (b) both surfactant and azo dye are packed almost perfectly in planes parallel to the (001) plane in the monoclinic cell, except for the hexyl chain of the azo dye which is at a small angle; (c) the angles between the three crystal axes are all very close or equal to 90°; (d) the hexyl chains of the ammonium cation are almost parallel to the b axis (small angle of ca. 3 and 15° , respectively, measured along the

line connecting N and the terminal C); (e) although the azo groups make an angle of ca. 58° to the hexyl chains on the ammonium cation, its hexyl tail makes a turn to adopt approximately the same direction as the ammonium hexyl chains (ca. 20° difference). The last point may be explained by the affinity between alkyl chains to force them to be parallel and facilitate the most compact packing. This tendency can be stronger for longer alkyl chains.

6.3.3.2 High temperature mesophase

Of the complexes with a single transition, only Azo-11p was investigated at higher temperatures, as representative of the complexes with shorter alkyl tails (Azo-6p to 11p). The diffractograms obtained at 134 °C, where the sample just formed an ordered structure after stepwise cooling from the isotropic phase, shows a crystalline structure that is similar but not identical to the one at room temperature before melting (due to the solid-solid transition mentioned earlier), but close to the one at room temperature after melting, with an identical lamellar Bragg spacing (Figure 6.5 and Table 6.4).

A similar procedure of taking diffractograms during stepwise cooling from the isotropic phase allowed the higher temperature mesophase of Azo-12p and 16p to be investigated, shown in Figure 6.5 at 133 °C for both complexes. Another diffractogram taken at 127 °C was identical to the one at 134 °C, indicating that the form of the diffractograms and the Bragg spacings are invariant with temperature within this mesophase. The lower angle region, with 3-4 diffraction orders detected, indicates that this mesophase has a well-defined lamellar structure, with Bragg spacings that increase with alkyl chain length (Table 6.4) and that are ca. 3 Å larger than in the corresponding crystalline phase. A broad halo is evident at high angles, indicative of significant liquid crystal type disorder. The halo is superposed by a weaker peak at 19.4°, accompanied by very weak peaks at 10.0° and 13.7°. These three peaks are almost identical for Azo-12p and 16p (Table 6.4), indicating some higher order structure within the lamellar phase that is identical for both complexes. No other (weak) peaks were detected at higher angles (maximum angle scanned: 40°).

For additional information, efforts were made to obtain an oriented 2D X-ray diffractogram of the mesophase. This was possible only for Azo-16p, because of its

relatively wide temperature range of mesophase stability. Two methods were used to get the oriented pattern: (1) by shearing of the sample in the mesophase and (2) from crystalline (essentially single-crystal) flakes that self-orient in the capillary (during multiple dropping of the capillary in a long tube on a hard surface). Both methods gave the same oriented pattern, which is shown in Figure 6.8 (obtained by method 2), along with azimuthal scans. It can be observed that the diffraction peaks identified with lamellar packing are orthogonal to the three high-angle diffraction peaks identified with in-plane order, indicating that the in-plane order is effectively orthogonal to the lamellar normal.

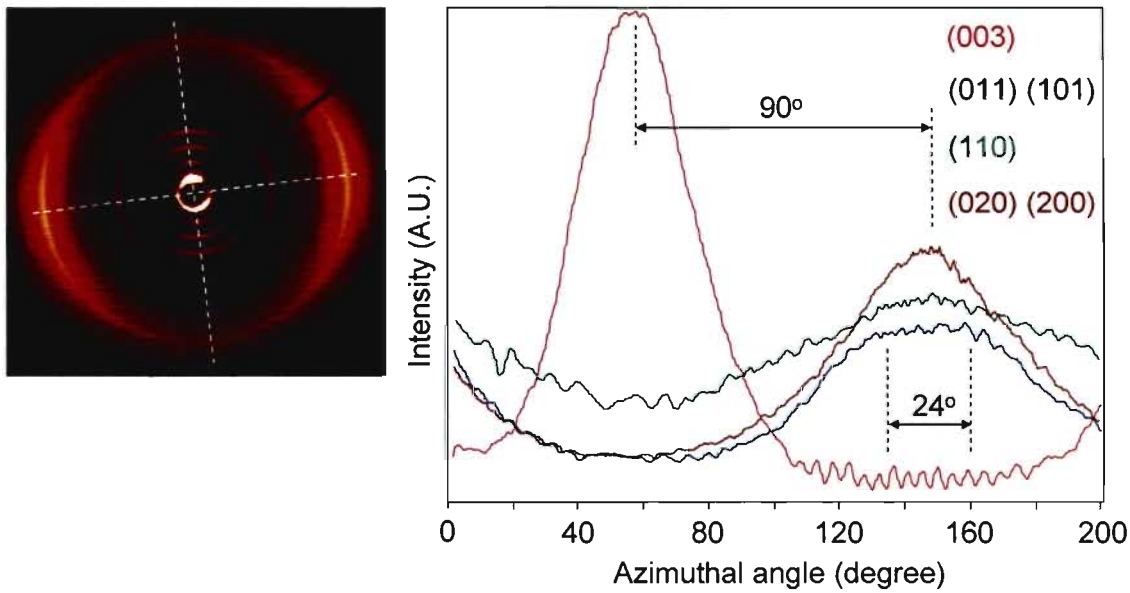

Figure 6.8 Oriented XRD pattern of Azo-16p in the high-temperature mesophase at 130 °C. Azimuthal scans are given at the right, with the planes indicated (see text for details).

To determine the structure of the high-temperature mesophase, the three wide-angle peaks have to be indexed. It is noticed that the ratio of their reciprocal Bragg spacings are 1: 1.37:1.94, which is insufficiently close to $1:\sqrt{2}:2$ [the ratio that, for example, a 2D tetragonal lattice would give for the (10), (11) and (20) planes]. If the peaks at 13.7° and 19.4° only are considered, they have a reciprocal spacing ratio of $1:\sqrt{2}$, which could be consistent with the (11) and (20) planes in a 2D tetragonal lattice, as identified in the

literature.[15,18] If this is considered to apply to the mesophase of Azo-12p and 16p, it gives a and b dimensions of the tetragonal cell that are almost identical at 9.1 Å (Table 6.4).

In that case, the peak at 10° could arise from the (101) or (011) plane. However, these planes make an angle of 78.1° to the (001) plane in the reciprocal lattice,[43,44] which appears contrary to the 2D diffractogram of the oriented sample (Figure 6.8). On the other hand, a close look at the azimuthal scans in Figure 6.8 suggests that the peak at 10° actually forms a broad plateau at its maximum, which can be the consequence of two separate peaks. Considering the 78.1° angle above, the two peaks should be separated by 23.8°. Figure 6.8 shows the maximum positions of the two peaks assuming that they form an angle of 24°, and are at 12° on either side of the orthogonal to the (003) lamellar plane. The other two peaks, the sharpest one from the (020) and (200) planes [(20) above] and the shallower one from the (110) plane, clearly have their maxima at 90° relative to the (003) plane. With these assignments, the calculated X-ray profile matches the experimental profile almost perfectly (Table 6.4).

It may also be noted that the lateral area of the tetragonal cell (relative to the lamellar normal) is 83 $Å^2$ (Table 6.4) compared to 80 $Å^2$ for the rectangular lateral area of the single crystal cell (Table 6.5). This increase in area, combined with a more symmetric lateral area that could permit rotation about the molecular long axis, may be just enough to allow the alkyl chains to become disordered in the mesophase compared to the crystalline phase. The disorder is evident from the wide-angle halo centered near 19-20°. The greater lamellar thickness of the mesophase compared to the crystal phase (Tables 6.3 and 6.4) also indicates that there is less interdigitation (overlap) and/or less tilting: one strong possibility is less tilting of the azobenzene moiety.

Different models have been proposed for mesophases of dimethyl, dialkylammonium salts, based on the conformation of the dialkyl chains relative to the ammonium cation, such as fully extended on opposite sides [(a) in Figure 6.9],[18] V-shaped folding on one side [(b) in Figure 6.9],[25] and close folding on one side [(c) in Figure 6.9].[24,35] As for the bromide salt in the first report of a SmT phase, it was not possible to clarify how the dialkyl chains extended relative to the ionic plane.[15] This was not addressed either in other references for the same compounds.[16,20] For an ammonium salt with one long alkyl chain and one shorter one terminated with a cyano or hydroxyl substituent, Skoulios and coll.

suggested that the extended conformation ("a" in Figure 6.9) the relatively more extended conformation applied to the SmT mesophase found.[23,45] On the other hand, the close folding conformation ("c" in Figure 6.9) was suggested to apply to the SmA mesophase[25] and crystalline phase for complexes where the anions are composed of much bigger azobenzene groups, such as with naphtholate and multi-sulfonate groups.[35] In these cases, the closely folded alkyl chain matches better the lateral area of the bulky counterions.

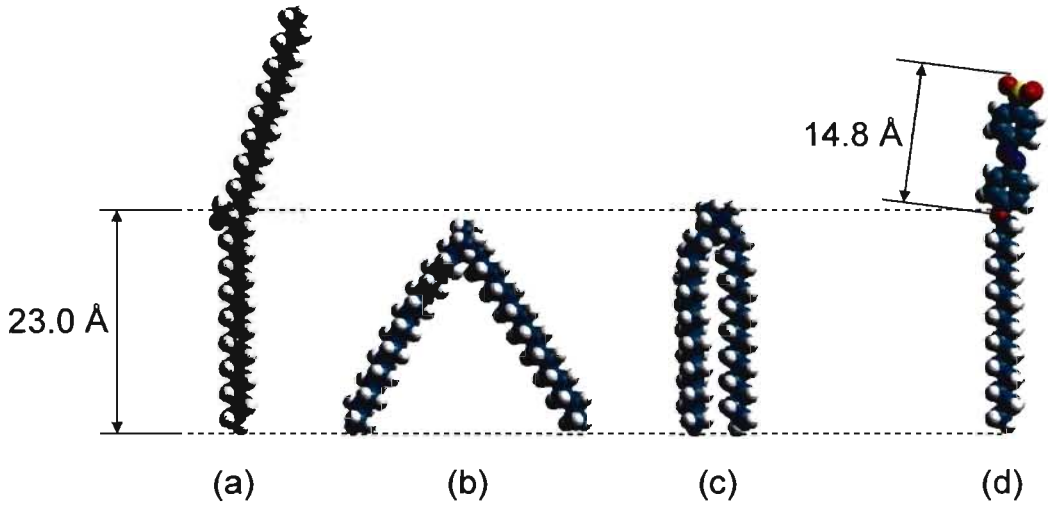

Figure 6.9 Lengths of the different parts of Azo-16p; (a), (b) and (c) are the dimethyl, dihexadecylammonium cation, (d) is the azo-sulfonate anion.

For the complexes studied here, the fully extended model has to be used to facilitate compact packing (consistent also with the single crystal structure). A possible packing model with tetragonal in-plane ordering is shown in Figure 6.10. The affinity of the alkyl chains of both components, as observed in the single crystal structure of Figure 6.7, as well as an optimal arrangement of opposite charges are considered. It also takes into account that the length of the fully extended chains in opposite directions relative to the ammonium cation is quite close to the observed spacing by XRD. It must be emphasized that the in-plane order in the SmT phase occurs at the level of the ionic groups (see refs. 15,18), whereas the alkyl chains are in a disordered state, as indicated by the wide-angle XRD halo.

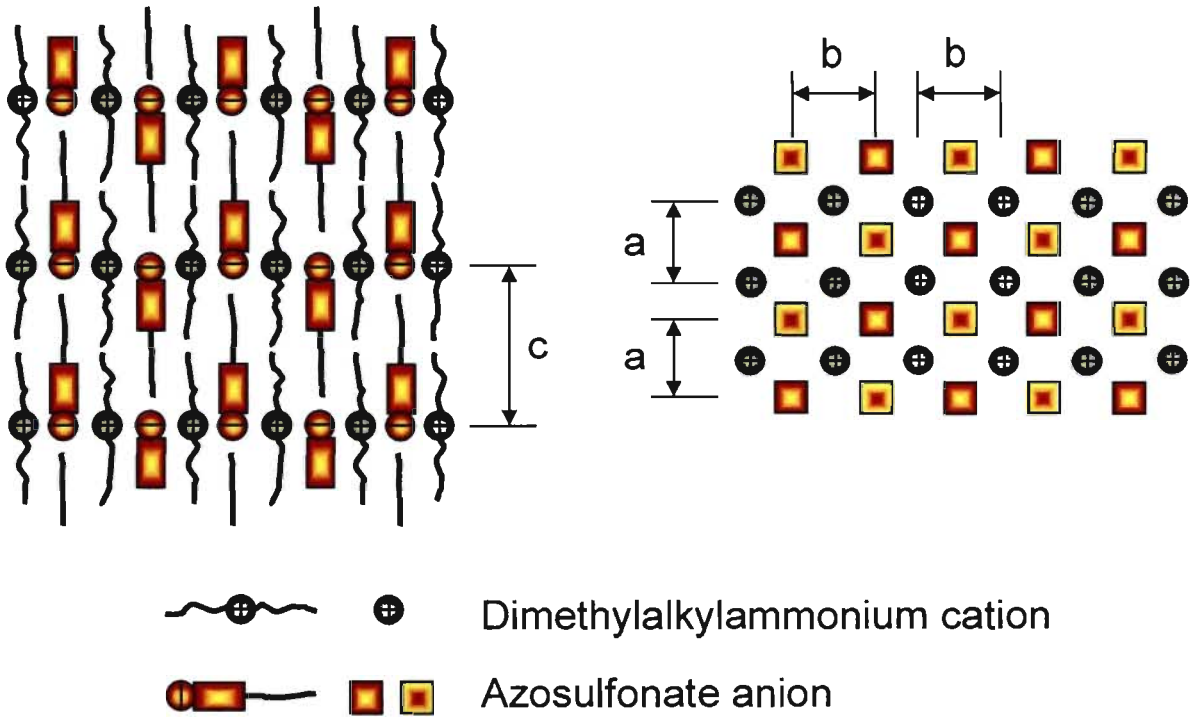

Figure 6.10 Proposed SmT-type packing model for the complexes. Front view (left) and top view (right) are shown. The direction of the azosulfonate in the top view is discriminated by inverted colours in the squares.

6.3.4 Photoisotropization

The trans isomer of the azobenzene core is its most stable form and is generally required for ordered phases to appear.[28] It is well known that light causes trans-cis isomerization,[28,46] and that the bent shape of the cis isomer can destroy LC phases (called "photoisotropization", observed to date in nematic,[47-51] smectic A[52,53] and chiral[53] phases) It was of interest to investigate if the high temperature mesophase of Azo-16p is subject to photoisotropization (the temperature stability of Azo-12p is too small, especially considering that the laser may heat the sample to a small extent and thus simply raise its temperature into the isotropic region). The experiment with Azo-16p was conducted at 127 °C, 10 °C below the isotropization temperature. Three cycles of 10-min X-ray diffractograms were taken one after the other with the laser turned alternately off and on. The results of the experiment are given in Figure 6.11, showing the photoisotropization phenomenon. In particular, with the laser on, the wide-angle peak disappears, leaving only the halo, and the lower-angle peaks associated with lamellar order are essentially extinct,

leaving a low-intensity, relatively broad peak at 2.67° (Bragg spacing 33.0 Å). This peak is found in the isotropic phase, as shown in Figure 6.5, and can be associated with cybotactic-like structures (short-range order within an otherwise disordered phase). Actually, a residue of the mesophase peak at 2.05° is still apparent in diffractograms b and d. This is probably due to an imperfect alignment of the laser and X-ray beams on exactly the same spot of the sample, since a small adjustment of the laser before taking the diffractogram eliminated this residual peak almost completely (only a slight shoulder is still detected). It should be added that the phase switching is rapid, as indicated, first, by the fact that the laser was turned on for 25, 60 and only 10 s before the start of the XRD recording for diffractograms b, d and f, respectively. Second, the mesophase profile was detected on the computer screen in less than 2 s after the simultaneous start of recording diffractogram c and turning off of the laser,

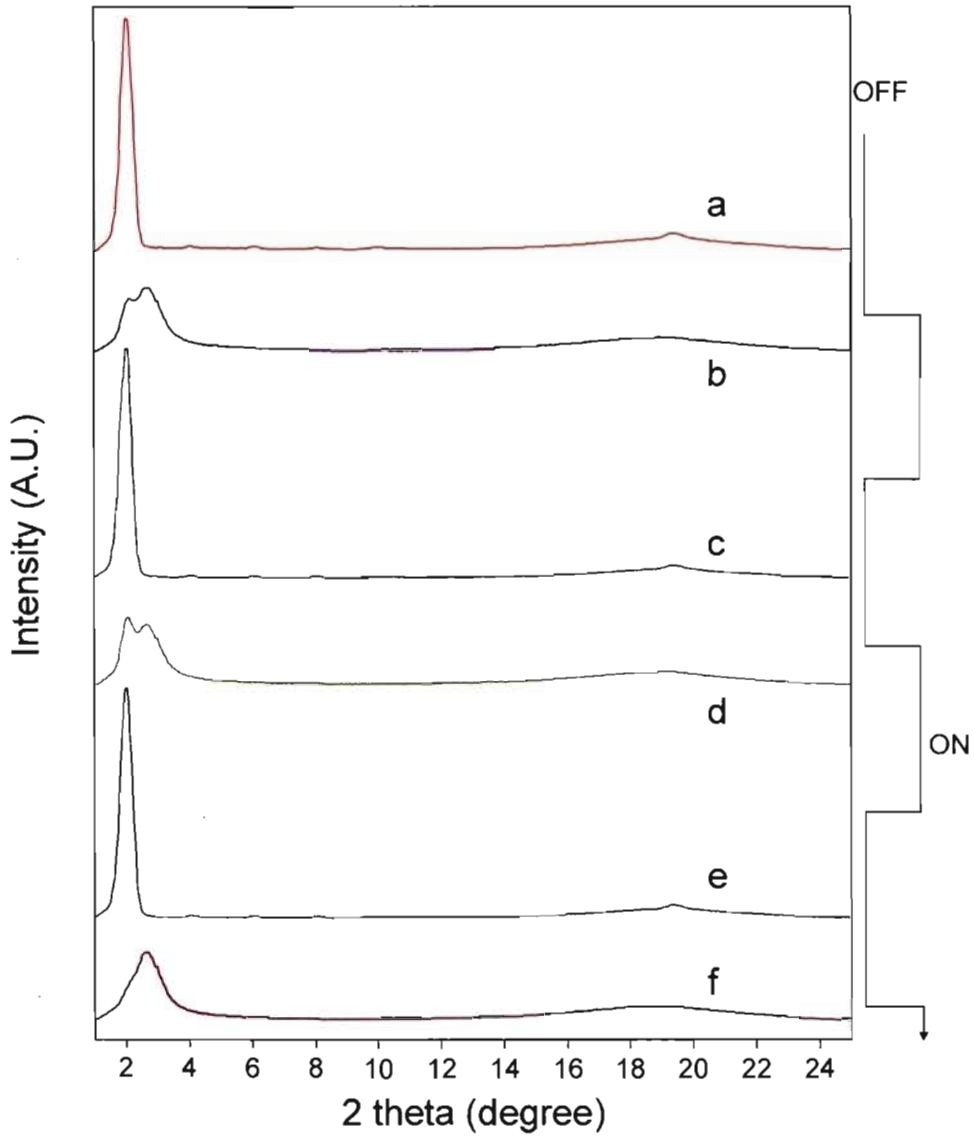

Figure 6.11 Photoisotropization of the high temperature mesophase in Azo-16p, tracked *in situ* by XRD at 127 °C and taken in order from a to f with the ON/OFF state of the laser indicated.

6.4 Conclusions

Ionic complexes of an azo dye with a surfactant were successfully prepared in a one-pot synthesis by making use of the hydrolysis of the reaction solvent, DMF. This allowed simultaneous incorporation of an alkyl chain to the mesogenic core, the preparation of a dimethyl, dialkyl ammonium surfactant counterion and the ionic complexation of the two

components. The synthesis method can be generally applied to many other phenol-functionalized dyes. It also constitutes a novel method to synthesize N,N-dimethyl, dialkylammonium surfactants.

The complexes prepared all had lamellar-like crystalline structure to high temperature, shown to be a monoclinic system for an Azo-6p single crystal. A liquid crystal mesophase with SmT-like in-plane order at the level of the ionic groups occurs at high temperature for the complexes with dodecyl and hexadecyl alkyl chain lengths. The alkyl chains in this mesophase are disordered. Light induced isotropization of this mesophase, due to trans-cis isomerization of the azobenzene moiety, was also demonstrated.

6.5 Acknowledgments

The financial support of NSERC Canada and FQRNT Québec is gratefully acknowledged. QZ thanks Université de Montréal for a final year graduate scholarship.

6.6 References

1. Binnemans, K. *Chem. Rev.* **2005,** 105, 4148-4204.
2. Lin, I. J. B.; Vasam, C. S. *J. Organomet. Chem.* **2005,** 690, 3498-3512.
3. Mirnaya, T. A.; Volkov, S. V. *NATO Sci. Ser., II* **2003,** 92, 439-456.
4. Welton, T. *Chem. Rev.* **1999,** 99, 2071-2083.
5. Busico, V.; Cernicchiaro, P.; Corradini, P.; Vacatello, M. *J. Phys. Chem.* **1983,** 87, 1631-1635.
6. Busico, V.; Corradini, P.; Vacatello, M. *J. Phys. Chem.* **1982,** 86, 1033-1034.
7. Gault, J. D.; Gallardo, H. A.; Muller, H. J. *Mol. Cryst. Liq. Cryst.* **1985,** 130, 163-177.
8. Ito, M.; Matsunaga, Y.; Matsuzaki, H.; Shimojima, S. *Bull. Chem. Soc. Jpn.* **1989,** 62, 3919-3922.
9. Matsunaga, Y.; Tsujimura, T. *Mol. Cryst. Liq. Cryst.* **1991,** 200, 103-108.
10. Tsiourvas, D.; Paleos, C. M.; Skoulios, A. *Liq. Cryst.* **1999,** 26, 953-957.
11. Tsiourvas, D.; Mihou, A. P.; Couladouros, E. A.; Paleos, C. M. *Mol. Cryst. Liq. Cryst.* **2001,** 362, 177-184.
12. Tsiourvas, D.; Paleos, C. M.; Skoulios, A. *Chem.--Eur. J.* **2003,** 9, 5250-5258.
13. Iwamoto, K.; Ohnuki, Y.; Sawada, K.; Seno, M. *Mol. Cryst. Liq. Cryst.* **1981,** 73, 95-103.
14. Malliaris, A.; Christias, C.; Margomenou-Leonidopoulou, G.; Paleos, C. M. *Mol. Cryst. Liq. Cryst.* **1982,** 82, 161-166.

15. Alami, E.; Levy, H.; Zana, R.; Weber, P.; Skoulios, A. *Liq. Cryst.* **1993,** 13, 201-212.
16. Godlewska, M.; Wrobel, S.; Borzecka-Prokop, B.; Michalec, M.; Dynarowicc, P. *Mol. Cryst. Liq. Cryst.* **1997,** 300, 113-126.
17. Shimizu, J.; Nogami, T.; Mikawa, H. *Solid State Commun.* **1985,** 54, 1009-1011.
18. Ohta, K.; Sugiyama, T.; Nogami, T. *J. Mater. Chem.* **2000,** 10, 613-616.
19. The two alkyl chain may be different and with other terminal groups.
20. Przedmojski, J.; Dynarowicz-Latka, P. *Phase Transitions* **1999,** 70, 133-146.
21. Tittarelli, F.; Masson, P.; Skoulios, A. *Liq. Cryst.* **1997,** 22, 721-726.
22. Arkas, M.; Paleos, C. M.; Skoulios, A. *Liq. Cryst.* **1997,** 22, 735-742.
23. Arkas, M.; Yannakopoulou, K.; Paleos, C. M.; Weber, P.; Skoulios, A. *Liq. Cryst.* **1995,** 18, 563-569.
24. Kadam, J.; Faul, C. F. J.; Scherf, U. *Chem. Mater.* **2004,** 16, 3867-3871.
25. Zakrevskyy, Y.; Smarsly, B.; Stumpe, J.; Faul, C. F. J. *Phys. Rev. E: Stat., Nonlinear, Soft Matter Phys.* **2005,** 71, 021701/1-021701/12.
26. Barrett, C. J.; Mamiya, J.-i.; Yager, K. G.; Ikeda, T. *Soft Matter* **2007,** 3, 1249-1261. Yamada, M.; Kondo, M.; Mamiya, J.-i.; Yu, Y.; Kinoshita, M.; Barrett, C. J.; Ikeda, T. *Angew. Chem., Int. Ed.* **2008,** 47, 4986-4988.
27. Ikeda, T.; Mamiya, J.-i.; Yu, Y. *Angew. Chem., Int. Ed.* **2007,** 46, 506-528. Ikeda, T. *J. Mater. Chem.* **2003,** 13, 2037-2057.
28. Natansohn, A.; Rochon, P. *Chem. Rev.* **2002,** 102, 4139-4175.
29. Yager, K. G.; Barrett, C. J., In *Polymeric Nanostructures and Their Applications*, Nalwa, H. S., Ed.; American Scientific Publishers: Los Angeles, 2007; Vol. 2, pp. 243-280.
30. Fuhrmann, T.; Tsutsui, T. *Chem. Mater.* **1999,** 11, 2226-2232.
31. Stracke, A.; Wendorff, J. H.; Goldmann, D.; Janietz, D.; Stiller, B. *Adv. Mater.* **2000,** 12, 282-285.
32. Nakano, H.; Takahashi, T.; Kadota, T.; Shirota, Y. *Adv. Mater.* **2002,** 14, 1157-1160.
33. Chigrinov, V.; Prudnikova, E.; Kozenkov, V.; Kwok, H.; Akiyama, H.; Kawara, T.; Takada, H.; Takatsu, H. *Liq. Cryst.* **2002,** 29, 1321-1327.
34. Faul, C. F. J.; Antonietti, M. *Chem.--Eur. J.* **2002,** 8, 2764-2768.
35. Guan, Y.; Antonietti, M.; Faul, C. F. J. *Langmuir* **2002,** 18, 5939-5945.
36. Zakrevskyy, Y.; Stumpe, J.; Faul, C. F. J. *Adv. Mater.* **2006,** 18, 2133-2136.
37. Zhang, Q.; Wang, X.; Barrett, C. J.; Bazuin, C. G. *Chem. Mater.* **2009,** 12, 3216-3227.
38. Study in progress.
39. Savitzky, A.; Golay, M. J. E. *Anal. Chem.* **1964,** 36, 1627-1639.
40. DeNoyer, L. K.; Dodd, J. G., Smoothing and Derivatives in Spectroscopy. In *Handbook of Vibrational Spectroscopy*, Chalmers, J.; Griffiths, P., Eds. John Wiley & Sons: Chichester, 2002; Vol. 3.
41. Clayden, J.; Greeves, N.; Warren, S.; Wothers, P., *Chmie Organique*. De Boeck: Paris, 2003.
42. Demus, D., *Handbook of liquid crystals*. Wiley-VCH: Toronto, 1998.
43. Ebert, F.; Thurn-Albrecht, T. *Macromolecules* **2003,** 36, 8685-8694.
44. Zhang, Y.; Leblanc-Boily, V.; Zhao, Y.; Prud'homme, R. E. *Polymer* **2005,** 46, 8141-8150.

45. Arkas, M.; Tsiourvas, D.; Paleos, C. M.; Skoulios, A. *Chem.--Eur. J.* **1999,** 5, 3202-3207.
46. Rau, H., Photoisomerization of azobenzenes. In *Photochemistry and photophysics*, Rabek, J. K., Ed.; CRC Press: Boca Raton, FL., 1990; Vol. 2, pp. 119-141.
47. Tazuke, S.; Kurihara, S.; Ikeda, T. *Chem. Lett.* **1987**, 911-914.
48. Ikeda, T.; Horiuchi, S.; Karanjit, D. B.; Kurihara, S.; Tazuke, S. *Macromolecules* **1990,** 23, 42-48.
49. Matczyszyn, K.; Chwialkowska, A.; Sworakowski, J. *Thin Solid Films* **2008,** 516, 8899-8904.
50. Kato, T.; Hirota, N.; Fujishima, A.; Frechet, J. M. J. *J. Polym. Sci., Part A: Polym. Chem.* **1996,** 34, 57-62.
51. Ikeda, T.; Tsutsumi, O. *Science* **1995,** 268, 1873-1875.
52. Kumaresan, S.; Mallia, V. A.; Kida, Y.; Tamaoki, N. *J. Mater. Res.* **2005,** 20, 3431-3438.
53. Tamaoki, N.; Aoki, Y.; Moriyama, M.; Kidowaki, M. *Chem. Mater.* **2003,** 15, 719-726.

Chapter 7: Surface Relief Gratings: A Unique Soft Workbench

Abstract

Azo-containing polymers are known for their ability to form high quality sinusoidal surface relief gratings (SRGs). This is a top-down method for fabricating well-controlled surface patterns. In this contribution, we investigated a new method to modify pre-fabricated SRG profiles, notably by exposure of the SRGs to solvent atmospheres (especially 100% RH), without and with partial shadowing of the SRG by gold. A liquid crystalline ionically bonded polymer complex, made from methyl orange and methylated poly(4-vinylpyridine) (MO/PVP), was used to inscribe SRGs. The difference in response to 100% RH exposure of SRGs fabricated in high (summer, 50-60%RH) and low (winter, <10%RH) humidity conditions was compared. The winter sample showed almost complete erasure of SRG in 30 s, whereas the summer sample showed partial erasure, attributed to a full versus partial elastic character in the SRG. Interestingly, pits with depths ranging from a few to more than 100 nm, were discovered in the winter SRG after longer exposure times. The profile of the SRGs could be modified - e.g. showed peak doubling - by selectively protecting one side of the sinusoids by a gold coating before exposure to 100% RH. Although the control is imperfect, the investigation indicates that this approach is promising and could be exploited for possible applications in nano-fabrication and optics.

7.1 Introduction

Well-controlled nano-structured patterns on surfaces have raised a great deal of interest in nanofabrication, electronics, bioscience, sensors, catalysis, etc. in recent years.[1-13] Many techniques have been developed so far, from conventional photolithography, imprint-based lithography, scanning probe lithography, to self-assembly, etc.[2] Polymer materials play an important role in the preparation process, such as the photo-sensitive or -resistive resin in photolithography,[14] elastomers in soft lithography,[15,16] elastomeric masks in replica molding,[17,18] and block copolymers in self-assembly processes.[11-13,19-22] The role of polymers has evolved progressively from top-down to bottom-up concepts, from passive assistance to active control. Polymers are used for their properties of flexibility, elasticity, chemical reactivity, etc.

Azo-containing polymers are well-known for their light-induced isomerization and consequent orientation process,[23-27] and are widely studied in photomechanics,[28] optoelectronics,[29-32] photochemistry,[33] molecular machinery,[34,35] life[36,37] and surface[23,25,38] sciences, etc. One of the most interesting and unique discoveries, also with very practical applications, is the fabrication of surface relief gratings (SRGs).[39-41] The mechanism of SRG formation is still not completely understood (see review [42]). However, it is generally agreed that it is based on the macroscopic motion of material caused by the photoisomerization of the azobenzene moieties.[23] In this connection, we discuss SRG formation from the viewpoint of photoorientation using circularly polarized light[43] in the Appendix to this chapter.

The successful formation of SRGs depends on temperature. A recent study has shown that SRGs cannot be fabricated in amorphous polymers at temperatures approaching or higher than the T_g.[44] This can be explained by the idea that stress is inevitably induced by the photoisomerization[45] and macroscopic displacement of mass is necessary for SRG formation.[44,46] As the temperature of SRG fabrication approaches the T_g, the total photoinduced stress decreases to the point that it becomes too weak to overcome the required yield stress for inducing deformation, and thus SRG formation is inhibited.[44]

As the SRG is formed, the material's inherent mechanical properties like elasticity oppose the driving force exerted by light, and act as a restoring force. Surface tension is also considered to act as a restoring force running counter to SRG formation.[42] It is

therefore necessary to be well below the glass transition temperature (T_g) to minimize the contribution of the restoring forces that can allow relaxation to occur. This means that high stability of SRGs well below the T_g should be attributed to a frozen-in out-of-equilibrium elastic state of the material. On the other hand, the photoinduced stress might also cause (local) plastic – i.e. permanent – deformation of the material during SRG fabrication.

Besides temperature, solvent or moisture can also help release the stress in SRG films. This occurs due to a plasticization effect that lowers the T_g, thus allowing collapse of the SRG through relaxation. It is of interest to investigate the stability of SRGs in external vapour conditions, especially in humidity, which is useful and instructive for applications. Surprisingly, very few studies of this kind are found in the literature.

With reference to the patterned surfaces mentioned at the beginning of this introduction, SRGs can provide a useful workbench for fabricating patterned surfaces. Their periodicities can range from hundreds of nanometers to micrometers, and can be tuned precisely by proper adjustment of the laser setup.[23,41,42] Besides the conventional one-dimensional surface variation, microstructures in a two-dimensional array can also be prepared very conveniently.[23,47] Thus, SRG fabrication in azo-containing polymers provides us with a unique top-down method to prepare patterned surfaces. To make it even more powerful, this chapter will introduce additional external factors involving selective shadowing of the SRGs with subsequent exposure to moisture for post-modification of the SRG profiles. This work was inspired by an earlier investigation into making use of SRGs for fabricating nanowires.[48]

To simplify our study, we will focus only on conventional SRGs. The material used is a spacer-free side-chain liquid crystalline complex between methyl orange and methylated poly(4-vinyl pyridine), abbreviated MO/PVP, whose LC structure and light induced performance has been studied previously.[49,50] We will first discuss the fabrication of SRGs in different humidity conditions (summer versus winter), and then expose them to 100% relative humidity (RH) and to DMF vapour, to observe how the SRGs respond to these environments. Finally, SRGs will be selectively shadowed with a thin gold layer, and then placed in a 100% RH environment to monitor the profile evolution.

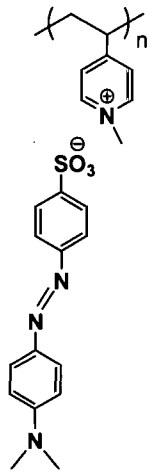

MO/PVP

Scheme 7.1 Molecular structure of the complex used for the SRG experiments.

7.2 Experimental section

7.2.1 Materials and sample preparation

The preparation and characterization of MO/PVP is the same as described elsewhere.[49,50] Deionized water (a nonsolvent for the complex) was obtained from a Millipore Gradient A10 Milli-Q system (resistivity 18.2 MΩ.cm at 25 °C). DMF (a good solvent for the complex) was passed through drying columns (Glass Contour system) before use. 3"x1" glass slides (Fisher Scientific) were cleaned by acetone. Polymer films were prepared by spin-coating (EC101, Headway Research) at 2500 rpm for 20 sec from a 3/1 DMF/dichloromethane (w/w) solution of 10 wt% onto the cleaned glass slides. The films were dried at 100 °C for at least 3 d, then sealed in polyethylene zipper bags and placed in a minidesiccator containing indicator drierite and P_2O_5 powder for storage and transportation. Based on measurements of other films of this material spin-coated under exactly the same conditions, it is estimated that the thickness of the films is 300-500 nm.

7.2.2 Instrumentation

The setup for SRG inscription is the same as described previously,[50] and based on a one-beam system using circularly polarized light,[42] The laser power was between 320-400 mW/cm^2 and the wavelength 488 nm. Initial SRGs were inscribed on the dried films taken

from the desiccator and mounted immediately in the SRG setup, exposed to ambient conditions. The beam crossing angle was set at ca. 15 °, which gives a grating spacing of ca. 1 μm. Ambient humidity was measured by a hygrometer (VWR). The duration of inscription ranged from several min to 10 min. The process was tracked by a probe laser (632 nm) using the first order diffraction. The SRG-inscribed film was then sealed again in the zipper bag and returned to the mini-desiccator. Then, as soon as possible, it was characterized by AFM (atomic force microscopy), using a Digital Instruments Dimension 3100 instrument in tapping mode. Metal shadowing technique, which is widely used in electron microscopy to enhance contrast and real topographic feature of specimens,[51] was applied on SRGs here. SRGs were shadowed at an angle of ca. 25° (relative to film surface) by a 15-30 nm-thick layer of gold using a Cressington 208R or 308R sputter coater.

For exposure to 100% RH (or DMF), the SRGs, following initial AFM characterization, were placed in a sealed chamber saturated with the desired atmosphere at room temperature for specified times, and then taken out and characterized by AFM immediately. The procedure was repeated as desired.

7.3 Results and discussion

SRG fabrication in winter and summer, when the ambient humidity varies greatly, (<10%RH in winter and 50-60%RH in summer), were compared using instrumental conditions that were as similar as possible. Not surprisingly, there were significant differences in the SRG properties. First, the maximum diffraction efficiency achieved was much higher (ca. >30%) in winter than in summer (ca. < 5%). Second, the SRG amplitude (valley to peak) in the diffraction efficiency plateau region reached significantly higher values in winter than in summer.

This can be attributed to some hygroscopic character in the complex due to the presence of the ionic bonds, where water molecules may be selectively absorbed in humid conditions (even though water is not a good solvent for the complex). The direct consequence should be some decrease in T_g due to plasticization during SRG inscription, which must increase the elastic restoring force, analogous to what occurs when increasing the temperature.[44] The presence of liquid crystalline structure and domains and a possible

change in the clearing temperature may complicate the issue further. It would be of interest to investigate this aspect in future work.

The effect of humidity was further investigated by exposing SRG-inscribed films to controlled humidity conditions, specifically to 100% RH, with periodic characterization by AFM. The amplitude (the height from valley to peak, estimated from recorded AFM topographical profiles) change as a function of exposure time to 100% RH (and DMF) for films inscribed with SRG in the winter and summer, is shown in Figure 7.1.

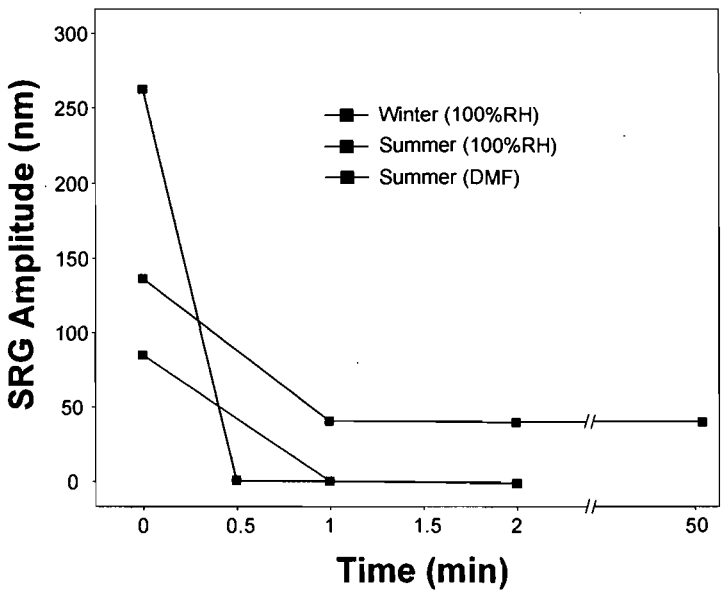

Figure 7.1 SRG amplitude as a function of exposure time to 100% RH and saturated DMF atmospheres. SRG inscription was done on initially dry films in winter (low humidity) or summer (high humidity), as indicated. The uncertainty of the value is about ±10%.

The initial SRG amplitudes are 260±26 nm, 135±14 nm and 85±9 nm, respectively, for the SRG inscribed in the winter and the two SRGs inscribed in the summer. Strikingly, the winter-fabricated SRG, despite its much higher amplitude, was almost flattened in less than 0.5 min of exposure to 100% RH. The residual, very indistinct SRG (less than 2 nm amplitude) completely disappeared in less than 2 min of exposure. In contrast, the lower amplitude summer-fabricated SRG was reduced in height but still clearly visible, with a 40-nm amplitude, after 1 min of 100% RH exposure, and underwent no further decrease for

longer exposure times up to 57 min. The summer-fabricated SRG exposed to saturated DMF atmosphere completely disappeared in less than 1 min.

The results show very well, first of all, that the SRGs are very sensitive to the presence of small molecules. Second, the response of the SRGs to 100% RH exposure appears to depend on the humidity conditions during their fabrication. The winter-fabricated SRG seems to be in a frozen elastic state, and, when subsequently exposed to 100% RH, this frozen state can be completely released in a very short time. The summer-fabricated SRG seems to be in a partial frozen elastic state, so that the SRG collapsed only partly after exposure to 100% RH. It may be explained by the relatively higher content of water present in the summer-fabricated SRG during its inscription in the higher humidity environment. These absorbed water molecules (via plasticization) may have released part of the stress caused by the SRG formation so that the deformation is partly irreversible (plasticity). Obviously, when exposed to DMF, which is a good solvent for the complex (and which can also eliminate the liquid crystal phase[52]), the SRG cannot survive.

Very interestingly, the winter-fabricated SRG, after exposure to 100% RH for 30 s, showed many round small pits (see Figure 7.2), whereas no pits were found on the parts of the sample where no SRG was inscribed. The summer-fabricated SRG, after exposure to 100% RH, showed a roughened surface, but without round pits. The surface of the DMF-exposed SRG was smooth. Despite the pits, a very indistinct SRG of very small (< 2 nm) amplitude can still be detected (vertical strips in the leftmost image in Figure 7.2). The pits have depths ranging from 5 to 15 nm and diameters of ca. 1 μm, which is close to the spacing of the original SRG. With longer exposure to 100% RH (2 min total; see images on the right in Figure 7.2), the residual SRG disappeared completely, and the pits were further accentuated, becoming a little wider and much deeper, more than 50 nm (even more than 100 nm in some places).

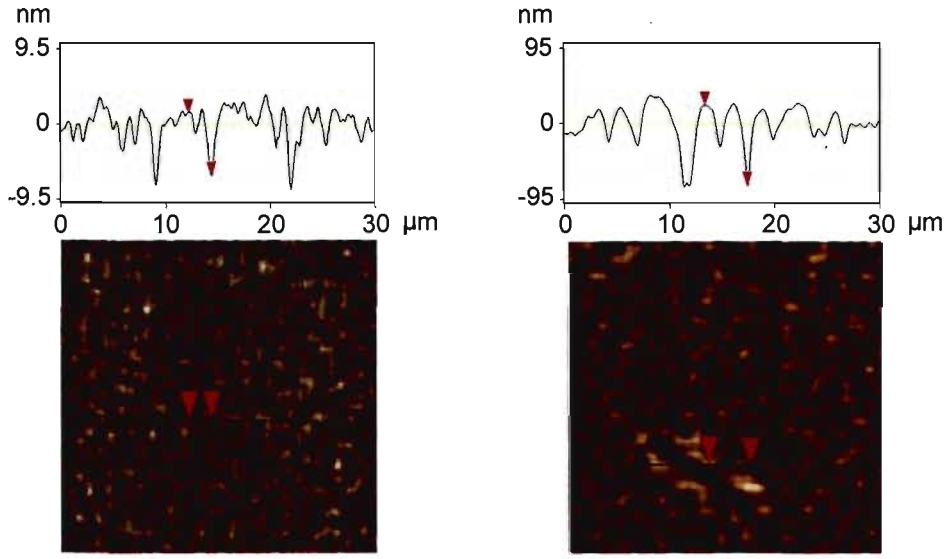

Figure 7.2 Winter-fabricated SRG after exposure to 100% RH for 0.5 min (left) and for 2 min (right).

It seemed of interest to further manipulate the SRGs by selectively protecting part of the SRG profile (left side in Scheme 7.2) to expose only the unprotected part (right side in Scheme 7.2). To do this, the SRG was shadowed by gold from an angle of about 25° relative to the film surface. It was estimated that this angle is optimal for shadowing only one side and not the other side of the sinusoids. The success of the shadowing could not be directly verified (and is not expected to be as perfect as shown in Scheme 7.2), but the evolution of the shadowed SRGs after exposure to 100% RH constitutes indirect evidence that the shadowing was at least approximately successful.

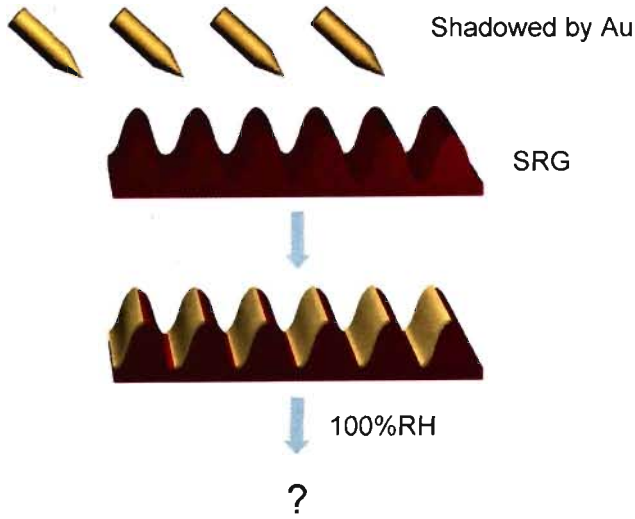

Scheme 7.2 Selective protection of the SRG profile by gold shadowing from an angle, for subsequent exposure to 100% RH.

The results of exposure of the gold-shadowed summer- and winter-fabricated SRGs to 100% RH for various times are shown in Figure 7.3 in the form of 3D and 2D AFM images, as well as a 1D height profile scan. Both initial gold-shadowed SRGs (0 min in Figure 7.3) have sinusoidal profiles. After exposure to 100% RH for 1 min for the summer sample and 10 s for the winter sample, the sinusoids show deformation on their unshadowed sides and the valley-to-peak height decreases by ca. 35% and 20%, respectively. This becomes more pronounced at longer exposure times, with a tendency to asymmetric splitting of the original sinusoidal profile. This effective (but asymmetric) frequency doubling is particularly evident (and the least asymmetric) for the summer sample after an exposure time of 3 min. The winter SRG at 7 min shows clear evidence of its unique pit morphology, located only on the side unprotected by gold. Further evolution of the summer profiles at longer exposure times is less clear since they also become increasingly irregular (show increasing "noise"). It is noteworthy that the average SRG amplitudes for the longest exposure times are significantly larger for the summer-fabricated SRG than the winter-fabricated one, in line with the results for the bare (gold-free) SRGs (Figure 7.1). A similar experiment with DMF was inconclusive, because the evolution of the SRG profile was too fast to permit successful tracking. DMF also resulted in much greater irregularity on the film surface, which can be explained by its strong dissolution effects on the material.

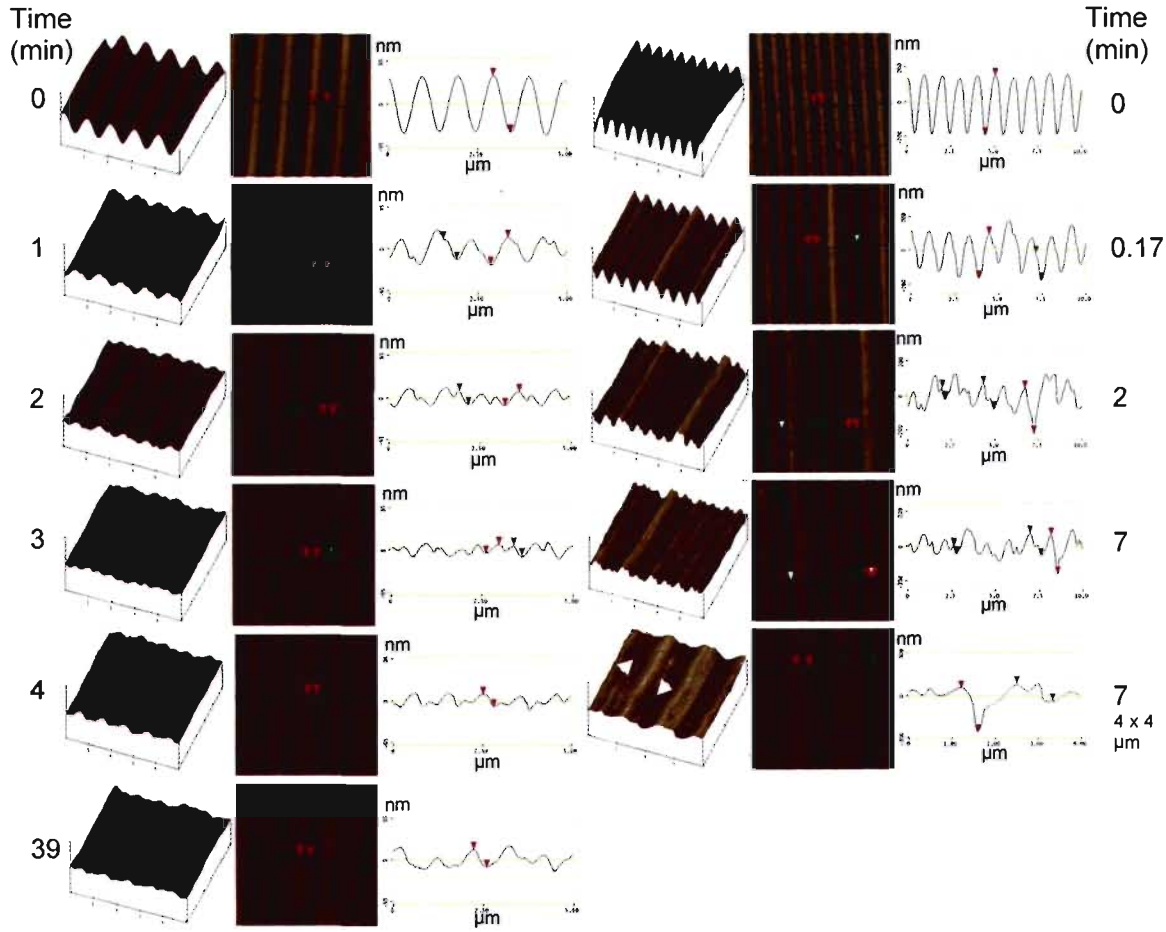

Figure 7.3 Evolution of gold-shadowed SRGs fabricated in summer (left) and in winter (right), during exposure to 100% RH for the times indicated. The shadowing was performed at an angle from the left hand side.

The SRG profile evolution during exposure to 100% RH may be illustrated as shown in Scheme 7.3. It can be assumed that water molecules penetrate the sample only where there is no gold covering. The tendency to peak doubling suggests that the resultant decrease in sinusoidal amplitude that relieves surface stress pulls over part of the gold protected surface to the unexposed side (unless it was there to begin with, noting that the steepest part of the unprotected slope is also where there is the least probability of gold coverage). Then the continuing evolution of the unprotected surface causes the secondary peak formation due to the relative immobility of the gold-coated tops. A second possibility is that the steep region where the secondary peak appears is also where there is the greatest surface stress and therefore the fastest relaxation kinetics. As a third possibility, it may also

be where the surface molecular composition (which could well be non-uniform over the SRG surface) is the most hydrophilic and therefore where water molecules preferentially penetrate into the material. At longer exposure times, as the profile becomes still shallower, the secondary peak becomes less prominent.

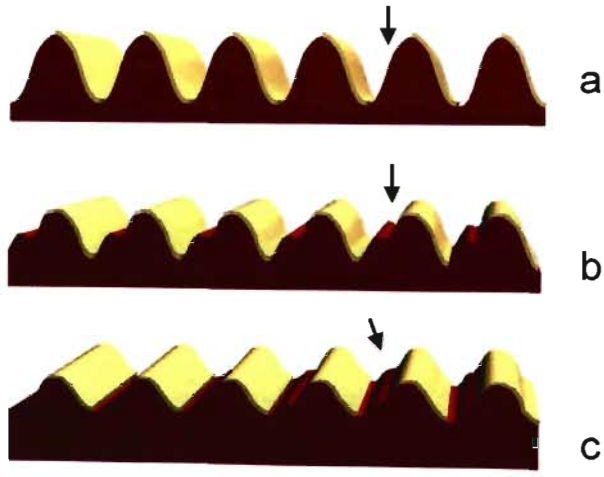

Scheme 7.3 SRG profile evolution during exposure to 100% RH: (a) original SRG, (b) short time exposure and (c) longer time exposure.

The formation of pits in the winter-fabricated SRGs is not clear. The fact that it was observed in both the bare and partially gold-coated SRGs (but not in the gold-coated areas nor outside of the SRG), and only in the winter-fabricated SRGs indicates that it is not an artefact. One possible reason might be related to the nature of the structural (liquid crystal) order and orientation in the film that may be different in the dry winter film compared to the less dry summer film (as shown to be different in the bulk[53]). This may have particular consequences on the distribution of the surface and sub-surface composition (hydrophilicity) and/or the surface and sub-surface stresses of the SRG. For example, the pits may result from something like ion channels formed by the ionic moieties in the complex that are perhaps opened at the surface by the SRG fabrication process (local hydrophilic surface spot for preferential and rapid absorption of water molecules), and that penetrate into the film.

As a second possibility, the mass motion during SRG formation in combination with the particular structural order and elastic nature of the winter sample may somehow create

stress concentration in such a way that consequent relaxation motion results in the pits. An illustration of how this might be initiated is shown in Scheme 7.4. In the initial sinusoidal SRG profile (two sinusoids are shown), the A, B and C areas have the same height. Upon exposure to 100% RH, due to relaxation, the A_1, A_2, B_1 and B_2 areas sink simultaneously with the rising of the valleys between A_1 and A_2 and between B_1 and B_2. Area C remains untouched. In this way, a depression (or "pucker") is generated between the C_1 and C_2 areas. If combined with a surface chemical composition difference, it may be speculated that this pucker may allow preferential sucking in of water and thus somehow becomes deeper.

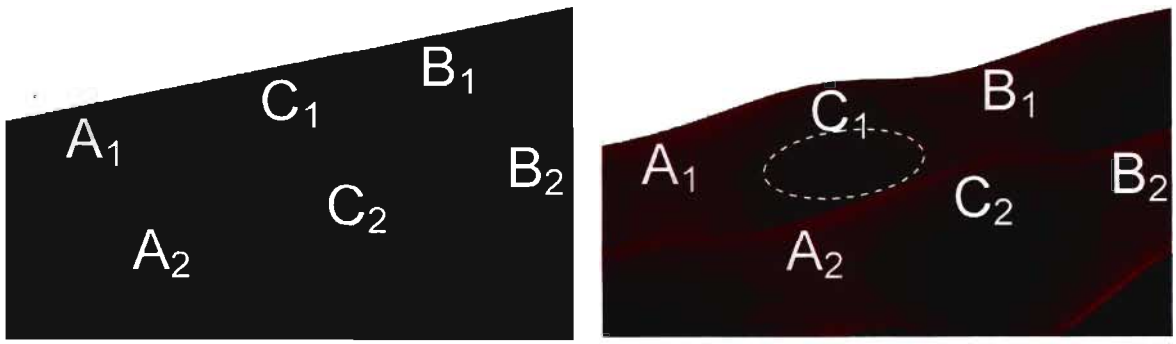

Scheme 7.4 A possible mechanism for pit's starting formation. Winter sample (a) before and (b) immediate after 100% RH exposure. The circle represents a local depressed area (see text for details).

Whatever the mechanism, it must somehow be related to penetration and diffusion of water inside the material to relieve the stress at specific points. One is reminded of the observation that solvent molecules in block copolymer films can play an important role in forming well-ordered surface patterns during the evaporation process, which acts as a "highly directional field".[54-56] Solvent annealing can also aid in constructing highly oriented nanostructures.[57-59] These studies suggest that the movement of small molecules and their interaction with a material can be quite complicated, even without taking into consideration the liquid crystalline property of the MO/PVP complex.

Although this study is preliminary in nature, and leaves many questions, it can be stated that the ultimate profile of an SRG and the control of the surface pattern lie in the cooperation between many factors, including the intrinsic properties of the material, the

SRG fabrication conditions, the presence, type and concentration of small molecules, the utilisation of shadowing, etc. From this viewpoint, the SRG, which is built from soft azo-containing polymers, provides us with a unique workbench that can be exploited to fabricate various surface patterns. If the shadowing-exposure technique can be perfected and further controlled, it may be useful in the field of optics, such as for the fabrication of blazing gratings.

7.4 Conclusions

SRGs fabricated on films of azo-containing polymers provide a unique soft workbench to modify and design surface patterns. The present study using a methyl orange/methylated poly(4-vinyl pyridine) complex shows that the ambient condition in which the SRG is fabricated affects its subsequent response to 100% RH exposure. SRGs prepared in low humidity have higher amplitudes after inscription, but relax more completely than those prepared in higher humidity. Furthermore, an interesting pit-like morphology was found in the SRG fabricated under dry conditions after a few minutes exposure to 100% RH. By selectively protecting one side of the SRG sinusoids with a gold coating, it is possible to modify the profile in interesting ways, including doubling of the peaks.

7.5 Acknowledgments

The financial support of NSERC Canada and FQRNT Québec is gratefully acknowledged. Prof. Christopher J. Barrett (Chemistry Dept., McGill University, Montreal) is thanked for making available his laboratory for SRG fabrication. Prof. Jean-François Masson (Chemistry Department, Université de Montréal, Montréal) is thanked for providing the gold sputter coater.

7.6 References

1. Xia, Y.; Rogers, J. A.; Paul, K. E.; Whitesides, G. M. *Chem. Rev.* **1999,** 99, 1823-1848.
2. Gates, B. D.; Xu, Q.; Stewart, M.; Ryan, D.; Willson, C. G.; Whitesides, G. M. *Chem. Rev.* **2005,** 105, 1171-1196.
3. Rosi, N. L.; Mirkin, C. A. *Chem. Rev.* **2005,** 105, 1547-1562.
4. Huang, Y.; Duan, X.; Cui, Y.; Lauhon, L. J.; Kim, K. H.; Lieber, C. M. *Science* **2001,** 294, 1313-1317.
5. Salaita, K.; Wang, Y.; Mirkin, C. A. *Nat. Nanotechnol.* **2007,** 2, 145-155.
6. Truskett, V. N.; Watts, M. P. C. *Trends Biotechnol.* **2006,** 24, 312-317.
7. Mueller, W. T.; Klein, D. L.; Lee, T.; Clarke, J.; McEuen, P. L.; Schultz, P. G. *Science* **1995,** 268, 272-273.
8. Hwang, H. S.; Zakhidov, A. A.; Lee, J.-K.; Andre, X.; DeFranco, J. A.; Fong, H. H.; Holmes, A. B.; Malliaras, G. G.; Ober, C. K. *J. Mater. Chem.* **2008,** 18, 3087-3090.
9. DeFranco, J. A.; Schmidt, B. S.; Lipson, M.; Malliaras, G. G. *Org. Electron.* **2006,** 7, 22-28.
10. Park, S.; Lee, D. H.; Xu, J.; Kim, B.; Hong, S. W.; Jeong, U.; Xu, T.; Russell, T. P. *Science* **2009,** 323, 1030-1033.
11. Chai, J.; Buriak, J. M. *ACS Nano* **2008,** 2, 489-501.
12. Mizuno, H.; Buriak, J. M. *J. Am. Chem. Soc.* **2008,** 130, 17656-17657.
13. Qiao, Y.; Wang, D.; Buriak, J. M. *Nano Lett.* **2007,** 7, 464-469.
14. Willson, C. G.; Trinque, B. C. *J. Photopolym. Sci. Technol.* **2003,** 16, 621-627.
15. Xia, Y.; Whitesides, G. M. *Annu. Rev. Mater. Sci.* **1998,** 28, 153-184.
16. Xia, Y.; Whitesides, G. M. *Angew. Chem., Int. Ed.* **1998,** 37, 550-575.
17. Xia, Y.; Kim, E.; Zhao, X.-M.; Rogers, J. A.; Prentiss, M.; Whitesides, G. M. *Science* **1996,** 273, 347-349.
18. Kim, E.; Xia, Y.; Whitesides, G. M. *Nature* **1995,** 376, 581-584.
19. Fasolka, M. J.; Mayes, A. M. *Annu. Rev. Mater. Res.* **2001,** 31, 323-355.
20. Krausch, G.; Magerle, R. *Adv. Mater.* **2002,** 14, 1579-1583.
21. Park, S.; Kim, B.; Wang, J.-Y.; Russell, T. P. *Adv. Mater.* **2008,** 20, 681-685.
22. Zschech, D.; Kim, D. H.; Milenin, A. P.; Hopfe, S.; Scholz, R.; Goering, P.; Hillebrand, R.; Senz, S.; Hawker, C. J.; Russell, T. P.; Steinhart, M.; Goesele, U. *Nanotechnology* **2006,** 17, 2122-2126.
23. Natansohn, A.; Rochon, P. *Chem. Rev.* **2002,** 102, 4139-4175.
24. Rau, H., *In Photochemistry and Photophysics*. CRC Press: Boca Raton, FL., 1990; Vol. 2, p 119.
25. Ichimura, K. *Chem. Rev.* **2000,** 100, 1847-1873.
26. Kumar, G. S.; Neckers, D. C. *Chem. Rev.* **1989,** 89, 1915-1925.
27. Dumont, M.; El Osman, A. *Chem. Phys.* **1999,** 245, 437-462.
28. Barrett, C. J.; Mamiya, J.-i.; Yager, K. G.; Ikeda, T. *Soft Matter* **2007,** 3, 1249-1261. Ikeda, T.; Mamiya, J.-i.; Yu, Y. *Angew. Chem., Int. Ed.* **2007,** 46, 506-528.
29. Yesodha, S. K.; Pillai, C. K. S.; Tsutsumi, N. *Prog. Polym. Sci.* **2004,** 29, 45-74.
30. Kucharski, S. H., In *New Research on Optical Materials*, Litchitika, S. J., Ed.; Nova Science Publishers: 2007; pp. 119-156.
31. Hvilsted, S.; Ramanujam, P. S. *Monatsh. Chem.* **2001,** 132, 43-51.

32. Burland, D. M.; Miller, R. D.; Walsh, C. A. *Chem. Rev.* **1994,** 94, 31-75.
33. Peters, M. V.; Stoll, R. S.; Kühn, A.; Hecht, S. *Angew. Chem., Int. Ed.* **2008,** 47, 5968-5972.
34. Balzani, V.; Credi, A.; Marchioni, F.; Stoddart, J. F. *Chem. Commun.* **2001**, 1860-1861.
35. Cheetham, A. G.; Hutchings, M. G.; Claridge, T. D. W.; Anderson, H. L. *Angew. Chem., Int. Ed.* **2006,** 45, 1596-1599.
36. Gorostiza, P.; Isacoff, E. Y. *Science* **2008,** 322, 395-399.
37. Woolley, G. A. *Acc. Chem. Res.* **2005,** 38, 486-493.
38. Wang, S.; Song, Y.; Jiang, L. *J. Photochem. Photobiol., C* **2007,** 8, 18-29.
39. Kim, D. Y.; Tripathy, S. K.; Li, L.; Kumar, J. *Appl. Phys. Lett.* **1995,** 66, 1166-1168.
40. Rochon, P.; Batalla, E.; Natansohn, A. *Appl. Phys. Lett.* **1995,** 66, 136-138.
41. Viswanathan, N. K.; Kim, D. Y.; Bian, S.; Williams, J.; Liu, W.; Li, L.; Samuelson, L.; Kumar, J.; Tripathy, S. K. *J. Mater. Chem.* **1999,** 9, 1941-1955.
42. Yager, K. G.; Barrett, C. J., Light-induced nanostructure formation using azobenzene polymers. In *Polymeric Nanostructures and Their Applications*, Nalwa, H. S., Ed.; American Scientific Publishers: Los Angeles, 2007; Vol. 2, pp. 243-280.
43. *In Appendix to this Chapter.*
44. Veer, P. U.; Pietsch, U.; Rochon, P. L.; Saphiannikova, M. *Mol. Cryst. Liq. Cryst.* **2008,** 486, 66-78.
45. Matsumoto, M.; Miyazaki, D.; Tanaka, M.; Azumi, R.; Manda, E.; Kondo, Y.; Yoshino, N.; Tachibana, H. *J. Am. Chem. Soc.* **1998,** 120, 1479-1484.
46. Saphiannikova, M.; Neher, D. *J. Phys. Chem. B* **2005,** 109, 19428-19436.
47. Barrett, C. J.; Natansohn, A. L.; Rochon, P. L. *J. Phys. Chem.* **1996,** 100, 8836-8842.
48. Noel, S.; Batalla, E.; Rochon, P. *J. Mater. Res.* **1996,** 11, 865-867.
49. Zhang, Q.; Bazuin, C. G.; Barrett, C. J. *Chem. Mater.* **2008,** 20, 29-31.
50. Zhang, Q.; Wang, X.; Barrett, C. J.; Bazuin, C. G. *Chem. Mater.*, **2009,** 21, 3216-3227.
51. Bozzola, J. J.; Russell, L. D., *Electron Microscopy - Principles and Techniques for Biologists*. 2 ed.; Jones and Bartlett: Toronto, 1992.
52. *Discussed in Chapter 3.*
53. Zhang, Q.; Bazuin, C. G. *in Chapter 3 and to be submitted.*
54. Kim, S. H.; Misner, M. J.; Russell, T. P. *Adv. Mater.* **2004,** 16, 2119-2123.
55. Kimura, M.; Misner, M. J.; Xu, T.; Kim, S. H.; Russell, T. P. *Langmuir* **2003,** 19, 9910-9913.
56. Kim, S. H.; Misner, M. J.; Xu, T.; Kimura, M.; Russell, T. P. *Adv. Mater.* **2004,** 16, 226-231.
57. Cavicchi, K. A.; Russell, T. P. *Macromolecules* **2007,** 40, 1181-1186.
58. Kim, S. H.; Misner, M. J.; Russell, T. P. *Adv. Mater.* **2008,** 20, 4851-4856.
59. Park, S.; Kim, B.; Xu, J.; Hofmann, T.; Ocko, B. M.; Russell, T. P. *Macromolecules* **2009,** 42, 1278-1284.

7.7 Appendix: SRG formation – a discussion from the viewpoint of photo-orientation

Since their discovery in 1995,[1,2] SRGs have raised enormous interest in the study of its formation and potential applications, which have been reviewed.[3-5] Although there is hardly complete agreement on the mechanism,[6-17] especially when dealing with amorphous vs. LC material,[16,18-20] high vs. low power radiation,[21] etc., it is generally accepted that photoisomerization plays a crucial role in SRG formation.

In the present discussion, we will fix our angle of view on the orientation effects on chromophores based on the light polarization direction. SRGs are fabricated using two crossed beams of circularly polarized light. They are generally considered to have no intensity variation but only polarization variation.[4,22] The setup, shown in Figure 7.S1, is well known for its very high effectiveness. The period (Λ) is determined by the wavelength (λ) and the angle between the two beams (2θ). When θ is fixed at 15°, the period is fixed at 1 μm. The two circularly polarized beams interfering on the film surface are orthogonal to each other.

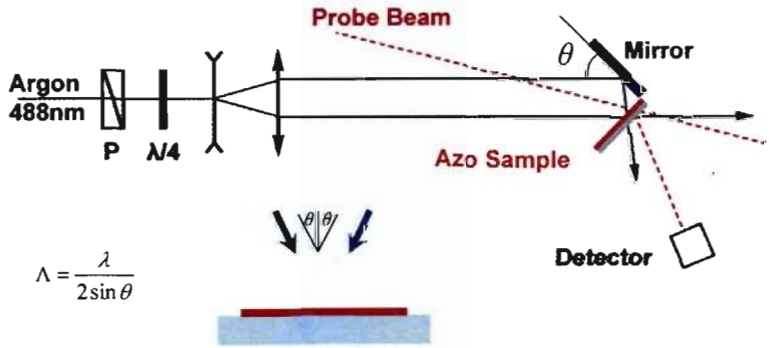

Figure 7.S1 Two-beam SRG setup (Courtesy of Prof. C. Barrett, partly modified). The lower part is a close-up of how the two beams cross at the sample plane.

This setup is thought to be composed of "pure polarization patterns, where the light intensity is uniform over the sample surface." [4,12,23] But in-depth examination suggests that this may not be entirely valid, especially when considering that the SRG amplitude is at a

maximum at a certain θ (~ 15°).[13,24] It is worth clarifying this point here, although it may be a minor consideration.

The interference of the two beams on a film surface (shown in red) is illustrated in Figure 7.S2. The two planes normal to the film plane are **n1** and **n2**. The two light beams ($\mathbf{E}_1$ and $\mathbf{E}_2$, electric vector) are at an angle 2θ to each other and are parallel to plane **n2**. Each beam at a specific film position can be expressed in its cross section as:

$$A = A_0 e^{i(\omega t + \delta)}$$

where A represents the electric field, A_0 its amplitude, ω the angular frequency, and δ the phase angle.

In this setup, two typical conditions are met when the polarization directors of the two beams are in phase and out of phase (see Figure 7.S2; θ change due to refraction and other factors inside the material are not considered in this simple model). When $\mathbf{E}_1$ and $\mathbf{E}_2$ are in phase, the additive electric vector's locus is an ellipse with long axis $2A_0$ and short axis $2A_0\sin\theta$. When $\mathbf{E}_1$ and $\mathbf{E}_2$ are out of phase, the additive locus is a linearly polarized light with maximum amplitude $2A_0\cos\theta$. Consequently, alternative lines of elliptic polarization and linear polarization are constructed (Figure 7.S3). Since the azo group will be orientated by the polarized light accordingly and result in a population with the azo axis preferentially perpendicular to the polarization direction, [called photo-orientation[3,4,25], also known as "rotational diffusion"[26]], the resultant distribution of the azo axis will be as shown in Figure 7.S3. Furthermore, this distribution will push and pull the azo group along the grating vector direction to form the SRGs by exerting local compression and stretching forces (Figure 7.S4).

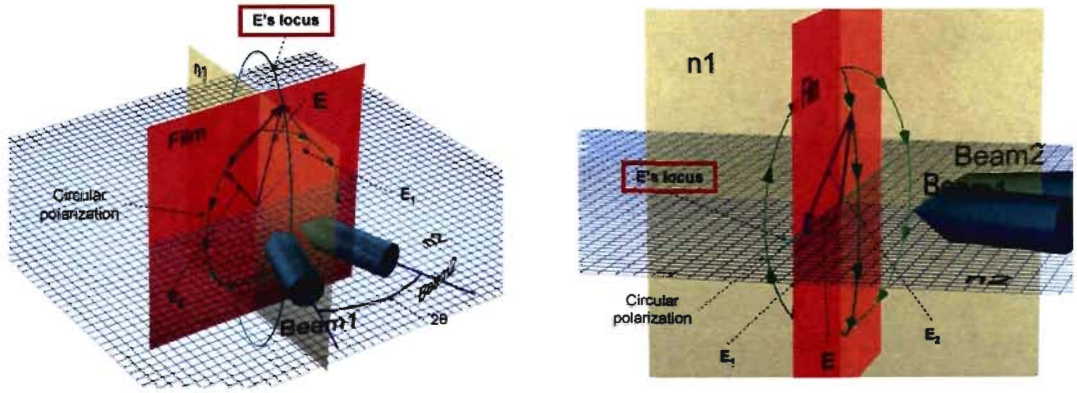

(a) $\mathbf{E}_1$ and $\mathbf{E}_2$ in phase (b) $\mathbf{E}_1$ and $\mathbf{E}_2$ out of phase

Figure 7.S2 E vector addition of two interference beams.

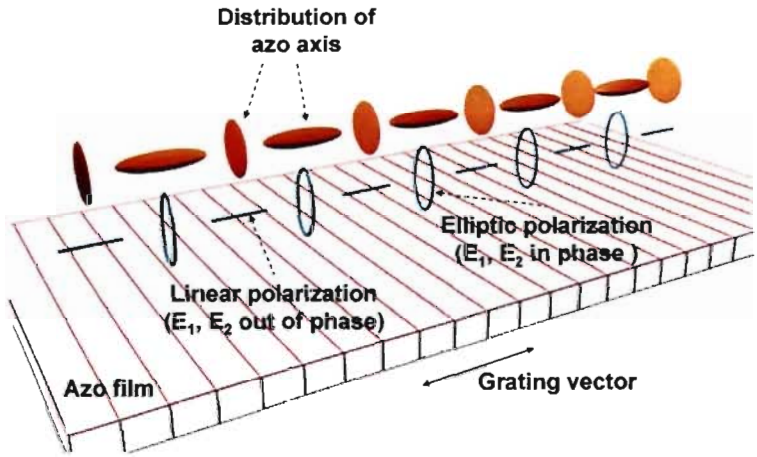

Figure 7.S3 Polarization patterns constructed on a film under two typical conditions, and the resultant distribution of the azo long axis.

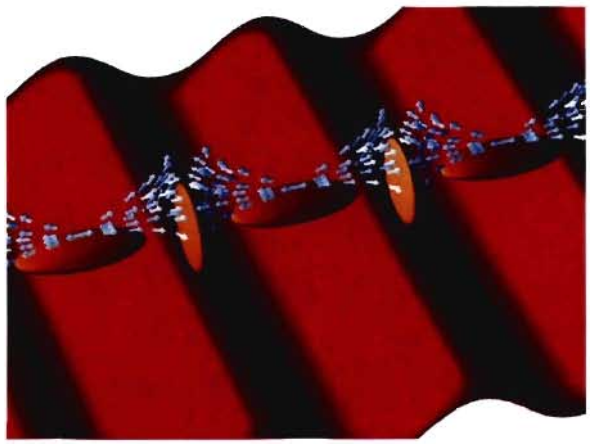

Figure 7.S4 An SRG is formed as a result of enriched populations of the most desired orientation of azo axis, induced by the corresponding light polarization strength and direction. The changing orientation of the azo long axis is illustrated by blue arrows. Local compression occurs on the peak and local stretching in the valleys.

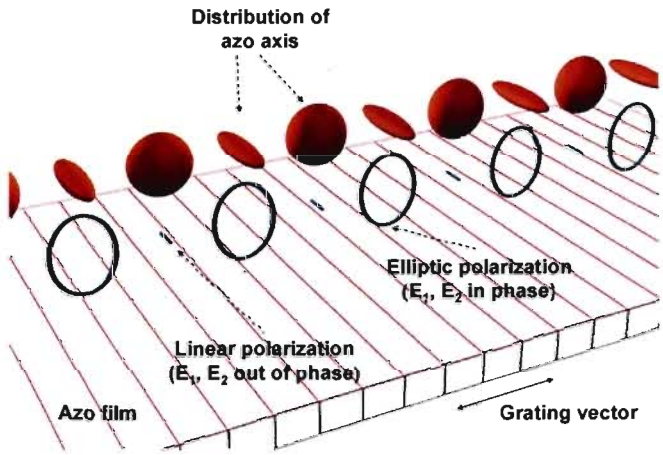

Figure 7.S5 Polarization patterns constructed in case of polarization in same way.

It is of interest that it is reported that the worst quality SRG is formed when the two light beams have circular polarization that rotates in the same direction.[4] We will briefly discuss this here (see Figure 7.S5). Compared to Figure 7.S3, there are two main differences in Figure 7.S5. First, the in-phase elliptic polarization is parallel to the grating vector, while the out-of-phase linear polarization is perpendicular to it, which is the inverse of that in Figure 7.S3. Second, because the beam angle is small (~15°), the linear polarization is much smaller, only $2A_0\sin\theta$ maximum, whereas the elliptic polarization is larger at the short axis with a maximum of $2A_0\cos\theta$ and unchanged at the long axis with a

maximum of $2A_0$. Consequently, as illustrated in Figure 7.S6, we can find that although the out-of-phase linear polarization can force the azo axis to "stand up", it is very limited because the magnitude of polarized light is much smaller. On the other hand, although the in-phase elliptic polarization is stronger, it forces the azo axis to lie down and, most importantly, to be perpendicular to the grating direction. As a consequence, the elliptic polarization works to drain the azo in the "standing up" linear polarized part, and therefore makes the grating hard to form. In this case, it is hard to pinpoint where the peaks and valleys are exactly.

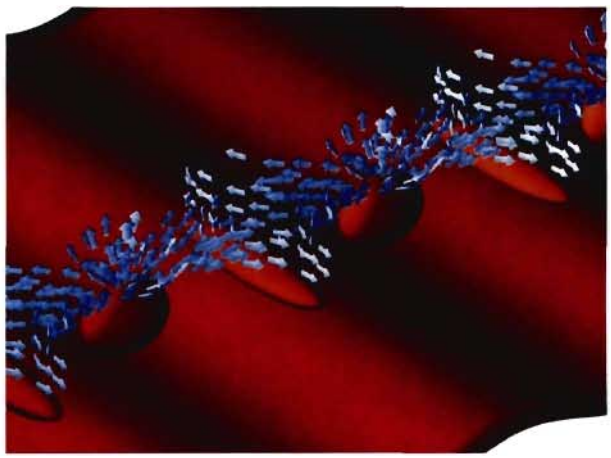

Figure 7.S6 Poor quality SRG is formed when two circularly polarized light beams have the same polarization direction.

It should be noted that the polarization pattern has been described as early as in 1996,[13] but was not discussed in detail. The discussion here is based on the photo-orientation process of the azo group, which plays a key role in SRG formation,[4] but the azo group is part of a larger system whose other parts also influence the photo-orientation process. The SRG obtained is the result of movement of all these parts, where the azo group plays a driving force.[27] We must keep in mind the complexity of the azo system. Whether it is liquid crystal or amorphous,[27] whether the azo moieties are in the main-chain or side-chain, etc., can make a difference.[28] SRG formation also depends on the mechanical properties of material, such as that related to the Tg.[29] Generally, the higher the Tg, the more stable the SRG and the higher its amplitude.[30-32] As described in the main text

of this chapter, stress induced in the photoisomerization process is an important factor in SRG formation.[17,29]

7.7.1 References

1. Kim, D. Y.; Tripathy, S. K.; Li, L.; Kumar, J. *Appl. Phys. Lett.* **1995,** 66, 1166-1168.
2. Rochon, P.; Batalla, E.; Natansohn, A. *Appl. Phys. Lett.* **1995,** 66, 136-138.
3. Natansohn, A.; Rochon, P. *Chem. Rev.* **2002,** 102, 4139-4175.
4. Yager, K. G.; Barrett, C. J., Light-induced nanostructure formation using azobenzene polymers. In *Polymeric Nanostructures and Their Applications*, Nalwa, H. S., Ed.; American Scientific Publishers: Los Angeles, 2007; Vol. 2, pp. 243-280.
5. Viswanathan, N. K.; Kim, D. Y.; Bian, S.; Williams, J.; Liu, W.; Li, L.; Samuelson, L.; Kumar, J.; Tripathy, S. K. *J. Mater. Chem.* **1999,** 9, 1941-1955.
6. Lefin, P.; Fiorini, C.; Nunzi, J.-M. *Opt. Mater.* **1998,** 9, 323-328.
7. Mechau, N.; Neher, D.; Borger, V.; Menzel, H.; Urayama, K. *Appl. Phys. Lett.* **2002,** 81, 4715-4717.
8. Lefin, P.; Fiorini, C.; Nunzi, J.-M. *Pure and Applied Optics* **1998,** 7, 71-82.
9. Pedersen, T. G.; Johansen, P. M. *Phys. Rev. Lett.* **1997,** 79, 2470-2473.
10. Pedersen, T. G.; Johansen, P. M.; Holme, N. C. R.; Ramanujam, P. S.; Hvilsted, S. *Phys. Rev. Lett.* **1998,** 80, 89-92.
11. Baldus, O.; Zilker, S. J. *Appl. Phys. B: Lasers Opt.* **2001,** 72, 425-427.
12. Viswanathan, N. K.; Balasubramanian, S.; Li, L.; Tripathy, S. K.; Kumar, J. *Jpn. J. Appl. Phys., Part 1* **1999,** 38, 5928-5937.
13. Barrett, C. J.; Natansohn, A. L.; Rochon, P. L. *J. Phys. Chem.* **1996,** 100, 8836-8842.
14. Barrett, C. J.; Rochon, P. L.; Natansohn, A. L. *J. Chem. Phys.* **1998,** 109, 1505-1516.
15. Lee, J.-D.; Kim, M.-J.; Nakayama, T. *Langmuir* **2008,** 24, 4260-4264.
16. Kumar, J.; Li, L.; Jiang, X. L.; Kim, D.-Y.; Lee, T. S.; Tripathy, S. *Appl. Phys. Lett.* **1998,** 72, 2096-2098.
17. Saphiannikova, M.; Neher, D. *J. Phys. Chem. B* **2005,** 109, 19428-19436.
18. Helgert, M.; Wenke, L.; Hvilsted, S.; Ramanujam, P. S. *Appl. Phys. B: Lasers Opt.* **2001,** 72, 429-433.
19. Holme, N. C. R.; Nikolova, L.; Hvilsted, S.; Rasmussen, P. H.; Berg, R. H.; Ramanujam, P. S. *Appl. Phys. Lett.* **1999,** 74, 519-521.
20. Zettsu, N.; Fukuda, T.; Matsuda, H.; Seki, T. *Appl. Phys. Lett.* **2003,** 83, 4960-4962.
21. Bian, S.; Williams, J. M.; Kim, D. Y.; Li, L.; Balasubramanian, S.; Kumar, J.; Tripathy, S. *J. Appl. Phys.* **1999,** 86, 4498-4508.
22. Henneberg, O.; Geue, T.; Saphiannikova, M.; Pietsch, U.; Chi, L. F.; Rochon, P.; Natansohn, A. L. *Appl. Phys. Lett.* **2001,** 79, 2357-2359.
23. Bo, Q.; Yavrian, A.; Galstian, T.; Zhao, Y. *Macromolecules* **2005,** 38, 3079-3086.
24. Kim, D. Y.; Li, L.; Jiang, X. L.; Shivshankar, V.; Kumar, J.; Tripathy, S. K. *Macromolecules* **1995,** 28, 8835-8839.
25. Yavrian, A.; Galstian, T. V.; Piche, M. *Opt. Eng.* **2002,** 41, 852-855.
26. Henneberg, O.; Geue, T.; Pietsch, U.; Saphiannikova, M.; Winter, B. *Appl. Phys. Lett.* **2004,** 84, 1561-1563.

27. Bublitz, D.; Helgert, M.; Fleck, B.; Wenke, L.; Hvilsted, S.; Ramanujam, P. S. *Appl. Phys. B: Lasers Opt.* **2000,** 70, 863-865.
28. Keum, C.-D.; Ikawa, T.; Tsuchimori, M.; Watanabe, O. *Macromolecules* **2003,** 36, 4916-4923.
29. Veer, P. U.; Pietsch, U.; Rochon, P. L.; Saphiannikova, M. *Mol. Cryst. Liq. Cryst.* **2008,** 486, 66-78.
30. Lee, T. S.; Kim, D. Y.; Jiang, X. L.; Li, L.; Kumar, J.; Tripathy, S. *Macromol. Chem. Phys.* **1997,** 198, 2279-2289.
31. Nakano, H.; Tanino, T.; Takahashi, T.; Ando, H.; Shirota, Y. *J. Mater. Chem.* **2008,** 18, 242-246.
32. Sukwattanasinitt, M.; Wang, X.; Li, L.; Jiang, X.; Kumar, J.; Tripathy, S. K.; Sandman, D. J. *Chem. Mater.* **1998,** 10, 27-29.

Chapter 8. Towards Light-responsive Fibers: Preparation and Characterization

Abstract

Electrospinning was applied to a mixture of poly(methyl methacrylate) (PMMA) and MO/PVP, which is an azo-containing liquid crystalline complex between methyl orange (MO) and methylated poly(4-vinylpyridine) (PVPMe), to obtain composite fibers. The fibers had average diameters ranging from 800 nm to 2 μm depending on the composition. The fibers showed good birefringence and orientation under polarized optical microscopy. X-ray diffraction confirmed the presence of the two components and of a liquid crystalline phase from the MO/PVP component, but the liquid crystalline phase was found to be unoriented. Transmission electron microscopy showed phase separation perpendicular to the fiber cross-section, forming nano-strips of tens' of nanometers in thickness. This study paves the way towards the preparation of light-responsive fibers.

8.1 Introduction

Fibers play an important role in many aspects of life, such as for clothing,[1] housing,[2] personal security,[3] in reinforced compound materials,[4] in medical[5,6] and biological[7] applications, in functional surfaces,[8] and in sports equipment.[9,10] In materials science, the main application of fibers is to reinforce the mechanical properties of composite materials. Nowadays, various preparation techniques allow the preparation of functional nano-fibers.[11-17] Among these techniques, electrospinning has received much attention recently for its low cost, simple implementation in laboratory conditions and, above all, its applicability to a wide variety of starting materials.[7,18-20] An example is the preparation of polymer fibers with well controlled hierarchical nano-structures via the combination of electrospinning and molecular self-assembly.[21,22] Submicron fibers with complex structures, such as core-shell hollow fibers, can be fabricated through a two-fluid coaxial electrospinning process.[23,24]

In this paper, electrospinning is applied to the fabrication of azo-containing polymeric nanofibers. Azobenzene (or azo for short) molecules are well known for their highly efficient photoisomerization process[25] that allows controlling molecular orientation in polymer films.[26] It has been widely used in areas such as optoelectronic[26-28] and photochemical[29] applications, in life[30,31] and surface[32] sciences, etc. It has been demonstrated that macroscopic deformation and movement of polymer films can be induced by simple irradiation due to the photoinduced alignment of chromophores and internal structure re-arrangement. [33-36] Very recently, a light-driven motor was invented by Ikeda's group based on 3D light-induced movement,[37] revealing the potential of azo-containing polymers as artificial muscles.[38] Light-induced size change was first discovered in fibers as early as 1966, when nylon filaments were dyed with azobenzene-derivatives; they were found to have a limited shrinkage of 0.1% upon irradiation.[39] It may be expected that improved photomechanical effects may be possible with higher loading of azo material in fibers and especially through careful design. For example, azo-containing polymers can be used to make fibers. Very little work has been undertaken on this subject to date. A second goal is the control of molecular orientation in the electrospinning process. Many groups have investigated the orientated structure of electrospun fibers,[24,40-42] but the

orientation is usually moderate, and stretching is sometimes needed to enhance the orientation.[40] Recently, Pellerin and coll. fabricated highly oriented electrospun fibers of poly(ethylene oxide) and urea inclusion complexes.[43] However, it remains difficult to adjust the level of orientation in these fibers. Azo-containing liquid crystalline polymers may be an interesting alternative to control the orientation level, since the azobenzene moiety provides a second degree of freedom to obtain oriented structures by light-induced isomerization and orientation.

In this work, fibers have been prepared from mixtures of PMMA with MO/PVP (to be abbreviated as MMA/MO). MO/PVP, which was recently reported as a high performance azo-containing liquid crystalline polymer complex,[44] is a unique material: first, it is an intractable material with high glass transition (T_g=183 °C) and degradation ($T_d^{1\%}$=222 °C) temperatures; second, it is able to form a single layer smectic A (SmA) liquid crystalline phase in the absence of any flexible spacer or tail from room temperature up to its degradation; and third, laser irradiation leads to a very large photoinduced birefringence (PIB) with very good temporal and thermal stability; fourth, it has high efficiency in fabricating surface relief gratings (SRGs).[44,45] This paper reports the preparation of fibers and their characterization.

8.2 Experimental section

8.2.1 Materials

PMMA (M_w=540K) was obtained from Scientific Polymer Products and used as received. Methyl orange, nitromethane (95+%) and DMSO (99.9%, spectrophotometric grade) were all purchased from Aldrich and used as received. Poly(4-vinyl pyridine) was purchased from Scientific Polymer Products (M_v=200K). DMF (EMD) was dried by passing through drying columns (Glass Contour system) before use. Deionized water was obtained from a Millipore Gradient A10 Milli-Q system (resistivity 18.2 MΩ.cm at 25 °C). The stoichiometric MO/PVP complex was prepared according to the procedures described elsewhere.[44,45] Basically, poly(4-vinyl pyridine) was fully methylated, both components (with MO in 14% excess) were dissolved separately in DMSO, then mixed together, and finally dialyzed against deionized water for a few days. The 1:1 molar ratio of MO and VP

was confirmed by NMR and elemental analysis. The chemical structures of PMMA and MO/PVP are shown in Figure 8.1.

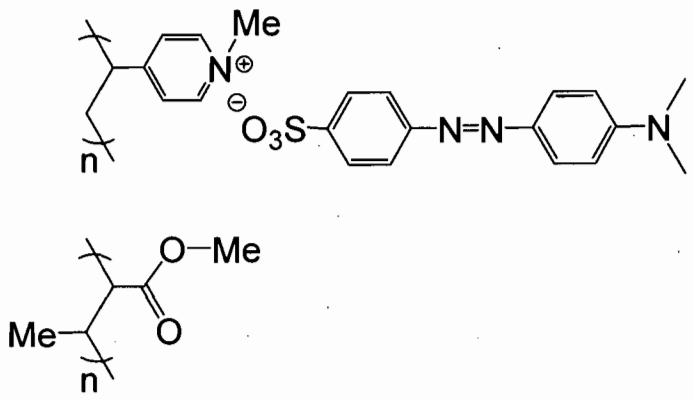

Figure 8.1 Molecular structures of MO/PVP (top) and PMMA (bottom).

8.2.2 Fiber preparation

Mixtures (about 15-40 mg per sample) of PMMA and MO/PVP (1:2, 1:1 and 2:1 by weight; abbreviated as MMA/MO 1/2, MMA/MO 1/1 and MMA/MO 2/1 respectively), as well as PMMA alone and MO/PVP alone, were prepared in DMF, and warmed by a heat gun to ca. 60 °C while stirring (Vortex mixer, Fisher Scientific) to form transparent solutions with a total solid content of 15 wt% (unless otherwise specified). Each solution was transferred to a syringe, mounted on a syringe pump (PHD 2000, Harvard Apparatus), and extruded through a 0.41 mm diameter needle at a rate of 0.008 mL/min. A +20 kV voltage was applied to the needle using a FC series 120 W regulated high voltage DC power supply (Glassman High Voltage). The collector was made of two parallel electrodes[19] with a gap of 3.4 cm and connected to -2 kV cathode of a Nim Standard HV power supply (Power Design). The distance between the tip of the needle and the collector was 10 cm. The fibers were dried in a vacuum oven at 60 °C for 12 h.

8.2.3 Characterization

Polarizing optical microscopy (POM) micrographs were recorded using an Axioskop 40 microscope (Carl Zeiss) with a 20X objective. Scanning electron microscopy (SEM) was performed with a FEI Quanta 200 FEG environmental scanning electron microscope,

for which the sample was first coated with gold (Sputter Coater, Agar Scientific). Differential scanning calorimetry (DSC) thermograms were obtained with a Q2000 calorimeter (TA Instruments) at a 10 °C/min scanning rate. Thermogravimetric analysis was done with a TGA 2950 from TA Instruments. X-ray diffraction (XRD) was performed with a Bruker AXS D8 Discover system equipped with a 2D wire-grid detector, using Cu Kα radiation. Transmission electron microscopy (TEM) micrographs were obtained with FEI Tecnai 12 working at 120 kV and equipped with a Gatan 792 Bioscan 1k x 1k wide angle multiscan CCD camera. To enhance the contrast, the fiber was immersed in a 0.1 wt% $K_2Cr_2O_7$ aqueous solution for 24 h, then in deionized water for 24 h, then freeze-dried and embedded in LR White (London Resin) and cured at 60 °C for 48 h. Finally, the sample was cut into thin slices with a microtome (Ultracut E, Reichert-Jung) equipped with Diatome knife.

8.3 Results and discussion

A preliminary study showed that electrospinning of the MO/PVP complex by itself in DMF solution at concentrations between ca. 5 and 17 wt% does not lead to fibers. At higher concentrations, the viscosity was too high and solution transfer was difficult. PMMA was therefore added to assist in forming fibers in electrospinning, with the consideration that PMMA has excellent optical properties, fairly good mechanical properties and low cost. It has a relatively high T_g at 117 °C with 1% weight loss at 162 °C. The optical transparency of PMMA permits light penetration through the fiber bundles. The high T_g will preserve the mechanical integrity of the fiber during drying at 60 °C, and during later photoirradiation of the fibers. In addition, electrospinning of pure PMMA fibers has been well studied, so that good processing parameters to avoid beading and other defects are already known.[46-48] Figure 8.2 shows that very well dispersed fibers can be obtained with a good yield when the MO/PVP complex is mixed with PMMA in 1:2, 1:1 or 2:1 mass ratios. Good fibers can also be obtained using the more conventional spinning additive poly(ethylene oxide) (PEO). However, the low T_m (65 °C) and scattering due to the crystalline phase renders PEO less desirable than PMMA.

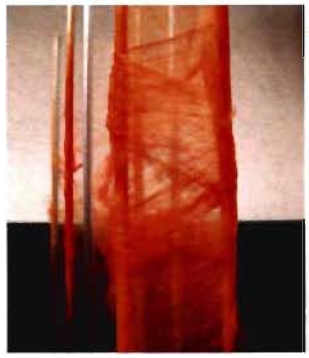

Figure 8.2 Electrospun fibers obtained on the collector. Some fibers missed the collector and were wrapped around the parallel rods.

POM micrographs of the fibers prepared at the three compositions, in comparison with pure PMMA fibers prepared under the same conditions, are shown in Figure 8.3. All of the fibers show continuous shape and relatively uniform diameter along the fiber axis. Very few beads were found. Occasionally, branching or sticking can be observed. Breaking was only observed when fibers were mechanically stretched. The diameter of the fiber is about one micrometer. All of the fibers show a significant level of birefringence. Maximum birefringence is observed when the fibers are aligned at 45° from the polarizer (and analyzer), and is completely extinguished when a fiber section is parallel to the polariser or analyser direction (see arrow in Figure 8.3a). This birefringence indicates a certain level of molecular orientation in the fibers, which arises at least partly from PMMA, since pure PMMA fibers also show orientation birefringence, albeit with less intensity than for the composite fibers (Figure 8.3d). Since PMMA is essentially amorphous, its birefringence must be due to the partial orientation of polymer chains during electrospinning.

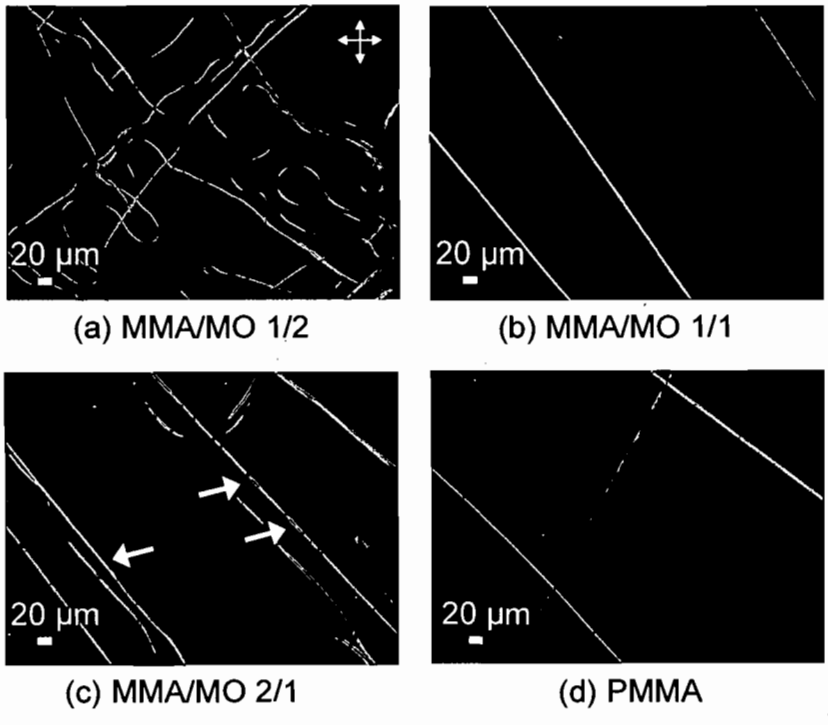

Figure 8.3 Morphology of the electrospun fibers investigated, as observed by POM.

It is interesting to note that regions with discontinuous birefringence can be found for fibers MMA/MO 1/1 and 2/1, but not for MMA/MO 1/2 (indicated by arrows in Figure 8.3c). The reason is not clear, but it may be related to inhomogeneity or nanophase separation between the complex and PMMA.

The fiber morphology was also studied by SEM (Figure 8.4), which shows that all of the fibers have round cross-sections, smooth surfaces, and varying diameters. The average diameters, calculated by randomly sampling at least 100 fiber cross-sections, are shown in Figure 8.5. The average diameter appears to increase with MMA content, going from 800 nm to 1.5 μm for MMA/MO ratios increasing from 1:2 to 2:1. At the same time, the diameter distribution broadens as more PMMA is used in the spinning solution.

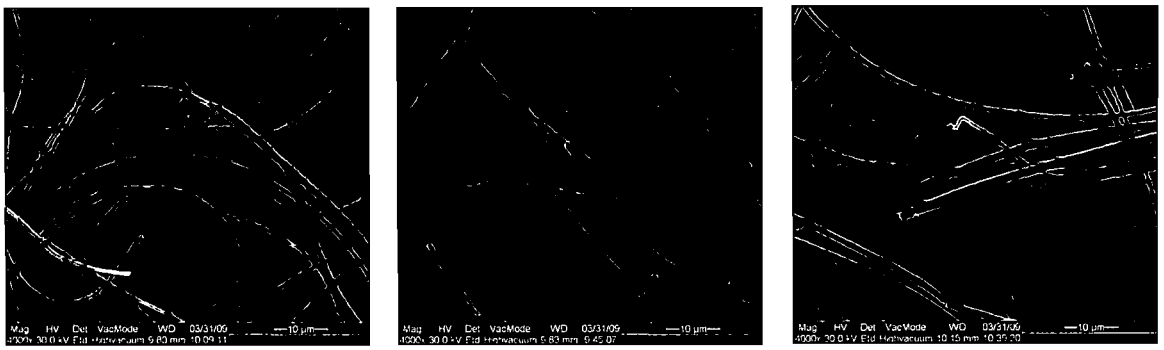

Figure 8.4 SEM micrographs of the fibers studied.

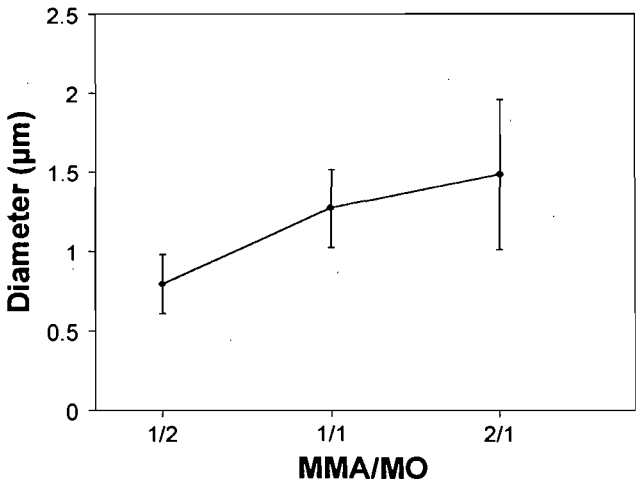

Figure 8.5 Average diameter of the fibers as a function of MMA/MO ratio. The error bar shows the standard deviation of at least 100 measurements.

XRD was used to determine if the liquid crystalline phase of MO/PVP is preserved as well as to investigate its possible orientation. Figure 8.6 compares the diffractograms of the fibers to those of the starting materials in powder form. Except for pure PMMA, all show the presence of a diffraction peak at small angles (ca. 3.55°). whose intensity, for the composite fibers, decreases with increase in PMMA content. This, along with the wide angle halos (see below), confirms the liquid crystalline structure of MO/PVP in the electrospun fibers. The Bragg spacing of the diffraction peak at small angle for the fibers is very close to that of the powder form of the complex, indicating that the LC phase of the complex is little disturbed and that the SmA mesophase is preserved.

At large angles, MO/PVP shows a broad halo centered at 19° and PMMA a broad halo centered at 13°. These halos are superimposed in the composite fibers, with intensities that reflect the fiber composition. In MO/PVP, the halo reflects the average lateral distance between MO side chains. In PMMA, it reflects the average distance between the PMMA chains. In the composite fibers, these halos are superimposed, with relative intensities that reflect the fiber composition.

By fitting the two halos for the composite fibers, and comparing the area of the 3.5° diffraction peak relative to the area of the 19° halo in the starting complex and the fibers, it is observed that the decrease in area of the 3.5° peak with increase in PMMA content is greater than expected from the composition change. This indicates that the ability of MO/PVP to form a liquid crystalline phase is decreased by the presence of PMMA.

The 2D XRD patterns reveal that none of the fibers show orientation of the liquid crystalline structure (not shown). This can actually be a positive feature since it provides a possible basis for orientation of this phase to be controlled instead by light irradiation. Similarly, no liquid crystal orientation was found in composite fibers made from a mixture of a different side chain liquid crystalline polymer and PEO.[49] In another example, electrospun fibers of a main-chain liquid crystalline polymer elastomer showed considerable birefringence; however, no XRD diffractograms were shown to further confirm the origin of the orientation.[50]

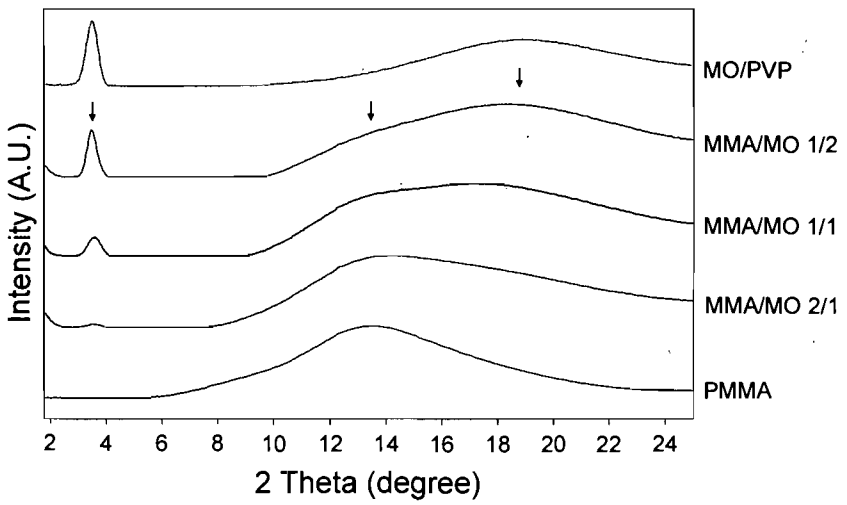

Figure 8.6 X-ray diffractograms of the electrospun composite fibers and of MO/PVP and PMMA in powder form.

The composite fibers and PMMA fiber were also investigated by DSC (Figure 8.7). The scan was terminated at 140 °C because the thermogravimetric analysis curve of PMMA starts to deflect at this temperature. All of the complexes show a T_g at ~126 °C, compared to 121 °C for the pure PMMA fibers, and 183 °C for the MO/PVP complex powder.[45] The 5 °C increase of the T_g in the composite fibers compared to the PMMA fibers indicates that the former is due to a phase highly enriched in PMMA, therefore indicating that almost all of the MO/PVP forms a separate phase. Such phase separation between MO/PVP and PMMA is not surprising owing to their chemical structure differences. It should be noted that the T_g of the pure PMMA fiber is about 4 °C higher than that of the powder form. This may be related to the orientation of PMMA in the fibers, as indicated by POM (Figure 8.3d). This suggests that higher orientation of PMMA in the composite fibers compared to the pure PMMA fibers may also contribute to the increase of T_g from 121 to 126 °C. The latter point needs further investigation in orientation studies by polarized infrared spectroscopy.

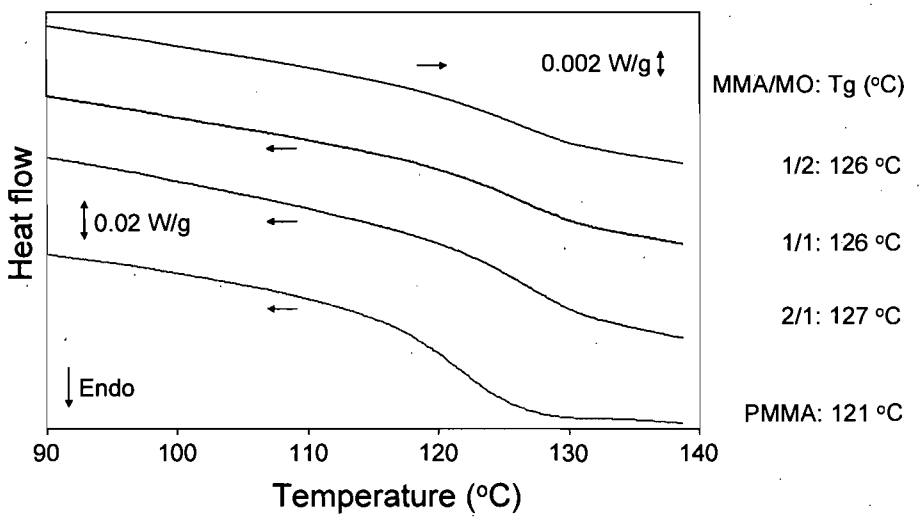

Figure 8.7 DSC thermograms of the electrospun fibers. All curves are from the third heating scan.

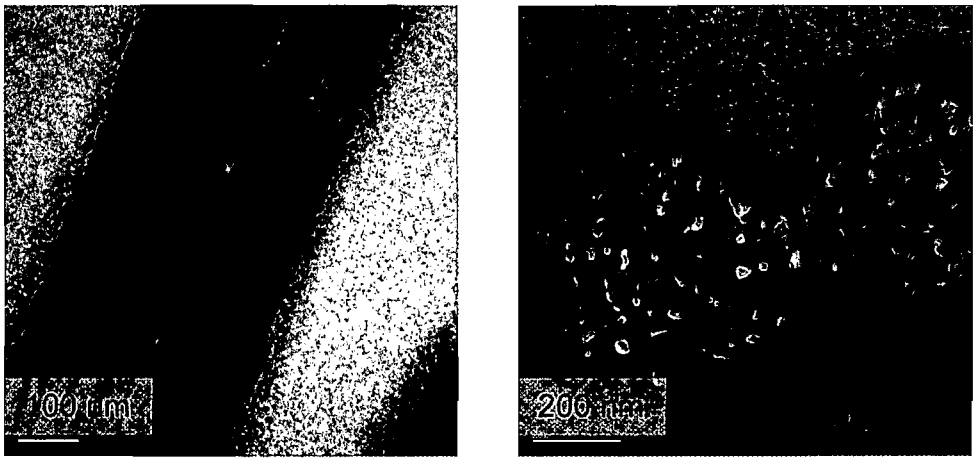

Figure 8.8 TEM micrographs of the MMA/MO 1/2 fiber: longitudinal (left) and cross (right) section.

Figure 8.8 shows longitudinal and cross-sectional pictures of the MMA/MO 1/2 fiber taken by TEM. A longitudinal fine structure consisting of alternating dark and bright strips of less than ca. 10 nm thickness along the fiber axis can be identified. Since the fiber was stained with $K_2Cr_2O_7$, the dark part should be from the MO/PVP complex, whereas the bright part is due to the PMMA-rich phase. When the polymer solution was highly deformed along the fiber direction during electrospinning, PMMA and MO/PVP could phase separate to form such nanostructure. The fast drying that occurs during electrospinning can freeze in this structure, similarly to what can be seen in the two-fluid electrospinning process.[23,24] In the cross-section of the fiber (Figure 8.8, right), irregular dark and white domains can be found. Their size matches very well with what is observed along the fiber axis. This confirms that phase separation takes place all across the fiber section. The aligned strips can lead to "form birefringence" [51] and explain part of the birefringence observed in the POM study, thus reconciling the large birefringence in the composite fibers despite the absence of orientation for the liquid crystalline phase in the 2D XRD patterns.

8.4 Conclusions and future work

Nanophase-separated fibers were prepared through electrospinning from solutions of PMMA mixed with an azo-containing ionically bonded liquid crystalline complex in varying ratios. The average diameters range from 800 nm to 2 μm, increasing with PMMA fraction. POM showed a uniform fiber shape and birefringence along the fiber axis, indicating the presence of anisotropic structure within the fibers, at least partly due to the amorphous PMMA component. In contrast, XRD showed that there is no orientation of the liquid crystalline complex. The XRD diffractograms were consistent with the constitutional ratio of the components. Phase separation of the two components within the fiber was clearly observed by TEM. Alternating strips of several nanometers' thickness along the fiber axis are thought to be a consequence of nanophase separation between PMMA and MO/PVP that occurs during the spinning process.

The fibers prepared in this report pave the way for the study of light-responsive behaviour in these materials. Future work can focus on (a) control of photo-induced orientation in the azo-containing LC phase; (b) investigations of photomechanical properties of the fiber, such as photo-regulated shrinkage, stretching and other complicated movement. This will require the construction of specialized experimental setups.

8.5 References

1. Mark, H. F. *Chem. Eng. Prog.* **1987,** 83, 44-54.
2. Habel, K.; Charron, J.-P.; Braike, S.; Hooton, R. D.; Gauvreau, P.; Massicotte, B. *Can. J. Civ. Eng.* **2008,** 35, 217-224.
3. Song, J. W.; Lee, B. L. In *Fabrics and composites for ballistic protection of personnel*, Lightweight Ballistic Composites, 2006; 2006; pp 210-239.
4. Jancar, J. *J. Mater. Sci.* **2008,** 43, 6747-6757.
5. Shanmugasundaram, S.; Griswold, K. A.; Prestigiacomo, C. J.; Arinzeh, T.; Jaffe, M. In *Applications of electrospinning: tissue engineering scaffolds and drug delivery system*, Proceedings of the 30th IEEE Annual Northeast Bioengineering Conference, Springfield, MA, Apr. 17-18, 2004, pp 140-141.
6. Vallittu, P. K. In *Fibre-reinforced composites for dental applications*, Dental Biomaterials, 2008; 2008; pp 239-260.
7. Schiffman, J. D.; Schauer, C. L. *Polym. Rev.* **2008,** 48, 317-352.
8. Tuteja, A.; Choi, W.; Ma, M.; Mabry, J. M.; Mazzella, S. A.; Rutledge, G. C.; McKinley, G. H.; Cohen, R. E. *Science* **2007,** 318, 1618-1622.

9. Caswell, S. V.; Gould, T. E.; Wiggins, J. S. In *Protective helmets in sports*, Materials in Sports Equipment, 2007; 2007; pp 87-126.
10. Jarrell, C. M. In *Composites reinforced with Kevlar 49 aramid for aircraft, marine, automotive, and sporting goods applications*, 1977; 1977; pp 45-60.
11. Ma, P. X.; Zhang, R. *J. Biomed. Mater. Res.* **1999,** 46, 60-72.
12. Nakata, K.; Fujii, K.; Ohkoshi, Y.; Gotoh, Y.; Nagura, M.; Numata, M.; Kamiyama, M. *Macromol. Rapid Commun.* **2007,** 28, 792-795.
13. Ondarcuhu, T.; Joachim, C. *Europhys. Lett.* **1998,** 42, 215-220.
14. Duvail, J. L.; Retho, P.; Garreau, S.; Louarn, G.; Godon, C.; Demoustier-Champagne, S. *Synth. Met.* **2002,** 131, 123-128.
15. Wu, C. G.; Bein, T. *Science* **1994,** 264, 1757-1759.
16. Liu, G.; Qiao, L.; Guo, A. *Macromolecules* **1996,** 29, 5508-5510.
17. Weitz, R. T.; Harnau, L.; Rauschenbach, S.; Burghard, M.; Kern, K. *Nano Lett.* **2008,** 8, 1187-1191.
18. Huang, Z.-M.; Zhang, Y. Z.; Kotaki, M.; Ramakrishna, S. *Compos. Sci. Technol.* **2003,** 63, 2223-2253.
19. Teo, W. E.; Ramakrishna, S. *Nanotechnology* **2006,** 17, R89-R106.
20. Subbiah, T.; Bhat, G. S.; Tock, R. W.; Parameswaran, S.; Ramkumar, S. S. *J. Appl. Polym. Sci.* **2005,** 96, 557-569.
21. Ruotsalainen, T.; Turku, J.; Heikkilae, P.; Ruokolainen, J.; Nykaenen, A.; Laitinen, T.; Torkkeli, M.; Serimaa, R.; ten Brinke, G.; Harlin, A.; Ikkala, O. *Adv. Mater.* **2005,** 17, 1048-1052.
22. Ruotsalainen, T.; Turku, J.; Hiekkataipale, P.; Vainio, U.; Serimaa, R.; ten Brinke, G.; Harlin, A.; Ruokolainen, J.; Ikkala, O. *Soft Matter* **2007,** 3, 978-985.
23. Moghe, A. K.; Gupta, B. S. *Polym. Rev.* **2008,** 48, 353-377.
24. Wang, M.; Yu, J. H.; Kaplan, D. L.; Rutledge, G. C. *Macromolecules* **2006,** 39, 1102-1107.
25. Rau, H., Photoisomerization of azobenzenes. In *Photochemistry and Photophysics*, Rabek, J. K., Ed.; CRC Press: Boca Raton, FL., 1990; Vol. 2, pp. 119-141.
26. Natansohn, A.; Rochon, P. *Chem. Rev.* **2002,** 102, 4139-4175.
27. Yesodha, S. K.; Pillai, C. K. S.; Tsutsumi, N. *Prog. Polym. Sci.* **2004,** 29, 45-74.
28. Kucharski, S. H., In *New Research on Optical Materials*, Litchitika, S. J., Ed.; Nova Science Publishers: 2007; pp. 119-156.
29. Peters, M. V.; Stoll, R. S.; Kühn, A.; Hecht, S. *Angew. Chem., Int. Ed.* **2008,** 47, 5968-5972.
30. Gorostiza, P.; Isacoff, E. Y. *Science* **2008,** 322, 395-399.
31. Woolley, G. A. *Acc. Chem. Res.* **2005,** 38, 486-493.
32. Wang, S.; Song, Y.; Jiang, L. *J. Photochem. Photobiol., C* **2007,** 8, 18-29.
33. Barrett, C. J.; Mamiya, J.-i.; Yager, K. G.; Ikeda, T. *Soft Matter* **2007,** 3, 1249-1261.
34. Camacho-Lopez, M.; Finkelmann, H.; Palffy-Muhoray, P.; Shelley, M. *Nat. Mater.* **2004,** 3, 307-310.
35. Yu, Y.; Nakano, M.; Ikeda, T. *Nature* **2003,** 425, 145.
36. Mamiya, J.-i.; Yoshitake, A.; Kondo, M.; Yu, Y.; Ikeda, T. *J. Mater. Chem.* **2008,** 18, 63-65.
37. Yamada, M.; Kondo, M.; Mamiya, J.-i.; Yu, Y.; Kinoshita, M.; Barrett, C. J.; Ikeda, T. *Angew. Chem., Int. Ed.* **2008,** 47, 4986-4988.

38. Ikeda, T.; Mamiya, J.-i.; Yu, Y. *Angew. Chem., Int. Ed.* **2007,** 46, 506-528.
39. Merian, E. *Text. Res. J.* **1966,** 36, 612-618.
40. Dersch, R.; Liu, T.; Schaper, A. K.; Greiner, A.; Wendorff, J. H. *J. Polym. Sci., Part A: Polym. Chem.* **2003,** 41, 545-553.
41. Fennessey, S. F.; Farris, R. J. *Polymer* **2004,** 45, 4217-4225.
42. Zong, X.; Ran, S.; Fang, D.; Hsiao, B. S.; Chu, B. *Polymer* **2003,** 44, 4959-4967.
43. Liu, Y.; Pellerin, C. *Macromolecules* **2006,** 39, 8886-8888.
44. Zhang, Q.; Bazuin, C. G.; Barrett, C. J. *Chem. Mater.* **2008,** 20, 29-31.
45. Zhang, Q.; Wang, X.; Barrett, C. J.; Bazuin, C. G. *Chem. Mater.* **2009,** 21, 3216-3227.
46. Piperno, S.; Lozzi, L.; Rastelli, R.; Passacantando, M.; Santucci, S. *Appl. Surf. Sci.* **2006,** 252, 5583-5586.
47. Carrizales, C.; Pelfrey, S.; Rincon, R.; Eubanks, T. M.; Kuang, A.; McClure, M. J.; Bowlin, G. L.; Macossay, J. *Polym. Adv. Technol.* **2008,** 19, 124-130.
48. Gupta, P.; Elkins, C.; Long, T. E.; Wilkes, G. L. *Polymer* **2005,** 46, 4799-4810.
49. Wu, Y.; An, Q.; Yin, J.; Hua, T.; Xie, H.; Li, G.; Tang, H. *Colloid Polym. Sci.* **2008,** 286, 897-905.
50. Krause, S.; Dersch, R.; Wendorff, J. H.; Finkelmann, H. *Macromol. Rapid Commun.* **2007,** 28, 2062-2068.
51. Ward, I. M., *Structure and Properties of Oriented Polymers*. 2 ed.; Chapman & Hall: New York, 1997.

Chapter 9. Conclusions and Future Perspectives

9.1 Conclusions

This thesis has focussed on studies of dye/polyelectrolyte liquid crystalline complexes, namely, relationships between chemical and packing structure, photoinduced performances and potential applications.

9.1.1 Ionic interactions and azo-containing LCs

9.1.1.1 Dye/polyelectrolyte complexes

A large series of stoichiometric ionically bonded side chain polymer complexes have been prepared from poly(styrene sulfonate) and quaternary ammonium-functionalized azo-containing surfactomesogens (Chapter 2). These complexes generally show a liquid crystal (LC) phase of the smectic A type for a spacer length of 10 CH_2 groups. When the polarity of azobenzene mesogen is relatively low, this LC phase is evident under "normal experimental conditions" which means a similar sample treatment as is usual for liquid crystals,[1-3] using standard techniques, notably POM, DSC and XRD. When the spacer length is 6, just one complex shows an LC phase by DSC, whereas XRD showed no clear LC structure in "normal experimental conditions". Further in-depth study found that most of these complexes, especially those with longer spacers, are actually intrinsically liquid crystalline. To show this, the necessary and critical condition is to anneal for long times at high temperatures, due to the very high viscosities of the materials.

Although only the SmA phase is observed in these series, the detailed structure varies: complexes with polar azo moieties show a larger Bragg spacing than less polar ones, which is surprisingly similar to results for all-covalent counterparts of the complexes.[3] Models were constructed to explain the difference, based, first, on interactions between the nonpolar tail of the azo moiety and alkyl spacer, and, second, on interactions between the ionic bond and the highly polar azo moiety.

The consensus from this series, compared to covalent counterparts, is the increased viscosity due to the ionic bond, inherited from the polyelectrolyte.[4] It prevents the

complexes from easily reaching a thermodynamic equilibrium LC phase, leaving the isotropic phase frozen in. This can only be overcome by long annealing times at high temperatures (although the danger is that the samples could be subject to degradation) or by a solvent assisted process. Other effects on LC phase formation, like the presence of lateral groups on the effective side chains in O_2N-N(Me)/PSS and O_2N-N(Et)/PSS, were also studied, where it was found that the ethyl substituent was large enough to prevent LC phase formation.

Solvent vapours, such as of H_2O and acetone, can be used to assist the complex in reaching an equilibrium LC state (Chapter 3). The identification of these LC phases remains a challenge in some cases. This study actually touches lyotropic LCs, which can form many unconventional LC phases that can be complicated to identify.[5,6]

As opposed to the above SCLCP complexes with conventional spacers,[7,8] we found that when methyl orange, which is both spacer- and tail-free, is complexed to methylated P4VP (named MO/PVP), a SCLCP complex with a single-layer SmA phase can be obtained (Chapter 4).[9] A follow-up study with other spacer-free small molecules with various tails (synthesized by us) and including a different backbone with a short spacer, revealed that this may be a general phenomenon for rod-shaped azobenzene sulfonate compounds complexed with polycations (Chapter 5).[10] In addition, some data suggested a SmC phase for those with a long flexible alkyl tail. These complexes show a very high Tg (>180 °C) and clearing temperature (even beyond the onset of degradation).

9.1.1.2 Dye/surfactant complexes

A novel one-pot synthesis was discovered to form dye/surfactant complexes (Chapter 6). To our knowledge, this is the first time that (a) dialkyl chain quaternary ammonium surfactants are made this way; (b) small molecular complexes have been prepared where alkyl chains are present on both the surfactant and the dye. These complexes show only crystalline and isotropic phases for the shorter tails (n=6-11), and, in addition, a thermotropic SmT-like phase for longer tails (n=12, 16).

9.1.2 Photoinduced performances in ionically bonded SCLCP complexes

9.1.2.1 Photoisotropization

A new XRD technique with *in situ* coupled laser irradiation, shown in Figure 9.1, was used to induce photoisotropization for the first time. It was applied successfully to the crystal-like phase of O_2N-N(Et)10Q/PSS mixed with water, (Chapter 3) and to the SmT-like mesophase of Azo-16p (Chapter 6).

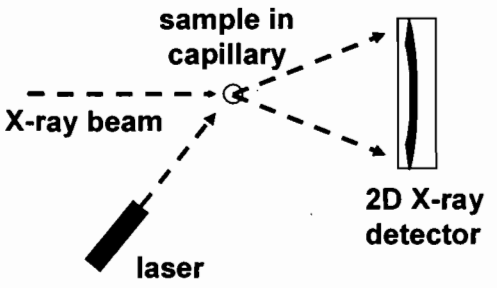

Figure 9.1 Experimental setup for photoisotropization.

9.1.2.2 Photoinduced birefringence (PIB)

For the complexes with long alkyl spacers, the PIB was found to be in the normal range for many azo polymers, with relatively low values and low temporal and thermal stability (Chapters 2 and 3). This suggests that the incorporation of ionic bonds as such is not so helpful in improving PIB. On the other hand, PIB can be highly dependent on the environment of the film: for example, the ionic complexes may be especially sensitive to ambient humidity, considering the well-known affinity between polyelectrolytes and water.[4] This was shown in Chapter 3 where the PIB in the films stored in different humidity conditions were compared. It is found that the extent/rapidity of relaxation does not necessarily follow the humidity sequence. Although this needs confirmation, this may be related to how the amount of humidity may affect the molecular packing structure. While plasticization may affect the relaxation of PIB in proportion to the water content, the induced LC phase can make the PIB response more complex.[11]

For the spacer-free LC complex, MO/PVP, the PIB value and its temporal and thermal stability are much higher (Chapter 4). This is attributed to the combination of molecular rigidity, of the LC structure, of the polymeric character, and of the ionic interactions.[9] The contribution of flexible components to the PIB properties was further investigated in a series of spacer-free SCLCP complexes, made of a less polar azo moiety (weaker push-pull substituents) (Chapter 5). This study clearly confirmed the deleterious effect of flexible components on the PIB. In contrast, an OH tail, which is not flexible and which can further rigidify the system through hydrogen-bond interactions, also promotes high birefringence and stability. The short spacer in a different polyelectrolyte backbone (methylated PDM) also leads to reduced PIB performance. The results confirm the importance of high rigidity (and consequently a high T_g) for stabilizing the PIB. The performance is comparable to that of high T_g all-covalent systems,[11] but with the benefit of ease of preparation.

It may be added that it was noted that some complexes sometimes showed somewhat more than their usually observed relaxation. It is thought that this might be caused by particular film conditions; for example, residual solvent, humidity exposure, or frozen-in molecular packing structure due to a different sample history. This indicates that special attention must be paid to both the preparation and storage conditions of the films.

9.1.2.3 Surface relief gratings (SRG)

SRG inscription was studied mainly on films made from the spacer-free complexes (Chapters 4 and 5). High (up to 360 nm) and stable (no change in almost two months) SRGs with good quality can be fabricated. In general, the trends in amplitudes of the inscribed SRGs followed the trends in PIB performance. Thus the MO/PVP complex formed the best SRGs (>300 nm amplitude), whereas the incorporation of flexible moieties, such as an alkyl tail or a short spacer in the polymer, reduced the SRG amplitude. For a hexyl tail in the spacer-free series, no SRG at all could be inscribed. Again, a hydrogen-bonding tail was beneficial.

9.1.3 Applications of SCLCP complexes

9.1.3.1 Nanofabrication

SRG fabrication provides a useful means for making well-defined surface patterns (Chapter 7). First, it was shown how the SRG amplitude is influenced by the ambient humidity during the SRG fabrication. Surprisingly, it was found that subsequent exposure of the SRG to 100% RH caused almost complete erasure in a very short time (30 sec) in the low humidity-fabricated SRG; whereas, in contrast, the higher humidity-fabricated SRG (50-60%RH) only showed partial erasure (ca. 70%). Pit-formation (several nanometers to more than one hundred nanometers in depth) was also noted in the 100% RH-exposed SRGs prepared in low humidity conditions. Second, the SRG profiles were further manipulated by combining partial shadowing of the SRGs by gold and post-humidity exposure. Gold shadowing protects the parts of the SRGs covered with gold from exposure to moisture. This provides a way to modify the SRGs to have non-sinusoidal profiles. This technique is expected to be applicable to any SRGs formed in azo materials, including 2D stubs.[11,12]

9.1.3.2 Photoresponsive fibers

We have shown that it is possible to prepare fibers with diameters of ca. 800 nm to 2 μm by electrospinning from a mixture of MO/PVP and PMMA in DMF solution (Chapter 8). Within the fibers, nano-strips of up to 10 nm in width were observed along the longitudinal direction of the fiber, indicating phase separation between the two components. Macroscopic orientation was found and explained by form orientation due to the nanophase separation and by orientation of the PMMA phase.

9.2 Future work and perspectives

9.2.1 Future work following the current research

Future investigations of the surfactomesogen/polyelectrolyte systems could focus on validating or further developing the models proposed in Chapter 2 to explain the differences in the SmA phase structures observed by XRD. A promising technique could

be the use of small-angle neutron scattering (SANS) of the complexes with deuterated solvents of the type studied in Chapter 3, since some of these solvents appear to control which type of SmA packing structure is preferred.

In view of optical applications, the spacer-free systems like those studied in Chapters 4 and 5 appear to be the most promising, and their study should be further pursued, to establish additional molecular structure – LC property – optical property relationships and further optimize optical performance. There are many commercially available azo dyes with ionic or ionisable groups. Some are rod-like, and others have different molecular shapes, which may or may not lead to LC systems when complexed with polyelectrolytes. Some have two or more ionic groups, which can be interesting for the conception of ionically crosslinked systems. Many others, of course, can be synthesized, with particular molecular architectures and functions in mind. Greater molecular bulkiness or the presence of two or more azo groups per molecule may enhance performance. The presence of H-bond functions simultaneously with ionic bonds, as in the spacer-free colorant with the OH tail (cf. Chapter 3), can allow further tweaking of the systems – for example, by adding a (bi)pyridyl-functionalized (azo) molecule. Mixtures of dyes may also be of interest. There are also many different polyelectrolytes, as well block and statistical copolymers with polyelectrolyte (i.e. ion-containing) moieties, that are commercially available or that can be synthesized.

Although humidity can be a deleterious factor that lowers PIB values and stability, it may be turned into an advantage to develop humidity responsive PIB materials. Furthermore, as suggested in Chapter 3, the unexpected PIB response of surfactomesogen/polyelectrolyte complexes to different humidity levels, which may be related to how the humidity affects the molecular packing structure, suggests that this may provide a unique opportunity to investigate the LC structure – PIB response relationship, which is currently still poorly understood. The PIB of MO/PVP in different humidity environments was also examined briefly in the course of our work (Figure 9.2). In this case, the film exposed to 100% RH relaxed the most quickly initially, but much less than the complexes with spacers studied in Chapter 3. However, surprisingly, the PIB then increases over time, which is difficult to rationalize at this time. Further investigations are needed to understand this phenomenon.

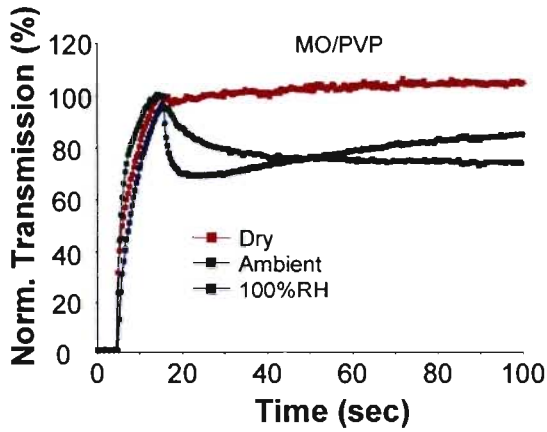

Figure 9.2 PIB of MO/PVP exposed to different humidity conditions. The humidity in ambient is 45±5%RH.

SRGs on the azo-containing polymers provide us with a potentially unique soft workbench for making well-defined surface patterns (Figure 9.3). They are fabricated by a highly efficient "top down" light-involved process, and can be precisely and conveniently tuned by the angle between two laser beams in inscription. Knowing that ionically bonded LC complexes are very sensitive to moisture and other small molecules, we can try to modify the profile of pre-fabricated SRGs by controlled exposure to humidity (or other solvent vapour). This might also give a chance to learn about the stress below the SRG surface, and may help to better understand the mechanism of SRG formation.

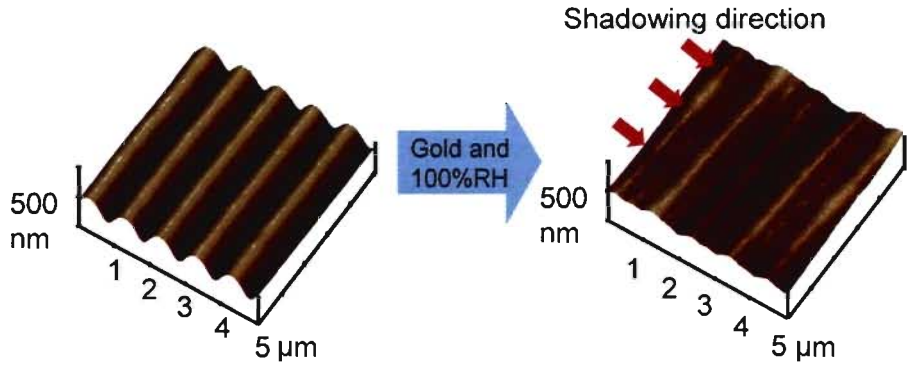

Figure 9.3 Modification of SRG profiles by partial coating with gold and subsequent exposure to 100% RH.

Following the study in Chapter 7, the modified SRG morphology can, in principle, be perfected and controlled by adjusting parameters like initial SRG height and periodicity, shadowing control (gold or other material, shadowing angle, shadowing time, etc.),

humidity level (or other small molecules), exposure time, etc. Reactive shadowing or high energy irradiation-induced crosslinks may also be exploited.

The photoresponse of the electrospun azo-containing fibers, including photoorientation and photomechanics, will be studied in future work. This will include the preparation of other azo-containing materials to make the fibers.

9.2.2 Future perspectives

9.2.2.1 Optical properties: PIB, SRG, NLO and fluorescence

Major interest still remains in new optical materials that can achieve high values and stability of PIB. Large conjugate systems (which are highly anisotropic) are expected to give very high PIB. To this ends, azo-tolane[13-15] and diazo systems[16] were prepared. They indeed show high PIB (up to 0.4); however, still higher values are desired. Thus even larger conjugate systems may be expected to break the record. Linear conjugate polymers may be good candidates, as highlighted by a recent preparation of polyazostilbene through electropolymerization.[17] Another possibility may involve large azo conjugate cycles. However, a serious hurdle is the poor solubility that is often encountered. Recently, a coordination polymer was prepared to achieve very high birefringence ($\Delta n = 0.43$ vs. 0.172 for calcite).[18] This material may be exploited as a new way to target high PIB by incorporating azo groups.

Most of the above possibilities involve challenging and/or expensive synthetic procedures. The procedures can be simplified by recourse to ionic complexation of azo-containing small molecules, an approach whose promise has been demonstrated in this thesis. To further increase both rigidity and stability inside the complexes, ionic crosslinks may be introduced. More rigid groups, such as the iptycene unit,[19] may be introduced to improve the stability of photoorientation.

SRG is a practical application of azo materials in optics. Diffraction gratings with sinusoidal profiles can be grouped into different classes based on the ratio between the amplitude and the periodicity.[20,21] MO/PVP can achieve 0.36, which is in the class of high modulation gratings ($0.25 < \text{ratio} \leq 0.4$).[20,21] It is thought to "have the maximum useful first order efficiency of sinusoidal-groove gratings",[20,21] and one potential application is for

making high performance blazing gratings. So, a reasonable question is "How can we fabricate reflection gratings based on SRG from azo materials"? It deals with treating the SRG as master and making replicas from it, etc.[20,21] This may be more of an engineering issue.

However, the mechanism of SRG formation also still remains an issue to study.[22] Although spectroscopic methods have been used to show the orientation evolution of the azo moiety between peak and valley in SRGs,[23-26] it should be more enlightening for better understanding of the mechanism of SRG formation if the mass migration could be tracked *in situ*. Labeling techniques may be conceived for this end.

Nonlinear optics (NLO) has been another intensely investigated topic for azobenzene materials for quite a long time.[27] Recently, an azobenzene material showing very intense fluorescence has been synthesized,[28] which opens the door for a whole new area. Ionic complexes of the type developed in this thesis may also have something to contribute in these two areas.

9.2.2.2 Azo-containing materials designed using novel polymer structures

Much work has been done with azo-containing main-chain and side-chain LCPs. Supramolecular chemistry has been in this area since about 15 years, and shows very interesting and promising aspects. Supramolecular azo materials combined with more complicated polymer structures are just starting to be studied: these include dendrimeric, hyperbranched, and macrocyclic polymers as well as block copolymers.[29,30] Interesting possibilities, like introducing different mesogens cores into different block components within one block copolymer, can provide a unique way to understand and exploit the interaction between blocks and its effects on LC phases and properties.[29,31]

The importance of block copolymers may lie in the rising popularity of nanofabrication by self-assembly.[32] Besides this, delicate fibers with fine nanostructures can also be prepared.[33,34] These ideas can be incorporated into azo-containing LC fibers for future development.

9.2.2.3 Photomechanics

Photomechanical (PM) materials show promising applications in noncontact automatic control processes where it is necessary to transform energy from one form to

another, such as from light to mechanical force.[35-37] To this end, much work has been done by the Ikeda group on liquid crystalline elastomers (LCEs).[37,38] The alignment of mesogens in LCEs can make it possible to induce very large anisotropic deformations in cooperation with phase transitions.[37] Work has also been done on LCE fibers that exhibit very high (35%) thermoelastic response through the nematic-isotropic phase transition.[39] Recently, very interesting work has been done on 2D azopolymer films to achieve photobending.[37,38,40] We believe that azo-containing LCE fibers can also show interesting photomechanical properties. For example, large photo-stretching or photo-shrinkage might be possible in 1D fibers made of azopolymers. The preliminary work on preparing fibers with the MO/PVP complex by electrospinning (Chapter 8) may be explored for those purposes. The basic idea can be modified by designing an elastomeric thermotropic material with an accessible phase transition temperature (as opposed to the invariable SmA structure of MO/PVP up to degradation). Main-chain supramolecular azo-containing LCEs may be a promising candidate.[41]

9.2.2.4 Other applications

Azobenzene can be incorporated in almost any material where light response is desired. Functional surfaces are another popular topic nowadays. Ever since the invention of "command surfaces" by Ichimura in 1988,[42] azo materials have been receiving much attention for making light responsive surfaces.[43-45] Considering the moisture affinity of ionically bonded LC complexes studied in this thesis, it may be expected to show different surface phenomena from covalent systems that can be exploited.

Azo properties can also be used in our bodies. Cell signalling can be controlled by light through photoisomerization of azobenzene.[46] Drug delivery can also be controlled by light, simply by adding a photosensitive azo surfactant to liposomes, for example.[47] A similar idea was used in amphiphilic block copolymers that form micelles in water for drug delivery.[48] These ideas are based on the possibility of destabilizing the drug carrier by the shape and polarity changes of azo molecules exposed to light. In a study of azobenzene-modified silica, Zhu and Fujiwara attributed photo-regulative release to a mechanical stirring effect during photoisomerization.[49]

These topics can no doubt be further developed combining azo moieties, liquid crystalline properties and self-assembly.

9.3 Summary

Azobenzene materials appear to be an inexhaustible source of novelty. Wherever light is considered as an external stimulus, azobenzene is at the top of the list. Its advantage is not only the well-known photoisomerization process and subsequent orientation, but also its use as mesogens in liquid crystal science. Our imagination can run freely to design complicated and versatile materials with hierarchical structures in liquid crystals, even without mentioning the versatile chemical structures available with polymer materials. Supramolecular chemistry provides a second tool, from a different angle, to study, design and control the performance of materials. It has redirected the study of azobenzene and thus enhanced the vigour of azobenzene science. Furthermore, supramolecular chemistry can allow the development of more efficient and more economical procedures than all-covalent chemistry. I believe that, with environmental, energy and sustainable development problems which need urgent solutions nowadays, this is more and more important. This in itself justifies this Ph.D thesis. Recently, the Ikeda group invented a light-driven motor based on the photomechanics of azo polymers (Figure 9.4).[50] This promises new opportunities for azo materials in the future. Hopefully, our world will become "greener" with the contribution, small as it is, from the orange dye, azobenzene.

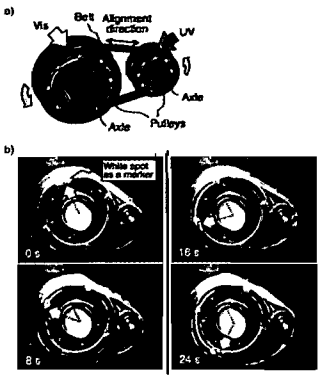

Figure 9.4 A light-driven motor based on an azobenzene liquid crystalline elastomer.[50]

9.4 References

1. Imrie, C. T.; Karasz, F. E.; Attard, G. S. *Macromolecules* **1993,** 26, 3803-3810.
2. Imrie, C. T.; Karasz, F. E.; Attard, G. S. *Macromolecules* **1993,** 26, 545-550.
3. Imrie, C. T.; Schleeh, T.; Karasz, F. E.; Attard, G. S. *Macromolecules* **1993,** 26, 539-544.
4. Eisenberg, A.; Kim, J.-S., *Introduction to ionomers*. John Wiley & Sons, Inc.: New York, 1998.
5. Tschierske, C. *Annu. Rep. Prog. Chem., Sect. C: Phys. Chem.* **2001,** 97, 191-267.
6. Antonietti, M.; Goltner, C. *Angew. Chem., Int. Ed.* **1997,** 36, 911-928.
7. Finkelmann, H.; Ringsdorf, H.; Wendorff, J. H. *Makromol. Chem.* **1978,** 179, 273-276.
8. Finkelmann, H.; Wendorff, H. J., *Polymeric Liquid Crystals*. Plenum Press: New York and London, 1985; p 295-302.
9. Zhang, Q.; Bazuin, C. G.; Barrett, C. J. *Chem. Mater.* **2008,** 20, 29-31.
10. Zhang, Q.; Wang, X.; Barrett, C. J.; Bazuin, C. G. *Chem. Mater.* **2009,** 21, 3216-3227.
11. Natansohn, A.; Rochon, P. *Chem. Rev.* **2002,** 102, 4139-4175.
12. Barrett, C. J.; Natansohn, A. L.; Rochon, P. L. *J. Phys. Chem.* **1996,** 100, 8836-8842.
13. Okano, K.; Shishido, A.; Ikeda, T.; Shiono, T. *Mol. Cryst. Liq. Cryst.* **2005,** 441, 275-285.
14. Okano, K.; Shishido, A.; Tsutsumi, O.; Shiono, T.; Ikeda, T. *J. Mater. Chem.* **2005,** 15, 3395-3401.
15. Okano, K.; Tsutsumi, O.; Shishido, A.; Ikeda, T. *J. Am. Chem. Soc.* **2006,** 128, 15368-15369.
16. Lachut, B. L.; Maier, S. A.; Atwater, H. A.; de Dood, M. J. A.; Polman, A.; Hagen, R.; Kostromine, S. *Adv. Mater.* **2004,** 16, 1746-1750.
17. Dufresne, S.; Gaultois, M.; Skene, W. G. *Opt. Mater.* **2008,** 30, 961-967.
18. Katz, M. J.; Kaluarachchi, H.; Batchelor, R. J.; Bokov, A. A.; Ye, Z.-G.; Leznoff, D. B. *Angew. Chem., Int. Ed.* **2007,** 46, 8804-7.
19. Swager, T. M. *Acc. Chem. Res.* **2008,** 41, 1181-1189.
20. Palmer, C., *Diffraction Grating Handbook*. Milton Roy Company: Rochester, 1994.
21. Hutley, M. C., *Diffraction gratings*. Academic Press: New York, 1982.
22. Yager, K. G.; Barrett, C. J., Light-induced nanostructure formation using azobenzene polymers. In *Polymeric Nanostructures and Their Applications*, Nalwa, H. S., Ed.; American Scientific Publishers: Los Angeles, 2007; Vol. 2, pp. 243-280.
23. Henneberg, O.; Geue, T.; Pietsch, U.; Saphiannikova, M.; Winter, B. *Appl. Phys. Lett.* **2004,** 84, 1561-1563.
24. Labarthet, F. L.; Bruneel, J. L.; Buffeteau, T.; Sourisseau, C. *J. Phys. Chem. B* **2004,** 108, 6949-6960.
25. Labarthet, F. L.; Bruneel, J. L.; Sourisseau, C.; Huber, M. R.; Borger, V.; Menzel, H. *J. Raman Spectrosc.* **2001,** 32, 665-675.
26. Labarthet, F. L.; Bruneel, J.-L.; Buffeteau, T.; Sourisseau, C.; Huber, M. R.; Zilker, S. J.; Bieringer, T. *Phys. Chem. Chem. Phys.* **2000,** 2, 5154-5167.

27. Yesodha, S. K.; Sadashiva Pillai, C. K.; Tsutsumi, N. *Prog. Polym. Sci.* **2004,** 29, 45-74.
28. Yoshino, J.; Kano, N.; Kawashima, T. *Chem. Commun.* **2007**, 559-561.
29. Zhao, Y.; Qi, B.; Tong, X.; Zhao, Y. *Macromolecules* **2008,** 41, 3823-3831.
30. Marcos, M.; Alcala, R.; Barbera, J.; Romero, P.; Sanchez, C.; Serrano, J. L. *Chem. Mater.* **2008,** 20, 5209-5217.
31. Zhao, Y., Azobenzene-containing block copolymers. In *Polymeric Nanostructures and Their Applications*, Nalwa, H. S., Ed.; American Scientific Publishers: Los Angeles, 2007; Vol. 2, pp. 281-311.
32. Gates, B. D.; Xu, Q.; Stewart, M.; Ryan, D.; Willson, C. G.; Whitesides, G. M. *Chem. Rev.* **2005,** 105, 1171-1196.
33. Ruotsalainen, T.; Turku, J.; Heikkilae, P.; Ruokolainen, J.; Nykaenen, A.; Laitinen, T.; Torkkeli, M.; Serimaa, R.; ten Brinke, G.; Harlin, A.; Ikkala, O. *Adv. Mater.* **2005,** 17, 1048-1052.
34. Ruotsalainen, T.; Turku, J.; Hiekkataipale, P.; Vainio, U.; Serimaa, R.; ten Brinke, G.; Harlin, A.; Ruokolainen, J.; Ikkala, O. *Soft Matter* **2007,** 3, 978-985.
35. Barrett, C. J.; Mamiya, J.-i.; Yager, K. G.; Ikeda, T. *Soft Matter* **2007,** 3, 1249-1261.
36. Camacho-Lopez, M.; Finkelmann, H.; Palffy-Muhoray, P.; Shelley, M. *Nat. Mater.* **2004,** 3, 307-310.
37. Ikeda, T.; Mamiya, J.-i.; Yu, Y. *Angew. Chem., Int. Ed.* **2007,** 46, 506-528.
38. Yu, Y.; Nakano, M.; Ikeda, T. *Nature* **2003,** 425, 145.
39. Naciri, J.; Srinivasan, A.; Jeon, H.; Nikolov, N.; Keller, P.; Ratna, B. R. *Macromolecules* **2003,** 36, 8499-8505.
40. Mamiya, J.-i.; Yoshitake, A.; Kondo, M.; Yu, Y.; Ikeda, T. *J. Mater. Chem.* **2008,** 18, 63-65.
41. Toh, C. L.; Xu, J.; Lu, X.; He, C. *Liq. Cryst.* **2008,** 35, 241-251.
42. Ichimura, K.; Suzuki, Y.; Seki, T.; Hosoki, A.; Aoki, K. *Langmuir* **1988,** 4, 1214-1216.
43. Feng, C. L.; Qu, G.; Song, Y.; Jiang, L.; Zhu, D. *Surf. Interface Anal.* **2006,** 38, 1343-1347.
44. Moeller, G.; Harke, M.; Motschmann, H.; Prescher, D. *Langmuir* **1998,** 14, 4955-4957.
45. Paik, M. Y.; Krishnan, S.; You, F.; Li, X.; Hexemer, A.; Ando, Y.; Kang, S. H.; Fischer, D. A.; Kramer, E. J.; Ober, C. K. *Langmuir* **2007,** 23, 5110-5119.
46. Gorostiza, P.; Isacoff, E. Y. *Science* **2008,** 322, 395-399.
47. Liu, X.-M.; Yang, B.; Wang, Y.-L.; Wang, J.-Y. *Chem. Mater.* **2005,** 17, 2792-2795.
48. Zhao, Y. *Chem. Rec.* **2007,** 7, 286-294.
49. Zhu, Y.; Fujiwara, M. *Angew. Chem., Int. Ed.* **2007,** 46, 2241-2244.
50. Yamada, M.; Kondo, M.; Mamiya, J.-i.; Yu, Y.; Kinoshita, M.; Barrett, C. J.; Ikeda, T. *Angew. Chem., Int. Ed.* **2008,** 47, 4986-4988.